## I.1 Scientific Motivation

### I.1.1 The Heavy Ion Physics Program

### I.1.1.a Soft Physics

**Measurements of Global $E_T$**

The most interesting collisions at RHIC are those that produce the highest densities and temperatures. This is thought to be the most promising environment in which to search for novel phenomena and signatures of a deconfined phase of quarks and gluons. The most characteristic feature of these conditions is expected to be the observation at mid-rapidity of a high multiplicity of particles and high transverse energy deposition ($E_T$).

The distribution of $E_T$ characteristically observed in relativistic nuclear collisions consists of a plateau region followed by a region of rapidly decreasing probability at the highest $E_T$ values as shown in Fig I.1.1-1[1]. The slope of the distribution in the high $E_T$ region is determined by fluctuations in the energy-transferring interactions of the nuclear constituents. It has been suggested that a measurable part of these fluctuations may be due to fluctuations in the partonic states of the incident hadronic systems[2], and are interesting for this reason. Whatever their origin, the fluctuations in $E_T$ represent variations in the energy density produced in the collisions and must be measured accurately if that range of energy densities is to be understood.

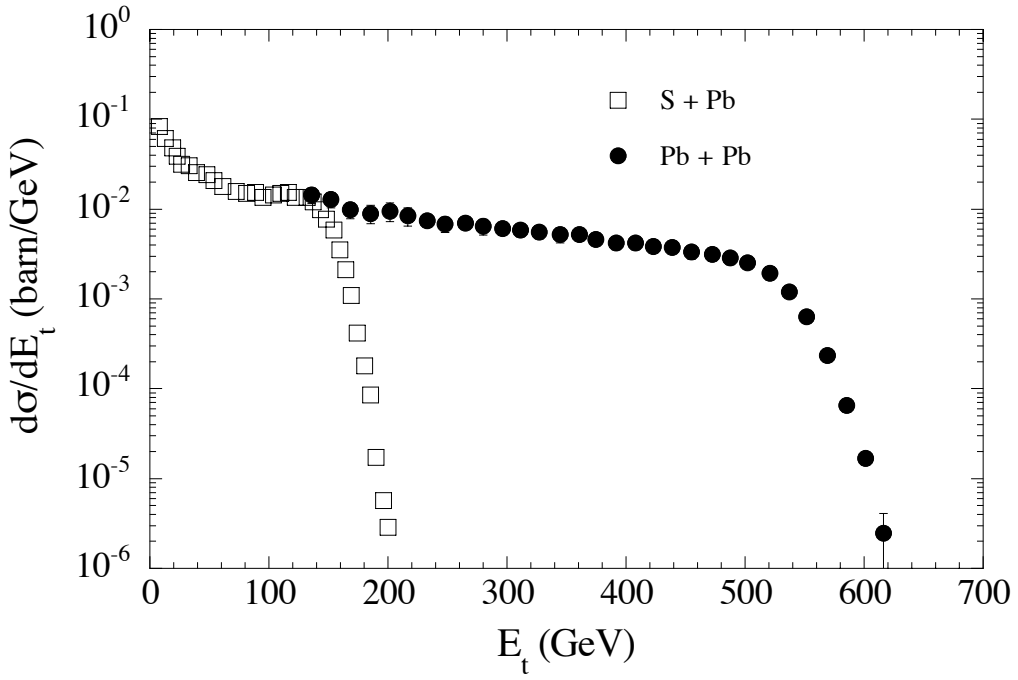


Figure I.1.1-1. The distribution of $E_t$ observed by NA49[1] for 158 GeV/nucleon S + Pb and Pb + Pb collisions for $2.1 < \eta < 3.4$. The distribution exhibits a plateau followed by a region of rapidly decreasing probability at the highest $E_t$ values.

[1] T. Alber et al. (NA49), Phys. Rev. Lett. **75**, 3814 (1995).
[2] B. Blättel et al., Nucl. Phys **A544** (1992) 479.

Experimental resolutions that are comparable to, or larger than, the natural physics width of the parent distribution lead to a dilution of the sample of high $E_T$ events and are therefore undesirable. With the proposed barrel electromagnetic calorimeter, which is the only device that measures $E_T$ (as opposed to multiplicity), the resolution for determining $E_T$ improves to ~2%, such that ~90% of the events in the top 5% of the observed distribution will originate from the parent distribution of interest. The parent distribution is assumed to have an intrinsic width of $\sigma = 5\%$. This is comparable, for example, to the results obtained for S+Pb collisions at 200 A GeV with the Helios[3] spectrometer. In this instance, the experimental resolution was $\sigma = 3.8\%$, and the observed $E_T$ falloff of 7% could be interpreted in terms of physical processes.

**Searching for Rare Events Indicating a Phase Transition**

It has been argued[4,5,6] on rather general grounds for some time that the mean transverse momentum, $<p_{Tt}>$,_of particles produced in hadronic interactions, observed as a function of the multiplicity

$$N = \int (dN/dy)\, dy \qquad \text{(I.A-1)}$$

in a given rapidity interval, reflects the properties of the equation of state of high temperature hadronic matter. Assuming that a description in terms of hydrodynamics is appropriate, dN/dy is related to the entropy, whereas the $p_T$ spectrum reflects the combined effects of temperature and transverse expansion. Except in the vicinity of a phase transition, higher entropy production in normal hadronic matter requires higher temperature, a correlation observed experimentally, for example, at the CERN collider.[7] In the vicinity of a first order phase transition however, the large latent heat required to melt the hadronic matter into a plasma of quarks and gluons leads to a situation in which the energy density and entropy density may increase dramatically, while the temperature and pressure remain essentially constant. In this instance one would expect to observe a departure from the usual correlation between dN/dy and $<p_T>$ in which the increase in the mean $p_T$ as a function of multiplicity slowed, or even decreased slightly due to reduced transverse expansion in a limited range of dN/dy. Above the transition, one would again recover the standard correlation, the thermodynamic relations for an ideal gas of massless quarks and gluons being similar to that for a gas of massless pions. The behavior one might expect to observed experimentally is indicated qualitatively in Fig. I.1.1.-2.

While this picture suffers from a number of oversimplifications, more detailed studies[8] of the hydrodynamic evolution of matter in ultrarelativistic nucleus-nucleus collisions appear to indicate the behavior expected based on the simple arguments presented above survives the refinement of proper treatment of the longitudinal and

---

[3]T. Akesson et al., Nucl. Phys. **B353** (1991) 1.
[4]E.V. Shuryak, Phys. Rep. **61** (1980) 71.
[5]E.V. Shuryak and O. Zhirov, Phys. Lett. **89B** (1980) 253; Sov. J. Nucl. Phys. **28** (1978)247.
[6] L. Van Hove, Phys. Lett. **118B** (1982) 138.
[7]UA1 Collaboration, G. Arnison et al., "Transverse Momentum Spectra for Charged Particles at the CERN Proton-Anti-proton Collider," presented XXIth International Conference on High Energy Physics, July 1982, Paris, France.
[8]M Kataja, P.V. Ruuskanen, L.D. McLerran, and H. von Gersdorff, Phys. Rev. **D34** (1986) 2755.

transverse expansion which occur during the mixed phase. The mean $p_T$ in this instance does not decrease in any interval of dN/dy, although the increase in the vicinity of the phase transition is once again slowed considerably (Fig. I.1.1.-3). Perhaps the most important conclusion however, is that the correlation between $<p_T>$ and dN/dy does in fact reflect properties of the equation of state. While the order and nature of the transition are matters for experiment, the sensitivity of this correlation to the fundamental character of the matter being probed makes this correlation potentially a useful tool in identifying events in which a transition has occurred.

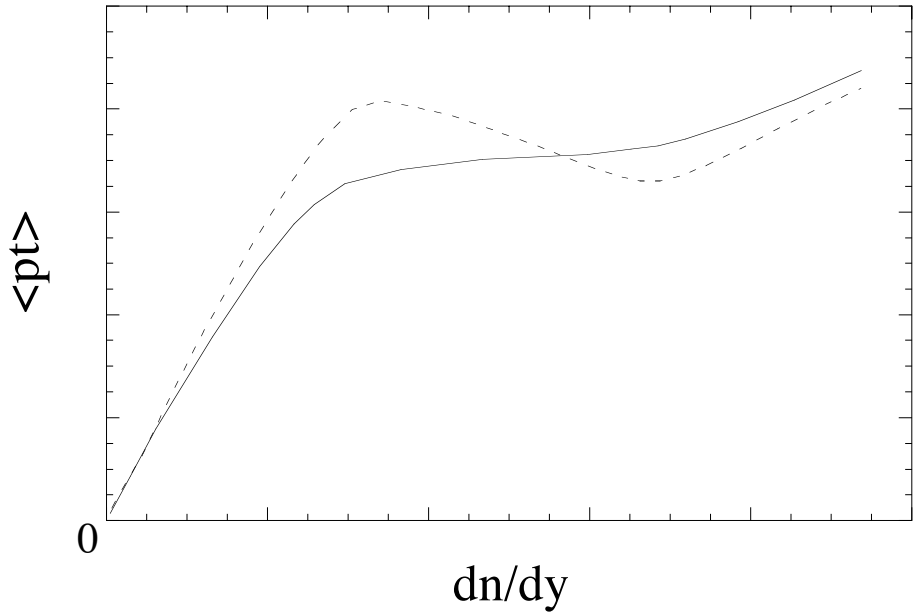


Figure I.1.1-2. The expected structure in the $<p_t>$ versus dn/dy correlation at a given impact parameter resulting from a first order phase transition. Further details may be found in Reference 6.

If the transition to a plasma of quarks and gluons occurs with high probability, the correlation between $<p_T>$ and dN/dy is best studied within STAR using single particle inclusive data provided by the time projection chamber (TPC). Aside from possible Coulomb effects which should be small, there is no reason to expect a priori that the mean $p_T$ measured for charged pions should be different than that for $\pi^0$'s. In that event, the resolution and systematic uncertainties in determining the mean $<p_T>$ using tracks in the TPC will be better than can be obtained by reconstructing low momentum $\pi^0$'s in the EMC, although some account will need to be taken of the fact that charged pions having $p_T < 40$ MeV/c spiral in the magnetic field and do not reach the TPC. The effective $p_T$ cutoff may in fact be somewhat higher in nucleus-nucleus collisions due to the high occupancy for the inner pad rows, although the silicon vertex tracker (SVT) will in principle recover most low momentum tracks. Use of the TPC tracking would in any event be preferable for studying this correlation since it would provide the most precise minimum bias data.

If the transition to the deconfined phase is rare however, it will be necessary, due to the overhead in analyzing large data samples, to develop a highly selective trigger to identify such events. Since complete tracking information from the TPC will not be available at the trigger level, the TPC alone can not provide such a trigger. If the

correlation between $<p_T>$ and dN/dy were known to be similar to that in Fig. I.1.1-3, for example, this could be accomplished simply by using the STAR central trigger barrel (CTB) to search for events with a given dN/dy. In reality however, the correlation between $<p_T>$ and dN/dy is completely unknown even for normal events in this energy range. In practice therefore, one would establish the behavior of the correlation for normal events, and then develop a trigger to search for a sample of events exhibiting an unusual correlation between $<p_T>$ and dN/dy. Since such events might occur as fluctuations in a normal range of dN/dy , the most exhaustive search would be conducted by examining the correlation between $<p_T>$ and dN/dy at the trigger level, rather than triggering on multiplicity alone.

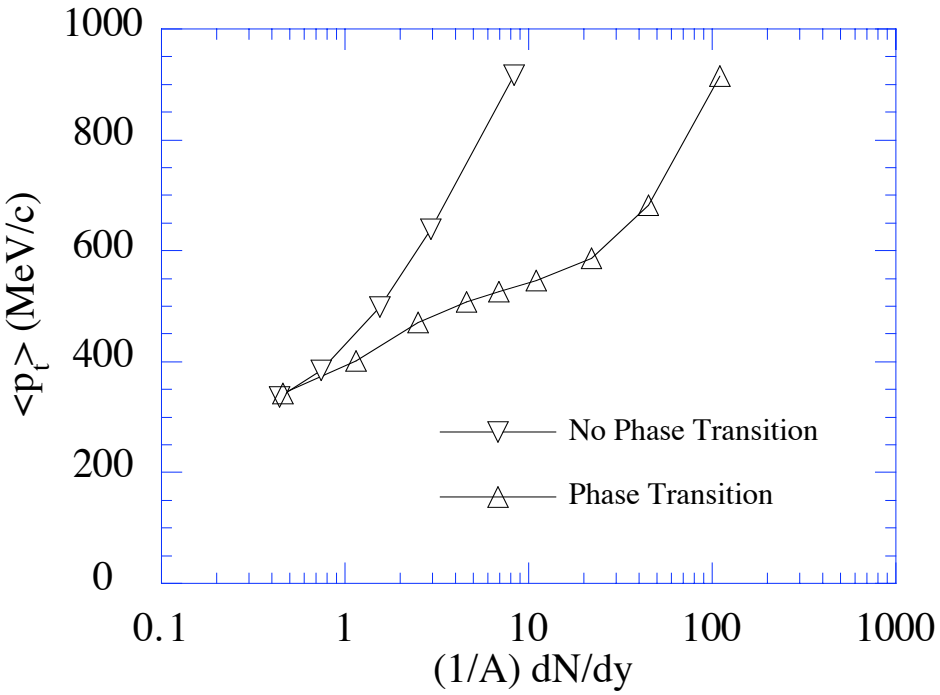


Figure I.1.1-3. The prediction from Reference 8 for the average $p_t$ as a function of the normalized multiplicity (1/A) dN/dy with ($\Delta$) and without ($\nabla$) a first order phase transition. At the point indicated by $\varepsilon = \varepsilon_o$, pure plasma state at $T_c$ is reached.

The STAR EMC provides a useful means to test this correlation at the trigger level. Because the calorimeter is sensitive to the ionization energy loss of charged particles as well as that from electromagnetic showers, the STAR EMC is sensitive to changes in the mean $p_T$ in a given event. When correlated with the multiplicity information provided by the STAR CTB on an event-by-event basis, or by using the EMC multiplicity information (available at higher levels of the trigger) the EMC provides a unique capability in STAR to search for events with an unusual correlation between energy density and entropy density. If such events are rare, the use of this highly selective trigger may be the only means by which to observe them.

**Isospin Fluctuations and Chiral Symmetry Restoration**

A number of conjectures have recently been put forward suggesting that one may expect large fluctuations in the photon to hadron ratio in ultra-relativistic heavy ion collisions. The interest in such possibilities stems from the apparent observation of large fluctuations in this ratio in recent cosmic ray data.[9,10] Although the physical bases for these predictions vary, all depend upon the high density and temperature that can be reached in central nucleus-nucleus collisions at RHIC.

Panagiotou et al.[11] consider that, assuming isospin is conserved, the low number of photons from $\pi^0$ decay observed in cosmic ray emulsion data may result from ultra-relativistic nucleus-nucleus collisions in which all pion production is suppressed in a given interval of rapidity. This is noted to be possible if a quark-gluon fireball with non-zero net baryon number is formed, since the high baryochemical potential in such a state suppresses the thermal production of quarks and anti-quarks and therefore the production of pions as well. A fireball of this type would most likely appear in the fragmentation region at RHIC and would be characterized by the suppression of all pion species. A related observation would be that baryons produced in the decay of the fireball would be characterized by a higher than average $<p_T>$.

A somewhat less speculative hypothesis by Pratt[12] expands on an earlier possibility suggested by Anslem and Ryskind[13] that a coherent pion field may be produced. More precisely, when the density of possible emission sources of identical bosons within a given volume exceeds a certain critical density, quantum interference effects and symmetrization of the N-body wave function become important. The consequence of symmetrization may be striking. In particular, stimulated emission of pions into low momentum states (pion lasing) might result. The multiplicity of pions is enhanced in general with large fluctuations in the number of pions of a given species possible, due to the fact that the interference depends upon the indistinguishability of bosons of a given isospin. This prediction is especially relevant for $\pi^0$ production where the unknown effects of Coulomb interactions are not a consideration. As a consequence, instead of a low photonic to hadronic ratio, one might expect some events to exhibit "anti-Centauro" behavior, with $\pi^0$ decay photons greatly outnumbering the charged pions observed in a limited region of rapidity ($|\Delta y| < 1$). Empirical estimates from S + Pb collisions at CERN suggest that the pion densities reached are within a factor of two of the critical density required for stimulated emission, and that in any event, this effect will need to be accounted for in order to understand high-multiplicity events. An enhancement of the observed pion spectra at low $p_T$, and two-particle HBT correlations indicating coherent production would be other indications that symmetrization was important.

Taking a deeper look at the QCD vacuum, Bjorken[14] suggests that a collision between two ultra-relativistic heavy ions may result in a highly excited, colorless system whose isospin orientation may be quite arbitrary. As a consequence, the ratio of neutral to charged pions may fluctuate widely from the normal isospin expectation. Bjorken

---

[9]Chacaltaya and Pamir Collaboration, Tokyo University preprint ICRR Report-232-91-1 (1991).
[10]C.M.G. Lattes, Y. Fugimoto, and S. Hawegawa, Phys. Rep. **65** (1980) 151.
[11]A. Panagiotou et al., Phys. Rev. **D45** (1991) 3134.
[12]S. Pratt, Phys. Lett. **B301** (1993) 159.
[13]A.A. Anselm and M. Pyskind, Phys. Lett. **B266** (1991) 482.
[14]J.D. Bjorken, Acta Physica Polonica **B23** (1992) 637.

expects that heavy ions may be the most effective way to produce this phenomenon. This prediction is similar to that of Wilczek[15], who suggests that a disoriented chiral condensate may be one consequence of a quench of the quark-gluon plasma which may be formed.

Investigation of these phenomena depends entirely on the ability to identify neutral electromagnetic energy ($\pi^0$ daughters) and charged particles over a wide range of acceptance. This study is therefore not possible in STAR without the capabilities provided by the electromagnetic calorimeter. The TPC and charged-particle multiplicity detectors together with the proposed EM calorimeter can accomplish this task with reasonable spatial and energy resolution. The potential for discovery of such wide fluctuations in the photon to hadron ratio is therefore a distinct possibility. Simulations designed to determine the limits of the ability of the EM calorimeter to identify, trigger upon, and measure these fluctuations are described in elsewhere in this report. The results indicate clearly, that with the coverage projected in the STAR EMC proposal, a sensitive search for these exciting possibilities in heavy ion collisions at RHIC is feasible.

### 1.1.1.B. High $p_T$, Hard Probes, and Parton Physics

**Parton Energy Loss**

The measurement of jets, direct photons, electrons from heavy flavor and quarkonium decays, and high $p_T$ particles using the STAR electromagnetic calorimeter is essential, since these processes presently represent the only means within STAR of probing the high temperature, gluon-dominated, pre-equilibrium stage of the collision. A goal of studying the products of hard QCD processes in relativistic heavy ion collisions is to use the propagation of quarks and gluons as a penetrating probe of nuclear matter, hot hadronic matter, and quark matter. Since the hard-scattering processes occur at the very earliest stage of the collision ($t < 1$ fm/c), their production rates are dependent only upon the incoming state. Given the quark and gluon structure functions of the colliding nuclei, the rate as a function of $p_T$ of hard parton scattering is entirely calculable using perturbative QCD. This situation is unique to RHIC, which will be the first accelerator to provide nuclear collisions at energies where rates of detectable partonic debris (jets, high-$p_T$ particles, and direct photons) from hard partonic scattering permit accurate measurements.

Various calculations have predicted that the propagation of quarks and gluons through matter depends strongly upon properties of the medium,[16,17,18,19,20] and that a measurement of the yield of hard-scattered partons as a function of transverse energy may be sensitive to the state of the surrounding matter. It has been suggested, for example, that there will be observable changes in the energy loss of propagating partons as the energy density of the medium increases, particularly if the medium passes through

[15] F. Wilczek, "Chiral Dynamics Near Equilibrium or After Quenching," Proceedings of the Tenth International Conference on Ultra-Relativistic Nucleus-Nucleus Collisions, June 20–24, 1993, Borlänge, Sweden.
[16] J.D. Bjorken, Fermilab Report 82/59/59-THY (1982).
[17] D. Appel, Phys. Rev. **D33** (1986) 717.
[18] J.P. Blaizot and L.D. McLerran, Phys. Rev. **D34** (1986) 2739.
[19] M. Rammersdorfer and U. Heinz, Phys. Rev. **D41** (1990) 306.
[20] M. Gyulassy and M. Pluemmer, Phys. Lett. **B243** (1990) 432.

a phase transition to the QGP.[21] Interest in this possibility originally focused on the observation that the collisional energy loss of a quark of energy E propagating through an ideal plasma of quarks and gluons at temperature T could be expressed[22] as

$$(dE/dx) \quad \alpha \quad \alpha_s^2 \, T^2 \log (4ET/M^2) \exp(-M/T) \, (1 + M/T) \quad , \qquad \text{(I.A-2)}$$

where M is an infrared cutoff on the order of the Debye mass. The strong dependence of this expression on $\alpha_s$ lead to speculation that in the vicinity of a phase transition the normal energy loss experienced by propagating quarks and gluons might be reduced due to decreased coupling between partons in this environment. More recently, it has been noted[23] that another sensitive probe may be the radiative energy loss of propagating partons,

$$(dE/dx) \;\; \alpha \;\; \alpha_s \, M^2 \, (\log(s/4M^2))^2 \quad . \qquad \text{(I.A-3)}$$

whereas the radiative energy loss for high-energy partons propagating through nuclear matter would normally be strongly suppressed due to the Landau-Pomeranchuk effect, the reduced Debye screening length predicted[24] for the plasma ($\lambda_D = M^{-1} \sim 0.4$) could increase the radiative energy loss significantly. This same effect is predicted to lead to the suppression of vector meson production ($J/\psi$, $\psi'$, $\Upsilon$) Correlation of these results could help determine if effects that might be observed for vector meson production are due to plasma formation, or result instead from propagation within the nuclear medium.

The consequence of parton energy loss in a medium is jet quenching, or the reduction of the jet yield at a given $p_T$. This effect, which is most important for intermediate energy jets (5-10 GeV), has already been observed in deep inelastic lepton scattering from nuclear targets.[25] It is most effectively studied using the qg $\leftrightarrow$ qg Compton subprocess, since for this process complications due to the fragmentation function are not a consideration and the $p_T$ of the parton scatter may be determined from the $p_T$ of the direct photon, modulo $k_T$ smearing of the $p_T$ balance from initial state radiation of the quarks and gluons. (An effect measurable from diphoton production in p+A collisions)

It may also be studied using di-jets. In this instance it is essential to measure the energy of both jets in di-jet events. The sum of the jet energies and the di-jet invariant mass are sensitive to interactions of the partons with the medium. The yield as a function of invariant mass of back-to-back jets at mid-rapidity may be the best tool for studying effects of the matter on propagation, since in this case the overall path length in the medium is maximized. The difference of di-jet energies may be sensitive to the

---

[21]M. Gyulassy et al., Lawrence Berkeley Laboratory Report LBL-31002, to be published in Proceedings of 4th Conference on the Intersections between Particle and Nuclear Physics, Tucson, Arizona, 1991.

[22]J.D. Bjorken, Fermilab Report 82/59/59-THY (1982).

[23]M. Gyulassy, "Nuclear Chromodynamics in eA, pA, and AA Interactions," proceedings of the Future Directions in Particle and Nuclear Physics at Multi-GeV Hadron beam Facilities Meeting, March 4–6, 1993, Brookhaven National Laboratory, Upton, New York.

[24]B. Muller, "Physics of the Quark-Gluon Plasma," Proceedings of the NATO Advanced Study Institute on Particle Production in Highly Excited Matter, July 12–24, 1992, Il Ciocco, Italy; Duke Report No. DUKE-TH-92-36

[25]L. S. Osborne et al., Phys. Rev. Lett. **40** (1978) 1624; P.B. Renton et al., Oxford Nuclear Physics Laboratory preprint 55/88 (1988); M Gyulassy and M. Plummer, LBL preprint LBL-27234.

difference in path lengths traversed by the partons. In addition, measurement of both jets in a di-jet event suppresses background due to fluctuations of soft production processes that can mimic a jet. A measurement of the di-jet differential cross section for p-nucleus collisions will in itself be of interest for understanding the parton structure functions in nuclear matter.

Jet quenching is also expected to lead to significant effects in the spectra of single high $p_T$ particles, di-hadrons, and jets in AA collisions at RHIC.[26] This is not surprising since virtually all particles observed above $p_T \sim$ 2-3 GeV/c arise as fragmentation products from hard parton scatters.

In general, the reconstruction of the parton-scattering kinematics is limited by acceptance and detector resolution effects, and by the superposition of particles from other, incoherent processes which occur during the collision. This last problem is especially serious in high-multiplicity AA collisions, where the jet can be entirely obscured. The technique of jet reconstruction to extract parton information with the STAR EMC in pA and AA collisions is presently being investigated. Nontheless, because the heart of any jet identification algorithm is the correlations between nearby particles, the ability to measure photons as well as high $p_T$ charged particles is an important element in any jet reconstruction program. The yield of jets as a function of $p_T$, as well as the ability of the STAR EMC to trigger upon jets is discussed further elsewhere in this report.

A systematic study of parton energy loss in pA and AA interactions using the STAR EMC will provide a unique tool to search for a transition to a quark gluon plasma in ultra-relativistic nucleus-nucleus collisions. Additionally, events identified as candidates for further study using other signatures may be probed with this technique to determine the nature of the medium in the initial phase of the collision. The STAR EMC is essential for this study of jets and direct photons, since measurement of the neutral electromagnetic energy is necessary to reconstruct jets or detect direct photons. Although the study of single high $p_T$ particles may in principle be accomplished using tracking information from the STAR TPC, without the EMC it is not presently possible to trigger upon high $p_T$ particles. Additionally, energy resolution as measured in a calorimeter improves with increasing energy, while momentum resolution as measured in a spectrometer degrades with increasing momentum.

**Mini-Jets and High $p_t$ Tails of Distributions**

Mini-jets are expected to be produced copiously in collisions at RHIC.[27,28] As is the case for high $p_T$ jets, the observed yield of mini-jets is expected to be influenced strongly by the state of the high-density medium through which they propagate.[29] However, direct measurement of mini-jets is virtually impossible because of their large opening angle and the strongly varying background. Thus, it is important to study the degree of fluctuation of the transverse energy and multiplicity as a function of pseudo-rapidity and azimuthal angle ($d^2 E_T /d\eta d\phi$ and $d^2n/d\eta d\phi$) event-by-event, which should be

[26]X.N. Wang and M. Gyulassy, Phys. Rev. Lett. **68** (1992) 1480.
[27]K. Kajantie, P.V. Landshoff, and J. Lindfors, Phys. Rev. Lett. **59** (1987) 2527.
[28]K.J. Eskola, K. Kajantie, and J. Lindfors, Nucl. Phys. **B323** (1989) 37.
[29]P.V. Landshoff, Nucl. Phys. **A498** (1989) 217; X.N. Wang, Lawrence Berkeley Laboratory Report LBL-28790 (1990), submitted to Phys. Rev. **D**.

strongly affected by the mini-jets.[30-31] The STAR EMC is essential for this study since without measuring the neutral transverse energy, the true degree of fluctuation due to mini-jets can not be determined. It is essential that this be systematically studied in pp and pA collisions, as well as AA.

Inclusive $p_T$ distributions of hadrons at $p_t > 3$ GeV/c will also be influenced by jets and mini-jets. It should be emphasized that the single particle cross sections fall off more rapidly as a function of $p_T$ than the jet cross sections.[32] However, Wang and Gyulassy[33] have shown that the inclusive single particle yield is very sensitive to the state of the matter through which the parent scattered partons propagate. Figure I.1.1.-4 shows the charged particle pseudorapidity distribution and the ratio of charged particle yields for Au-Au and p-Au collisions compared to p-p collisions as a function of $p_T$ , under various assumptions about the nuclear structure functions (shadowing) and energy loss of the scattered partons (quenching). From the middle panel of Fig. I.1.1.-4, it is seen that the introduction of quenching (in addition to shadowing) leads to a reduction in yield above $p_t$ ~4 GeV/c of a factor 5. Although effects of this magnitude may be observed by examining single particle inclusive spectra provided by the TPC, unfolding the effects of shadowing and quenching in order to interpret these data will require systematic studies using the STAR EMC.

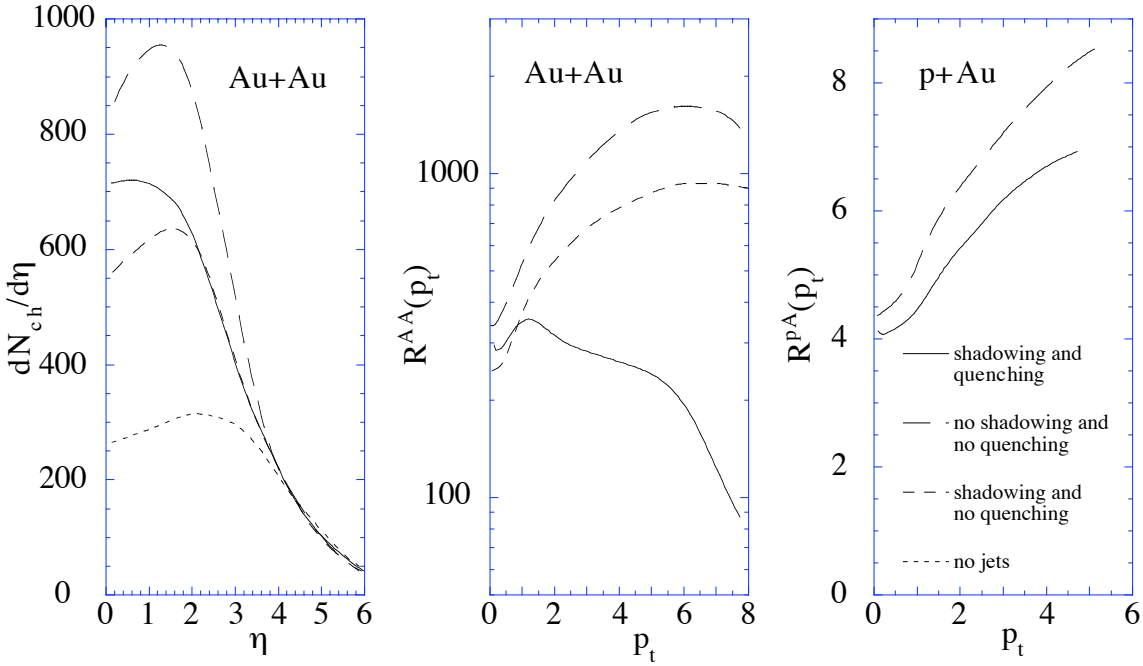


Figure I.1.1-4. Results from HIJING calculations on the dependence of the inclusive charged hadron spectra in central AuAu and pAu collisions on mini-jet production (dash-dotted), gluon shadowing (dashed) and jet quenching (solid) assuming that gluon shadowing is identical to that of quarks. $R^{AB}$ $(p_t)$ is the ratio of the inclusive $p_t$ spectrum of charged hadrons in A+B collisions to that of pp. Details may be found in Reference 33 in this chapter.

[30] D. Appel, Phys. Rev. **D33** (1986) 717.
[31] X.N. Wang, Lawrence Berkeley Laboratory Report LBL-28789 (1990), submitted to Phys. Lett. B.
[32] See W. Geist et al., CERN/EP Report 89-159 (1989) to be published in Phys. Rep. (1990).
[33] X.N. Wang and M. Gyulassy, Phys. Rev. Lett. **68** (1992) 1480.

**Gluon Shadowing**

One of the primary advantages of RHIC is that unlike the situation at lower energy, where only a phenomenological approach was possible, firm predictions as to the early stages of the collision are possible using perturbative QCD. The ability to make full use of this potential, however, depends upon having knowledge of the parton structure functions in the nucleus. Deep inelastic scattering measurements presently underway will provide the necessary measurements for determination of the quark structure functions in nuclei, but little is expected to be known concerning the nuclear structure function for gluons at low Bjorken x. Simulations of the early stage of ultra-relativistic nucleus-nucleus collisions indicate it is precisely gluons at low Bjorken x which make the largest contribution to the energy density of the system produced at mid-rapidity, and dominate this phase of the evolution. The manifestation of this phase may be striking, including a dramatic increase in the production of open charm and mini-jets from semi-hard gluon-gluon scatters. Mini-jet production may account for up to 50% of the total transverse energy observed at mid-rapidity. Without measurement of the gluon shadowing, however, the theoretical predictions for $dn_{ch}/d$, and $d^2n/dydp_\perp$ are uncertain by ~30%. The interpretation of these data will be much less certain, and the understanding seriously compromised, if the incident gluon flux has not been determined. Some information on the gluon structure function will be provided by the NMC experiment at CERN, and Fermilab experiments E665, E706, E772, and E789. The available data in the low-x region of interest ($0.01 < x < 0.05$) tends to be limited either by systematics or low statistics. STAR, however, can measure the gluon densities in nuclei by measuring jet and direct photon production in pA collisions. Again the the $qg \leftrightarrow qg$ and $qg \leftrightarrow q\gamma$ Compton subprocess dominate here. These measurements in pA collisions are at exactly the same rapidity and $p_T$ (or, equivelently, Bjorken x) as we are interested in for AA, further reducing the systematic uncertainties.

### I.1.2 The Spin Physics Program

After decades of being regarded as an inessential complication to the strong interaction at high energy, spin has again come to the attention of the theoretical and experimental community. This is largely due to the fact that recent results from deep inelastic scattering experiments have shown that the spin of the nucleon is not accounted for by the spin of the quark constituents.[34,35] A NLO fit to the available data indicates that $\Delta\Sigma$, the spin component of the nucleon carried by the light quarks, is $0.27 \pm 0.04 \pm$ systematic experimental and theoretical uncertainty[36]. For the spin of the nucleon,

$$\frac{1}{2} = \frac{1}{2}\Delta\Sigma + \Delta G + L_Z \qquad \text{(I.1.2-1)}$$

Since only one-fourth of the nucleon spin comes from the quark spins, the spin must be carried by the gluon field, $\Delta G$, or by the orbital angular momentum $L_Z$.

This nucleon spin anomaly has generated several theoretical explanations. In the chiral soliton model, spin arises from the coherent rotation of a meson cloud and $\Delta G$ is expected to be near zero[37]. Single spin inclusive meson production using 200 GeV/c polarized proton and anti-proton beams has been interpreted in terms of quark-antiquark annihilation processes suggesting the existence of orbiting valence quarks inside polarized protons.[38] In theory based on the axial U (1) anomaly, $\Delta G$ is taken as a NLO correction to $\Delta u$, $\Delta d$, and $\Delta s$, and $\Delta G$ is expected to be large and positive[39]. Spin distribution functions have recently been published which extract $\Delta G$ (x) from scaling violations in the existing data for $\Delta u$ and $\Delta d$[40]. These generally predict moderate values for $\Delta G$ with $0 < \Delta G < 1$, but $\Delta G$ (x) can take on negative values for some range of x. There is also a theory that attempts to associate $\Delta G$ with the correct term in the momentum tensor for QCD and predicts $\Delta G < 0$[41].

There is also an abundance of data showing large and inexplicable spin effects at relatively low values of transverse momenta. Some of these effects have been studied: the polarization of inclusively produced hyperons, as well as the analyzing power in pion production persist at the highest energies and transverse momenta. Experiments with polarized hadron (and also polarized lepton) beams have been limited to fixed target energies of a few hundred GeV. Perhaps these hadronic spin effects are low energy, low $p_t$ phenomena, which will vanish at higher energies. On the other hand, perhaps they are asymptotic properties of the strong interaction. Continuing these measurements to very high energies would give much-needed answers. In fact, with a complete understanding of QCD and the spin structure of the proton, the spin effects observed in proton-proton collisions at RHIC energies should be calculable.

---

[34] J. Ashman *et al.*, Phys. Lett. B206 (1988) 364; Nucl. Phys. B328 (1989) 1.

[35] B. Adeva *et al.*, Phys. Lett. B302 (1993) 533. D.L. Adams *et al.*, Phys Lett B **336** (1994) 125; Phys Lett B **339** (1994) 332.

[36] J. Ellis, hep-ph/9611208.

[37] S.J. Brodsky, J. Ellis, and M. Karliner, Phys. Lett. B **206**, 309 (1988). J. Ellis and M. Karliner, Phys Lett B **313** (1993) 131; Phys Lett B **341** (1995) 397.

[38] C. Boros, Liang Zuo-tang and Meng Ta-chung, Phys. Rev. Lett. **70** (1993) 1751.

[39] A.V. Efremov and O.V. Teryaev, Dubna report JIN-E2-88-287 (1988); G. Altarelli and G. Ross, Phys. Lett. B **212**, 391 (1988)**;** R.D. Carlitz, J.D. Collins and A.H. Mueller, Phys. Lett B **214**, 219 (1988).

[40] M. Gl¸ck *et al.*, hep-ph/9508347; T Gehrmann and W.J. Stirling, hep-ph/9512406; R.D. Ball, S. Forte, and G. Ridolphi, Phys. Lett. B **378**, 255 (1996).

[41] R.L. Jaffe, hep-ph/9509279.

A critical ingredient in these calculations is the spin distribution of the various constituents of the proton: valence, sea quarks, and gluons. The helicity distributions of the valence plus sea quarks in the proton and the neutron have been measured in deep inelastic scattering of longitudinally polarized muons and electrons from longitudinally polarized proton (deuteron) targets at CERN and SLAC. The separate helicity distributions of sea quarks and gluons and the transversity distribution of quarks are also fundamental properties of the proton that cannot be measured in lepton scattering, but can easily be measured at RHIC with polarized proton beams. Knowledge of the quark and gluon spin distribution is essential information for calculation of spin observables in various parton-parton scattering processes, e.g., dijet production and $W^{\pm}$ and Zo production. All spin observables in pp $\rightarrow$ jet + jet + X should then be calculable, beginning at $Q^2$ values where higher twist effects must be included and extending out to $Q^2$ where only leading twist should be important. These measurements can easily be made at RHIC and afford stringent tests of QCD and of current models of the nucleon. Measurement of parity-violating asymmetries in weak boson production can further test the standard model and probe for new physics.

Measurement of all of the spin structure functions of the proton (quark, gluon, helicity, and transversity) at polarized RHIC would constitute a significant and important physics program.[42,43,44,45] These structure functions could then be used to make detailed tests of QCD by measurement of spin asymmetries in hadronic scattering processes, which would allow the most detailed test of QCD and our understanding of the nucleon that have ever been made. The addition of the EMC would not only increase the capability of STAR for searching for the quark-gluon plasma (QGP) but also afford complimentary tests of QCD at modest cost.

### I.1.2.a. Status of Present Knowledge

Experimental programs using polarized beams and polarized targets at high energies have been active during the past three decades. Many asymmetry measurements in a number of scattering processes (e.g., elastic scattering, deep inelastic scattering, and inclusive meson production) have been carried out at various laboratories in the world. As unique measurements often bring surprises, many exciting and unexpected results in hadron-hadron and muon-nucleon scattering have been observed using polarized beams and targets. These include large spin effects in pp elastic scattering,[46,47,48] inclusive pion production,[49,50,51,52,53,54,55,56,57] and in $\rho$ production.[58] The importance of spin as a funda-

---

[42]C. Bourrely, J.Ph. Guillet, and J. Soffer, Nucl. Phys. **B361** (1991) 72.
[43]M.A. Doncheski, F. Halzen, C.S. Kim, and M.L. Stong, University of Wisconsin report MAD/PH/744 (1993).
[44]For a review of spin physics possible at RHIC, see proceedings of the Polarized Collider Workshop, AIP Conference Proceedings No. 223, University Park, PA, 1990.
[45] G. Bunce *et al*., Particle World **3** (1992) 1.
[46]R.V. Kline *et al*., Phys. Rev. **D22** (1980) 553.
[47]G. Fidecaro *et al*., Phys. Lett. **105B** (1981) 309.
[48]F.Z. Khiari *et al*., Phys. Rev. **D39** (1989) 45.
[49]L. Dick *et al*., Phys. Lett. **57B** (1975) 93.
[50]R.D. Klem *et al*., Phys. Rev. Lett. **36** (1976) 929.
[51]D. Aschman *et al*., Nucl. Phys. **B142** (1978) 220.
[52]W.H. Dragoset *et al*., Phys. Rev. **D18** (1978) 3939.
[53]J. Antille *et al*., Phys. Lett. **94B** (1980) 523.
[54]S. Saroff *et al*., Phys. Rev. Lett. **64** (1990) 995.

mental degree of freedom has also been observed experimentally in deep inelastic lepton scattering[59,60] and hyperon production.[61,62,63,64,65,66] Thus far, experiments with polarized proton beams have been limited to about 200 GeV/c. It is extremely important to explore spin effects at much higher energies where high $p_t$ phenomena as well as parity-violating asymmetries in $W^{\pm}$ and $Z\infty$ production can be studied.

Programs to test quantum chromodynamics and explore the electroweak coupling at CERN and Fermilab have provided a wealth of information on the standard model of particle physics. However, these experiments at high-energy colliders do not cover the area of spin physics. Tests involving the spin-dependence in fundamental scattering processes such as jet, direct photon, Drell-Yan, and $W^{\pm}$, Zo boson production are yet to be carried out.

Polarized proton-proton collisions have previously been limited to a relatively low range of $\sqrt{s}$ and $Q^2$. Large polarization effects have been seen in many different experiments. Because of the low $Q^2$, spin physics has been relegated to a soft physics compartment in high energy physics since interpretation of these data using QCD has been problematic. A comprehensive program of spin physics experiments at RHIC using the STAR EMC would allow measurement of the spin-dependent parton distributions of the proton (both longitudinal and transverse) and would provide fundamental spin tests of QCD and the electro-weak interaction. The high energy and luminosity at RHIC will permit experiments in which an interpretation in terms of perturbative QCD will be unambiguous.

### I.1.2.b The Gluon Spin Distribution of the Proton

In this and subsequent sections, we present estimates of the acceptance of STAR and expected event rates for several reactions of interest.

In general, the luminosity at RHIC for pp running is energy dependent. The integrated luminosities used to calculate event rates discussed below are: $\int \ell dt = 800\ pb^{-1}$ at $\sqrt{s} = 500$ GeV, assuming $\ell = 2 \times 10^{32}\ cm^{-2}\,sec^{-1}$, and $\int \ell dt = 320\ pb^{-1}$ at $\sqrt{s} = 200$ GeV, assuming $\ell = 8 \times 10^{31}\ cm^{-2}sec^{-1}$. The beam polarization is assumed to be 0.7. The assumed running time is 10 weeks at 67% efficiency, or $4 \times 10^6$ sec.

Information on the gluon spin distribution in polarized protons can be obtained by measuring asymmetries in the cross section for various scattering processes which depend on the helicities of the colliding beams. Such processes include inclusive direct-$\gamma$ production, inclusive jet production, direct-$\gamma$ + jet, and jet-jet coincidences. Inclusive di-

---

[55]V.D. Apokin *et al.*, Phys. Lett. **243B** (1990) 461.
[56]B.E. Bonner *et al.*, Phys. Rev. Lett. **61** (1988) 1918.
[57]D.L. Adams *et al.*, Phys. Lett. **261B** (1991) 201; Phys. Lett. **264B** (1991) 462; Z. Phys. **C56** (1992) 181.
[58]S. Heppelmann *et al.*, Phys. Rev. Lett. **55** (1985) 1824.
[59]J. Ashman *et al.*, Phys. Lett. **B206** (1988) 364; Nucl. Phys. **B328** (1989) 1.
[60]B. Adeva *et al.*, Phys. Lett. **B302** (1993) 533.
[61]G. Bunce *et al.*, Phys. Rev. Lett. **36** (1976) 1113.
[62]S. Erhan *et al.*, Phys. Lett. **82B** (1979) 301.
[63]B.E. Bonner *et al.*, Phys. Rev. **D38** (1988) 729.
[64]L.G. Pondrom, Phys. Rep. **127** (1985) 57 and references therein.
[65]B. Lundberg *et al.*, Phys. Rev. **D40** (1989) 3557.
[66]K.B. Luk *et al.*, Phys. Rev. Lett. **70** (1993) 900.

rect-γ and direct-γ + jet production in pp interactions are dominated by a single parton-level subprocess,

$$q + g \rightarrow \gamma + q \quad , \qquad \text{(I.1.2-2)}$$

and determining the spin-dependent gluon distribution of the proton from these processes is straightforward. On the other hand, inclusive jet and jet-jet production contain contributions from many parton-level subprocesses (e.g., gg, qq, qg, etc. scattering), and extraction of the spin-dependent gluon structure function using these processes is more difficult, despite their increased cross section. Consider the hadronic reaction, pp → (hadron or gauge boson) + X. When both initial protons are longitudinally polarized with polarization P, we measure an observable $A_{LL}$ defined as,

$$A_{LL} = (1/P^2)(N^{++} - N^{+-})/(N^{++} + N^{+-}), \qquad \text{(I.1.2-3)}$$

where $N^{+-}$, for example, is the yield observed when the helicities of the two colliding beams are anti-aligned. If one QCD subprocess is dominant, then

$$A_{LL} \approx P_a P_b \hat{a}_{LL(a+b\rightarrow c+d)}, \qquad \text{(I.1.2-4)}$$

where $P_a$ and $P_b$ are the polarizations of partons a and b in the proton, and $A_{LL}$ is the parton-level asymmetry for a given subprocess.

For the determination of the gluon spin distribution, measurements of direct-γ, direct-γ with away-side jet, inclusive jet, and dijet production are proposed.

**Direct-γ Production[67]**

Direct photons are produced through $q\bar{q}$ annihilation and the q-g Compton subprocess (q + g → γ + q.) The Compton process is the dominant one in pp interactions at mid-rapidity since there are no valence antiquarks in the proton. Then,

$$A_{LL} \approx \left\langle \left[\Delta u(x_1)/u(x_1)\right]\cdot\left[\Delta G(x_2)/G(x_2)\right]\cdot\hat{a}_{LL(qg\rightarrow\gamma q)} \right\rangle \quad \text{(I.1.2-5)}$$

where the u quark polarization is $\Delta u(x)/u(x) = [u_+(x) - u_-(x)]/[u_+(x) + u_-(x)]$, $\Delta u(x)$ is the u quark helicity distribution, and x is Bjorken x, the momentum fraction carried by the parton. Similarly, the gluon polarization is $\Delta G(x)/G(x) = [G_+(x) - G_-(x)]/[G_+(x) + G_-(x)]$, and $\Delta G(x)$ is the helicity distribution carried by gluon fields. The average in Eq. (I.1.2-5) is taken over the allowed kinematic range for the outgoing quark jet.

From deep inelastic scattering measurements, for example, $\Delta u(x)/u(x) \sim 0.4$ for $x_q \sim 0.2$. For the Compton process, $,_{LL} \sim 0.6$ at $\theta = 90^o$ in the parton center of mass frame. Consequently,

$$A_{LL} \approx 0.2 \times \frac{\Delta G}{G} \qquad \text{(I.1.2.6)}$$

and the uncertainty in the gluon polarization is related to the uncertainty in the measured asymmetry by

$$\delta\frac{\Delta G}{G} \approx 5 \times \delta A_{LL} \qquad \text{(I.1.2-7)}$$

With the proposed STAR barrel electromagnetic calorimeter ($|\eta| < 1$), using 1.5-cm-wide segmentation for the shower maximum detector, the estimated uncertainty in the measured asymmetry for 10 GeV/c < $p_t$ < 20 GeV/c is

[67] M.E. Beddo, H. Spinka, and D.G. Underwood, ANL-HEP-TR-92-59, STAR Note 77 (1992).

$$\delta\frac{\Delta G}{G} \approx \pm 0.006\sqrt{\frac{800\ \mathrm{pb}^{-1}}{\int \ell dt}} \qquad \text{(I.1.2-8)}$$

at $\sqrt{s} = 500$ GeV; at $\sqrt{s} = 200$ GeV,

$$\delta\frac{\Delta G}{G} \approx \pm 0.03\sqrt{\frac{320\ \mathrm{pb}^{-1}}{\int \ell dt}} \quad \text{(1.1.2-9)}$$

**Direct-γ Production with Away-Side Jet Detection**

In order to measure the x dependence of the gluon helicity distribution, ΔG(x), both the direct-γ and the away-side jet must be detected in coincidence so that the kinematics of the incoming partons can be calculated. For the STAR barrel EMC, it is possible to study γ-jet events in which $-0.3 < \eta_{jet} < 0.3$ and $-1.0 < \eta_\gamma < 1.0$. (With corrections for missing acceptance, it may be possible to extend the coverage for jets to $|\eta_{jet}| \le 0.7$.) Jets will be reconstructed in STAR using the EM calorimeter to measure the electromagnetic component and the TPC to detect charged particles.[68] In the calculations, it was assumed that particles within a cone of radius $\sqrt{(\Delta\eta)^2 + (\Delta\phi)^2} = 0.7$ were part of the jet. The dominant process is $u + G \rightarrow u + \gamma$ and the longitudinal double spin asymmetry $A_{LL}$ is approximately proportional to the product

$$\frac{\Delta u}{u}(x_1)\frac{\Delta G}{G}(x_2) + (x_1 \leftrightarrow x_2). \qquad \text{(I.1.2-10)}$$

For a u quark in the range $0.1 < x < 0.4$, the polarization is known experimentally to be large, $\frac{\Delta u}{u}(x) > x$.

We define a kinematic region for the measurement with $p_t > 10$ GeV/c and include jets (cone R = 0.7) in the rapidity range $-0.3 < \eta < 0.3(1.3)$ (endcap) and γ's in the range $-1 < \eta < 1(2)$. For this region the scale of asymmetry is given by $A_{LL} \approx \mathrm{constant} \times \frac{\Delta G}{G}$. The constant comes from a weighted integration of u quark polarization multiplied by parton level analyzing power and is typically 0.1 to 0.3 depending on kinematic cuts.

Because the gluon structure function is strongly peaked at $x < 0.1$ and the u quark polarization grows with x for $x > 0.1$, it is clear that asymmetric jet-direct photon detection requires the full rapidity coverage available in STAR. The expected errors in $\frac{\Delta G}{G}(x)$ from direct photon + jet events are shown in Fig. I.1.2-1.

The cutoff in data at small x results in the limits imposed by beam energy, minimum $p_t$, and the ratio $x_1/x_2$ (rapidity range). The best small x measurement comes from the highest energy pp running, $\sqrt{s} = 500$ GeV. It is clear, that if lower $p_t$ data could be interpreted, the region $x < 0.02$ would produce a very large number of events.

---

[68] B.Christie and K. Shestermanov, ANL-HEP-TR-95-11,STAR Note 196 (1995).

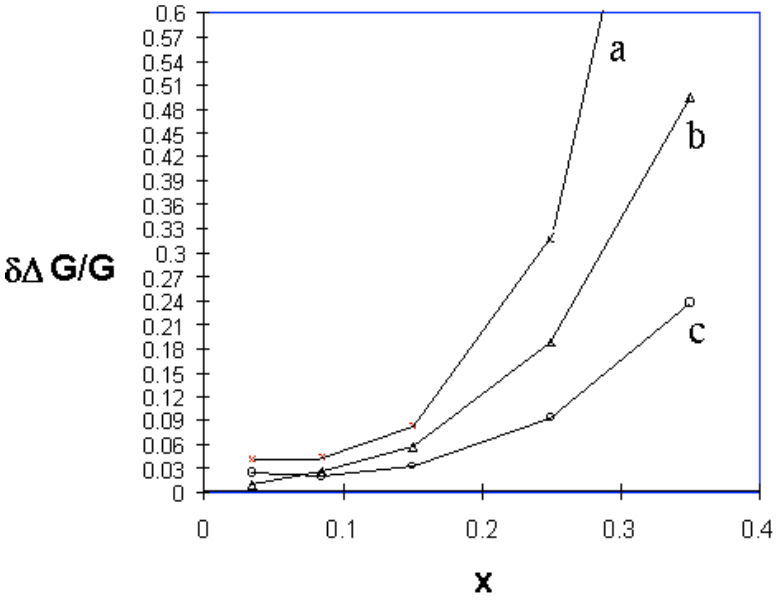


Figure I.1.2-1. Measurement error in ΔG/G vs. x for direct photon + jet events. Curve (a) represents errors for √s = 500 GeV with an EMC barrel only, curve (b) represents √s = 500 GeV with an EMC barrel + endcap.

**Single-Jet Production**

Several QCD subprocesses contribute to the cross section for jet production:

- Gluon-gluon scattering at low $p_t$ (gg → gg)
- Gluon-quark scattering at medium $p_t$ (gq → gq), and
- Quark-quark elastic scattering at high $p_t$ (qq → qq)

At low $p_t$, gluon-gluon scattering is expected to be the largest contribution to inclusive jet production, and to first order, therefore,

$$A_{LL} = \left[\Delta G(x_1)/G(x_1)\right] \times \left[\Delta G(x_2)/G(x_2)\right] \times \hat{a}_{LL(gg\to gg)} \qquad \text{(I.1.2-11)}$$

where ,$_{LL}$ is ~0.8 for scattering at 90° in the parton cm frame. Because the cross section for inclusive jet production is large, ~200 nb for $E_T$ jet > 15 GeV at $\sqrt{s}$ =500 GeV, error on $A_{LL}$ from a few weeks at very low luminosity is $\delta A_{LL} \approx 0.005$. This most elementary measurement at STAR will discriminate among the different theoretical models and place a large constraint on the parameterization of ΔG.

**Dijet Production**

When two back-to-back jets are detected, the kinematics of the incoming partons can be reconstructed to within a small correction that depends upon their intrinsic $p_t$. The reconstructed value of x for each parton may then be used to compute the parton-level subprocess asymmetry, $A_{LL}$. The measured value of $A_{LL}$ then determines the parton polarization. Thus, dijet production may be used to provide an independent measurement of ΔG(x). Since several QCD subprocesses contribute to the cross section for jet production, and the relative importance of each varies with the kinematic region which is studied, it is more complicated to extract the gluon polarization ΔG(x) from dijet production than from direct-γ + jet production. However, since the cross section for dijet production is ~20 times greater than for direct-γ + jet production, the increased statistics could offset the larger systematic uncertainties of this method.

The cross section for back-to-back jets in the barrel is ~60 nb. Given about three months running at $\approx 10^{31}$ cm$^{-2}$s$^{-2}$ (50 pb$^{-1}$), STAR can measure ΔG/G(x) in the range 0.07 < x < 0.14. Anticipated results for two different parameterizations of ΔG are plotted in Fig. I.1.2-2. Because the observable $A_{LL}$ is quadratic in ΔG/G, the measurement error be-

comes somewhat larger as ΔG/G becomes small. For example, if the y-axis in Fig. I.1.2-2 were scaled by 0.25, then ~10 times the integrated luminosity would be required to achieve the same statistical resolution.

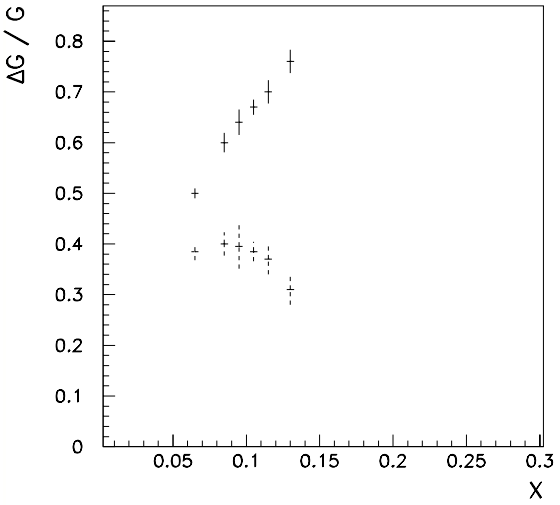


Figure I.1.2-2. Predicted values of ΔG/G as a function of x for two different parameterizations of ΔG.

### I.1.2.c Asymmetries in Inclusive $W^{\pm}$ and $Z^0$ Production

Inclusive $W^{\pm}$ and $Z^0$ production at RHIC will be a powerful tool for investigating parton distributions in the proton, and perhaps also in light nuclei. This is due to the large cross section for $W^{\pm}$ and $Z^0$ production and to the V-A coupling of the W. With the addition of an electromagnetic calorimeter, the STAR detector is especially well suited for the measurement of inclusive $W^{\pm}$ and $Z^0$ production due to its large acceptance for electrons produced by high mass particle decays. The rates for $W^{\pm}$ and $Z^0$ decays to electrons within the STAR detector acceptance have been estimated at $\sqrt{s}$ = 500 GeV using Pythia to be[69]

$$\sigma(pp \rightarrow W^+ + X \rightarrow e^+ + \nu + X) = 120 \text{ pb}$$
$$\sigma(pp \rightarrow W^- + X \rightarrow e^- + \nu + X) = 43 \text{ pb} \qquad \text{(I.1.2-12)}$$
$$\sigma(pp \rightarrow Z^0 + X \rightarrow e^+e^- + X) = 10 \text{ pb} \quad .$$

The $W^{\pm}$ single spin asymmetries provide a unique and sensitive probe of parton spin dependent distributions. Indeed, the unpolarized $\bar{u}$ and $\bar{d}$ distributions will be well measured at RHIC. Production of $W^{\pm}$ from polarized protons can determine the polarization of $\bar{d}$ quarks in the proton while corresponding $W^-$ measurements determine the polarization of the $\bar{u}$ quarks. In some models of the proton, the $\bar{d}$ quarks are unpolarized and the $\bar{u}$ quarks are highly polarized[70].

At $\sqrt{s}$ = 500 GeV, from 50,000 to 100,000 $W^+$ will be produced in a standard run period and about 25% as many $W^-$. The production of W's is peaked near central rapidity, with about half of the events produced at rapidity less than 0.5. The observed electron distribution is broader, however, due to the decay distribution of the W.

As an illustration, consider the case of electrons measured in the production of $W^-$. One can define the incident direction for one of the beams to be positive so that small angle scattering from that beam hits the end-cap. For a d quark in that positive incident beam, $W^-$ production and the parity violating decay will produce an electron at relatively small forward angles. The kinematics and structure functions for d and $\bar{u}$ quarks will tend toward the selection of a d quark with larger x than that of the $\bar{u}$ antiquark and thus positive rapidity for the $W^-$.

[69] A.A. Derevschikov and V.L. Rykov, Brookhaven National Laboratory report RSC-BNL/IHEP-4 (1992).
[70] C. Bourrely and J. Soffer, Nucl. Phys. B **423**, 329 (1994).

Therefore in the central rapidity region, $W^-$'s are produced with d quarks from either incident beam, but at larger (positive) rapidity, $W^-$'s are produced mostly with d quarks from the proton that was moving in the positive direction.

Thus, the electrons observed with $|\eta| > 0.5$ are most interesting because the incident direction of the d quark is more certain. For forward $W^-$ events, we can define a single spin asymmetry $A_L$ by flipping the spin of either beam. With one choice we measure $A_L = \Delta d/d$ ; with the other choice we measure $A_L = \Delta\bar{u}/\bar{u}$.

Recent results from the SMC collaboration illustrate the difficulty in assigning the x dependence of the quark contribution to the proton spin to specific quark and antiquark flavors[71]. In the region of x covered by STAR, the results from the W measurements should reduce the uncertainty in $\Delta u$, $\Delta\bar{u}$, $\Delta d$, and $\Delta\bar{d}$ by nearly an order of magnitude compared to errors reported by SMC (see Fig. I.1.2-3). The results are for a barrel and one endcap calorimeter.

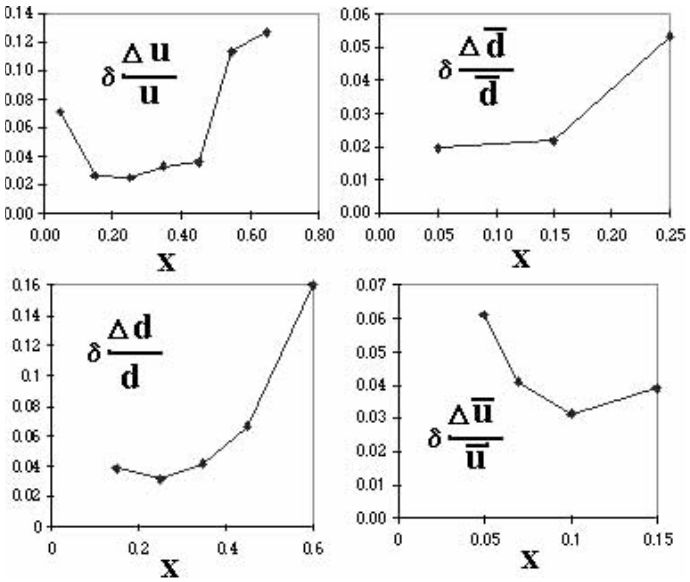


Figure I.1.2-3. Measurement error for quark and antiquark polarizations vs. x from W decays.

### I.1.2.d High-Energy Drell-Yan Electrons and the Sea Quark Polarization

The study of Drell-Yan pair production appears to be another way to determine the polarization of sea quarks. The $q\bar{q}$ annihilation into a vector boson gives a large asymmetry on a partonic level and selects sea antiquarks along with valence quarks.

The asymmetry $A_{LL}$ for Drell-Yan production in pp collisions is related to the sea quark helicity distribution $\Delta q(x)$,

$$A_{LL} = \hat{a}_{LL} \frac{\sum_i e_i^2 \left[\Delta q_i(x_1)\Delta\bar{q}_i(x_2) + \Delta q_i(x_2)\Delta\bar{q}_i(x_1)\right]}{\sum_i e_i^2 \left[q_i(x_1)\bar{q}_i(x_2) + q_i(x_2)\bar{q}_i(x_1)\right]} \qquad \text{(I.1.2-13)}$$

where $e^2$ is the square of the parton charge, and $A_{LL} = -1$. The sum in Equation I.1.2-13 is taken over parton flavor.

To determine if the study of Drell-Yan production might be possible, the PYTHIA event generator was used to estimate the yield in an ideal detector with the same total acceptance as the STAR barrel and endcap calorimeters. The results are presented in Table I.1.2-1 for a standard run at $\sqrt{s}$ = 200 GeV.

[71] B. Adeva *et al.*, Phys. Lett B **369**, 98 (1996).

| $M_{pp}$ (GeV/$c^2$) | 5-9 | 9-12 | 12-15 | 15-20 |
|---|---|---|---|---|
| Events | 28,000 | 20,000 | 8,400 | 5,400 |

Table I.1.2-1. The estimated yield of Drell-Yan pairs in the acceptance of the STAR barrel and endcap calorimeters.

### I.1.2.e New Physics

In January 1996 several groups[72] proposed a new neutral gauge boson $Z^0$ coupling only to quarks as an explanation of the $R_b$ anomaly at LEP. In May 1996, J. Lopez and D. Nanopoulos proposed a theoretical basis in superstring-derived flipped SU(5) for such a $Z^0$ [73]. The $Z^0$ in their model is naturally maximally parity violating with only left-handed coupling to u quarks. They concluded following a Marseilles paper[74] that this effect would be observable at RHIC. Although the interest in the $R_b$ anomaly has waned, the flipped SU(5) $Z^{'}$ has no necessary effect on $R_b$ so that $Z^0$ is still interesting.

We have made a preliminary study of STAR's ability to detect this $Z^0$. The observable effect is in the parity violating asymmetry $A_{pv} = (\sigma_{--} - \sigma_{++})/(\sigma_{--} + \sigma_{++})$, where the process measured is inclusive jet production. There is a small $A_{pv}$ (1 to 3% depending on jet $E_T$) in the standard model arising from t-channel interference between the gluon and the Z in quark-quark elastic scattering. This interference would be increased by a factor of 1.5 to 3 given the presence of a $Z^0$ from this model, as shown in Fig. I.1.2-4. For this study we chose jets with cone R=0.5 which can be measured accurately within $|\eta| < 0.5$. Given an integrated luminosity of 800 $pb^{-1}$, STAR would see a significant departure from standard model $A_{pv}$ for $m_{Z'} < 600$ GeV.

The standard model $A_{pv}$ will be an interesting measurement in itself since it is a prediction of the standard model that has not previously been experimentally verified. The standard model $A_{pv}$ as measured by STAR with 800 $pb^{-1}$ is shown in Fig. I.1.2-5.

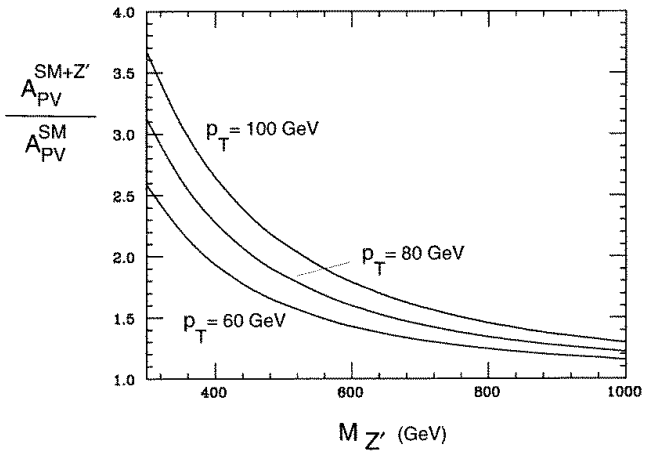


Figure I.1.2-4. Increase in the inclusive jet production parity violating asymmetry $_{Apv}$ for three values of jet $p_t$.

### I.1.2.f Transverse Quark Structure Functions of the Proton

There exists a third fundamental partonic structure function $h_1(x)$, which is a leading-twist distribution function like $f_1(x)$ and $g_1(x)$. This distribution can be determined by measuring the transverse spin asymmetry $A_{TT}$ in Z production,

[72] P. Chiappetta, J. Layssac, F. Renard, and C. Verzegnassi, hep-ph/9601306; G. Altarelli, N. Di Bartolomeo, F. Feruglio,R. Gatto, and M. Mangano, hep-ph/9601324.
[73] J. Lopez and D. Nanopoulos, hep-ph/9605359.
[74] P. Taxil and J. Virey, hep-ph/9604331.

$$A_{TT} \equiv \frac{\sigma^{\uparrow\uparrow} - \sigma^{\uparrow\downarrow}}{\sigma^{\uparrow\uparrow} + \sigma^{\uparrow\downarrow}}. \qquad \text{(I.1.2-14)}$$

$A_{TT} = \hat{a}_{TT} \frac{h_1^q}{q} \frac{h_1^{\bar{q}}}{\bar{q}}$ when one flavor is dominant. If $h_1^{\bar{q}}$ is close to zero, we can not measure $h_1$. However, we can measure $h_1(x)$ in dijet production from $A_{TT} = \hat{a}_{TT}\left(\frac{h_1^q}{q}\right)^2$ at high $p_t$ where quark-quark scattering dominates. These measurements are unique to the STAR detector.

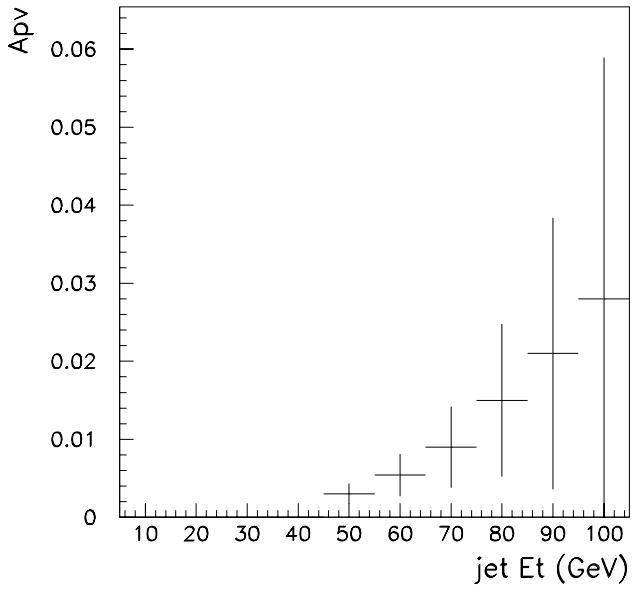


Figure I.1.2-5. Predictions of the standard model for the parity violating asymmetry $A_{pv}$.

### I.1.2.g Higher Twist Effects

Single transverse spin asymmetries are expected to vanish in lowest order, perturbative QCD. Even though the asymmetries vanish at the leading, or "twist-2" level, this is no longer true when higher order, "twist-3" diagrams are taken into account. For example, a large single spin asymmetry has been predicted in inclusive direct-$\gamma$ production ($p^{\uparrow}p \rightarrow \gamma + X$).[75]

The event rate for direct-$\gamma$ production can be estimated for the EMC barrel as in Section I.1.2.b. The corresponding estimate for the uncertainty in the single transverse spin asymmetry is

$$\delta A_T \approx \pm 0.006 \sqrt{\frac{320\ \text{pb}^{-1}}{\int \ell dt}}. \qquad \text{(I.1.2-15)}$$

## I.1.3 Trigger Concept and Capability

A sensitive trigger is essential for STAR. Rare phenomena can be studied effectively only if a selective trigger is employed. The STAR EMC provides a large range of possibilities for triggering in AA, pA, and pp collisions at RHIC.

### I.1.3.a Event Selection in AA Collisions

The most interesting collisions at RHIC are those that produce the highest densities and temperatures. These collisions are the most promising environment in which to search for novel phenomena and signatures of a deconfined phase of quarks and gluons. A characteristic feature of these conditions is the observation at mid-rapidity of high particle multiplicities and high transverse energy deposition. If the mean $p_t$ per particle and

[75] J. Qiu and G. Sterman, Phys. Rev. Lett. **67** (1991) 2264.

the global ratio of neutral to charged particle energy do not vary significantly from event to event, central impact parameter triggers based on the multiplicity of charged particles or the total transverse energy are essentially the same. However, exciting phenomena that can occur in central AA collisions such as disordered chiral condensates (CC) or Bose-Einstein condensates (BE) may alter the relationship between charged particle multiplicity and transverse energy. The STAR Central Trigger Barrel (CTB) is sensitive to the multiplicity of charged particles (mainly charged pions) while the EMC is sensitive to energy emitted in the form of electrons and photons (mainly photons from the decay of neutral pions). Thus the combination of the EMC and the CTB can provide information about the relative numbers of charged pions and neutral pions.

**I.1.3.b Use of EMC for Selection of Rare Events in AA Interactions**

It is in the selection of rare events in AA interactions that some of the unique capabilities provided by the electromagnetic calorimeter become apparent. As noted above, some of the most interesting physics may be found by triggering on events in which the average $p_t$ per particle[76,77] and/or the ratio of charged to neutral energy[78,79] depart significantly from that which is characteristically observed. If these events occur at low cross section and their observation therefore requires significant rejection of "background events" at the trigger level, they will not be observed unless the characteristic correlation between the charged-particle multiplicity and transverse energy can be tested at the trigger level. In the present circumstance in which full event reconstruction (i.e., tracking) will take longer than 10 ms, this correlation can not be accomplished for events having an unusual $\langle p_t \rangle$ without the electromagnetic calorimeter. Of course, searching for events exhibiting an unusual charged-to-neutral energy ratio cannot be accomplished in any circumstance without measurement of the neutral electromagnetic energy. With partial coverage of the electromagnetic calorimeter it would still be possible to search for rare events in selected regions of the STAR acceptance, although the sensitivity would be reduced.

To test the sensitivity of the STAR EMC to events exhibiting unusual isospin abundances, the response of this detector was examined in a full GEANT simulation of the STAR detector, using 75 "normal" central AuAu events generated using HIJING at $\sqrt{s_{nn}}$ = 200 GeV/nucleon. The same events with 50% of the $\pi^{\pm}$ mesons changed to $\pi^{o}$ mesons are used to estimate the response of STAR to phenomena like disordered chiral condensates (CC). To simulate the response of STAR to phenomena like Bose-Einstein condensates (BE), the momentum of the pions from the normal events were lowered by 30% and 30% more particle were added to conserve energy.

The results of these simulations are shown in Fig. I.13-1, in which the total sampled energy deposited in the EMC barrel has been plotted versus the charged particle multiplicity detected in the central trigger barrel for both the normal and anomalous AuAu collisions. The open circles represent HIJING calculations for the full range of

[76] L. Van Hove, Phys. Lett. 118B, (1982) 138.
[77] M. Kataja *et al*., Phys. Rev. D34, (1986) 2755.
[78] J.D. Bjorken, Acta Physica Polonica B23, (1992) 635.
[79] F. Wilczek, {Chiral Dynamics Near Equilibrium or After Quenching," Proceedings of the Tenth International Conference on Ultra-Relativistic Nucleus-Nucleus Collisions, June 20–24, 1993, Borlänge, Sweden.

impact parameter possible in AuAu reactions. The closed circled represent normal HIJING calculations for 0 fm < b < 2.5 fm. The open triangles stand for the BE events while the open squares signify the CC events. The minimum bias HIJING events fall on a straight line that passes through zero which implies that the ratio of EMC energy to CTB multiplicity is constant for normal events. The anomalous events also fall on a line that passes through zero but with a different slope.

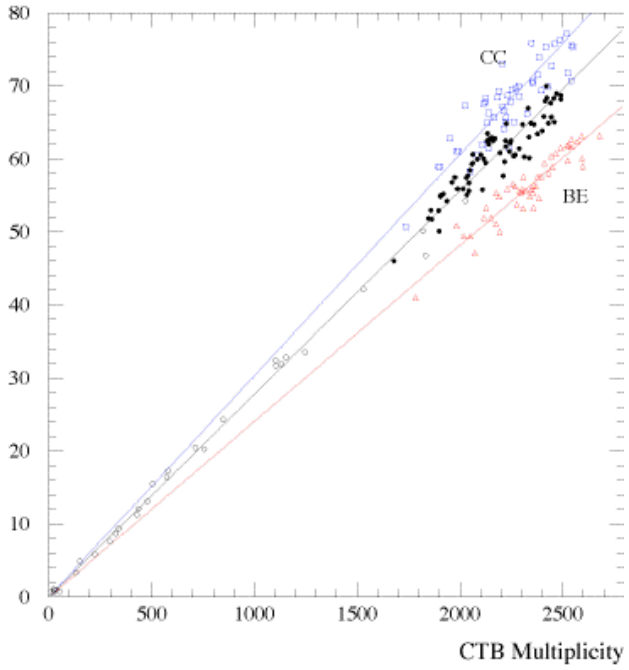


Figure I.1.3-1. HIJING calculations for AuAu collisions filtered through GEANT for STAR. The open circles represent normal HIJING calculations over all impact parameters. The closed circles depict central HIJING events with b ≤ 2.5 fm. The open triangles show the same events with the momentum of the pions reduced by 30% and the multiplicity increased by 30% while the open squares represent the same events with 50% of the charged pions changed to neutral pions.

The ratio of the energy deposited in the EMC barrel to the charged particle multiplicity detected in the CTB has been histogrammed in Fig. I.1.3-2 for the same events. In the left panel, the histograms are shown for the full barrel. The two kinds of anomalous events are clearly separated from the normal events. In the right panel, the same events are observed with a full GEANT calculation incorporating 1/4 of the barrel. Although the sensitivity is decreased somewhat, it is still possible to trigger on isospin fluctuations.

To gain an understanding of the EMC trigger with respect to isospin fluctuations, one can investigate the response to different fractions of charged pions being changed to neutral pions. In Fig. I.1.3-3, the distributions of the ratio of the EMC to the CTB for ordinary HIJING events (solid line labeled xx) and for CC events assuming 20% (dotted line), 40% (dashed line) and 50% (solid line labeled cc 50%) of the charged pions change to neutral pions are given. These distributions are obtained by fitting a Gaussian to the results for the full GEANT simulations and producing new distributions with the same centroids and widths. These distributions represent $10^8$ AuAu events, which would represent 100 days of RHIC running at 1 event per second. However, these distributions could be acquired much more quickly if only the EMC and CTB were recorded. Assuming 1000 events per second EMC/CTB-only events, these distributions could be obtained in 1 day and could be used to set trigger levels on rare events.

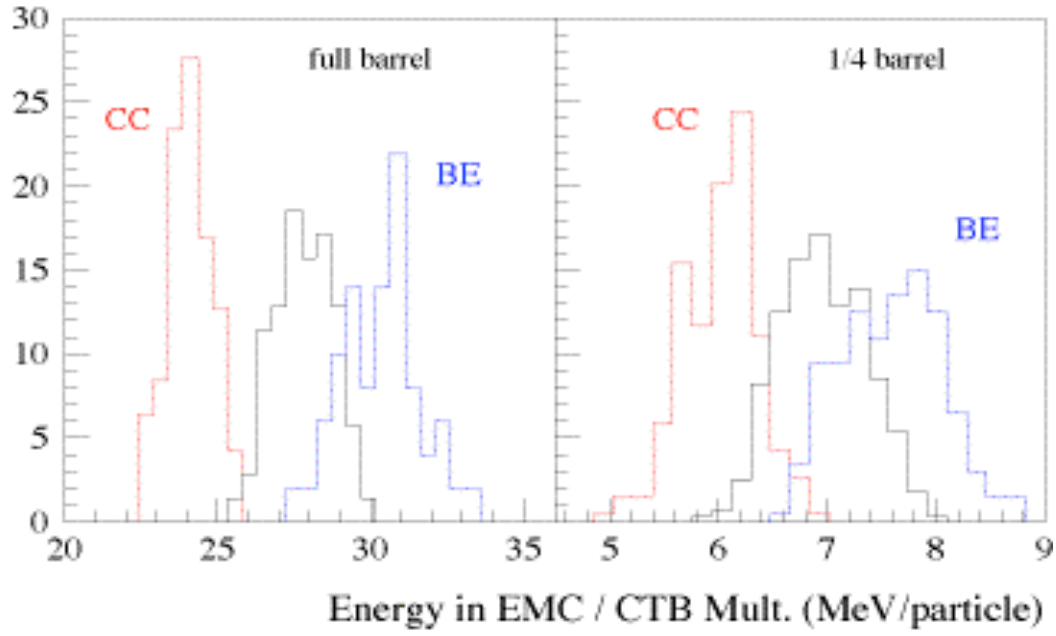


Figure I.1.3-2. Histograms of the energy in the EMC divided by the charged particle multiplicity in the CTB for the events shown in Figure I.1.3-1. The solid lines depict normal HIJING events while the dashed lines show the chiral condensate (CC) events and the dot-dashed lines represent the Bose-Einstein (BE) events. The left panel shows simulations for the full barrel while the right panel shows the same events measured with 1/4 of the barrel calorimeter.

In Fig. I.1.3-3b, similar results are shown for the case where one assumes that the CC effects only occur for low $p_t$ pions. The ordinary HIJING events and the 50% CC events are the same as in Figure I.1.3-3a. The dotted (dashed) line represents events in which all the charged pions with momenta below 300 (500) MeV/c change to neutral pions which is 34 (63) % of all the emitted pions. Thus one can see that a trigger based on the EMC can be sensitive to various types of anomalous isospin fluctuations.

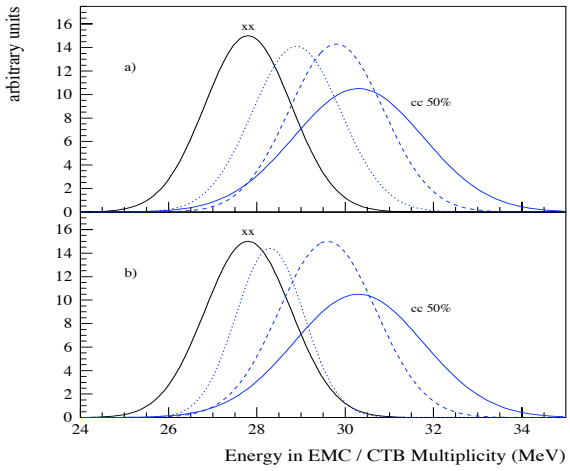


Figure I.13-3. Distributions extracted by fitting fully analyzed HIJING events for AuAu collisions using different assumptions about chiral condensates. These curves all have the same number of events. See text for explanation.

To trigger on rare events, one must be able to select a few interesting events from a large background of uninteresting events. To estimate the ability of the EMC we have constructed several sets of events in which the relative probability of occurrence is varied as well as the fraction of charged pions converted to neutral pions. In Fig. I.1.3-4a, the relative probability of occurrence is varied along with the fraction of charged pions converted to neutral pions. The solid line marked cc depicts the normal AuAu events. The solid line labeled cc 50% shows the case in which

one assumes that chiral condensates with 50% of the charged pions changing to neutral pions occur with 0.1% of the probability of normal events. The dashed curve represents the case where 40% of the charged pions change and these events occur with 1% of the normal probability. The dotted curve stands for events in which 20% of the charged pions flip with 10% the normal probability.

Within the assumptions of the schematic calculations, one can see that it would be possible to set a trigger level on the ratio EMC/CTB to select isospin fluctuations.

In Fig. I.1.3-4b, the effect of only lower momentum charged pions changing sign is shown. The solid lines labeled xx and cc 50% are the same as in Fig. I.1.3-4a. The dotted line shows the effect of all the charged pions with momenta below 300 MeV/c (34% of the total number of pions) changing to neutral pions with 10% the probability of normal events. The dashed line shows the distribution of ratios for the case of all the charged pions with momenta below 500 MeV/c (63% of all pions) occurring with 1% the frequency of normal events.

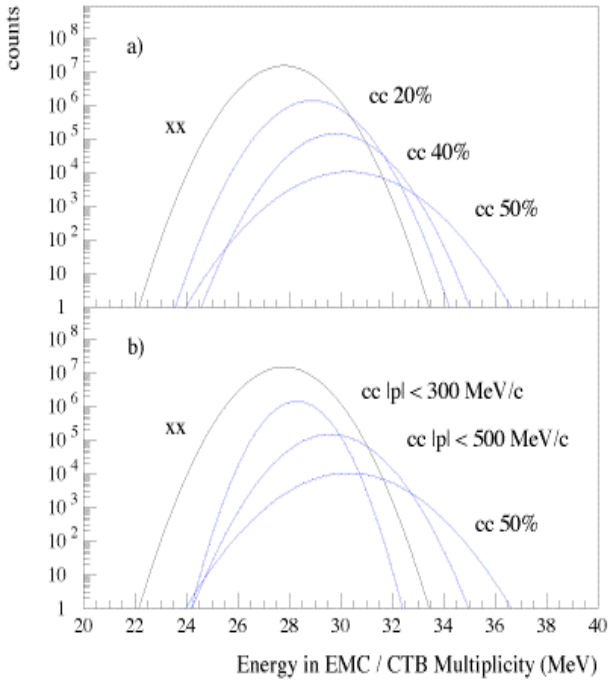


Figure I.1.3-4. Distributions extracted by fitting fully analyzed HIJING events for AuAu collisions using different assumptions about the occurrence of chiral condensates. See text for explanation.

One can see from Fig. I.1.3-4b that separating events where charged pions with momenta less that 300 MeV/c from normal events would be impossible. However, in the case of charged pions with momenta below 500 MeV/c, flipping could be selected.

**I.1.3c Triggering on Jets and Photons in pp and pA**

The study of hard parton scattering in pp and pA reactions in the form of jets and hard photons is crucial to the interpretation of AuAu results. In addition, the measurements of jets and hard photons are fundamental to the spin physics program using polarized pp reactions. The EMC provides a sensitive and selective trigger for these phenomena. In Fig. I.1.3-5, the sensitivity of the EMC to triggering on 20 GeV jets and photons is shown using fully reconstructed HIJING events for pAu reactions at $\sqrt{s}$ = 200 GeV for two cases. In the left panel, a correlation is made between the total energy observed in the EMC versus the maximum energy observed in the $(\Delta\eta,\Delta\phi) = (0.05,0.05)$ highest trigger towers for events without jets, events with 20 GeV jets, and events with 20 GeV photons. In the right panel, the same events are studied with an overlapping patch size of $(\Delta\eta,\Delta\phi) = (0.8,0.8)$. For the case of (0.05,0.05), the photons are clearly separated from the jets while the jets have some overlap with the nojet events. For the (0.8,0.8) patches, the trigger separates the jets more cleanly from the nojet events while overlapping slightly more with the photons, which are not affected by the different patch sizes.

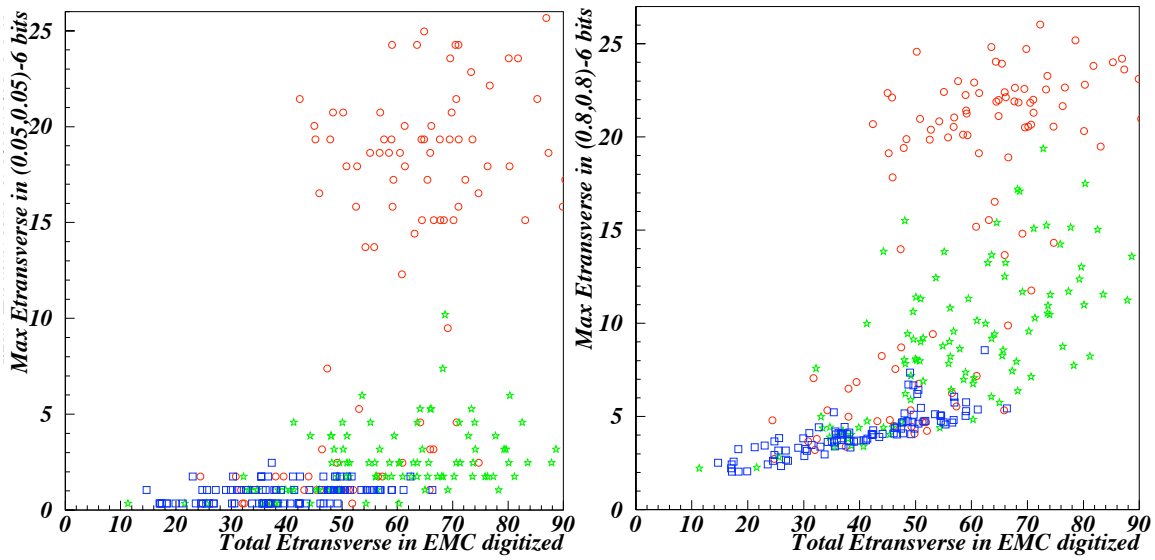


Figure I.1.3-5. Results for HIJING pp events filtered through the STAR analysis software for the (0.05,0.05) high towers (left) and the (0.8,0.8) patches (right).

The proposed lowest level trigger system hardware involves 300 $(\Delta\eta,\Delta\phi)$ = (0.2,0.2) trigger towers in the calorimeter. Each trigger tower is digitized to an accuracy of 6 bits. In addition, the highest tower within each trigger tower (0.05,0.05) will also be digitized to 6 bits. Higher levels of the trigger system can then produce overlapping patches of (0.8,0.8) from these trigger towers. To model the response of the trigger to jets and photons, using these assumptions, we have compared the number of events with 20 GeV jets above a given threshold on the (0.05,0.05) high towers to the number of 20 GeV photons above the same threshold using HIJING calculations for $\sqrt{s}$ = 200 GeV pAu filtered through the STAR acceptance. These results are presented in Fig. I.1.3-6.

To illustrate the effect of digitization, the results for the (0.05,0.05) trigger patches are compared with similar results using (0.8,0.8) patches calculated using the STAR trigger electronics and processors assuming a full-scale value of 40 GeV digitized to 6 bits. These results are shown in Figure I.1.3-7.

There is little difference between the full accuracy signals and the 6 bit signals for the (0.05,0.05) patches while an effect is observed jets in the (0.8,0.8) patches. One effect of the digitization for the (0.8,0.8) patches is simply a shift in the sum due to the finite width of the bins.

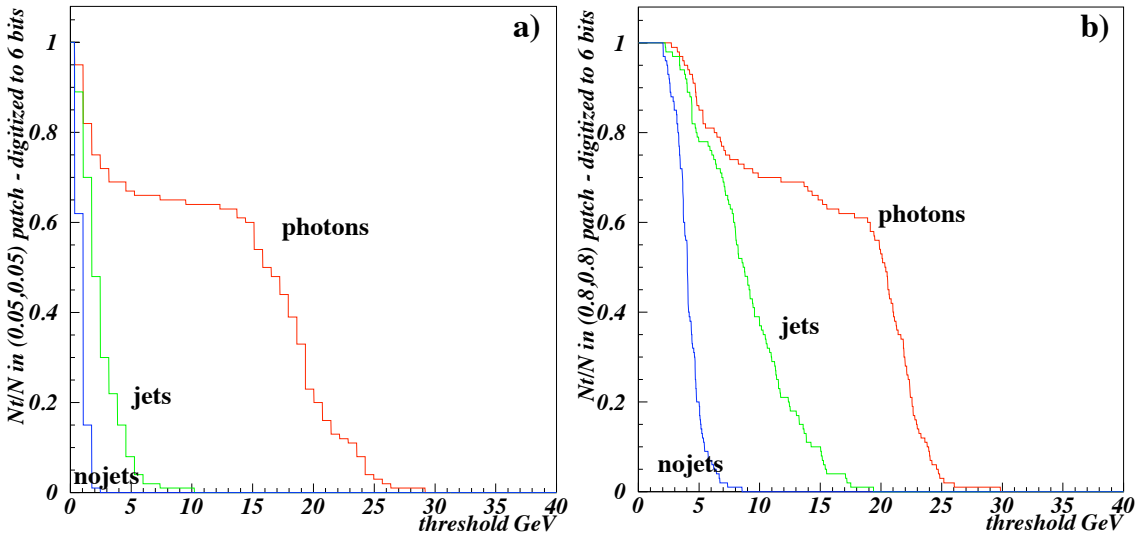


Figure I.1.3-6. Trigger efficiency for 20 GeV jets and photons and no jet events for the thresholds on the high tower bits (0.05,0.05) and (0.8,0.8) overlapping patches.

With these results for jets and direct photons at 20 GeV and other energies along with the known cross sections for the production of jets and photons, one can predict the counting rate for the design luminosity of 1 x $10^{32}$ $s^{-1}cm^{-2}$. In Fig. I.1.3-8, the counting rates for jets and photons from $\sqrt{s}$ = 200 GeV pAu interactions are shown as a function of the threshold on (0.05,0.05) high towers and (0.8,0.8) patches in the EMC.

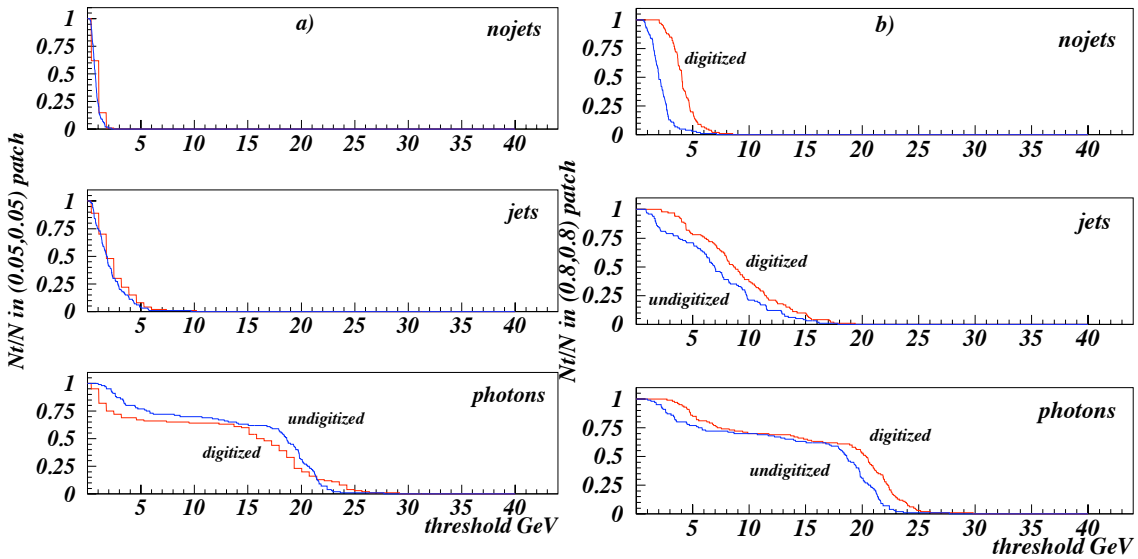


Figure I.1.3-7. Effect of digitization on the trigger efficiency for nojets, 20 GeV jets, and 20 GeV direct photons from pAu interactions.

g

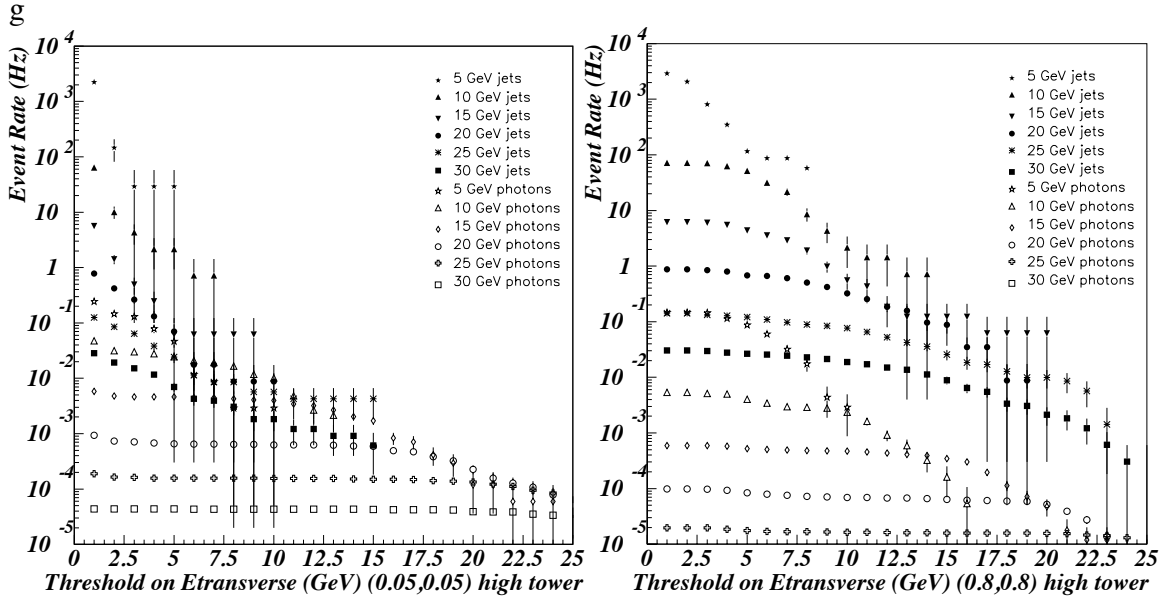


Figure I.1.3-8. Predicted counting rates for pAu reactions based on threshold on the (0,05,0,05) high towers and the (0.8,0.8) patches for various energy jets and direct photons using the design luminosity, extracted efficiencies, and calculated jet and direct photon cross sections.[80]

## I.2 Detector Concept

### I.2.1 Choice of Technology

A priori, there are many available technologies for an electromagnetic calorimeter. Crystals such as NaI, CsI and BGO have excellent resolution for individual low energy photons. Lead glass has better energy resolution than most sampling calorimeters. The primary problem with these detectors is cost, particularly for the depth, area, and geometry needed for STAR. The area that must be covered outside the TPC is over $100m^2$ for $|\eta| < 2$. To accomplish all the physics goals, the depth must be adequate to contain 40GeV showers within a few percent, including leakage fluctuations. This requirement implies a total depth of approximately $20X_o$. The geometrical constraint imposed by the solenoidal STAR geometry implies the EMC elements must be wedge-shaped at a minimum, if not truncated pyramid shapes as used in VENUS and UA2.

Gas calorimetry with wire chamber sampling between layers of lead has been used in some applications, but in general has demonstrated problems with non-uniform gain and extremely large signals from neutrons. Other sampling detectors have used liquid argon or some other liquid to detect the ionization caused between plates of converter or absorber by the passage of charged particles. Generally, the cryogenic vessels used to contain the liquid take up an unacceptable amount of space. This geometry leads to a lack of hermiticity and cracks within the sensitive volume of the detector. Liquid argon

[80] W. Christie and Hard Processes in Hadronic Interactions, Int. J. Mod. Phys., A10, 2881, LBL-36948 (CERN-95-05).

calorimeters also typically require more time to integrate signal than for example, scintillator tiles, although there was progress on this aspect with an SSC liquid krypton prototype. Although detailed studies of a liquid argon calorimeter were not performed, both the cost and GeV equivalent noise level are expected to be higher than for a lead-scintillator sampling calorimeter. The noise level can be a particularly serious problem in the present application, because for heavy ion interactions, the average $p_t$ of the charged particles and photons that reach the calorimeter is less than 400MeV/c.

A sampling calorimeter using lead and plastic scintillators has been chosen for the detection of electromagnetic energy in STAR. A significant advantage of this technology is that the calorimeter can be constructed from a number of relatively small modules. This approach will permit part of the calorimeter to be constructed and installed after the STAR baseline components (TPC, magnet, etc.) are complete. This staging would be significantly more difficult, for example, with liquid argon technology. Calorimeters of this design have been successful in a number of colliding beam and fixed target experiments, and as a consequence, the technology is well known. Recent examples of detectors incorporating this technology include the endcap upgrade for CDF and the proposed barrel calorimeter for SDC. In particular, the use of a lead-scintillating sampling calorimeter is a cost-effective way to cover the necessary area, employing a mechanical design flexible enough to accommodate the constraints imposed by the closed STAR geometry. The energy resolution is adequate to reconstruct $\pi^o$'s of $p_t$ well below 2GeV/c. For some kinds of measurements in heavy ion physics where a large number of very low energy photons are to be summed, the resolution is also adequate. The intrinsic resolution expected from sampling calorimeters with 5 mm (~0.9 $X_o$) lead plates is $\sim 14\% / \sqrt{E}$. With typical photostatistics (two photoelectrons / sampling layer / minimum ionizing particle) the resolution typically achieved is $16\% / \sqrt{E}$ plus a 1%-3% constant term (confirmed in STAR test beam runs and simulations). The constant or so-called "stochastic" term comes from tower-to-tower variations in the calibration and transverse and longitudinal non-uniformities in light collection from the pieces of scintillator.

The light generated by charged particles passing through the scintillator must be brought to photon detectors such as photomultipliers. In the STAR design the electromagnetic calorimeter will be located inside the solenoidal magnet. The photomultipliers must be located outside the magnet to avoid high magnetic fields, and to minimize the radius and cost of the magnet. The use of waveshifter plates such as those used in the CDF and ZEUS calorimeters would not be practical, because they would take up an unacceptable amount of space in traversing the coil pancakes. Consequently, plastic optical fibers that take up less space and require less labor to prepare have been selected for the STAR design.

Once the decision is made to use a sampling calorimeter with scintillator, the next concerns are how best to accomplish efficient light collection, what segmentation should be used, and how the mechanical structure should be designed. These choices are related and are discussed in detail in the sections that follow.

In order to make a choice of the technology for the shower maximum detector (SMD), three different SMD prototypes were tested inside a small EMC prototype at the BNL test beam over a period of two years. The scintillator strip version similar to the one used in the CDF endplug upgrade functioned well, but would have been very difficult to fit into the space available in STAR. The chost of over $3x10^4$ phototube channels,

even with multi-anode tubes, was also a serious consideration. We have decided on the wire-strip gas detector. In beam tests of our design showed that our detector performed extremely well and as expected on the basis of CDF experience.

### I.2.2 Summary of the Mechanical Structure

The barrel Electromagnetic Calorimeter, EMC, is located inside the aluminum coil of the STAR solenoid and covers $|\eta| \leq 1.0$ and $2\pi$ in azimuth, thus matching the acceptance for full TPC tracking and is shown schematically in Fig. I.2.2-1

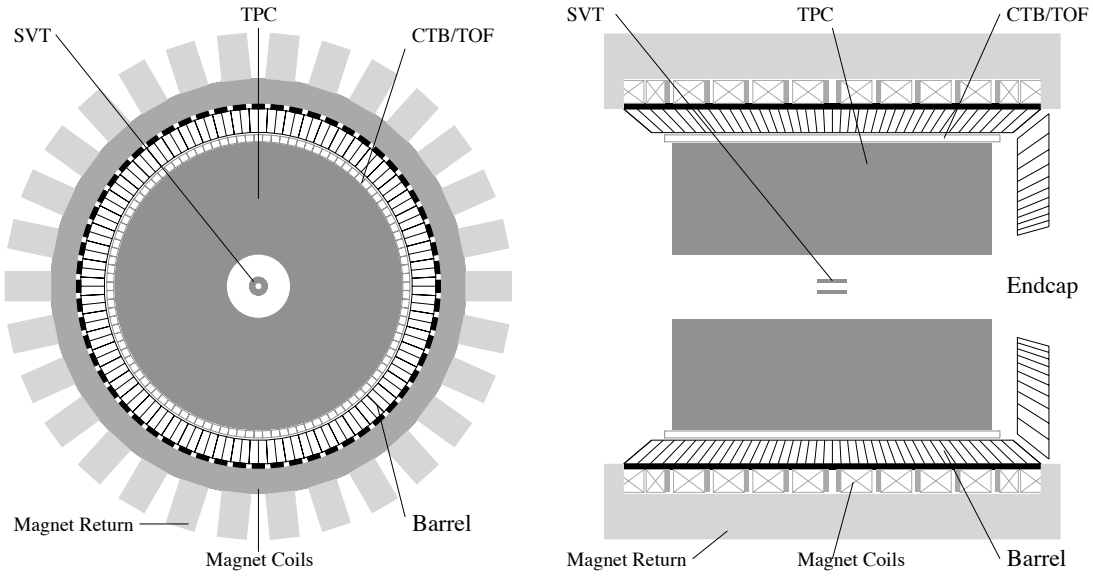


Figure I.2.2-1. Cross sectional views of the STAR detector. The barrel EMC covers $|\eta| \leq 1.00$. The Endcap Calorimeter covers $1.05 \leq \eta \leq 2.0$. The barrel EMC modules slide in from the ends on rails which are held by aluminum hangers which attach to the magnet iron between the magnet coils. Optical fibers from the towers pass through spaces between the coils and are subsequently routed between the iron flux return bars to the exterior of the magnet.

The design for the barrel electromagnetic calorimeter includes a total of 120 calorimeter modules, each subtending 6° in $\phi$ (0.1 radian) and 1.0 unit in $\eta$. These modules are mounted 60 in $\phi$ by 2 in $\eta$ as shown in Fig I.2.2-1. Each module is roughly 26cm wide by 293cm long with an active depth of 23.5cm plus about 6.6 cm in structural plates. A module is further segmented into 40 towers, 2 in $\phi$ and 20 in $\eta$, with each tower being 0.05 in $\Delta\phi$ by 0.05 in $\Delta\eta$. The calorimeter is thus physically segmented into a total of 4800 towers, each of which is projective and pointing back to the interaction diamond. Figure I.2.2-2 shows a side view of a module illustrating the projective nature of the towers in the $\eta$-direction.

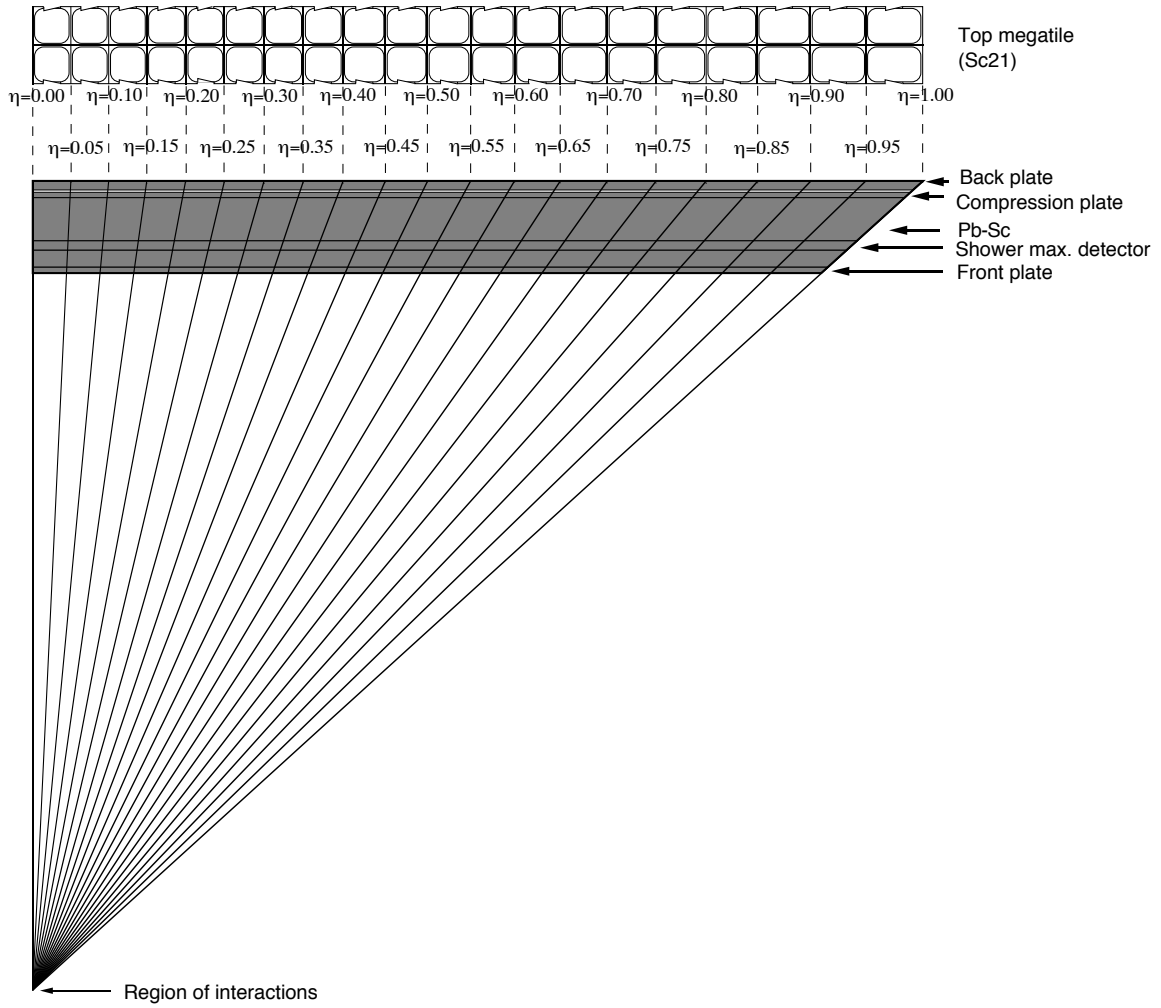


Figure II.2.2-2. Side view of a calorimeter module showing the projective nature of the towers. The 21st megatile layer is also shown.

The STAR EMC is a sampling calorimeter, and the core of the structure consists of a lead-scintillator stack and a shower maximum detector situated approximately 5 radiation lengths from the front of the stack. There are 20 layers of 5mm thick lead and 21 layers of 5mm thick scintillator. This core structure, the stack, is held together by friction aided by compressional forces. The compression is applied by a combination of 30 straps connecting the non-magnetic front and back plates of the structure, and a system of bolts and spring-loaded washers between the back plate and a compression plate. The plastic scintillator is in the form of "megatiles", with 40 optically isolated "tiles" or segments in each layer as shown in figure II.2.2-2.

## I.2.3 Summary of the Optical Structure

The Solenoidal Tracker detector of RHIC employs scintillating tile/wavelength shifting fiber readout technology[81] for the Barrel Electromagnetic Calorimeter. A significant advantage of this technique is that the calorimeter dead space can be made small compared to calorimeters based on the conventional scintillating plate / wavelength shifting bar read-out scheme. This technique has been successful in number of colliding beam and fixed target experiments, and as a consequence, the technology is well known. Recent examples of detectors incorporating this technology include the endcap upgrade calorimeter for CDF[82].

The design of the Barrel EMC comprises 120 calorimeter modules, each subtending 6° in $\phi$ (0.1 radian) and 1 unit in $\eta$ where $\phi$ is the azimuthal angle in radians and $\eta$ is the pseudorapidity. The calorimeter is a sampling calorimeter and the core of the structure consists of a lead-scintillator plate stack. There are 21 active scintillator layers of 5-mm thick alternating with 20 layers of 5-mm thick lead absorber plates. This core structure, the stack, is held together by friction and is compressed to 15 PSI to increase the frictional forces. The plastic scintillator is in the form of "mega-tiles" with 40 optically isolated "tiles" or segments in each layer. In order to simplify handling, the mega-tiles are produced from two pieces of approximately 1.6 m long scintillating plates for each layer in the calorimeter. The signal from each scintillating tile is read-out with a single wavelength shifting (WLS) fiber embedded in a $\sigma$-groove that is machined in the tile. After exiting the scintillator, the WLS fiber is routed along the side of the stack and terminated at a multi-fiber, optical connector at a back-plate of module. From there, 3.5 m long, multi-fiber, optical cables of clear fibers carry the light from optical connector through the magnet structure to decoder boxes containing the photomultiplier tubes (PMT′s), where the light from tiles comprising a single tower are merged. A light mixer is placed between these fibers and the photocathode of PMT to optimize the uniformity of the distribution of light across the photocathode. A schematic diagram of tile/fiber optical read-out scheme of Barrel EMC is shown in Figure *I.2.3-1*

We use extruded, polystyrene-based, scintillator (PS) as the active medium of calorimeter. For the WLS fiber, we use Kuraray multiclad Y11 (200 ppm) S-type wavelength shifting fiber, 0.83 mm in diameter. One end of the wavelength shifting fiber will be polished and aluminum sputtered. The clear fibers will be Kuraray double-clad fiber 0.9 mm and 1.0 mm in diameter. As a photodetector we will use green extended photomultiplier FEU115-M. The non-polished mega-tile edges are painted white with Bicron BC620 reflective paint. White bond paper, which has a high coefficient of friction, is used on both sides of the mega-tile as a reflector. With typical photostatistics ( two photo electrons/sampling layer/minimum ionizing particle) and typical sampling frequency (once every 0.9Xo), the intrinsic resolution expected from such a sampling calorimeter is about $16\%/\sqrt{E}$ plus a 1.5% constant term added in quadrature. The constant or so-called

[81] V.I.Kryshkin and A.I.Ronzhin, Nucl.Inst. and Meth. A247(1986)583. M.G.Albrow et al., Nucl. Inst. and Meth. A 256(1987)23.

[82] G.W.Foster, J.Freeman and R.Hangstrom, Nucl.Phys.B,A23(1991) 93 P.de Barbaro et al., Nucl.Inst.Meth.,A315(1992) 317

"stochastic" term comes from tower-to-tower variations in the calibration and both transverse and longitudinal non-uniformities in light collection from the pieces of scintillator. Based on EMC module in-beam test results[83] and simulations, this energy resolution will be achieved in practice with:

- a light yield from scintillating tile more than 2 p.e./tile/MIP;
- a surface uniformity of the scintillating tile better than 5% RMS;
- longitudinal uniformity to a level of less than 10% RMS within each tower;
- total cross-talk better than 2% between tiles for each of the tiles in the calorimeter.

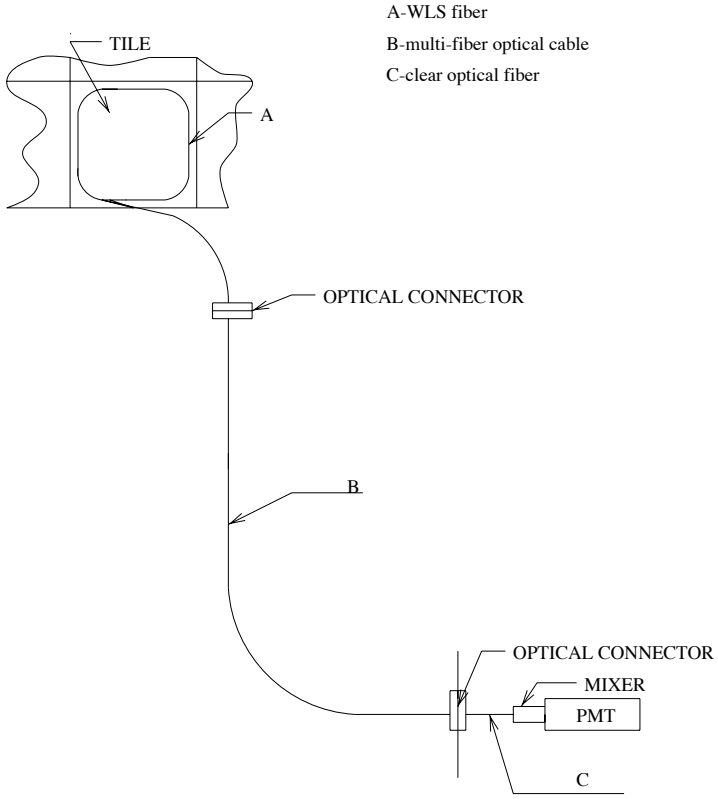


Figure I.2.3-1 A diagram of tile/fiber optical read-out scheme of Barrel EMC.

Much of the technology employed in the STAR EMC optical design has its origins in the original research and development conducted by the SDC, CDF, PHENIX, CMS and ATLAS groups, including megatile production, preparation of optical components (optical fibers, optical connectors) and fundamental measurements of the tile/fiber optical

[83] S.Bennett et al., The EMC and SMD Performance In 1997 Testbeam Run At BNL, STAR NOTE SN…..(To be published)

system. However to achieve optimization of the optical system for STAR, such as the design of tile, scintillating plastic material selection, optical fiber selection and optical connector selection, we have conducted an extensive R&D program described in chapter II.

### I. 2. 4 Summary of the Electronics System

The EMC electronics includes trigger, readout of phototube and wire detectors, high voltage system for phototubes, low voltage power, slow controls functions, calibration controls, and interfaces to the STAR trigger, DAQ and slow controls. The bulk of the Front end electronics including signal processing, digitization, buffering, formation of trigger primitives, and the first level of readout is located in custom EMC crates on the outside of the magnet iron. The exception is the preamplifiers and switched capacitor arrays for the SMD wire chambers. They reside on the EMC modules inside the STAR magnet. The EMC part of level 0 trigger is on the Electronics platform in the interaction hall, as is the overall STAR level 0 trigger. The EMC tower data collector is also on the platform. Data and trigger signals follow separate paths from the EMC barrel crates to the platform. The data is then shipped by fiber optics to the DAQ system interface in the counting house.

In STAR, the Level 0 trigger is the only level which does not incur large dead times from the opening of the gated grid in the TPC. The grid cycling rate is limited, and furthermore, there is not a great deal that can be done in the Level 1 system during the TPC drift time of 50 to 100 u sec. This makes it very important to concentrate as much functionality as possible in Level 0. The EMC is the premier detector for Level 0 because it is fast and it is the only detector sensitive to energy. For reasons of speed and limited bandwidth, the EMC trigger uses trigger primitives instead of the full EMC data. There are two kinds of trigger primitives from the EMC front end. The first set of primitives is the 300 tower sums of 6 bits each from patches of 0.2 by 0.2 in $\eta$-$\phi$. The second is the 300 high tower values of 6 bits from the single largest 0.05 x 0.05 tower within the 0.2 x 0.2 patch. These primitives are processed in EMC trigger on the platform to make final trigger decision on total Et, jet triggers, photon triggers, etc. These results are then passed to STAR Level 0 in 700 ns for the final Level 0 decision.

The full resolution data is processed via a separate path from trigger information. The Phototube signals from the towers are integrated and digitized in the front-end cards on every RHIC crossing. These data are pipelined until Level 0 trigger time, and if a trigger occurs it is transferred to a token-addressable memory on the card to await readout. All of STAR utilizes token-addressable memory in order to make a deadtimeless system. The SMD is two layers of wire chamber with pad readout. The signals from the pads are amplified and analog pipelined in a switched capacitor array on the detector before going to the front end processing cards outside the detector.

The EMC data collector on the platform receives signals from each of the crates. This data already has crate number, token number, and a simplified RHIC crossing number included by a multiplexer card in the crate. The collector can do pedestal subtraction, and zero suppression with addition of channel addresses. A standard STAR header for use in event building is also added.

### I.2.5 Summary of the Trigger Concept and Functionality

The STAR EMC is designed to provide triggers based on $E_t$, jets, and direct photons. The STAR Barrel calorimeter consists of 120 modules each covering $0 < \eta < 1$ and $\Delta\phi = 0.1$. Each modules has 40 physical towers covering $(\Delta\eta,\Delta\phi) = (0.05,0.05)$. The basic units of the EMC trigger at lowest level are a sum of 16 physical towers, which produces 300 trigger towers each covering (0.2,0.2) and the highest physical tower (0.05,0.05) in each of these trigger towers. These signals are digitized to 6 bits.

The sum of the 300 trigger towers produces $E_t$, which is used to trigger in AuAu collisions. $E_t$ carries information about the number of $\pi^o$'s produced in the reaction. Phenomena that can be selected using the charged particle multiplicity from the central trigger barrel (CTB) and $E_t$ include disoriented chiral condensates and Bose-Einstein condensates that signal the formation of a quark gluon plasma. In addition, trigger patches with $(\Delta\eta,\Delta\phi) = (1.0,0.8)$ can be correlated with similar patches in the CTB to provide triggering on localized domains of isospin fluctuations.

The high tower information is used to trigger on direct photons and electrons while suppressing jets in pp and pAu reactions. To trigger on jets in pp and pAu reactions, non-overlaping patches of 0.2x0.2 and 1.0x0.8 are used at level 0 and overlapping sums of the trigger towers can be used (subject to level 2 upgrade) to calculate patches with $(\Delta\eta,\Delta\phi) = (0.8,0.8)$ at level 2.

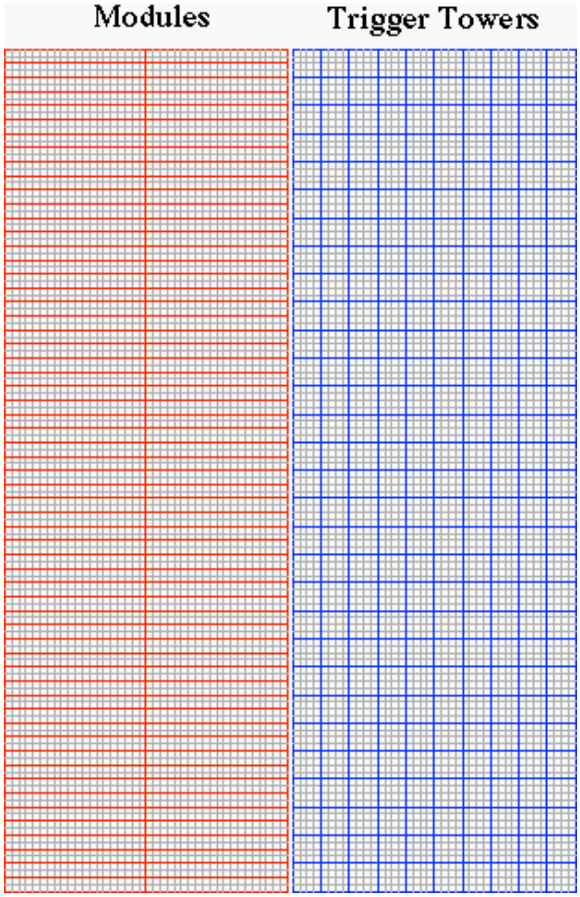


Figure I.2.4.1. Schematic drawing of STAR EMC showing the physical towers and the module boundaries (left) and the trigger tower boundaries (right). The vertical axis represents $\phi$ from 0 to $2\pi$ while the horizontal axis depicts $\eta$ from -1 to 1 for each frame.

Thus the STAR EMC will produce the following information for the STAR level-0 trigger:

- 300 trigger towers
$(\Delta\eta,\Delta\phi) = (0.2,0.2)$
6 bits each
- 300 high towers
$(\Delta\eta,\Delta\phi) = (0.05,0.05)$
6 bits each

Given this input, The STAR EMC level 0 trigger output is then

- Barrel $E_t$ > 3 threshold; 3 bits (1 bit/threshold)
- Jet tower (0.2,0.2) > 3 thresholds; 3x2 bits (2 bit counters)
- High tower > 3 thresholds; 3x2 bits (2 bit counters)
- Correlation of high tower> threshold and trigger tower > threshold; 2 bits (2 bit counter)
- Luminosity 3 bits barrel, 3 bits endcap

($E_t$ > 3 thresholds for barrel and endcap separately)
- Jet patch (1.0,0.8) > 3 thresholds; 3x2 bits (2 bit counters)

### I.2.6 Upgrade Options

The design of the EMC has left open several upgrade options. None of these will be addressed in any detail in this document, but they will be briefly outlined here for completeness.

1. The Pre-shower detector option

The primary tools for electromagnetic shower identification in the EMC are the shower maximum detector and the calorimeter tower response compared to momentum from tracking. The present design has been crafted to match the requirements of the EMC physics program. There are some aspects of the program that would be greatly enhanced by the improved electron – hadron separation that would be afforded by a pre-shower detector. In particular the identification of low energy electrons would greatly expand the J-Psi capability of STAR. This would have very significant impact on the reach of J/Psi as a diagnostic tool of Au+Au collisions, for example. The current EMC design includes a second set of read out fibers for the first layer of the calorimeter stack built into the detector and routed to the PMT boses on the magnet. An upgrade that would provide multi-anode photo tubes for these fibers and read-out electronics would be required to implement the pre-shower detector option.

2. SMD level – 0 trigger

The Shower Maximum Detector is designed with the provision to read out the wire signal from an eta-phi patch of 1.0 x 0.1. An amplifier-discriminator or ADC system could be built as an upgrade with the addition of the appropriate number of STAR trigger processor modules (DSM's) to permit the use of SMD primitives in the level 0 trigger as an enhancement to the direct photon tigger.

3. EMC Level – 2 Trigger

Overlapping Jet trigger towers of eta-phi = 0.8x0.8 would enhance jet threshold resolution beyond that achieved at level-0 with non-overlapping patches. It is prohibitively expensive to compute these patches in the level-0 trigger processors. As an upgrade, we have preserved the option to place the 0.2x0.2 EMC trigger tower data into a memory for use by processors that could be added to the STAR trigger system at level-2. A very early level-2 decision could have a significantly impact in pp running at RHIC's proposed upgraded luminosity.

Likewise, we have preserved the option to read out full resolution EMC and SMD data to a level-2 processor farm that would allow photon isolation cuts and other cuts utilizing correlation of the EMC and SMD to be made at the trigger level.

# II Mechanical and Optical Design of the EMC

## II.1 Overview of the Mechanical and Optical Systems

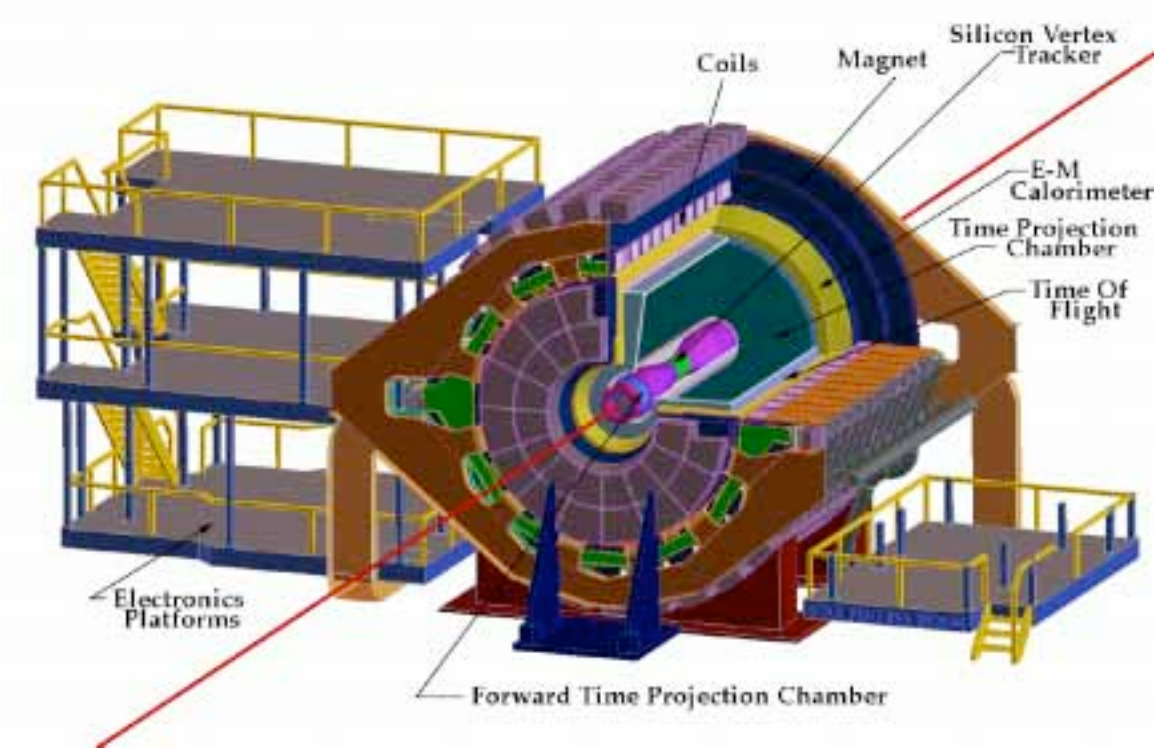


Figure II.1-1. Schematic illustration of the STAR detector showing the location of the EMC within the coils of the room temperature magnet, and the electronics boxes located on the outside of the magnet.

The overall design of the EMC has been heavily influenced by its location within the STAR detector, and hence it is helpful to review this location before explaining in detail the EMC's design. Figure II.1-1 shows a schematic illustration of the STAR detector at RHIC showing the principle sub-systems and the calorimeter. The EMC is located inside the large room temperature magnet within a cylindrical space approximately 41cm deep, by 6.2m in length, sandwiched between the Time of Flight system and the magnet coils. Due to the adverse affects of the magnetic field on the PMTs, they must be situated outside the magnet in the electronics boxes which are mounted on the flux return bars, or magnet backlegs, along with the rest of the associated readout electronics. Optical fibers run through the magnet coils to connect the EMC to its readout electronics.

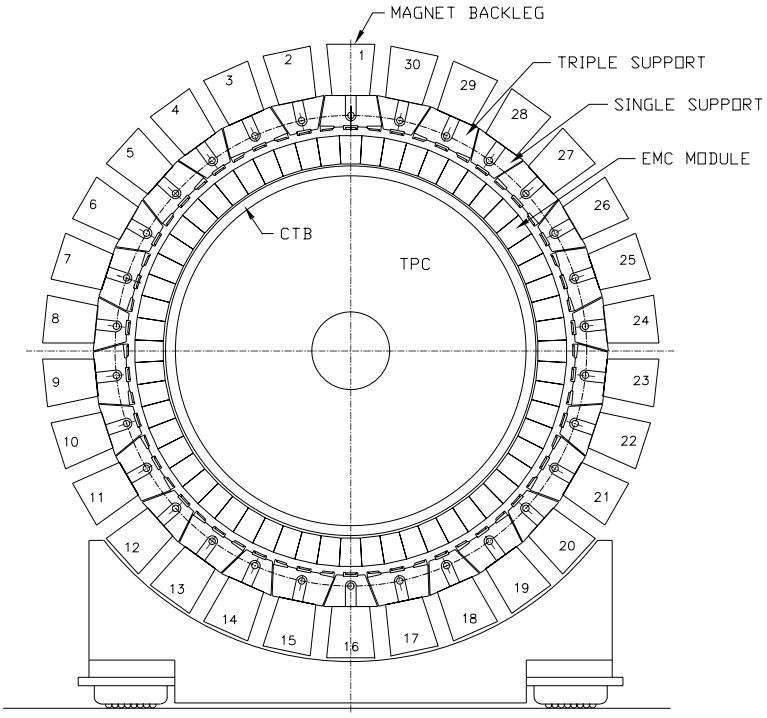


Figure II.1-2. End view of the EMC showing 60 modules, 30 flux return bars, and the alternating pattern of EMC support segments (single and triple).

The design for the barrel electromagnetic calorimeter includes a total of 120 calorimeter modules, each subtending 6° in $\Delta\phi$ (0.1 radian) and 1.0 unit in $\Delta\eta$. These modules are mounted 60 in $\phi$ by 2 in $\eta$ as shown in Fig II.1-2.

Each module is roughly 26cm wide by 293cm long with an active depth of 23.5cm plus about 6.6 cm in structural plates. A module is further segmented into 40 towers, 2 in $\phi$ and 20 in $\eta$, with each tower being 0.05 in $\Delta\phi$ by 0.05 in $\Delta\eta$. The calorimeter is thus physically segmented into a total of 4800 towers. Figure II.1-3 shows a side view of a module illustrating the projective nature of the towers in the $\eta$-direction, pointing back to the interaction region in the center of the barrel.

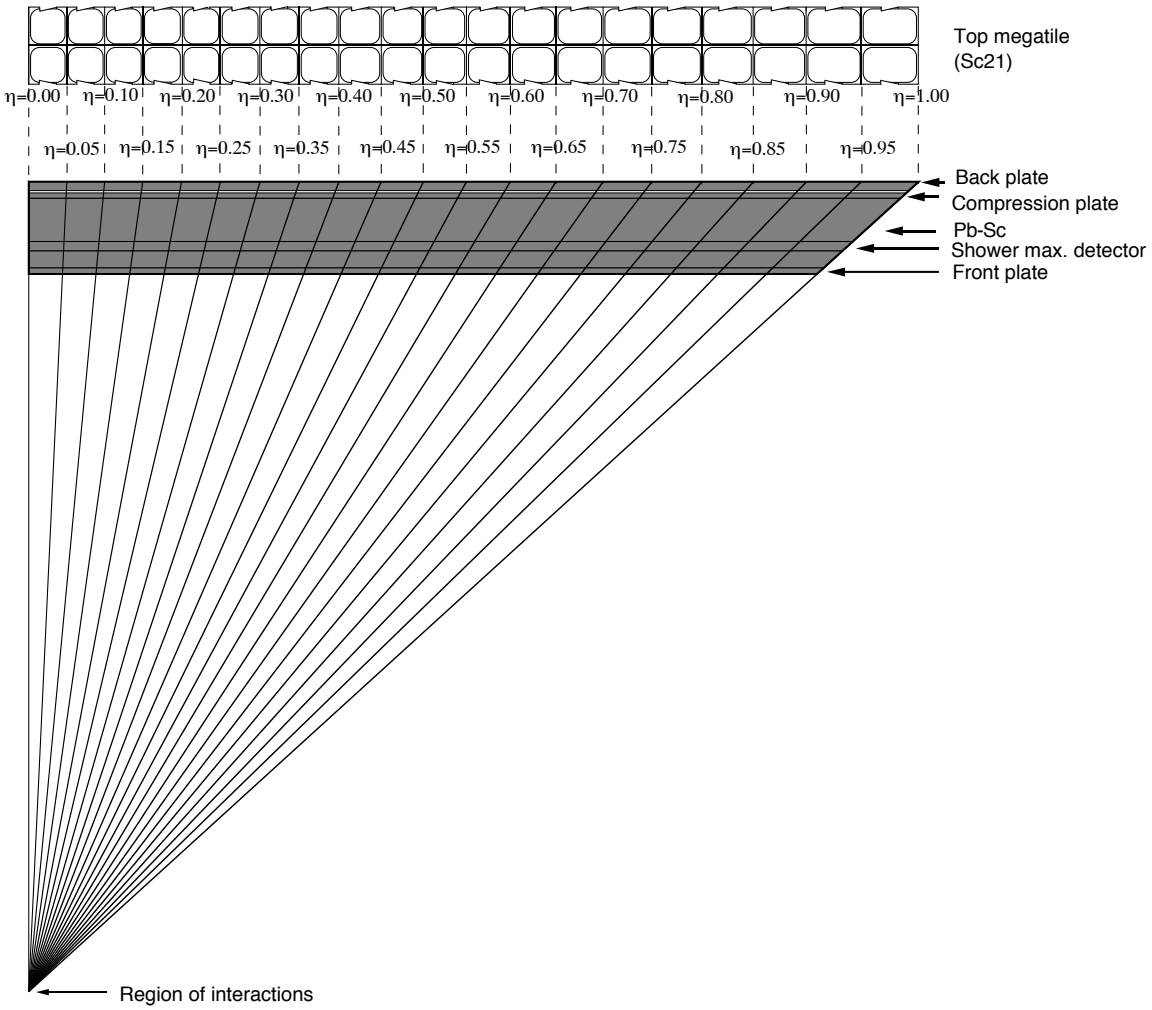


Figure II.1-3. Side view of a calorimeter module showing the projective nature of the towers. The 21st megatile layer is also shown.

The calorimeter is a sampling calorimeter, and the core of each structure consists of a lead-scintillator stack and a shower maximum detector situated approximately 5 radiation lengths from the front of the stack. There are 20 layers of 5mm thick lead and 21 layers of 5mm thick scintillator. This core structure, the stack, is held together by friction in the presence of compressional forces applied to the module stack. The compression is applied by a combination of 30 straps connecting the front and back plates of the structure, and a system of bolts and spring loaded washers between the back plate and a compression plate, as discussed in detail in section II.2.

The plastic scintillator is in the form of "megatiles", with 40 optically isolated "tiles" in each layer as shown in figure II.1-3. The true projective nature of the towers (constant size in $\Delta\phi$ and $\Delta\eta$) means that there are 420 different tile sizes in the calorimeter. This makes alternative scintillator production techniques such as injection molding impractical. In order to simplify handling, the megatiles are produced from two pieces of approximately 1.6 m long scintillating plates for each layer in the calorimeter. The signal from each scintillating tile is read-out with a wavelength shifting (WLS) fiber embedded

in a σ-groove that is machined in the tile as shown in figure II.1-4. After exiting the scintillator, the WLS fiber is routed along the side of the stack and terminated at a multi-fiber optical connector at the back-plate of module. 3.5 m long multi-fiber optical cables of clear fibers carry the light from the optical connector through the magnet structure to the electronics boxes mounted on the magnet backlegs where the PMT′s are located. Here the light from each of the tiles composing a tower is merged via a light mixer, which is placed between the fibers and the photocathode of the PMT to optimize detection uniformity.

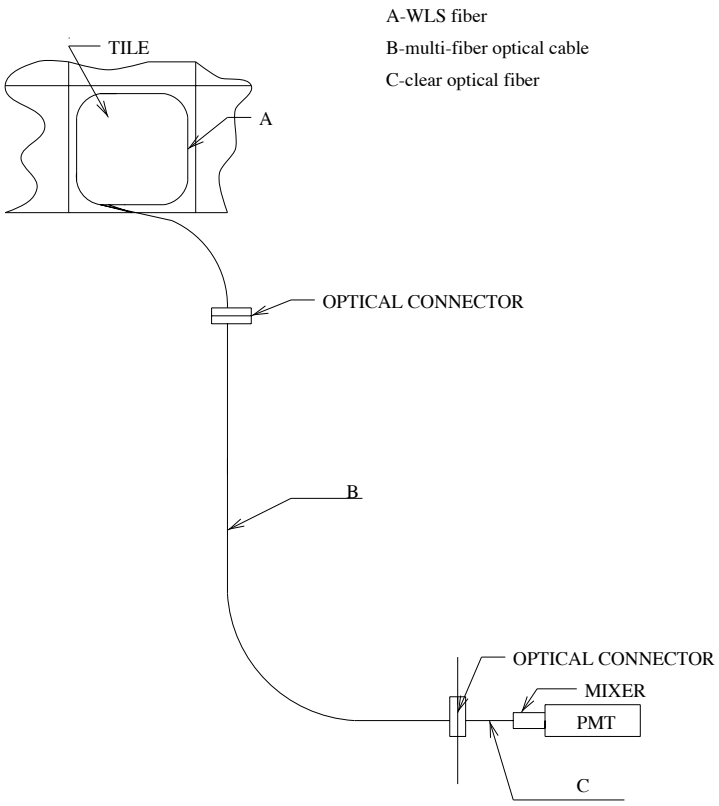


Figure II.1-4. A schematic illustration of the optical readout system for the EMC. The scintillator tile is readout by a short WLS fiber (A), which is coupled via a fiber ribbon cable (B), to the electronics boxes. Inside the electronics boxes the fibers are arranged into bundles corresponding to towers, by the clear fiber pigtails (C). The bundles then couple to the PMTs by light mixers.

The funding profile of the EMC is significantly delayed relative to the rest of STAR. This means that the calorimeter modules will be fabricated and installed into the magnet after the TPC and Central Trigger Barrel (and the initial implementation of the Time of Flight system) have been installed. In order to avoid removing the TPC during the EMC installation process, each EMC module is mounted on five sets of linear bearings which allow it to slide parallel to the axis of the magnet on linear rail systems which are anchored to the flux return bars. Part of the magnet, the linear rails systems, and the module, are shown in figure II.1-5. The linear rail systems themselves are each mounted to the magnet via five support segments, located between the magnet coils, which allow

the load of the calorimeter to be cantilevered back to the flux return bars of the magnet. The support segments have to be large enough to span the radial distance of the coils. Figure II.1-2 shows an end view of the magnet, illustrating the support segments and rail systems.

The readout fibers of the calorimeter have to be routed through the gaps between the coils. To facilitate this, vacuum-formed plastic fiber guides are inserted into the support segments. These allow the fiber cables to be pulled through the five gaps between the magnet coils at the same time as the module is slid into the magnet on its linear bearings. Cables from the wire-strip gas shower max detector situated in the stack at approximately 5 $X_o$ are routed out of the module at the $\eta$=1 end of the detector.

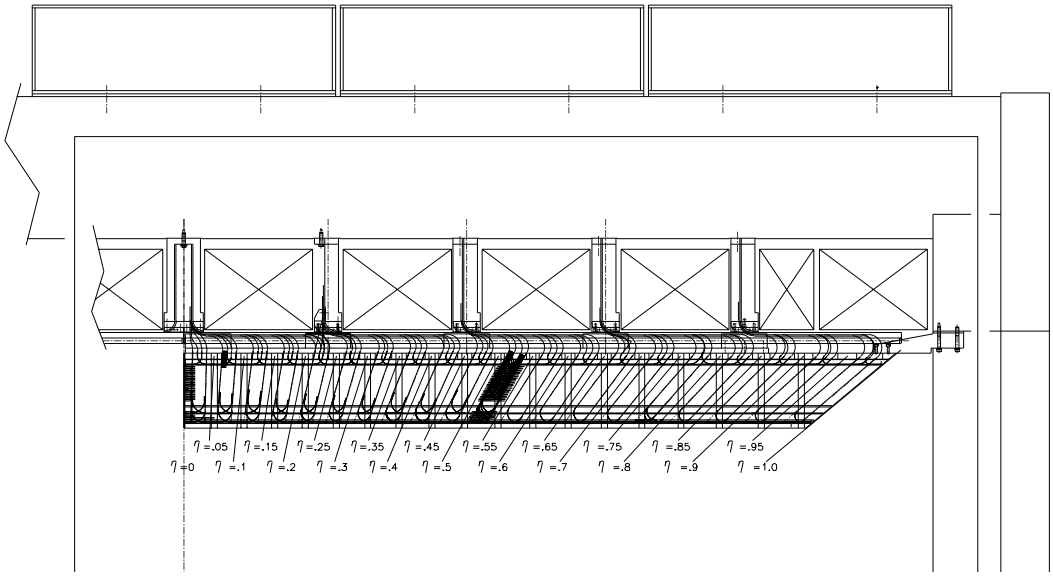


Figure II.1-5. Side view of an EMC module showing the scheme of routing the optical fibers between the coils of the magnet and the scheme of fiber routing on the sides of the module.

The mechanical and optical structure of the detector will be described in detail in the following sections, along with the research and development leading to verification of its design.

## II.2 The Mechanical Design of the EMC Module

### II.2.1 Compressed Module Design

The barrel electromagnetic calorimeter is composed of 120 calorimeter modules, each spans 6 degrees in azimuth and 1.0 in $\Delta\eta$. The 120 modules are located inside the aluminum coil of the STAR solenoid and are physically attached to the magnet flux return bars through sets of supports segments. These segments are alternately distributed in azimuth as “singles” (holds one module), and “triples” (holds three modules), as shown in Fig II.2.1.1. There are 30 flux return bars in the magnet, consequently there are 15 single and 15 triple supports on the same radius-phi plane. In the direction of the solenoid axis, the segments are distributed along the flux return bars in the spaces between coils. There are 9 segments total per flux return bar, one at the center that holds the eta=0 end

of two adjacent modules and 4 following in each opposite direction (Fig. II.2.1-2.) The center segments are distributed in azimuth in the radius-phi plane that intersects eta=0, dividing the barrel in two equal halves. On each half, linking the segments that runs along each flux return bar there is a double track for precision linear bearings that allows the modules to be slid into their final positions in the detector (Fig. II.2.1-2).

A compressed design has been adopted for the modules. The structural members of each module are: an aluminum back plate 31.7 mm thick, an aluminum front plate 19 mm thick, 30 stainless steel type 316 straps 2 mm thick and two stainless steel type 316 bulkheads 4.75 mm thick each. The back and front plates are held together at the proper boundary dimensions by the uniform distribution of the 30 straps and two bulkheads plates. The straps are mounted, 15 on each side of the module, and the bulkheads, one at eta = 0 and one at eta = 1 (Fig II.2.1.3). These straps, and bulkheads in particular, align the back and front plates and serve to resist the compressive force applied to the stack. On the outside face of the back plate is attached an aluminum interface plate 25 mm thick, 193 mm wide and just under the length of the module. This plate interfaces the back plate with a set of five linear bearing carriages. These carriages mate with the tracks mounted on the support segments, and are distributed along the back plate such that they align with the support segments when the module is fully inserted (Fig. II.2.1.2).

The dimensions of the module in the eta direction are 2930.4 mm (maximum length of the back plate) and 2574.3 mm (minimum length of the front plate). In the phi direction, the dimensions are 259.9 mm (maximum width of the back plate) and 228.1mm (minimum width of the front plate). In the radial direction the depth is 302.9 mm. The radius from the front plate to the central axis of the magnet is 2235 mm. The gap between two modules in phi is 5.6 mm cover to cover as shown in fig. II.2.1.4. The analysis of this gap and its relation to the module and rail system tolerances is discussed in chapter VIII.

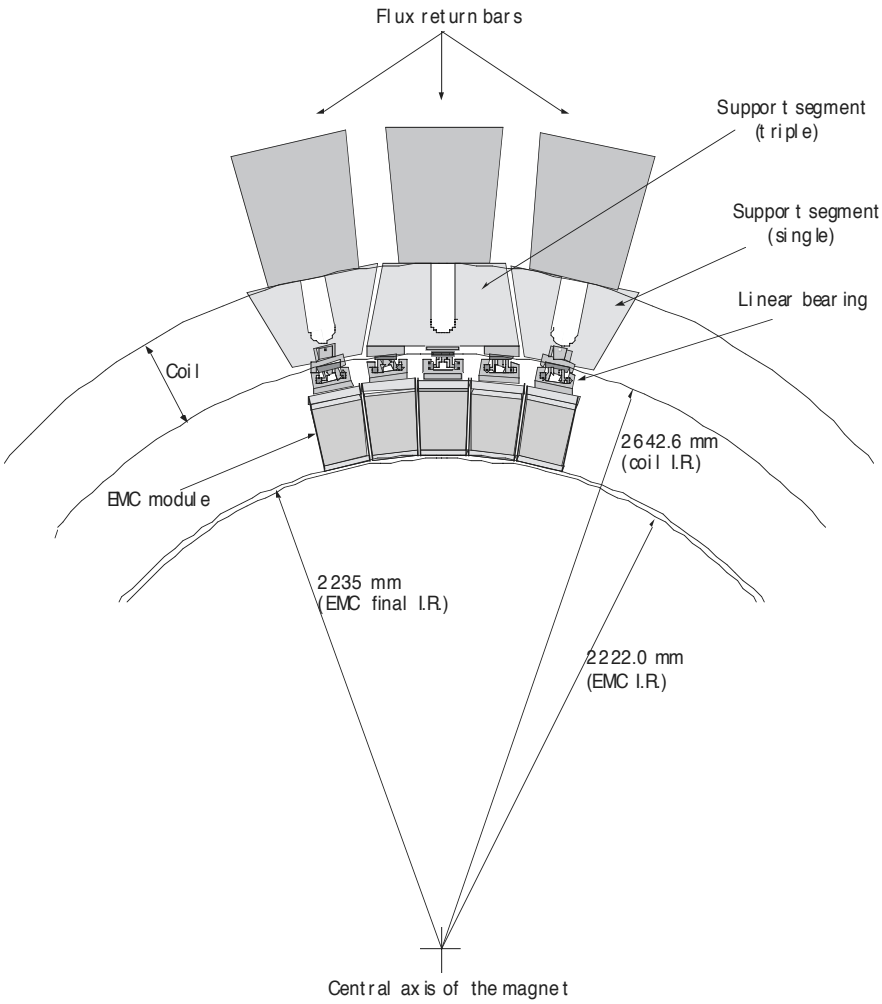


Figure II.2.1-1 Schematic illustration of the distribution of components and some radial boundaries in the barrel.

This is a lead-scintillatorsampling calorimeter. The mechanical construction of each module consists of 20 layers of 5 mm thick antimonial lead (1% Sb), 21 layers of 5 mm thick scintillator tiles, a ~ 20 mm thick SMD. Also a ~31 mm thick aluminum back plate, a ~19 mm thick aluminum compression plate and a~19 mm thick aluminum front plate. The order of components on the assembled stack is shown in Fig II.2.1-5. The scintillator layers consists of sheets called megatiles with two half megatiles making the length of a layer in the module. Individual optically isolated tiles are machined in the megatiles to obtain the 40 tiles required per layer. The tiles are sized to make the 40 projective towers in a module. The 40 towers in a module are arranged in two rows of 20 tiles of 0.05 by .05 in $\phi$ and $\eta$ running along the eta axis.

Destructive tests have been performed to determine the bending strength of the scintillator tiles with the separation grooves in place filled with epoxy, the conclusion is that failure happens in the scintillator-epoxy interface at a bending radius of 11 m implying that the tiles will be quite robust in relation to the handling they receive during module assembly.

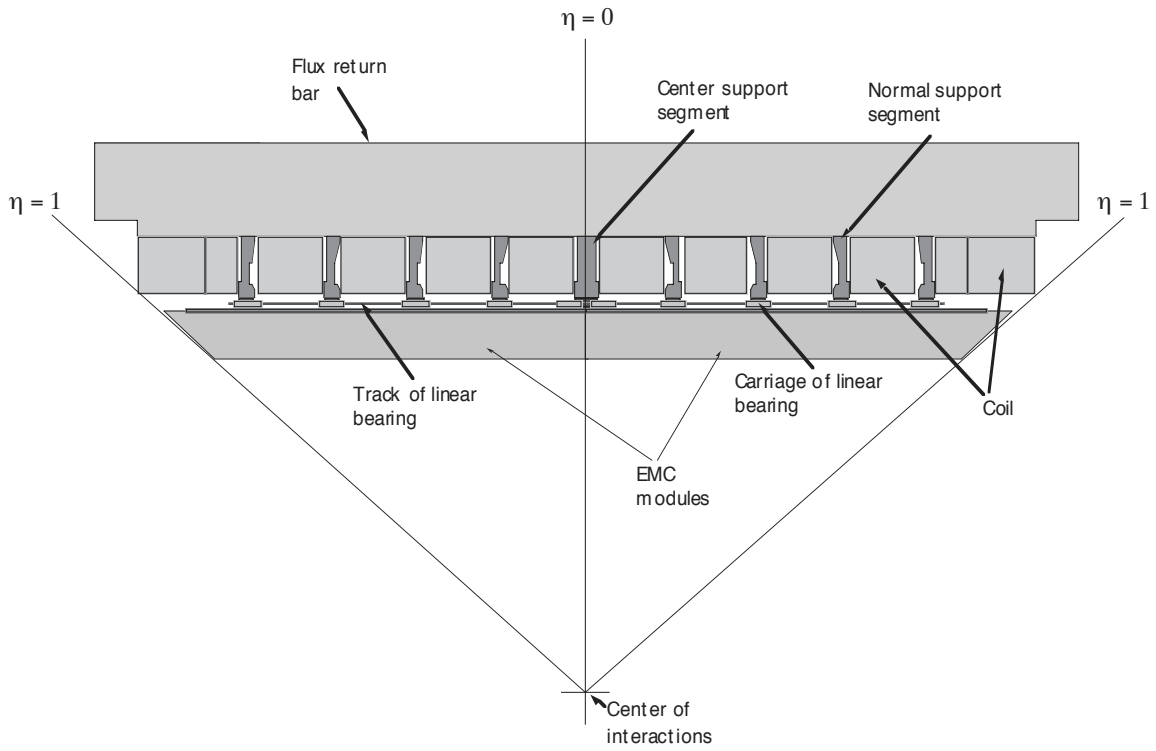


Figure II.2.1-2 Schematic illustration of one flux return bar and components linking the modules.

The wavelength shifting fibers come out at the border of each tile at a position correspondent to the eta center of the loop. This fibers are routed in the direction of the back plate where, through connectors mounted in this plate, they are connected to clear fibers. The pattern of fiber routing and connectors is shown in fig II.2.1-6.

Special care has been taken with the selection of materials used for the constru c-tion of the modules. Magnetic materials, in particular, which could distort the magnetic field of the STAR solenoid have been studied in detail. Some cases materials are used in the design. For example, the linear bearings system rods require the high strength and surface hardness of steel. Before any magnetic materials were used, however, the STAR magnet group was consulted for its approval. Where possible, of course, aluminum and stainless steel type 316 has been selected.

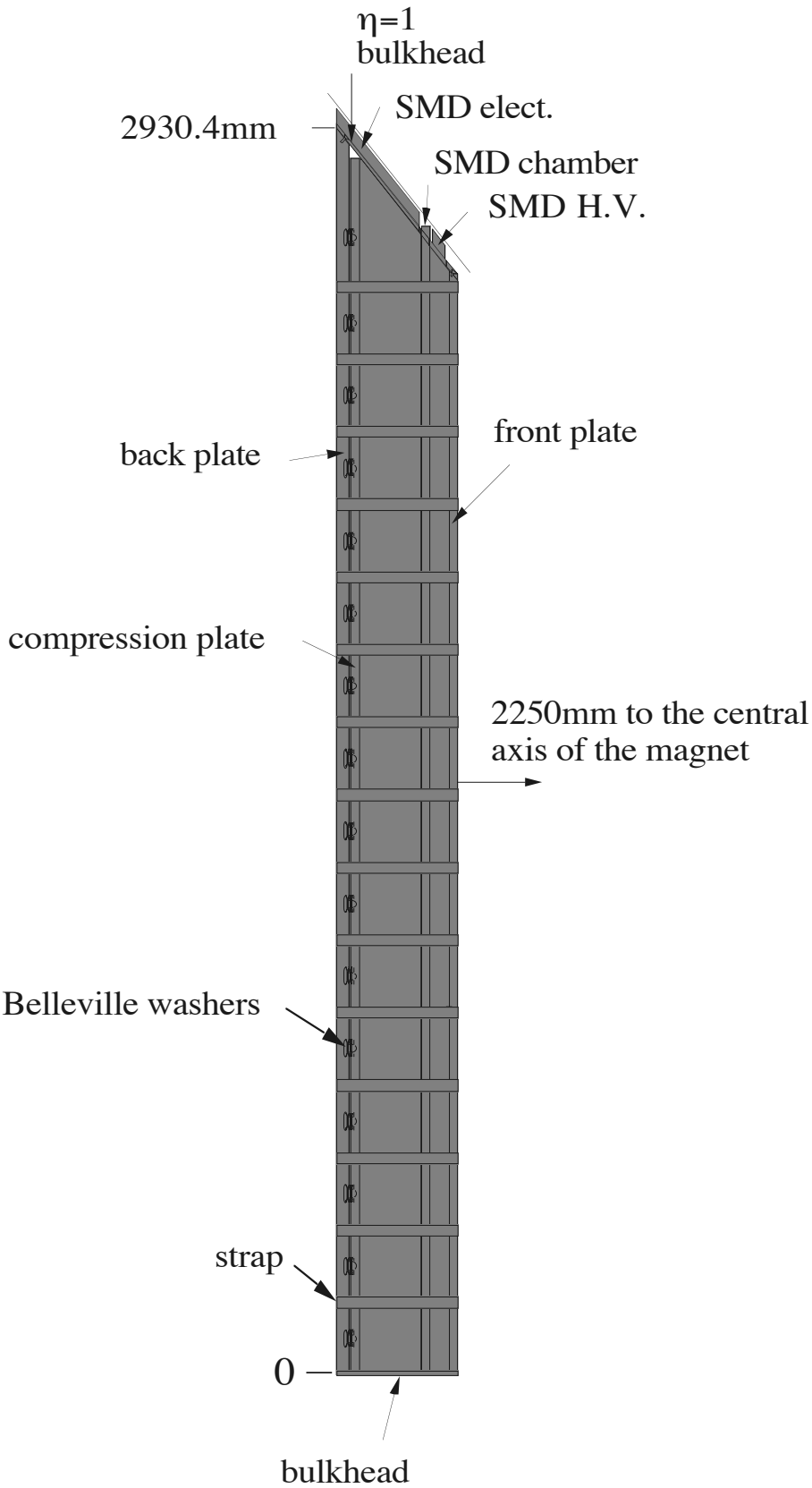


Figure II.2.1-3 Schematic illustration of the side view of the module showing components distribution.

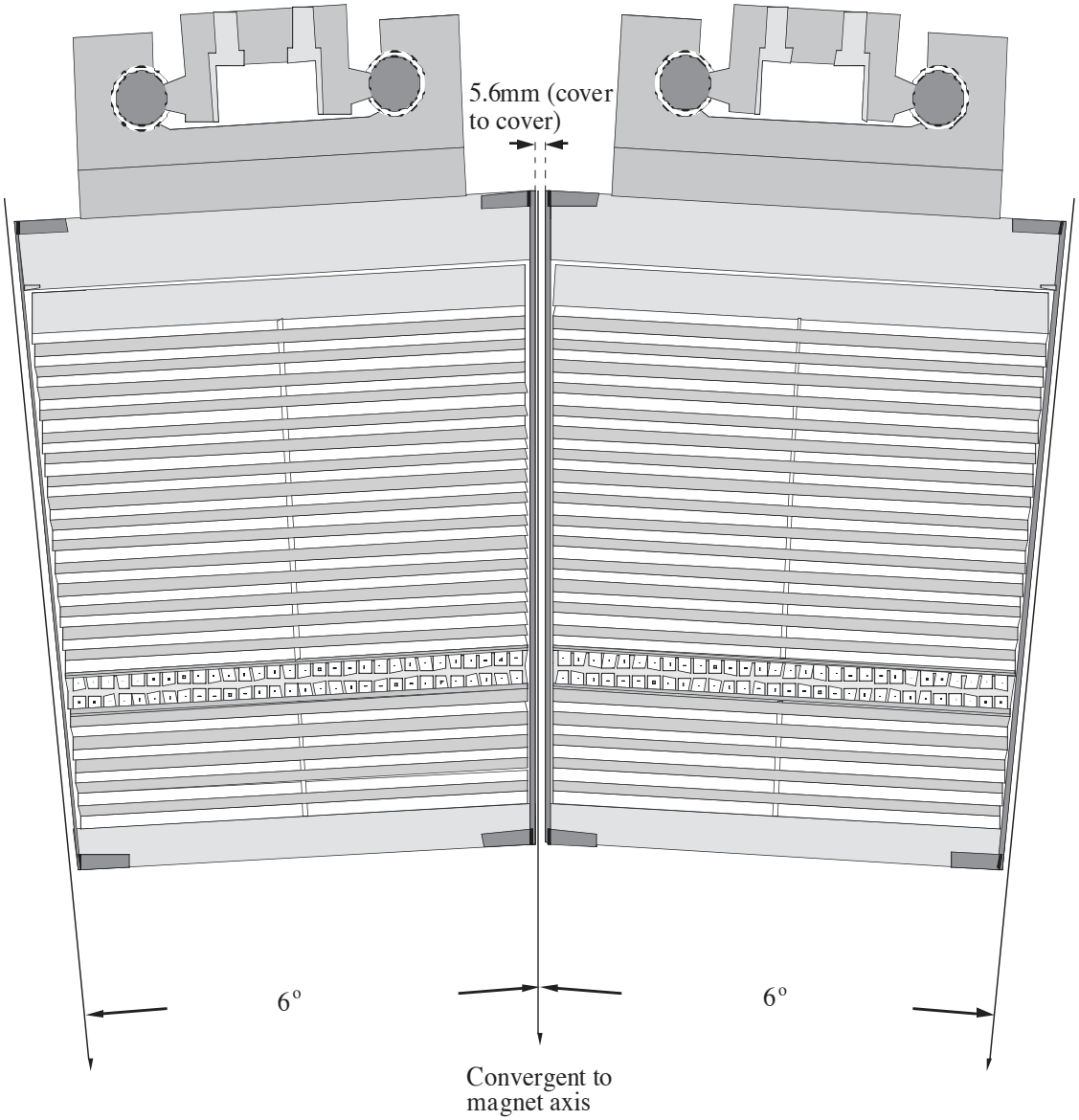


Figure II.2.1-4 View of two EMC modules showing the phi gap.

The weight of each module is ~2116 lb. and the different components of the stack are held in place by the friction that appears when a compressive force is applied between the front and compression plates. Extensive tests have been performed at WSU to determine the coefficient of static friction for every pair of materials in the stack. The minimum coefficient found was $\mu = 0.25$ corresponding to the bond paper-scintillator interface using Bicron scintillator material. Using the Russian scintillator material with its rougher surface chosen for the EMC, we find $\mu = 0.360$. Allowing a safety factor of

two and using the smaller coefficient, the compressive force needed for the stability of the stack is 2116 lb / 0.125 = 16,928 lb.

The pressure in the stack has significant variations, being ~18.7 psi on the scintillator closest to the front plate (Sc1) and~15.5 psi on the closest to the back plate (Sc21). The average pressure in the stack is ~17.1 psi.

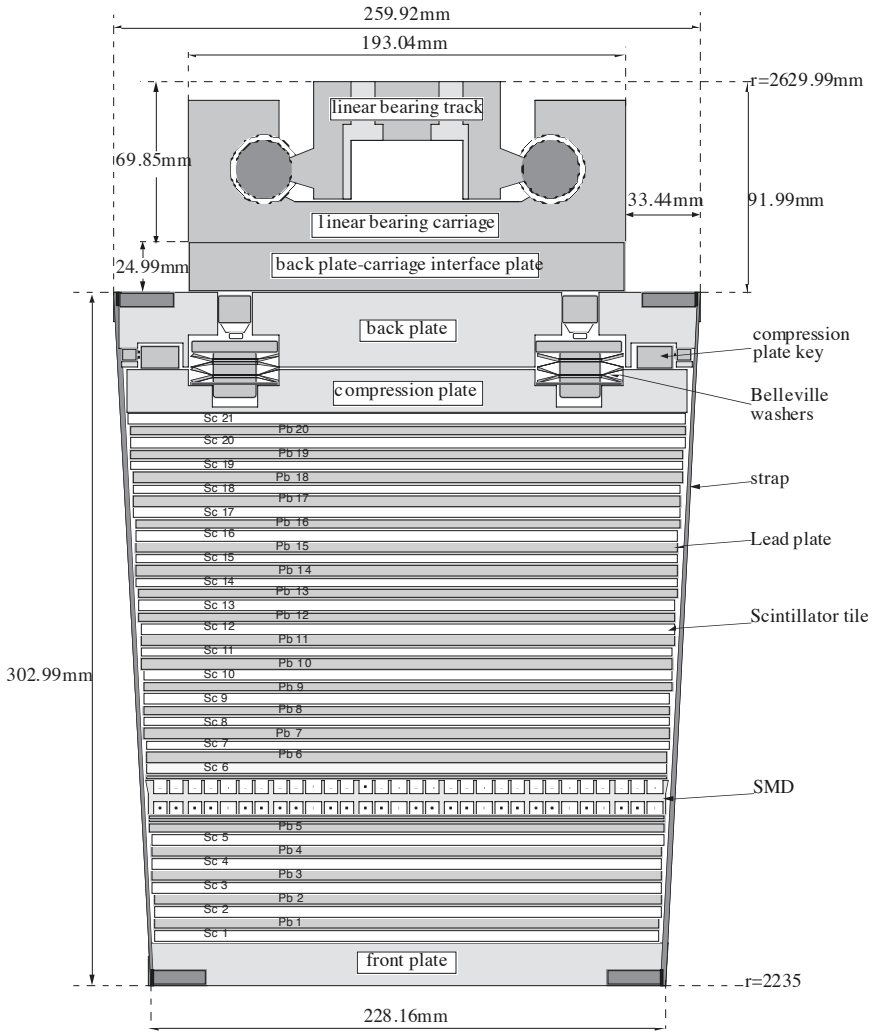


Figure II.2.1-5 Schematic illustration of a cross-section through a STAR EMC module.

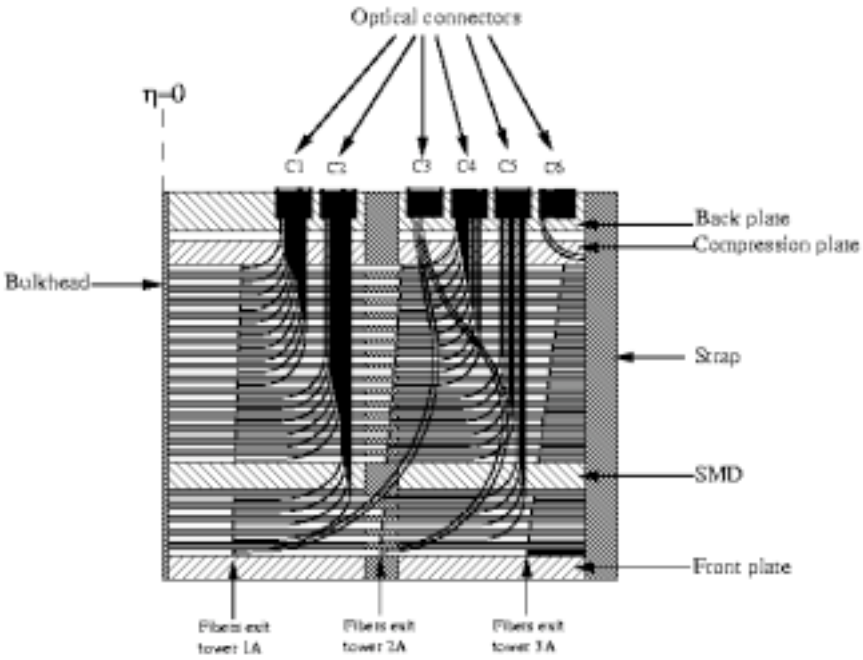


Figure II.2.1-6 Schematic view of the fiber routing at the low eta end of the module.

The required compressive force is transferred to the stack through the compression plate. This is a 19 mm thick aluminum tooling plate that is situated between the back plate and the stack. This plate receives the load from 32 sets of Belleville washers compressed by setscrews from the back plate or alternatively through 32 load cells immediately adjacent to the Belleville washers and pressed by setscrews from the back plate. The detail is shown in fig. II.2.1-7. Sensotec miniature load cell-amplifier matching sets are used for the pressure test of the prototypes and assembly of the production modules.

After stacking, the module is gradually compressed through the 32 load cells allowing the pressure to be gradually raised in a uniform fashion. After the module is stable under pressure, as indicated by readings of the load cells, the compressive force is transferred to the adjacent set of set screws which apply their force to the compression plate through Belleville washers. In this last step, the load cells are "zeroed" out in a uniform fashion preserving the uniform compression of the stack. Once the force has been transferred off of the load cells, the are removed from the stack.

Finite element analysis has been performed to study the distribution of stresses and deflections sustained by the different components of the module. Models were prepared for the $\phi$-r and $\eta$-r planes. The results of the analysis (Fig. II.2.1-8/9) show the extent of the non uniform distribution of stress in the stack that follows from the periodic placement of the straps and Belleville washer compression points. This flow generates a higher stress (~40 psi) along the stack concentrated in an area adjacent to the $\phi$ boundary and decreasing towards the center of the module to a pressure < 10 psi. To verify the results of the analysis, the stack was assembled with Prescale (pressure sensitive film) installed. The film was placed close to the front plate, at the center and close to the com-

pression plate. A combination of films and special pads was used to cover the range from 0 to 75 psi. The results of the Prescale film test validated qualitatively the FEA calculations. The FEA calculations which were performed primarily to examine the stress distribution in the scintillator (see below) have also shown that the stress and deflections on all the mechanical components of the module are well within very reasonable limits.

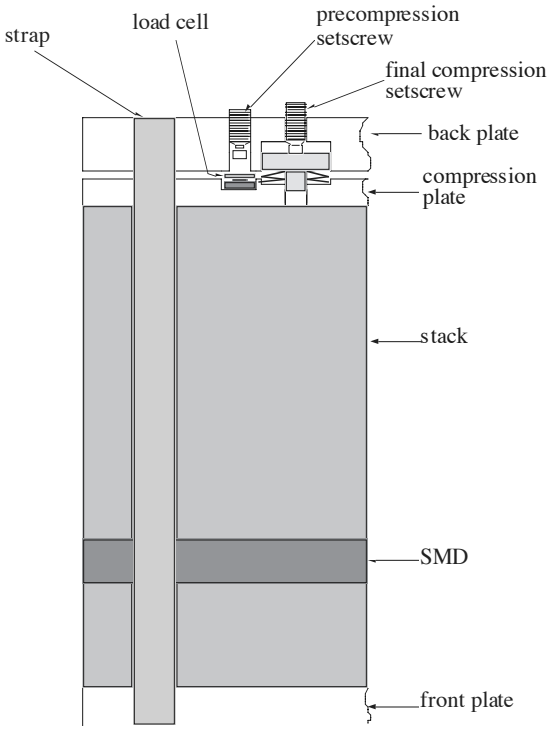


Figure II.2.1-7 Schematic view showing the opening for the load cell and Belleville washers.

The consequences of the non-uniform pressure in the stack have been carefully studied in relation to the light output of the scintillator tiles. An experimental setup was designed in a dark box that allowed us to scan the tiles with cosmic ray muons while under controlled temperature and pressure. The pressure was varied within a range of 0 to 50 psi. Temperatures ranging from 20 to 45 degree C were held constant within 1 degree C during these studies. The test setup is shown in Fig.II.2.1-10. The results of the tests, discussed in detail in section II.3 revealed that the range of pressures encountered in the stack will not impact the calorimeter performance.

The effects of lead creep have been analyzed in order to predict long term structural stability of the EMC modules. The rate of strain of antimonial lead plate (1% Sb), 5 mm thick, under a pressure of 3 kg/cm$^2$ is ~ $5*10^{-6}$ %/h or $2.5*10^{-7}$ mm/h. Thus the shrinkage rate for the stack considering 20 lead plates is ~0.044 mm/year. This rate leads to a very fast decay of pressure in the stack. To slow down this decay, a set of Belleville washers is incorporated in the force loop. These washers are characterized by their nonlinear relationship between load and deflection. The dimensions can be arranged so that a large deflection can be absorbed with very little change in load.

For the load range encountered in the EMC module, a set of certified Rolex Belleville washers XAM-402010, 2 in parallel and 4 in series, has been selected. These washer have been optimized for the 529 lb/screw load. The curve of load vs. deflection for these washers is shown in Fig.II.2.1-11.

The selected washers will control the stability of the module against Pb creep for well over 20 years once assembled. Strict procedures and controls are used in order to insure that the lead has been properly pre-compressed so as to minimize the elasticity of the stack itself at assembly. After stacking, a simple compression protocol is followed to verify that all of the elastic components of the stack are removed. The process of relaxation of the stack can take up to several weeks depending on the waviness of the individual

components used. For this reason, all of the lead sheets are pre-compressed between precision ground steel surfaces before stacking. For the removal of these elastic components, During compression of the stack, the procedure is to raise the pressure slowly in precisely controlled steps and record the rate of pressure decay of the stack as a function of time. Repeated adjustments are made to bring the stack pressure to the rated value. This procedure is continued until the pressure decay becomes ceases at the 1 part per $10^5$ level per day which is the sensitivity of the pressure measurement. At this moment, the load can be transferred from the load cells to the Belleville washers.

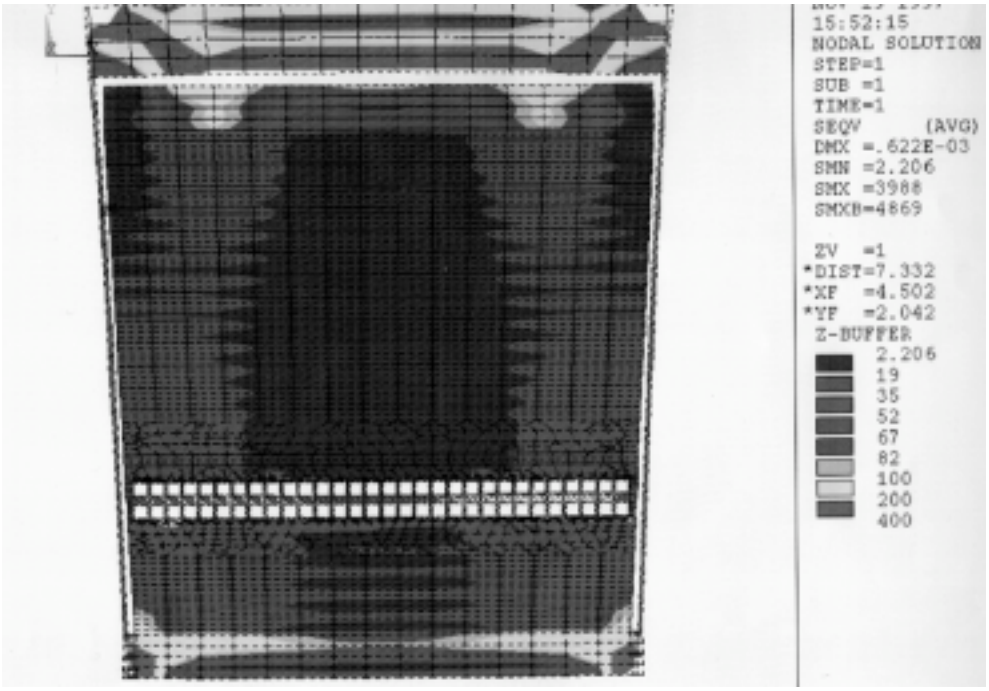


Figure II.2.1.8 Finite element analysis showing stress distribution in the EMC module stack.

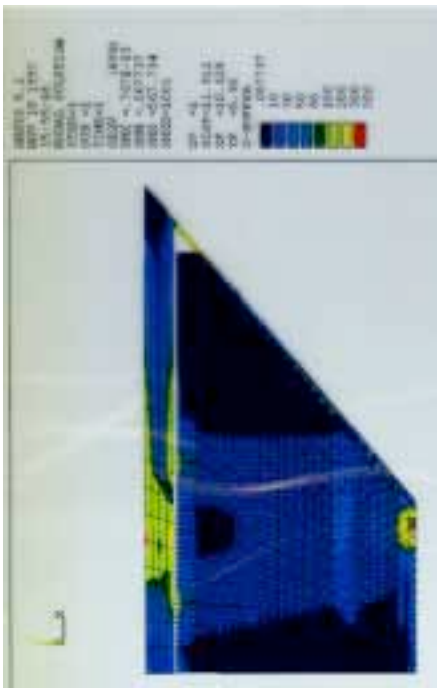

Figure II.2.1-9 Finite element analysis showing stress distribution in the EMC module stack at $\eta = 1.0$

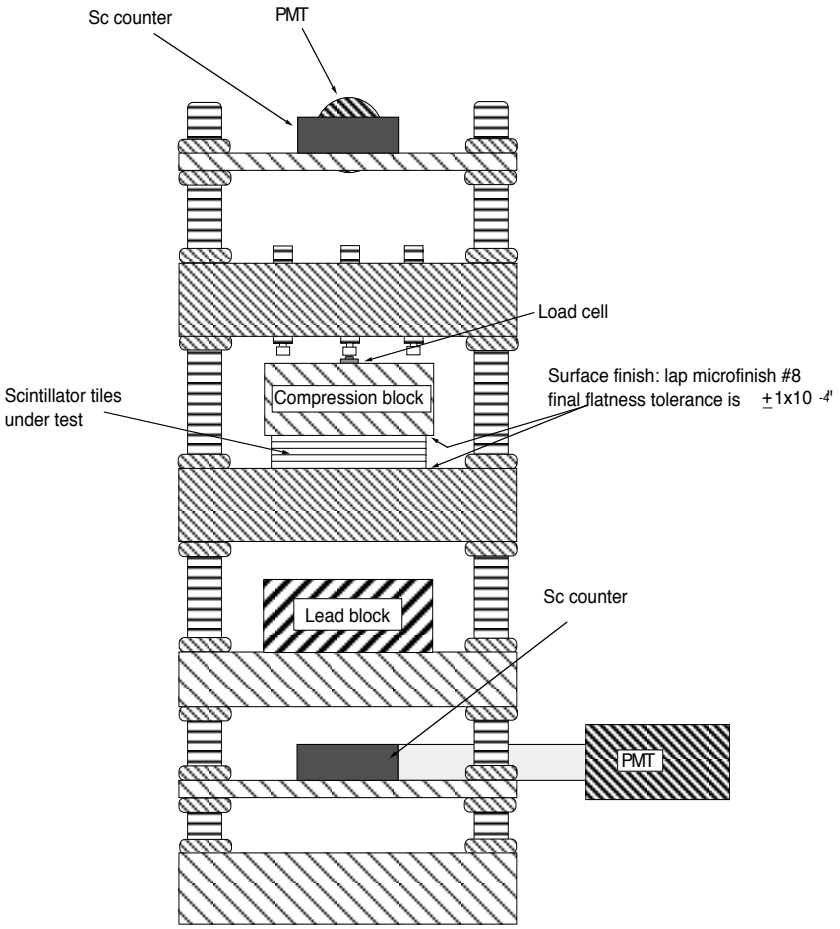


Figure II.2.1-10 Schematic view of the setup used to measure light output vs. pressure of scintillator tiles.

## II.2.2 Module Assembly and Production Plan

During the EMC module prototyping stages at WSU, efforts have been made to scale the facilities and handling equipment for the production requirements of full size EMC modules. These facilities have been upgraded during and have already been utilized in the assembly of a full size module.

For module stacking, a table has been designed that consists of a W12 I beam with 12" flanges weighing 136 lbs/ft. The beam is 12 feet long and rests on a very stable base. The stacking flange has been ground to obtain a final flatness < 0.004" along the

axis of the beam. A set of 10 precision spacers is attached to the top of the beam so that some free space is provided under the module once it is finished to mount straps, install handling arms, install and remove the stacking guides, etc. Two gutters are mounted on either side of the beam for fibers handling.

### II.2.3 Prototyping Activities

Several mechanical and functional prototypes have been made during the design phase of the project. Each of these prototypes has been made using final construction materials. The tests included: studies of mechanical behavior, tests with an AGS beam at BNL, optical tests, cosmic muons tests, long term pressure stability tests, etc. The result of these tests has been used as a feedback loop for the final design of the modules as well as peripheral systems.

The evolution of prototypes at WSU has been as follows. An engineering mechanical prototype was first designed and constructed. The test module design was ~ 80" long but otherwise virtually identical to the existing stack design. The module was used to establish compression protocols and to study the mechanical stability of the stack using a system capable of measuring deflections of the module smaller than 0.001" over 360 degrees of rotation around its center of mass (Fig II.2.3-1). These later tests were important to verify the suitability (coefficient of friction) of the selected construction materials. Using this prototype, tests were conducted to measure the coefficients of static friction, between different components. For this application, a special fixture was designed. This test module was also used to verify, by direct measurement, the calculated pressure distributions within a compressed module. Other studies were related to the pressurizing technique to be used and the measurement of loads in the stack, distribution of pressure in the stack, etc. During all of these various tests, the module was assembled and disassembled approximately 50 times allowing substantial experience to be gained in these procedures.

Fiber routing was also studied with the first mechanical prototype. Studies with both the sigma configuration and the alpha configuration with and without the protection notch were undertaken. Experience gained through these studies, was very important in establishing the final fiber routing scheme.

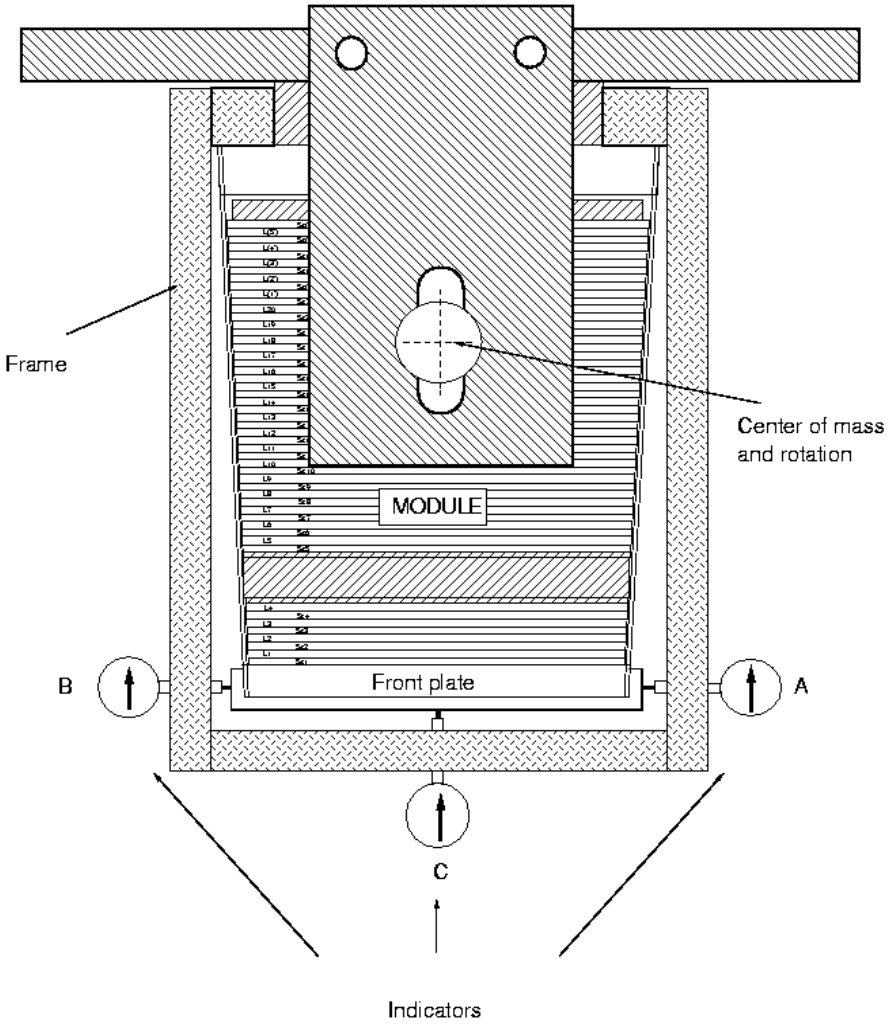


Figure II.2.3-1 Schematic view of the setup used to measure deflections of the module.

The mechanical model was also used to empirically study the thermal expansion characteristics of the stack and verify the analysis used to set some of the assembly tolerances and clearances.

The second prototype was fully instrumented as a detector. The module had eight towers (4 in eta by 2 in phi) assembled from megatiles that spanned the eta=.05 to 0.2 locations in STAR and was geometrically identical to the corresponding section of the STAR module. The module was fitted with a double layer shower maximum detector of a design that will be utilized in the production modules. The module used, however, a number of fiber techniques which have since been abandoned in favor of simpler and more robust techniques. These details of this prototype and its performance in-beam at the AGS are discussed in sections ** (towers) and ** (SMD) below. Pictures of this prototype at different stages of construction are shown in figures II.2.3-2/3/4

The third and possibly the last generation of prototypes is on going now with the construction of a full size EMC module that we plan to test in beam in October. All the

possible improvements suggested by the feedback of the previous prototypes regarding the physics and mechanics have been carried out to obtain a high quality detector.

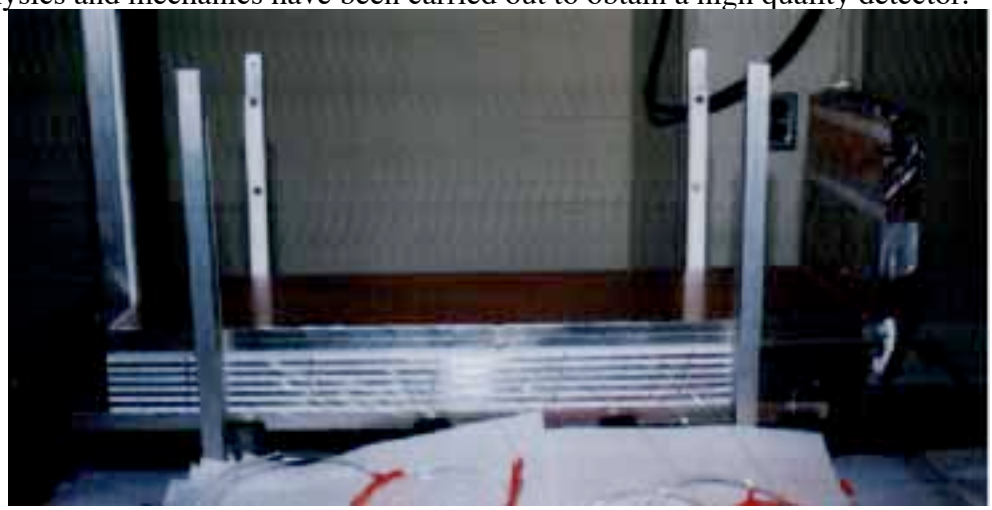

Figure II.2.3-2 Picture showing assembling of the prototype module for the test beam run 1997. The shower maximum detector and its prototype FEE package (on the right) are seen.

Figure II.2.3-3 Picture showing assembling of the prototype module for the test beam run 1997(compression stage).

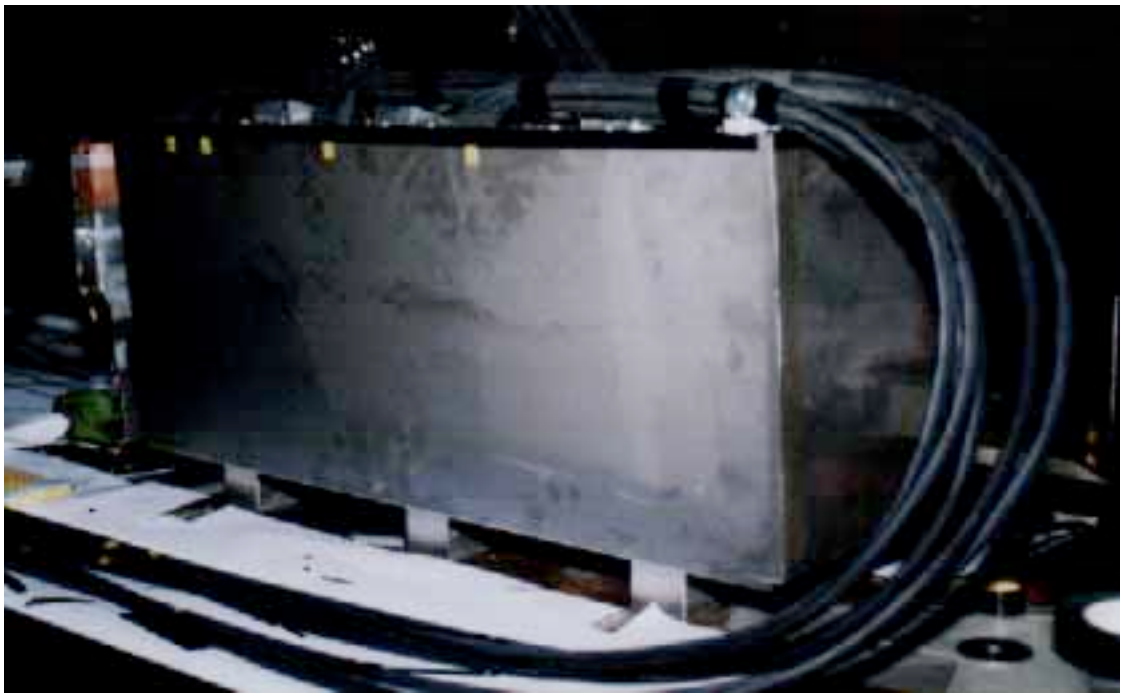

Figure II.2.3-4 Picture showing the assembled prototype module for the test beam run 1997.(ready to go).

### II.2.4 Quality Assurance Program

Virtually all of the mechanical components of the modules, with the exception of those few better suited for high volume production techniques, are manufactured in house at Wayne State. Regardless of the source, all components are subjected to 100% first part inspection to be followed by critical dimension checks on all parts thereafter. For major parts which will be built over the duration of the project, we will incorporate 100% inspection on a regular basis (e.g. monthly or as appropriate) to guard against gradual erosion of manufacturing standards.

The modules are assembled in precision jigs which provide for the accurate loc a-tion of individual lead and scintillator plates. It is essential to control the positioning of these plates as their location determines the open gap provided for fiber routing between the stack and the tensioning straps. The elements of the jigs which define the positions individual plates must be removed and reinserted for each module. 100% inspection of the assembly jig is thus undertaken before the assembly of a module may begin. Before packing for shipping, the finished modules are subject to an inspection rate of 100% of their critical dimensions.

Traveling documentation will move with each manufactured part to such that an archival record of each of the quality assurance steps is maintained for all the components of a completed module.

As this document is being written we have just completed the assembly of the first full size mechanical prototype and a draft set of assembly procedures now exists based on experience with this first module. This prototype module will shortly be disassembled and reassembled as module-0, the first fully instrumented EMC module (planned for use in the fall 1998 AGS test beam). The draft assembly documentation will be refined and finalized in this process thus archiving assembly procedures to insure uniformity over the duration of the project.

### II.2.5 Safety Matters

All the procedures and material handling at WSU are in compliance with State regulations and OSHA standards.

## II.3 The Optical Design of the EMC Module

### II.3.1 Scintillator Plates Production and Quality Control

The scintillating material used in the Optical system must produce enough light for easy identification of the minimum ionizing particle penetrating the calorimeter and must have good transverse uniformity of the response. Our baseline choice of scintillating material is standard polystyrene-based scintillator system.

**Standard polystyrene-based scintillator system:**
**PS (PSM115) →→→ Primary Dopant (pTP) →→→ Secondary Dopant (POPOP)**

This material has attracted the attention of researchers due to its comparatively high light yield and low cost. Polystyrene (PSM115, the grain size about 3mm) is mixed with finely dispersed scintillation dopants, most commonly used are 0.75%÷2% of paraterphenyl (pTP) and 0.01%÷0.04% of 1,2-bis- (2-(5-phenyloxazolyl))-benzene (POPOP). The choice and concentration of wavelength shifting dyes depends on the specific requirements (direct or WLS read-out) and are under the consumer's control. Figure *II.3.1-1*. shows the typical absorption and emission spectrum of pTP and POPOP [1].

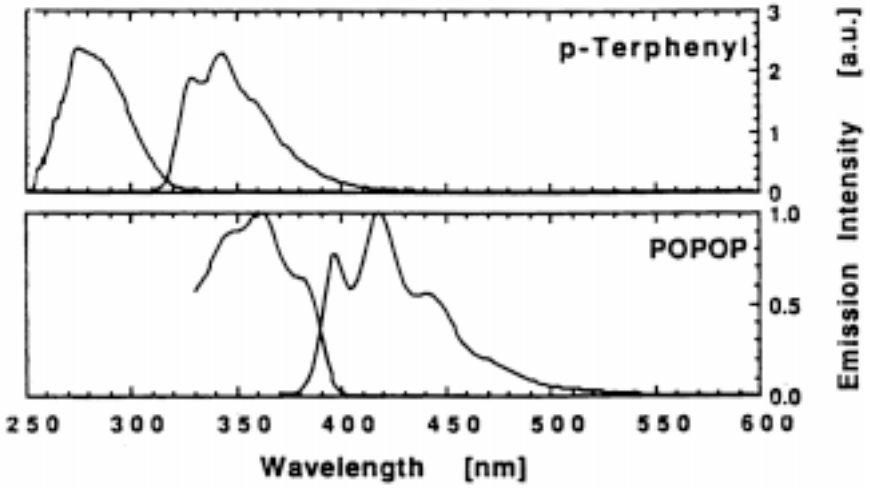


Figure II.3.1-1 Typical absorption and emission spectrums of pTP and POPOP.

The entire EMC contains 5040 megatiles. In order to be practical, the megatile must be machined from 1.6 m long by 0.3 m wide pieces of scintillator. The standard production technique (polymerization between glasses) used to produce scintillator sheets of such sizes are traditionally labor intensive (complicated procedures for glass surfaces preparation, long polymerization time lead to high price and long production time). In order to reduce the cost of scintillator production, the WSU Department of Physics and Astronomy group and collaborators in IHEP (Protvino) adapted extrusion technique that was developed in IHEP [2] for mass production of large scintillation plates required by EMC. The first production batch of scintillation plates, 26 plates (PSM115 + 1%pTP + 0.01%POPOP) with dimensions: 1600 mm x 300 mm x 5 mm were done at UNIPLAST for bench test in 1997. The schematic diagram illustrating the scintillator production and quality control for the EMC is shown in Figure *II.3.1-2*. The scintillating plates are produced in Vladimir – City Company UNIPLAST.

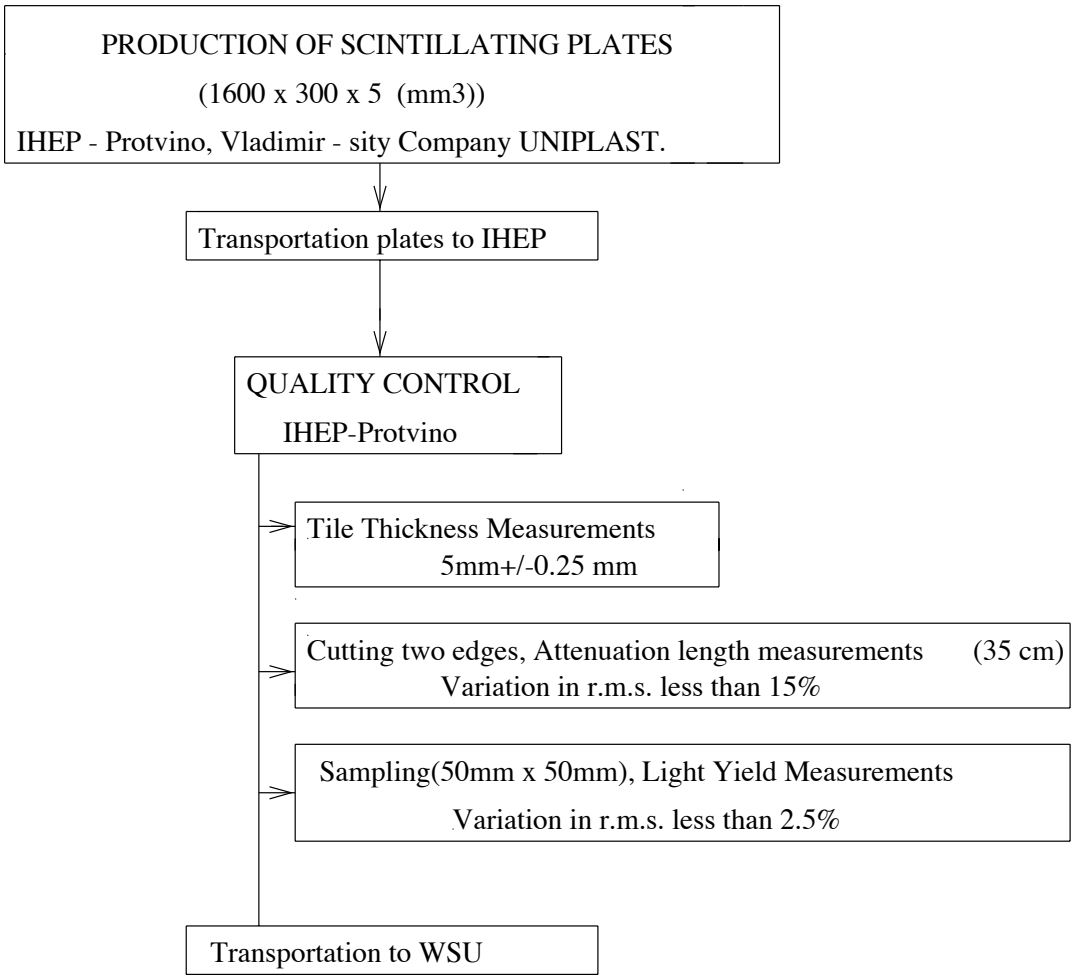


Figure II.3.1-2 Schematic diagram illustrating the scintillator production and quality control scheme for the EMC.

One production lot consists of 55 plates. The plate size is 1600 mm x 300 mm x 5 mm. Several production lots will be sent to IHEP after visual inspection. The program of quality control includes the following:

- plate thickness measurements;
- attenuation length measurements;
- light yield measurements.

The uniformity of response of the tile/fiber system depends on the geometry and the depth of the groove for the fiber, and the uniformity of the light yield of scintillating plates. The light yield of the plates depends on their thickness and the concentration of the wavelength shifting dyes in them. Thus the plate thickness and the dye concentration should be as uniform as possible.

**Tile thickness measurements**

The thickness of all plates will be measured as described below. The special experimental setup with an automatic scanning machine will be used for thickness measurements. The experimental setup is shown in Figure *II.3.1-3*. The scintillating plates will be positioned between two aluminum plates, which have protection cover. The differential transducers will scan tile through slots on the bottom and top aluminum plates. The output current is converted to voltage using a differential amplifier. The voltage values are recorded. The precision of motion is 0.02 mm. We will measure the thickness of a plate at 60 points on 16 lines along X direction. The non-uniform area of 20 mm inside from every edge of the plate will be excluded in this thickness measurement. The number of measured points is 960 in one scintillating plate (total). We require that the thickness of scintillating plates be in the range of 5 ± 0.250 mm.

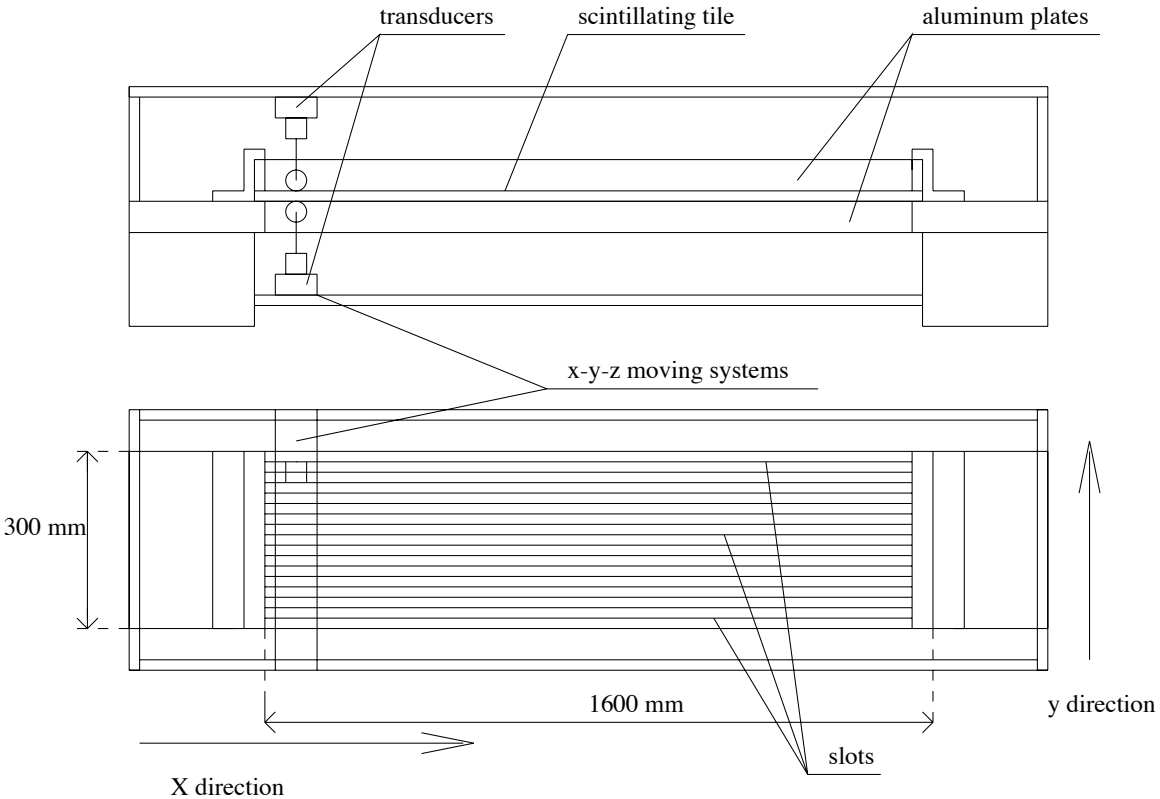


Figure II.3.1-3 Experimental setup for thickness measurements of scintillating plate.

**Attenuation length measurements**

After the thickness measurements, we will cut two edges of scintillating plate and determine the attenuation length of unwrapped plate. A good indication of the uniformity is the attenuation length of the scintillator. As is expected, the longer attenuation length gives the more uniform response. The light output of the scintillator plate as a function of distance from the photomultiplier is usually described by an exponential function. In practice, however, this dependence is notobserded to be exponential for several reasons: the path of the photons is usually longer than the distance between the production point and the photomultiplier due to reflections; light is attenuated by losses in the process of internal reflections. The method of the parameter determination for luminescence optics materials was developed in IHEP[3]. The reflection coefficients of surfaces have to be used in this procedure. The method to calculate absorption length and reflection coefficients uses the measuring amplitude of signals as function of illuminating points coordinates. Figure *II.3.1-4* shows measurements of attenuation length of scintillator sample. The curve drawn in Figure *II.3.1-4* represents calculations using the proposed functional and agrees satisfactorily with the measured values plotted in the same figure. In this method the radioactive source will move along the center of the tile. The source movement will be computer controlled. The systematic uncertainty of this method is typically 3%. We required that the attenuation length should be 35 cm with the rms variation less than 15%.

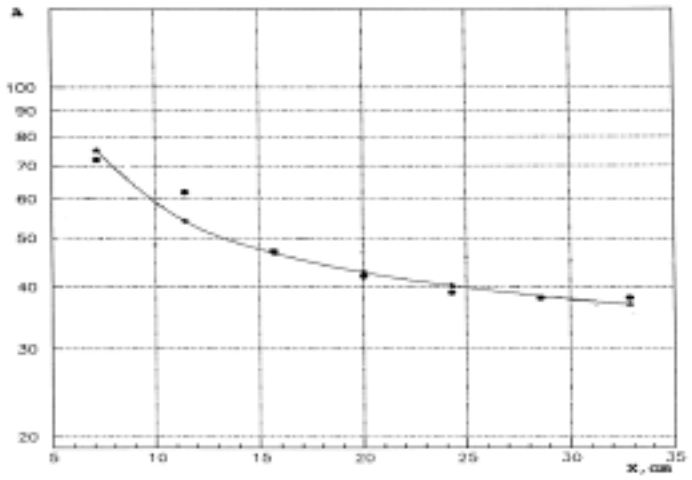


Figure II.3.1-4 Measurements of attenuation length and comparison with calculations.

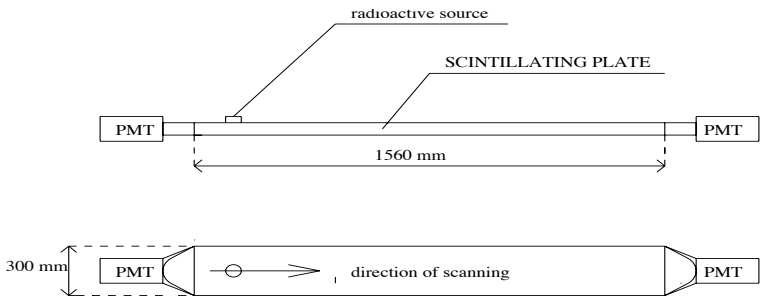


Figure II.3.1-5 shows the scheme of attenuation length measurements.

**Light yield measurements**

We will sample one scintillating block with size 50 mm x 50 mm x 5 mm from one plate of the production lot (one sample from 55 plates). This sample will be used for absolute light yield measurements to check the light variation between production lots. We require that the light yield variation between production lots should be less than 2.5%. Figure *II.3.1-6* shows the scheme of the measurements.

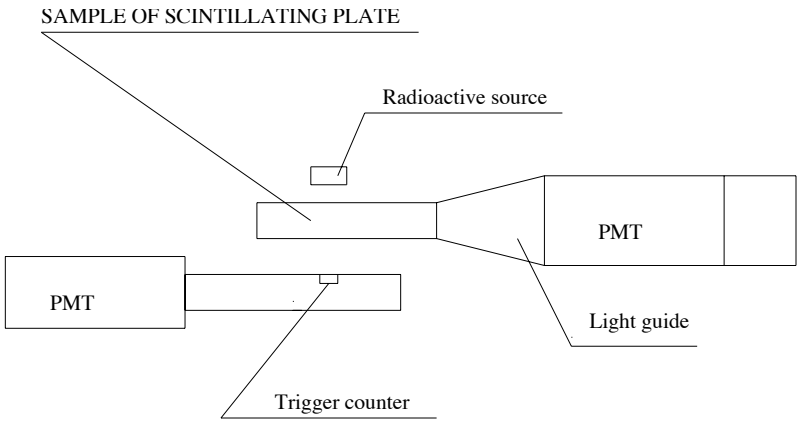


Figure II.3.1-6 Scheme of light yield measurements.

[1]-C.D'Ambrosio et al., CERN/PPE 90-96
[2] - T.V. Alimova et al., Preprint IHEP 86-35, Protvino, 1986.
[3] - V.S.Datsko, N.A. Datsko, Preprint IHEP 95-113, Protvino, 1995.

## II.3.2 Megatile Design, Fabrication, and Quality Control

### II.3.2.1 Megatile Design

As discussed in section II.1, the desire to have a calorimeter with segmentation that is not only projective in $\eta$ and $\phi$, but constant in $\Delta\eta$, leads to scintillator tile sizes that are mechanically different for not only for each tower, but also for each layer. With 40 towers per module, and 21 layers of scintillator per tower, there are a total of 420 different sized tiles in the calorimeter, with 2 tiles of each size. Due to the large number of different sized tiles needed, techniques such as injection molding become impractical because of the cost of the molds. The technology chosen for the construction of the STAR EMC is that of megatile production as used in the CDF Endplug upgrade project[i]. In this process, a single large sheet of scintillator is machined by a Computer Numerically Controlled (CNC) router into a large number of separate tiles. With the use of computer control, the tiles can easily be made to be different sizes using a single set of production tooling. The machining will be carried out in dedicated facilities currently being setup at WSU. The design of these facilities, and the scintillator machining techniques that will be employed, have benefited greatly by the large amount of prior experience gained at FNAL during the CDF Endplug upgrade project[ii]. The facilities and the stages involved in tile production are detailed in the following section.

II.3.2.2 Megatile Fabrication and Production Facilities

The scintillator material is obtained from UNIPLAST in the form of sheets 1.6m long, 0.3m wide, and 5mm thick. Two such sheets are needed for each scintillator layer, and hence the megatiles are roughly half the length of a module. The scintillator sheets will be machined into megatiles on a dedicated, flat bed, Technoisel 4' × 8' CNC controlled routing machine. The routing machine will be equipped with a vacuum chuck to secure the scintillator during machining. Two identical tiles will be cut at the same time by using two high-speed machine heads. Each head will be equipped with vacuum dust collection facilities and telephoto TV cameras to monitor the machining process. The FNAL group has found that the key requirements for successfully machining scintillator are to maintain low temperature and low humidity, and to critically control the material feed rates depending upon the environmental conditions. The scintillator is kept cold by high pressure cold air guns, and the entire machine will be situated in a climate-controlled room. Based upon prior experience machining scintillator at both FNAL and WSU, two such machines will be needed to keep up with a maximum production rate of 35 modules per year.

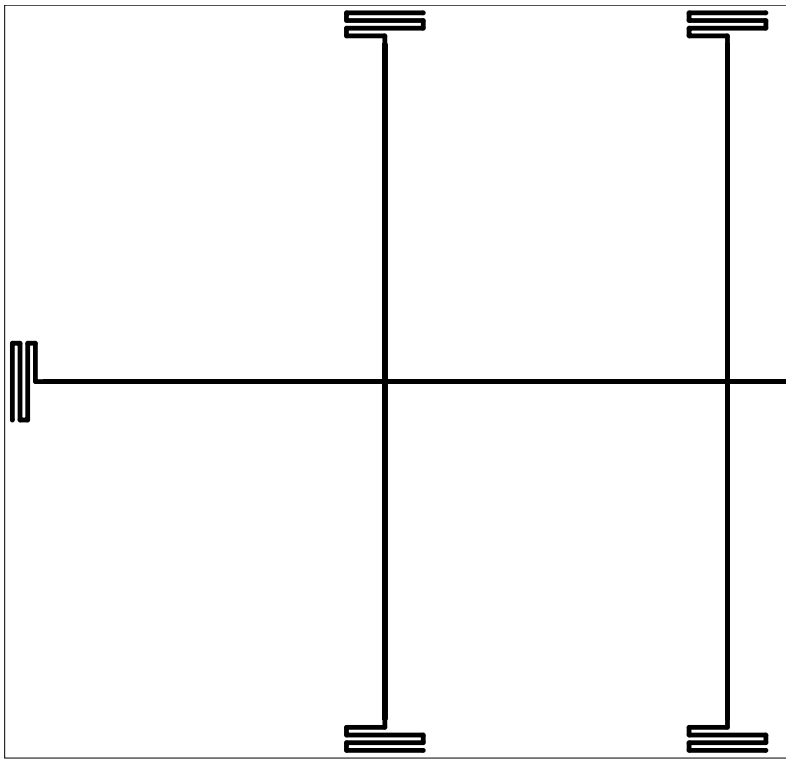

Figure II.3.2-1. Schematic drawing showing the end four towers of a megatile after the separation grooves and epoxy storage labyrinths have been machined.

The first stage in tile machining after the scintillator blank is qualified is to machine the grooves that will later be filled with reflective epoxy to optically isolate the individual tiles from their neighbors. These separation grooves are shown for part of a megatile in figure II.3.2-1. The grooves are machined through all but 0.25mm of scintillator, as shown in the tile cross-section in figure II.3.2-2, leaving the complete megatile physically connected through a thin bridge of scintillator. The scintillator tile is deliberately over-sized so as to leave a border around the tile. This border serves two purposes. Firstly, it provides mechanical strength for the tile prior to filling the grooves with epoxy, though careful handling of the tiles is still necessary at this stage to prevent irreparable damage. Secondly, it allows epoxy storage labyrinths to be machined at the end of each groove as seen in figure II.3.2-1. The labyrinths are described in more detail below.

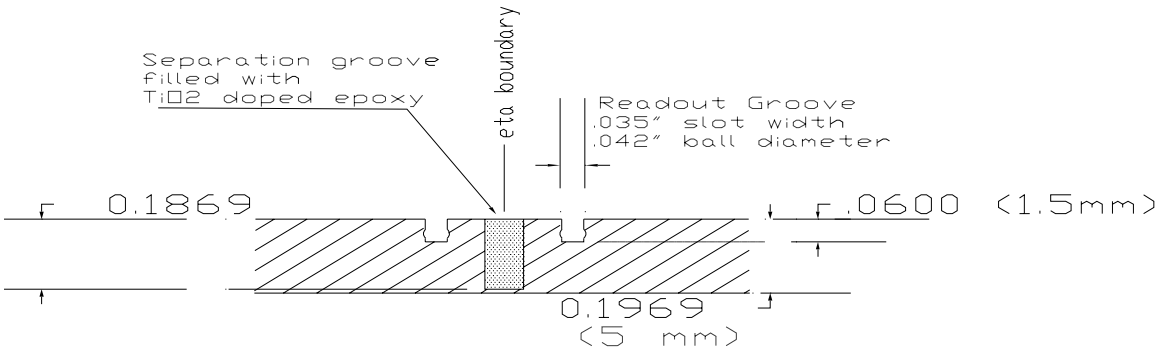


Figure II.3.2-2. Schematic diagram of a cross-section through a tile, showing the separation groove and the two ball grooves which contain the WLS fibers.

After machining the separation grooves, the next step involves injecting $TiO_2$ loaded epoxy resin into the grooves. The techniques used for this operation are identical to those developed during the CDF Endplug project[iii]. The megatiles are first inspected for flaws in the separation grooves that might complicate the process of epoxy injection. Next the top of each groove is covered with Kapton tape to form a closed tunnel into which the epoxy can be injected. Air release holes are added at the far end of the grooves, and epoxy is injected using an automated fluid injection system filling the whole groove and the labyrinths. The tiles are then cured at room temperature. The epoxy has the property that it shrinks upon curing, so the purpose of the labyrinths is to provide a reservoir of epoxy that could be drawn into the body of the tile during curing. This reduces the need to touch up the tile at a later point, and since the labyrinths are beyond the tiles fiducial boundary, they can be safely removed during the next step in the machining process. After curing, the Kapton tape is removed, and any imperfections in the epoxy such as small air bubbles are carefully touched up.

The next stage in manufacture involves returning the now much more robust tile back to the router, where the fiber readout grooves are now machined. After detailed study of the optical properties of various different configurations, the EMC collaboration has decided upon σ-grooves. These σ-grooves are machined into the tile to a depth of 1.5mm and then the tile border is machined away to leave the finished tile of which part is shown in figure II.3.2-3. Since the fibers must be routed along the sides of the modules exit notches are cut at the center of each tile. These allow the fibers to exit the tiles parallel to the module's surface.

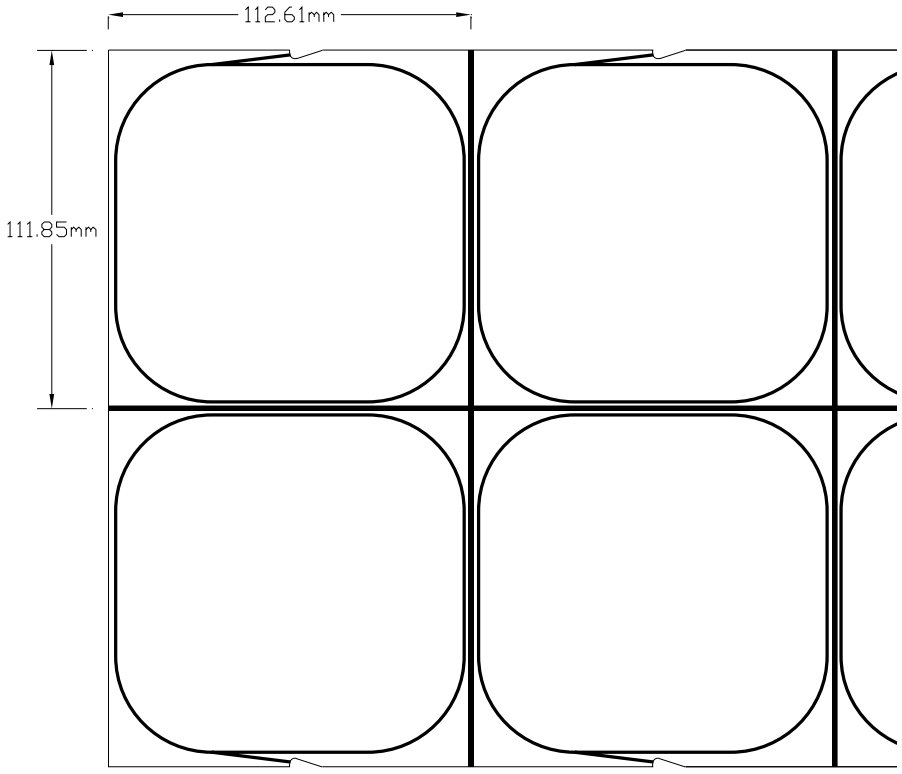


Figure II.3.2-3. Schematic drawing showing the end four tiles of a megatile after fabrication.

The final stage in megatile fabrication is to apply a black ink line to the underside of the tile along the separation grooves. Since the separation grooves do not go all the way through the scintillator, and there is 0.25mm bridge of scintillator left connecting the individual tiles, there is the possibility of optical cross talk. The CDF group[iv] found that this cross talk could be significantly reduced by the application of ink, since this absorbs any reflection off the back surface of the scintillator. The tile is now complete, and passes onto quality control described in the next section. Figure II.3.2-4 shows a photograph of a completed tile ready for assembly in the small prototype, which was tested in BNL in 1997.

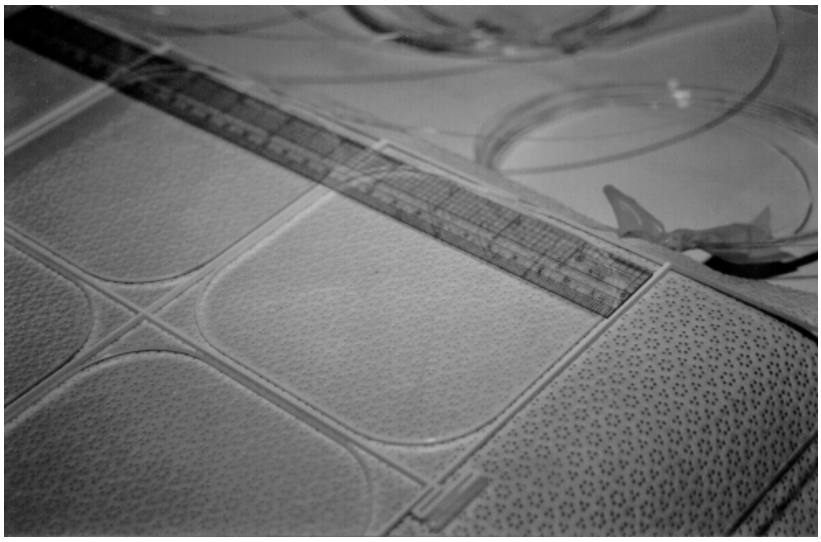

Figure II.3.2-4. Photograph of a completed megatile ready for installation into the small prototype. As this is a prototype tile, the tile border at each end of the tile has not been removed, and the epoxy storage labyrinth is clearly visible.

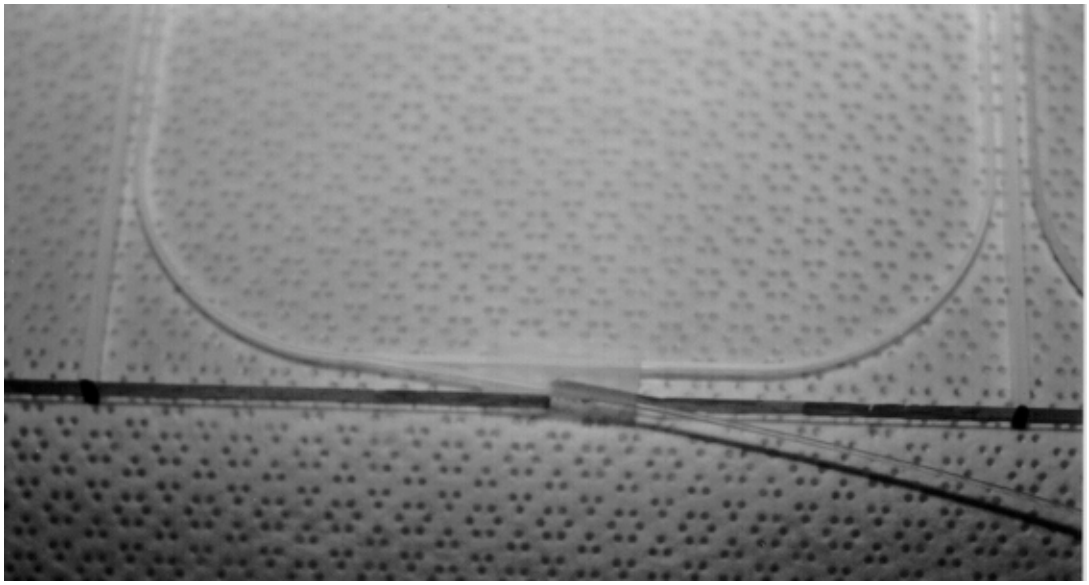

Figure II.3.2-5. Photograph showing a close-up of one of the tiles of the small prototype. Clearly visible are the epoxy filled separation grooves, the readout groove together with its WLS fiber, and the notch to allow the fiber to exit the tile along the side of the module.

### II.3.2.3 Megatile Quality Control

Quality control for the megatile happens at several stages during their manufacture. Because the scintillator is checked for its optical properties by the IHEP group prior

to shipping it to WSU, all the quality control checks performed during manufacture are mainly physical inspections. After the tile is completed it is moved to the testing laboratory. Here, 100% of all tiles will be measured by scanning them with a radioactive source modulated with a lead chopper. The source will be positioned at the center of each tile, and the light generated by the source is readout via a wavelength shifting fiber and PMT. The current from the base is used to feed a lock-in amplifier that is in turn logged by a personal computer. Data will be collected for each tile in the calorimeter, and megatiles failing the 10% RMS requirement will be reworked if possible or failing that rejected.

### II.3.3 Fiber Cable Fabrication and Quality Control

#### II.3.3.A Introduction

The EMC Modules are designed to have optical fibers running from the scintillator tiles through the backleg iron of the magnet to PMTs residing in boxes located on the backlegs. For mechanical and optical transmission efficiency reasons the fibers are broken up into three sections (see Figure II.3.3-1). The first section is composed of wavelength shifting fiber that runs from the tiles to the top of the module. The second section runs from the module through the backleg to the boxes housing the PMTs. The third section runs from the outside of the boxes to the PMTs.

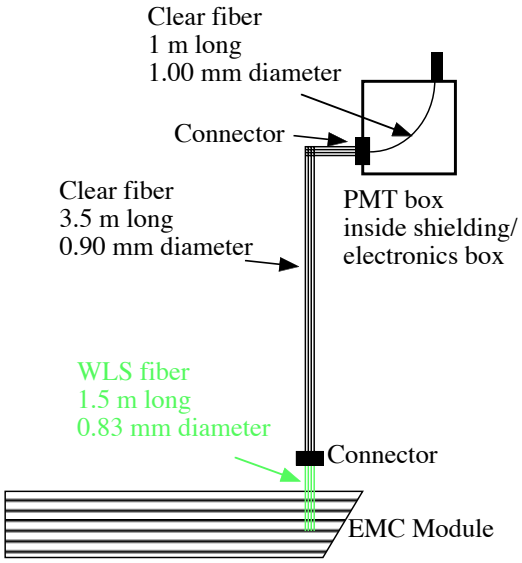


Figure II.3.3-1. Schematic drawing of the fiber read-out system.

#### II.3.3.B Design

The design, construction and fabrication of the EMC fiber bundles are patterned on the Michigan State University High Energy Physics (MSU-HEP) program for making fibers for CDF. Briefly, that experiment called for cable bundles of ten fibers but otherwise has a similar design. The fabrication facilities, personnel, etc. still exist at MSU and are partially available to the EMC project. Given the cost and time saving benefits, a decision was made to modify the EMC fiber scheme to the 10 fiber bundles and use the MSU facilities.

Each tower of the EMC has 21 scintillator layers each requiring an optical fiber. Two preshower layers, the first two layers of the calorimeter, will have two fibers each. The 23 fibers will be grouped into 2 cables with 10 fibers each and the remaining 3 will share a partial bundle with a neighboring tower. To maximize the light transfer though each of the 3 cable sections between the tiles and the PMTs, the fibers in each subsequent cable will be larger in diameter than those of the preceding cable. The diameters are 0.83, 0.9, and 1.00 mm. This scheme leads to 8 cable styles. The 0.83mm WLS fiber will have two styles of 10 fibers each with the fiber lengths cut to fit the appropriate depth in the tower. The third cable will share fibers with the neighboring tower. The 0.93mm fibers running through the backleg will all have the same length but one cable style will have 10 fibers and the second six. The 1.0mm fibers in the PMT boxes will also have three styles to match the various lengths needed to reach the PMTs as well as to match the one cable with six fibers.

| Style | 10 fibers top | 10 fibers middle | 6 fibers bottom |
|---|---|---|---|
| 0.83mm WLS | 4800 each | 4800 each | 2400 each |
| 0.93mm Clear | 9600 each | n.a. | 2400 each |
| 1.0mm Clear | 4800 each | 4800 each | 2400 each |

**II.3.3.C Fabrication**

The steps required to fabricate the cables are well understood by the MSU-HEP group. The general steps are as follows:

1. Prepare fibers
2. Prepare connectors
3. Epoxy fibers into connectors
4. Polish connector ends
5. Clean cables
6. Measure light transmission
7. Store in shipping boxes.

The cable fabrication facilities at MSU-HEP are in a dedicated room with “stations” for the aforementioned steps. Each of these stations has fixtures, jigs, etc, designed to hold multiple connectors and or fibers for mass production. Given the volume of cables that have to be made it is expected that facilities at NSCL will be built to compliment those of the HEP. Following is a list of the major stations.

1. Cutting
2. Gluing
3. Diamond Polishing Machine
4. Testing

Table 1 shows the detailed steps and the required time. These times are actual times based on previously constructed cables made by the HEP group. For the EMC additional steps are required to mirror the ends of the fibers that go to the tiles. This is done with a sputtering technique designed by and done at Fermilab. In addition, the sheathing used by the HEP group is not light tight and additional steps will be required to meet the EMC's requirement of the cables being light tight.

It is expected that the cables will be made over an approximately three to five year period. Given the 5000 man-days of labor required, 7 people working full time for three years is needed. Because student labor will be used and the number of hours a student can work is limited, it is expected that a crew of 14 or so people will actually be employed. MSU-EMC group, with technical support from the MSU-HEP group, will do the supervising and training. The module construction timetable and the shutdown periods of the STAR detector will dictate the actual fiber construction schedule.

| Task | Description | Est. time (min./cable) |
|---|---|---|
| 1 | Inspect cables for defects | 2 |
| 2 | Cut cables to length | 1 |
| 3 | Prepare and clean connectors | 2 |
| 4 | Prepare and attach labels to the cable | 2 |
| 5 | Trim cable ends | 1 |
| 6 | Hang the cable at the gluing station | 1 |
| 7 | Strip the covering from the cable ends | 5 |
| 8 | Prepare and attach the strain relief tape | 3 |
| 9 | Setup connectors in the gluing stand | 1 |
| 10 | Trim the covering and strain relief | 2 |
| 11 | Insert cable ends into the connectors and clips | 2 |
| 12 | Glue the cables into connectors | 5 |
| 13 | Transfer cables to carrying trays | 1 |
| 14 | Polish the connector ends | 8 |
| 15 | Remove excess glue and clean the cable ends | 2 |
| 16 | Attach the connector clips | 1 |
| 17 | Measure light transmission through cable | 5 |
| 18 | Analyze test results, examine failures | 3 |
| 19 | Make the storage/shipping boxes | 1 |
| 20 | Store/ship cables | 2 |
| 21 | Cable repairs, remakes (avg.) | 4 |
| 22 | Supervision, training, documentation*, etc. | 5 |
| 23 | Housecleaning, maintenance, etc. | 5 |
| TOTAL | | 64 |

(* Many tasks require an entry on a traveler sheet documenting cable#, date and person completing the task.)

Table II.3.3.C.

### II.3.3.D Quality Control

The EMC quality control will be similar to that of the MSU-HEP project. However, the final variations are still under discussion. In addition to visual inspection of the fibers before construction of the cables, the cables are checked after gluing and polishing. The MSU-HEP method for the clear fiber is:

> "The cables are tested by inserting each cable into an optical path consisting of a calibrated source and a photodiode detector. One source and one photodiode are used for each of the 10 fibers in the cable. The sources consisted of lengths of the same WLS fiber as used on the calorimeter, illuminated with a fluorescent UV bulb. The currents from the photodiodes are measured using a pico-ampmeter readout via GPIB bus to a PC. A low impedance multiple switch controlled by the PC is used to select the photodiode. Since we were interested primarily in the variation of light transmission from scintillators in the same readout cell, we tabulated the corresponding rms variation using fibers in the same position from a group of cables. For example, the rms variation from the average for fiber number 3 in set of similar length cables would be tabulated. Cables having any fiber with deviation greater than 10% from average would be examined for problems and those with deviation greater than 15% would be re-made. The rms variation/average transmission for the whole set of cables was about 2.5%."

In the case of the PMT box cables this concept will have to be modified to account for the varying lengths of fiber.

This method, however, will not work for the WLS fibers that are aluminized on one end. An alternate proposal is being made to measure these fibers. This proposal is designed after a method used at FERMI lab where the fibers are irradiated with UV light passing over the length of the fiber with the output continuously measured and recorded via a photodiode response.

### II.3.4 Scintillator and Megatile Performance Studies

The tile/fiber sampling technique is chosen for our calorimeter design. This technique uses scintillator tiles to sample the electromagnetic shower. Wave-shifting fiber (WLS) embedded in the scintillating tile traps the scintillator light and clear fiber connected to the WLS fiber carries the light to photomultiplier. The EMC requires a total of 90,800 scintillating tiles. The cost per tile is an important parameter in the choice of the tile material. This issue has led us to the choice of PS extrusion scintillator for EMC. The most important problems of optical system on the base of PS extrusion scintillator were to achieve and maintain a uniform, minimum light yield so that the resolution of EMC is not compromised by a lack of photostatistics. PS scintillator with the extrusion technique has been proved to have inferior light yields compared to cast scintillator. However, requiring light yield from tile more than 2 photoelectron/MIP, it is possible to use this material, but at the expense of optimization of all components of optical system. This optimization include the following:

1. studies of the dependence of the light output of the tiles on the pattern of fiber groove;
2. selections in the optical read-out chains, which include choice of material for other parts of the optical system (WLS and clear fibers, optical connectors);
3. detailed studies for identification the requirements for components of optical system;
4. studies of possible causes, which can change of the absolute light yield and uniformity response of the scintillator tile.

As a result, we found the pattern of fiber groove in tile and configuration of optical system, which produced light yield more than 2 photoelectrons/MIP and uniformity response over the surface of tile better than 3% rms. We have chosen this configuration of optical system to go into production for the Electromagnetic Calorimeter of STAR. Results optimizations of optical system are discussed in this Chapter.

### II.3.4.1 Absolute light yield measurements of different tile/fiber assemblies

In order to optimized optical system we study the dependence of the light output of the tiles on the pattern of fiber groove and type of read-out WLS fibers. The light from tile re-emitted by the WLS fiber is then transported directly by the WLS fiber or by the clear fiber thermally fused to a WLS fiber to the phototube located on the distance about 3 m from scintillating tile. We have compared the absolute light yield of eleven different tile/fiber system using $\alpha$- and $\sigma$-grooves. Extrusion PS scintillator of 5 mm thickness were used as a standard. Some date were taken for Bicron BC404A scintillator as a comparison.

Figure *II.3.4.1-1* shows the principal scheme of read-out chan for tile with $\alpha$ - and $\sigma$-groove pattern of fiber groove.

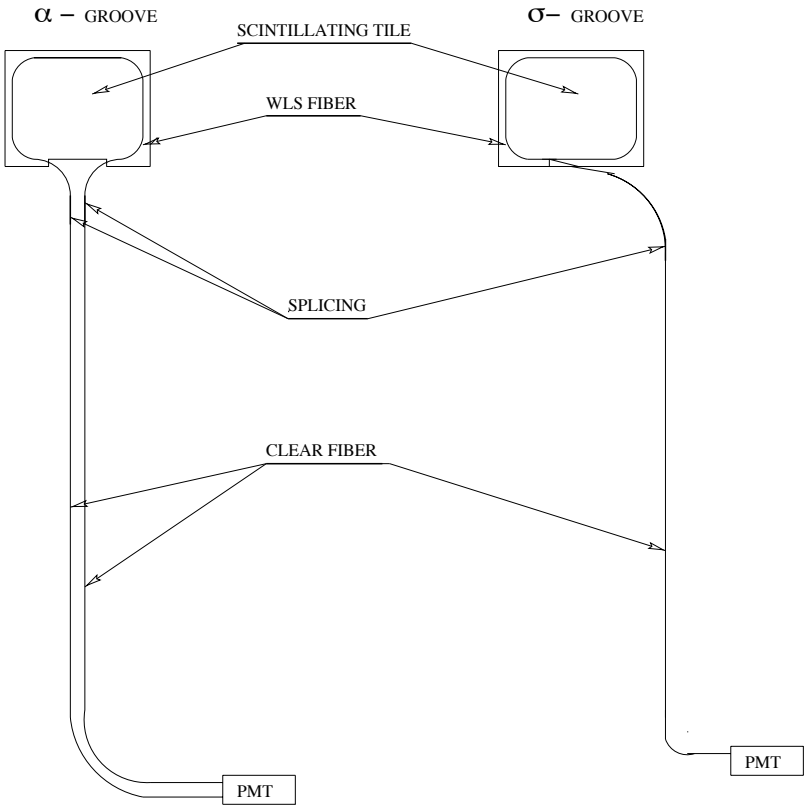

Figure II.3.4.1-1 Principal scheme of read-out chain for tiles with α - and σ - pattern of fiber groove.

Figure *II.3.4.1-2* shows a schematic drawing of geometry of the test setup[1], which has been designed and constructed at WSU during 1996. This experimental setup is a part of a quality control program of the calorimeter tile production, and is designed to monitor the absolute light yield and light yield variation of individual tiles.

The apparatus consisted of three independent parts: two fixed frames for mounting trigger counters and a radioactive source, together with a movable table used for mounting the scintillating tile currently under test and the phototubes (PMT). All parts of the setup were mounted in a light isolated box. The temperature inside box was continuously monitored. The tile under test was mounted on a table which is moved by stepping motors controlled by a personal computer, thus allowing the light output of tile (or megatile) to be scanned transversely as a function of position. The range of motion is 200 mm in both the X- and Y- directions. The precision of motion is 0.25 mm. The trigger counters are mounted on the fixed frame located above the movable table. Each trigger counter consisted of a 2 mm x 2 mm Bicron BCF-12 scintillator coupled to an Hamamatsu RC4044 PMT. By using two trigger counters in coincidence we eliminated non-local and non-penetrating backgrounds such as gamma rays and low energy electrons.

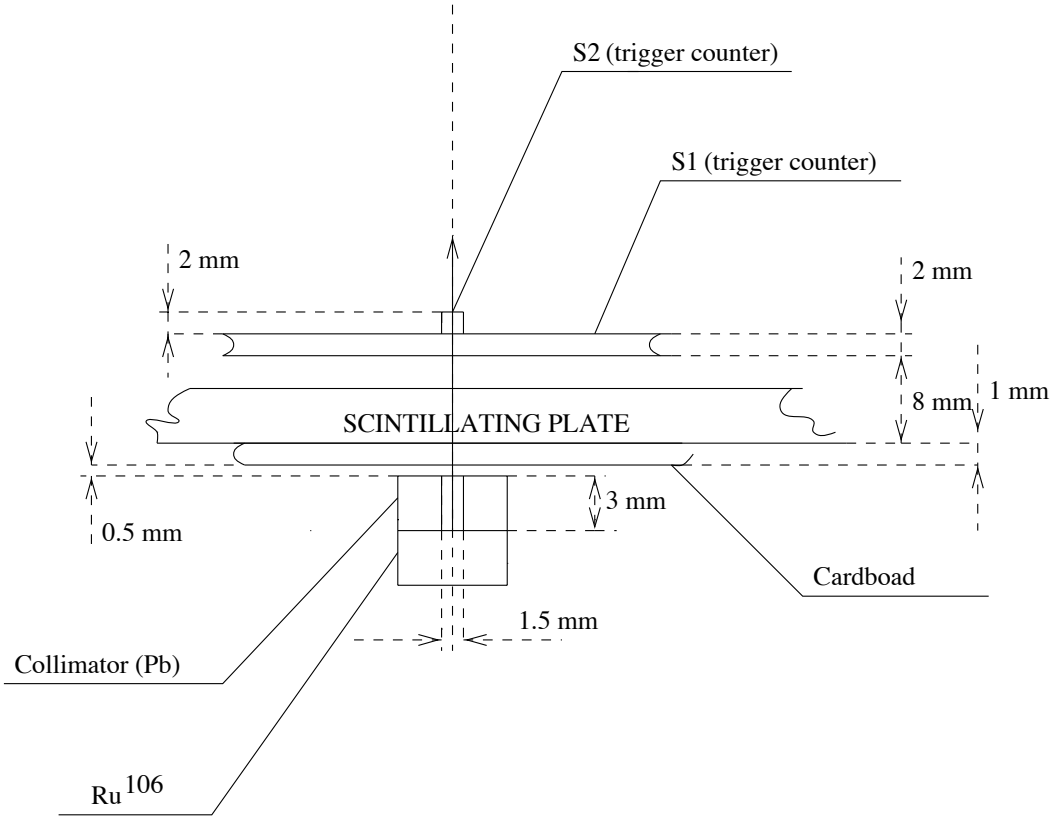


Figure II.3.4.1-2 Schematic drawing of geometry of the test setup.

The scintillator tile under test was excited by a Ru(106) 3 MeV β-ray source of 8 mm in diameter, which mounted on the fixed frame below the movable table. At this energy the electrons are approximately minimum ionizing in the first several mm of plastic scintillator. Their range is great enough to penetrate: 1mm of cardboard, the 5 mm thick scintillator tile under test, and a 2 mm thick trigger scintillator, to finally deposit a signal in the last 2 mm trigger scintillator. Multiple scattering in the scintillator is not too large considering our spatial resolution of 2 mm. Light from file/fiber assembly was detected by the PMT (Hamamatsu R580-17) currently under test. The signal from the PMT is digitized by LeCroy 2249A CAMAC ADC module with a maximum resolution of –0.25pC/channel and recorded by personal computer. The single photoelectron peak for the PMT under test had been obtained using the tile/fiber system by reducing the detection efficiency to approximately 0.1 so that the contribution of 2 photoelectrons was made negligibly small [2]. An LED based flasher system is also used for calibration purposes. The light from a blue LNG992CF9 LED is transported to the PMT via a green Bicron BCF91A WLS optical fiber of 1 mm in diameter. A comparison of the results obtained between the PMT calibration using the tile/fiber assembly and LED system has not shown significant differences. We estimated the light yield from a tile/fiber system in terms of an average number of photoelectrons produced by the photoelectric affect on the PMT photcathode [3]. For the uncertainty in the number of photoelectrons we evaluated

effect of the reproducibility of measurements due connection fiber to PMT. This uncertainty is not more than 10%.

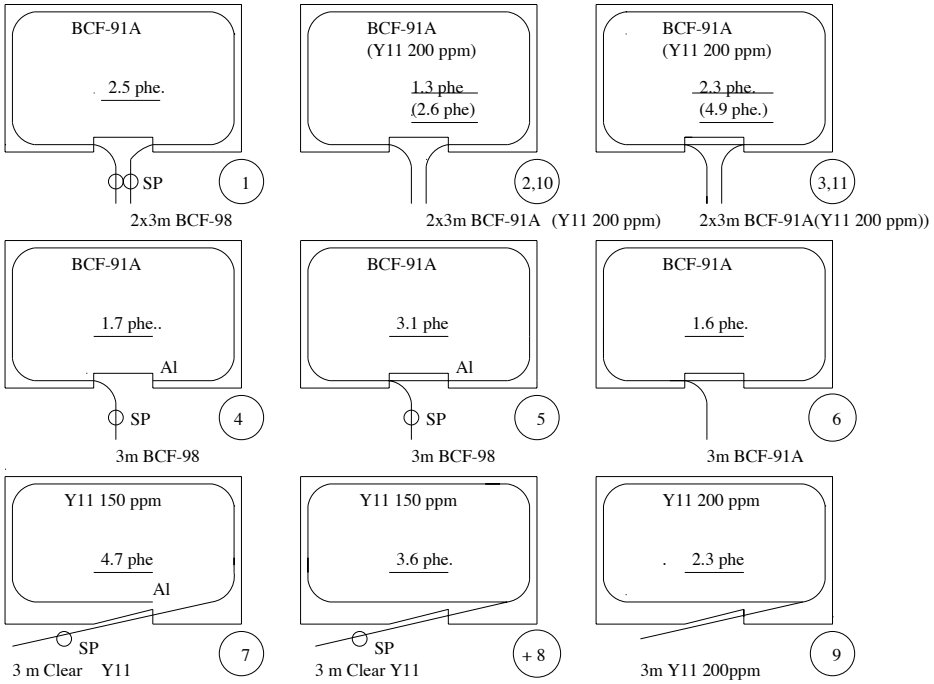


(Bicron)BCF-91A - green WLS fiber.

(Bicron)BCF-98 - clear fiber.

(Kuraray)Y11 150 ppm(200 ppm) - multiclad S-type green WLS fiber (ppm - the numbers in the parentheses . correspondent to number of parts per million by weight of fluorescent dye in the fiber core.

(Kuraray)Clear Y11 - multiclad clear fiber.

Al - aluminum mirroring.

SP - splicing.

Figure II.3.4.1-3 Schematic diagram of different optical schemes

The read-out patterns differed in the number of fibers laid in the groove (one or two loops of WLS fibers) and one ($\sigma$-groove) or two ($\alpha$-groove) fibers connected to a PMT. For schemes 1-6,10,11 we have used tile with dimensions: 125 mm x 132 mm x 5 mm and tile with dimensions: 125 mm x 190 mm x 5 mm for schemes 7-9 (biggest tile sizes). WSU Department of Physics and Astronomy group fabricates the sample tiles. Many aspects of the scintillator tile design, such as the depth of the read-out groove, the groove shape, the groove location with respect to the tile borders are based on research done by the CDF and SDC group[4, 5, 6, 7]. A peripheral groove was machined in the tiles with a dental drill bit at high speed and as close to the edge as possibly.

The groove has rectangle shape with width 1.25 mm. The distance of the groove from tile edge was 1.5 mm. The groove makes a turn by 90 degree at the tile cones at radius of 30 mm. As shown by the CDF and SDC studies, this radius of 30 mm is optimal. At a large radius the response near the tile corner outside the fiber groove was measured to drop substantially. We chose the groove depth of 2 mm, which is optimal for 5-mm thick scintillator. Each sample tile has narrow notch or slot for fiber exit. The non-polished tile edges are painted white with Bicron BC620 reflective paint[8]. White bond paper is used

on both sides of the tile as reflector[9]. The main results of these measurements indicate that:

- all optical schemes ( exception: 2, 4, 6) met design criteria that the light yield should be more than 2p.e./MIP;
- the highest light yield corresponds to the α-groove with two loops of WLS fibers (scheme 11) and σ-groove with mirrored multiclad WLS fiber spliced to clear multiclad fiber;
- the light yield of the tile (σ-or α- groove) with two loops of WLS fiber embedded in one groove is 1.8 times higher than the light yield of the tile with one loop ( schemes: 2,10 – 3,11 and 4-5);
- comparison of the single ended aluminized σ-groove read-out (scheme 4) vs. α-groove read-out (scheme 1) have shown that 1.47 times the light is recorded with the latter;
- the use of a Kuraray multiclad Y11 WLS fiber spliced to a multi clad Kuraray clear fiber increases the light yield in 2.8 times, compared for Bicron singleclad WLS fiber spliced to single-clad Bicron clear fiber (schemes 4,7);
- comparative light yield measurements for the Bicron 404A scintillator and PS extrusion scintillator (PSM-115+1%pTP+0.01%POPOP) showed that the Bicron 404A scintillator yields a factor of 1.6 (scheme:7);
- test comparing the light collection efficiency from PS scintillator tiles with both Bicron and Kuraray multiclad Y11 (200) WLS fiber show that the Kuraray improves the light yield by a factor of 1.6.

### II.3.4.2 Study the uniformity of the response

The uniformity of the response of the tile/fiber assemblies has been measured using the ANL and WSU experimental setups with collimated Ru (106) source. Figure *II.3.4.2-1* shows the result of this measurement for PS scintillator with α-groove.

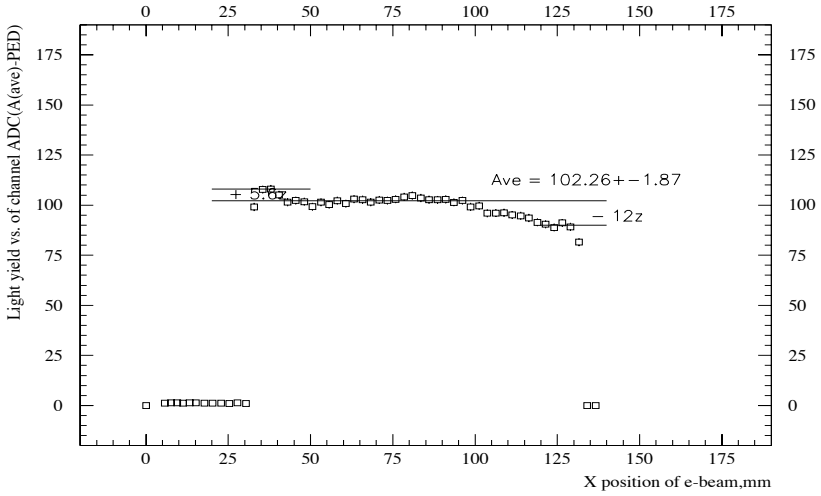


Figure II.3.4.2-1 Transverse scan of 125 mm x 132 mm and 5 mm thick tile with α - pattern of fiber groove.

This measurement has been made using 50 cm length of Bicron BCF91A WLS fiber in the α-configuration as the read-out fiber. Figure *II.3.4.2-2* shows geometry of tile and scheme of measurement.

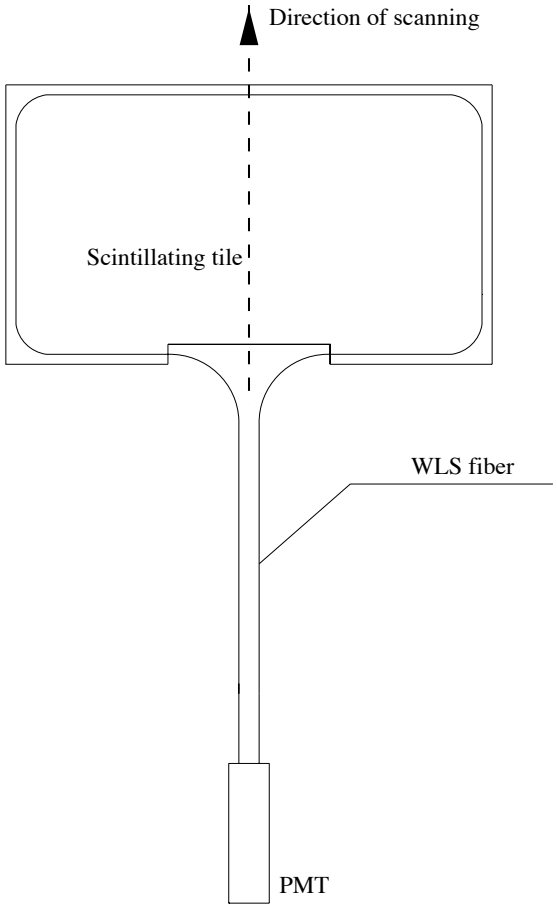


Figure II.3.4.2-2 Geometry of tile and scheme of measurement transverse uniformity.

Both the Bicron and PS scintillator with α-groove geometry show a non-uniformity of response, particularly, where the scan traverses the notch in the tile for fiber read-out. (See Figure *II.3.4.2-2*).

The PS tiles have a slightly higher non-uniformity due to their shorter attenuation length (approximately 35 cm). A simple mask will suffice to correct this non-uniformity and reduce average light yield by 30%, so the average light yield will be the same as for tile with σ-groove. Since the read-out of both fiber ends doubles the number of clear fibers and the space needed for fiber routing, we chose the tile with σ-groove read-out scheme. In this case only one end of a complete loop of the WLS fiber is connected to a clear fiber, while the other is mirrored. In order to simplify fiber routing and procedure of module assembling and mounting into a STAR magnet we exclude splicing of the green WLS to clear fiber and include optical connectors in optical design. There are two optical connectors: the first connector between green WLS fiber which embedded in tile and 3.5 m length optical cable, the second between optical cable and bundles of clear fiber that will connected to PMT. Multi-fiber optical connectors were developed by the CDF collaboration. These connectors are made via precision injection molding of mechanically

stable plastic. In this manner, all connectors are identical, and there is no need for pair matching of the connectors. The reproducibility of the optical connector transmission for many make/break operations has measured 0.6% with a transmission of 83% for a single fiber, and approximately 2% to 3% for all fibers in the connector. We will use connectors of type A for 10 fibers. The reduction of the number of read-out fibers and optical connectors lower the absolute light yield of tile/fiber system. However, combination of green multiclad WLS and clear multiclad fibers will compensate this reduction of the light output. As shown in our results, the use of multiclad Kuraray fibers will significant increase the light yield. In addition, testing at ANL of the mechanical stability of the light output using Bicron fibers indicates that Bicron BCF91A is unsuitable at the fiber bend radii encountered in routing the fibers through magnet coil.

Figure *II.3.4.2-3* shows the typical transverse uniformity of the unmasked σ-groove PS tiles from the 2x2 megatile. Figure *II.3.4.2-4* shows geometry of megatile and scheme of optical read-out system. The absolute light yield of megatile is plotted as a function of the position of the electron source. The depth of fiber groove is 2 mm. The distance of the fiber groove from the edge of tile is 1.5 mm. About 0.25 mm of the 5-mm thick scintillator are left uncut at the bottom of the grooves separating the tiles. The width of separating grooves is 1 mm. The grooves are filled with white epoxy for both structural support and light isolation. A black line is painted along the groove at the bottom surface of the scintillator, to reduce the optical cross talk, which is measured to be less than 1% per edge of the tile. The absolute light yield for this tile/fiber system is 2.28 p.e. /MIP.

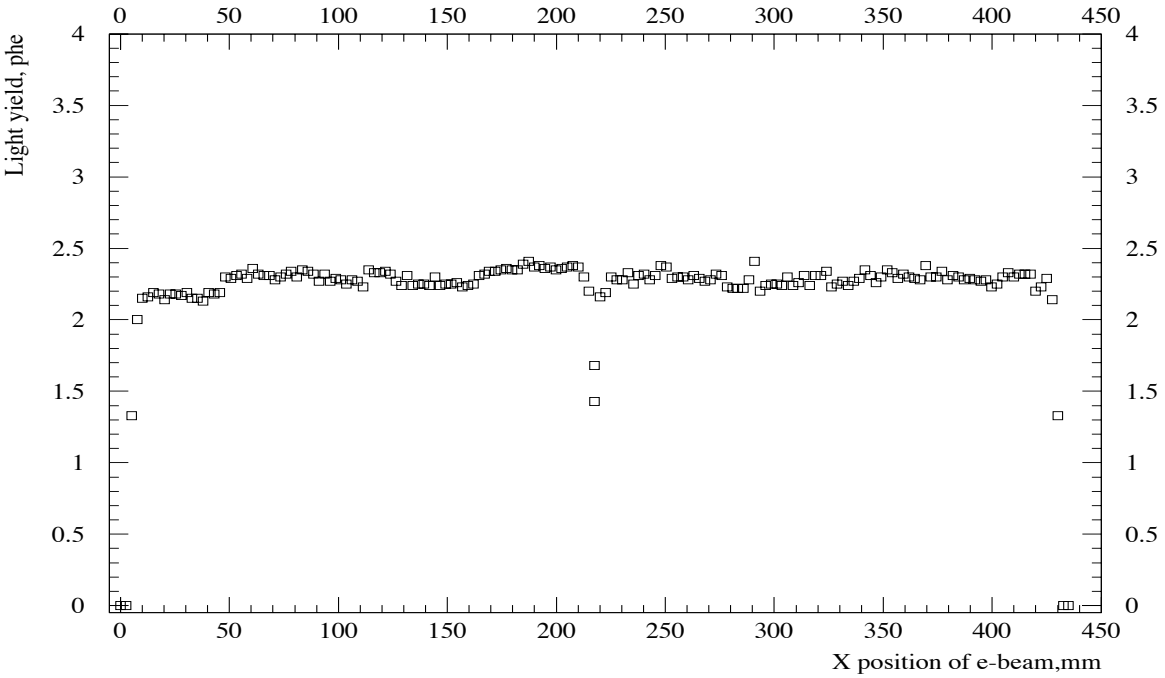


Figure II.3.4.2-3 The transverse uniformity of the two tiles (125 mm x 200 mm x 5mm) with σ-pattern of fiber groove from the 2 x megatile. The depth of fiber groove is 2 mm and the separating groove between tiles is 1 mm wide. The relative light yield of the megatile is plotted as a function of the position of electron source.

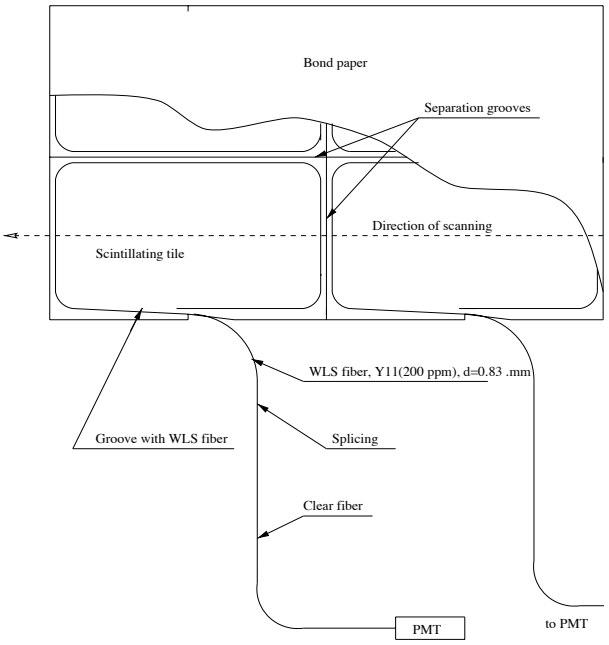


Figure II.3.4.-4 Geometry of megatile and scheme of optical read-out system

The photoelectron yield is a complex factor depending not only on the light output of the tile, light collection efficiency and fiber choice, but also on the PMT choice. For these measurements we have used Hamamatsu green extended R580-17 phototube. Measurements have also been made comparing the sensitivities of R580-17 phototube vs. the much cheaper Russian FEU115-M phototube. Initial measurements indicate that the FEU115-M is more sensitive than the R580-17 and the FEU115-M increases the light yields from the Y11 (200 ppm) green WLS fiber by 25%. Typical single-photoelectron peaks for FEU115-M and R580-17 are shown on Figure *II.3.4.2-5, II.3.4.2-6.*

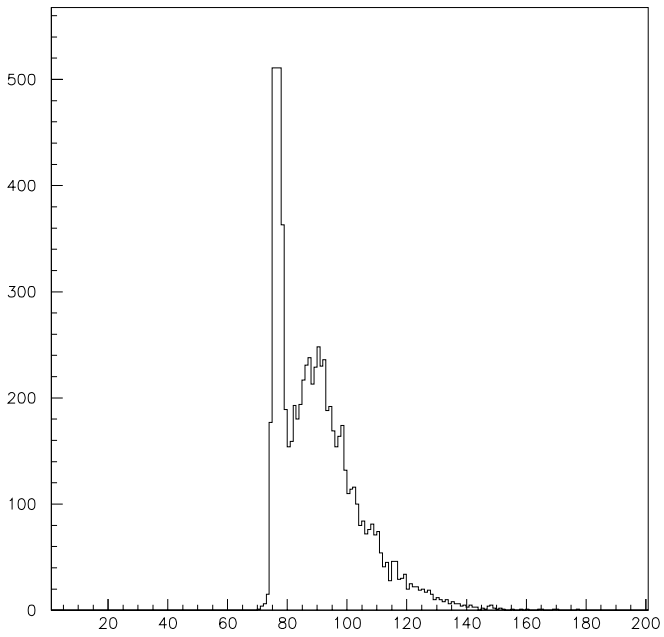

Figure II.3.4.2-5 Single photoelectron peak for phototube FEU 115-M

The uniformity over the surface of the tiles within the megatile is excellent with an rms /mean of approximately 3%, excluding the crack region. The response non-uniformity in the diagonal direction was measured to be smaller than the non-uniformity across the tile. This value is consistent with an attenuation length of PS scintillator/fiber system about 40 cm (without bond paper, the effective attenuation length is 35 cm). The measurements of uniformity and simulation [10] agree well. Our results of tile/fiber optimization

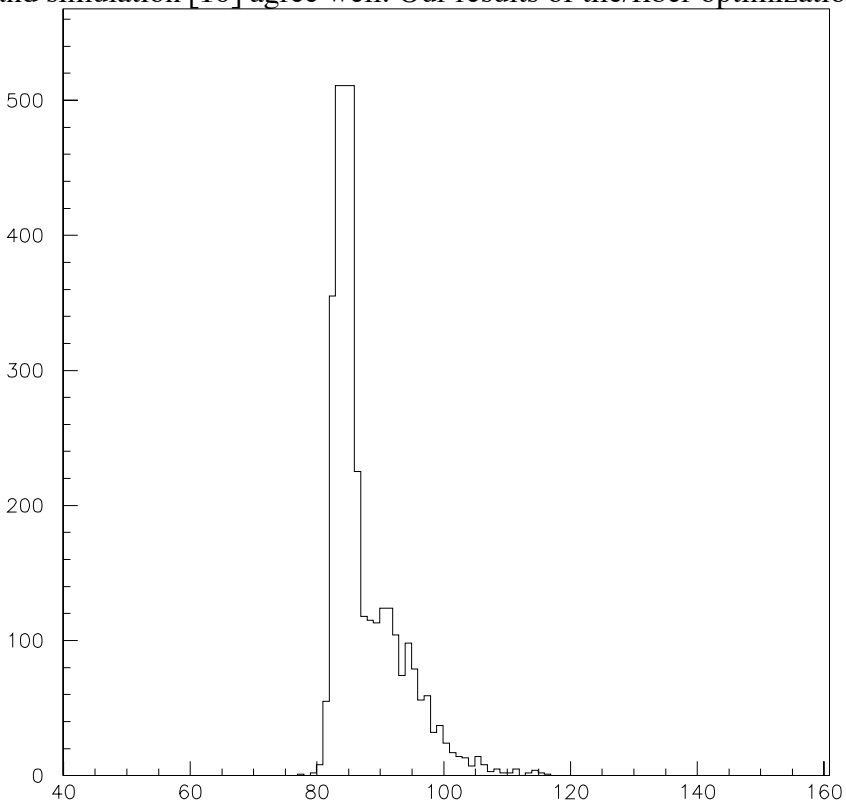

Figure II.3.4.2-6 Single photoelectron peak for phototube R580-17.

show, that for relatively small sizes of scintillating tiles with σ-groove, the Russian extrusion PS scintillator is good choice. Table *II.3.4.2-1* summarized of the design parameters of the scintillating tile for Barrel EMC of STAR. Figure *II.3.4.2-7* shows the design of optical read-out system. Our design of optical system is similar to the CDF endcap optical design.

| | |
|---|---|
| Scintillator material | PS(PSM115 scintillator) extrusion |
| Scintillator thickness | 5 mm |
| Fiber groove depth | 2 mm |
| Radius of fiber grooves | 30 mm |
| Distance of fiber groove from edge of tile | 1.5 mm |
| Tile edge treatment | White paint BC-620 |
| Tile wrapping | Bond paper |
| WLS fiber material | Kuraray Y11(200 ppm), multiclad, S-type |
| WLS fiber diameter | 0.83 mm |

Table II.3.4.2-1 Design parameters of the scintillator tile for Barrel EMC of STAR.

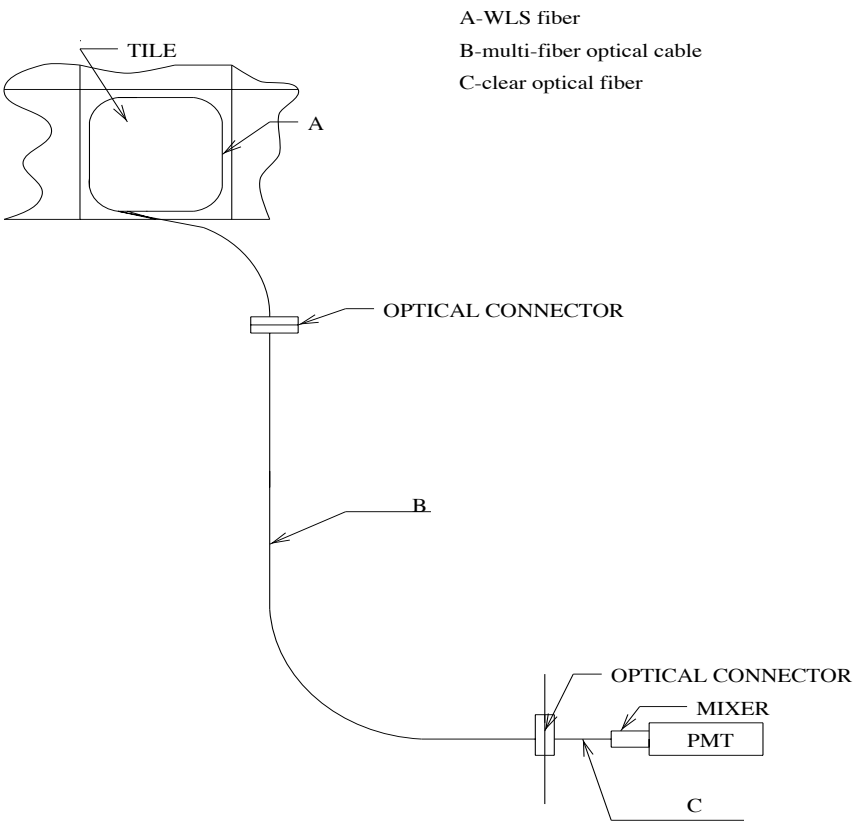


Figure II.3.4.2-7 Design of optical read-out system of Barrel EMC STAR.

### II.3.4.3 Light yield variation

For Barrel EMC with projective geometry, the tiles forming the front (inner) layers of a calorimeter are smaller than the tiles forming the back (outer) layers of the calorimeter. As we know [11] the relative light yield of different size tiles to scale with variable l/A, where l is the length of the WLS read-out fiber inside the tile and A is the area of the tile. Using this parameterization, the predicted ratio of the light yield of the front layer tiles to the back layer tiles would be 1.1. This factor 1.1 does not include the correction due to different length of clear fibers used in routing of light from optical connector inside light decoding box to PMT. This difference would be approximately equal to 100 cm. Taking the average attenuation length of clear fiber to be 10 m, the ratio of the light yield of front layer tiles to back layer tiles corrected for the different length of clear fibers would be 0.99. The scaling of the light yield of tile/fiber system with sigma-groove inside tile indicates that the response of the tiles within same readout tower can be adjusted by varying the length of the clear fibers between PMT and optical connector inside light decoding box.

The CDF Plug Upgrade group developed an independent method of equalizing the light yield of tiles. In this method, the absolute light yield of tiles in each layer was adjusted by changing the distance between the edge of the tile and the fiber groove, thus affecting the value l/A parameter. In addition, the light yield of tiles could be adjusted by extending the length of WLS fibers past the edge of tile.

Longitudinal uniformity to a level of less than 10% within each tower is significant technological issues relating to the optical system, where high performance is required. This uniformity includes contribution from: non-uniformity inside a tile, tile-to-tile variation, tile to fiber coupling, variation in fibers, variations in fiber-to-fiber coupling (optical connector) and variations of the response across the PMT photocathode. We have done detailed studies to identify the requirements on the optical system so that these variations do not contribute substantially to the constant term in the calorimeter resolution. We found that keeping the longitudinal uniformity to a level less than 10% rms within each tower is acceptable. Our studies of light variations for optical components translate to requirements:

- Tile-to-tile variations, including non-uniformity inside a tile and tile to green WLS fiber coupling: ≤ 7% in rms.
- Variations in fiber-to-fiber coupling (optical connector): ≤ 3% in rms.
- Variations in clear fibers: ≤ 3% in rms.
- Variations of the response across the PMT photocathode: ≤ 2% in rms.
- Light leakage to adjacent tiles:≤2%.

Our design of optical system is similar to the optical system of CDF End Plug calorimeter. The quality control strategy is the same as used by CDF. The thickness of each scintillating plate will be measured at several points by the IHEP (Protvino). In addition, IHEP will test scintillator plates for the attenuation length and light yield. Diameter and attenuation length of the fibers also will be well controlled. For production of fibers (cutting, polishing, and mirroring) and furnishing fibers with optical connectors we will use Fermilab and MSU facilities. The CDF End Plug calorimeter group has built several thousand tiles. The measured finished tile to tile variation of the light yield from set of 1000 tiles is found to be 6.4%. Their experience gives us confidence that the strategy will work for the Barrel EMC as well.

**II.3.4.4 Materials for optical system.**

The material used in the Barrel EMC optical system must have various properties. They must have good long-term stability, be non-demanding in handling, and easy for machining. Our baseline choice of materials are extruded PS scintillator, multiclad Kuraray Y11 (200ppm) S-type WLS fiber and multiclad Kuraray clear fiber. Some of these materials such as Kuraray multiclad green and clear fibers have been studied by the CDF and SDC groups and satisfy these requirements. Table *II.3.6.4* summarizes of the materials used in construction of Barrel EMC of STAR.

| Application | Material type |
|---|---|
| ScintillatorPS | (PSM115) extruded scintillator |
| WLS fiber | Kuraray Y11(200 ppm), 0.83 mm diam., multiclad |
| Clear fibers for cables | Kuraray, 0.93 mm diam., multiclad |
| Clear fibers for decoder box | Kuraray, 1.00 mm diam., multiclad |

Table II.3.4.4-1 Materials for optical system of Barrel EMC STAR

We concentrated on studying the extruded PS scintillator. Long-term stability of scintillating material includes variation of light output with temperature and time that must be known or controlled. In addition we have studied the effect of pressurizing the tile/fiber assemblies that can reduce absolute light output. The light yield variation can

effect the calorimeter calibration and possibly resolution. A cosmic ray test stand has been used for these studies.

The size of sample scintillator tiles was 110mm x 110mm x 5mm. Commercially available extruded PS scintillator (PSM -115 + 1%pTP + 0.01%POPOP) was used. WSU Department of Physics and Astronomy group fabricates the sample tiles. A peripheral σ-groove was machined in the tile, where green WLS fiber diameter 0.83mm was embedded. The non-polished tile edges are painted white with Bicron reflective paint. White bond paper is used on both sides of the tiles as reflector. 5 tiles are grouped into a package. The Packaged tiles were set between a pair of aluminum blocks. Light from 5 tiles re-emitted by Y11 (200 ppm) WLS fiber of 1m length is transported to a 10-stage R580-17 PMT isolated mechanically from dark box. The temperature inside the box was stabilized and was continuously monitored. There were two cosmic muon scintillating trigger counters with size 80mm x 80mm of 25mm thickness coupled by short light guide to a Hamamatsu phototubes. One muon counter was positioned in front of the package and another was positioned behind. In order to ensure minimum ionizing particle a 5 cm lead layer was insert between package of scintillating tiles and top cosmic muon scintillation counter. Figure *II.3.4.4-1* shows the scheme of the cosmic muon telescope.

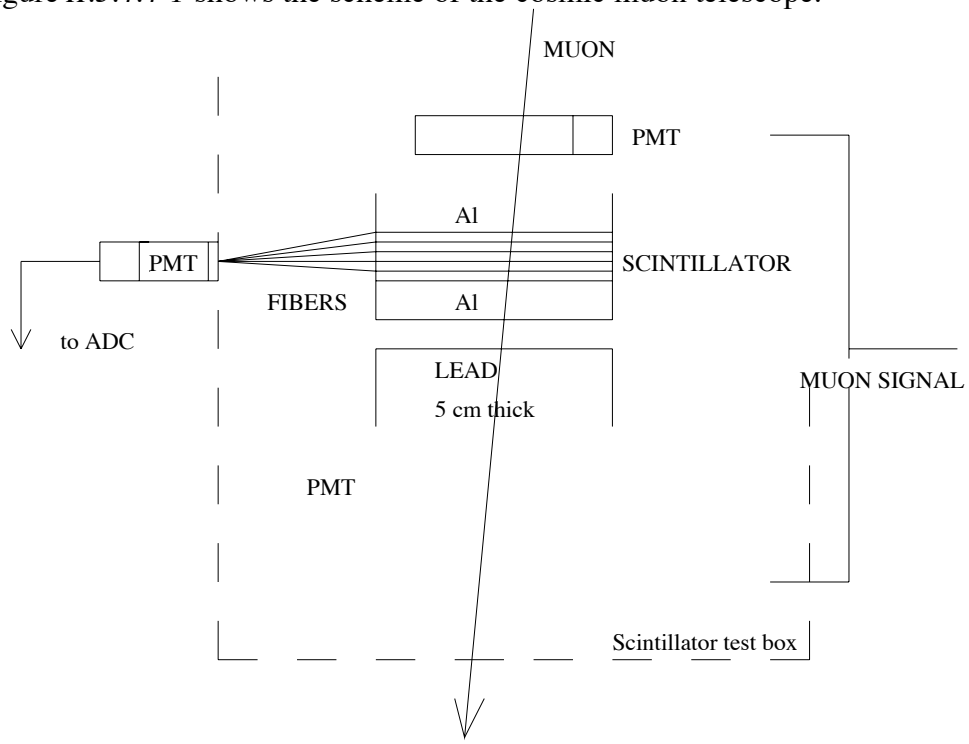


Figure II.3.4.4-1 Scheme of cosmic muon telescope.

Triggering was made with the coincidence signal of the two-muon counters. The trigger rate was 0.15 Hz. A LeCroy 2249A ADC was used for signal digitization. The ADC gate was 100 ns. Data were taken with a personal computer through CAMAC. Typically, 3000 events were collected for each point of measurements. To obtain light yield information, the spectra were fitted with a Gaussian function. Figure *II.3.4.4-2* shows the ADC pulse height spectrum from cosmic muons for tile/fiber assemblies.

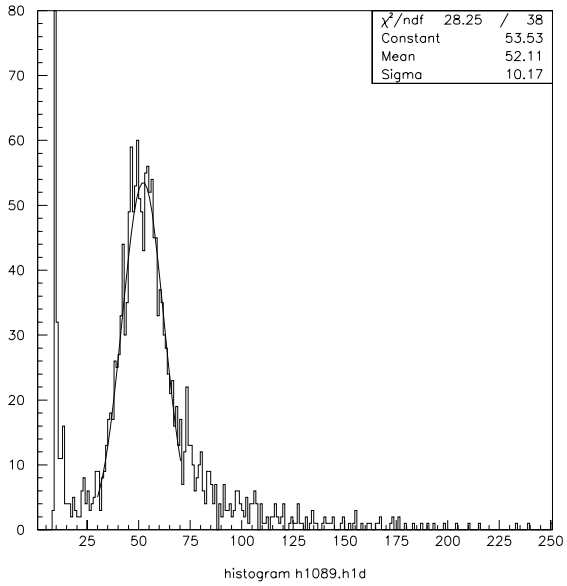


Figure II.3.4.4-2 The ADC pulse height spectrum from cosmic muons for tile tile/fiber assemblies.

### II.3.4.5 Pressurizing effect for the light yield of tile/fiber assemblies

This setup has been used to study the pressurizing effect on the light yield of tile/fiber assemblies. The packaging tiles were pressed between two aluminum blocks of 50-mm thickness. During these measurements we stabilized temperature of tile/fiber – PMT system on the level 30.1C-30.7C. Figure *II.3.4.5-1* shows the relative light yield as a function of pressure. The light yield is normalized by the yield without pressure. We have used bond paper as reflector. The light yields decrease to 1.5% at 20 PSI and to 2% at 50 PSI. Thus our measurement shows that in this case the light degradation will be 1% to 2% at the pressures encountered in our calorimeter. Most importantly, this result proves that the non-uniform pressure distribution that occurs within the stack will not influence the calorimeter performance. These results are in good agreement with the ANL result [12] that showed, for 6-mm thick polystyrene scintillator, the loss under pressure at 100 PSI is 5%.

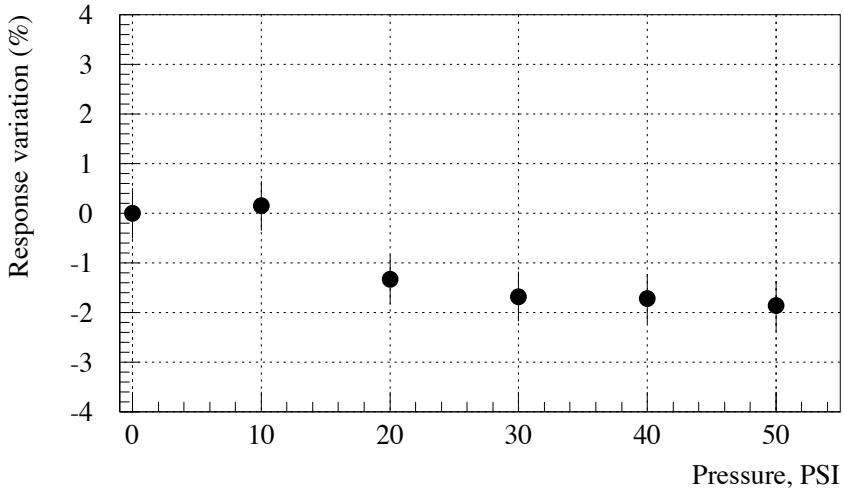

Figure II.3.4.5-1 The relative light yield as function of pressure for tile/fiber assemblies using bond paper as reflector.

### II.3.4.6 Temperature effect on scintillator tile/fiber system

We have studied the dependence of light yield of scintillator tile/fiber system on temperature. We heated samples of scintillator tiles with system of fans. The time for stabilizing of temperature inside box with accuracy 2% was typically 5-6 hours. Figure *II.3.6.6-1* presents the results of measurements. The light yield normalized by that with 24° C. The line on the figure is to guide the eye and are not fits. The light yield decreases between 3%-4% when the temperature increases from 24° C to 40° C. The large source of error ± 0.5% in these types of measurements is temperature stability of the photocathode of PMT. Temperature of PMT was continuously monitored and during measurements was 24° ± 1° C. As was established long ago, the light output of some commonly used plastic scintillators is practically temperature independent between –10° C and +20° C and has a temperature stability of about –0.125%/°C between +20° C and +60° C[13].

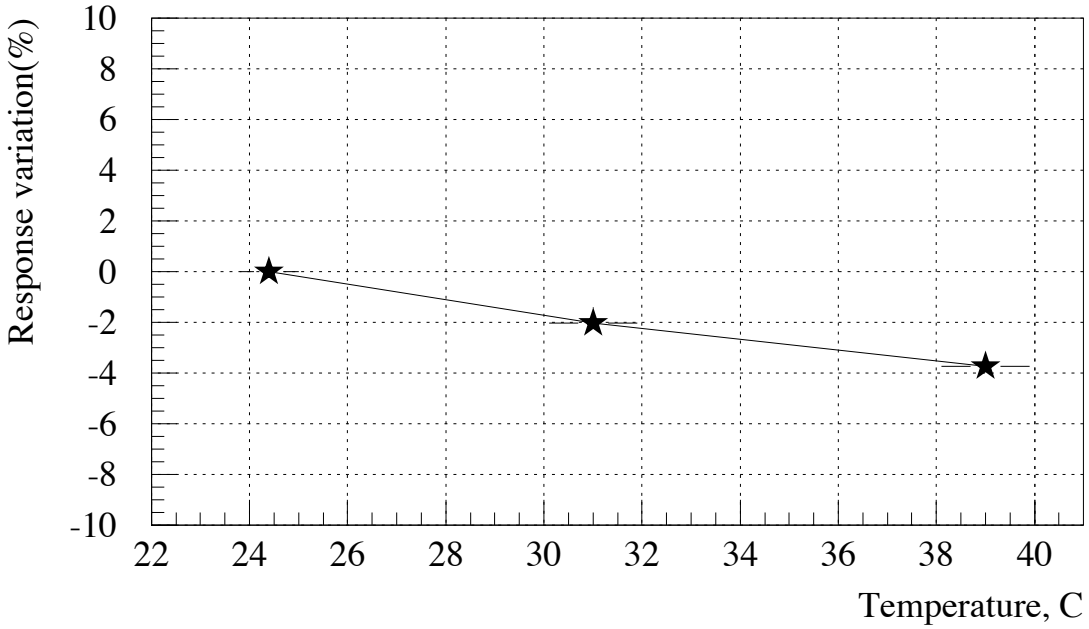


Figure II.3.4.6-1 Dependence of light yield on temperature for PS extruded scintillator.

According to our measurements, the light output stability of the PS scintillator is nearly –0.25%/C that is typical for PS scintillator[14].

### II.3.4.7 Aging

Aging is one of important issues of the Calorimeter performance. Extrusion PS scintillator has been used in many experimental setups of IHEP (Protvino) over many years and does not demonstrate any deterioration of detectors performance. To quantify this, aging of the scintillator tiles was estimated by increasing temperature action for the acceleration of chemical reactions[15].

We kept samples of extrusion PS scintillator at temperature of 50 ± 1° C during 53 days and measured light output every day. Some results are shown in Figure II.3.4.7-

1. The decrease of 8.8 % was observed after 53 days. Using result of these measurements we can evaluate possible degradation of scintillator resulting from natural aging. In accordance with our calculations, that result corresponds to the total natural aging of up to 6 years. According to our measurements the light degradation caused by natural aging should not exceed 8.8 % level after 6 years of operation.

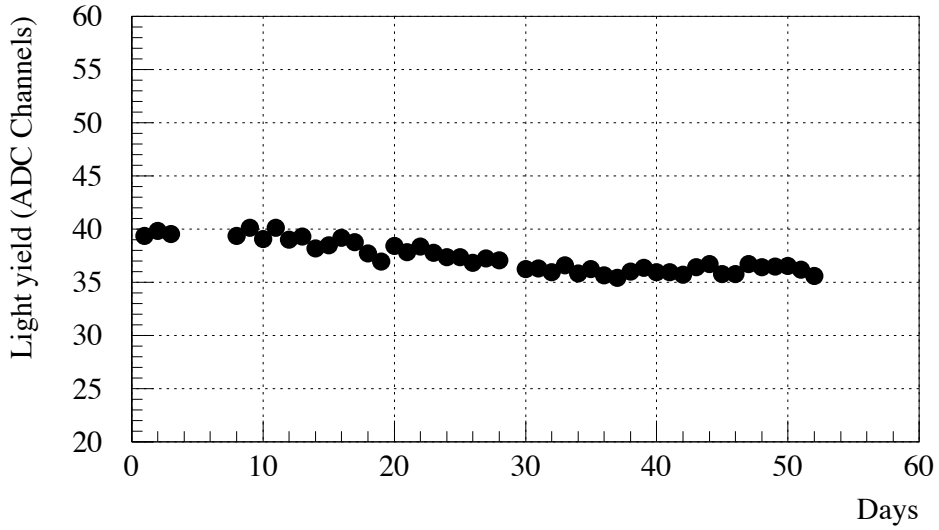


Figure II.3.4.7-1 Light degradation of PS extrusion scintillator tile/fiber system.

### II.3.4.8 PS scintillator performance in magnetic field

Experimental data have shown that the light yield output of a scintillator depends on the magnitude of the externally applied magnetic field[16,17]. The tests [18] were performed in FNAL proton area magnet facility. The samples of scintillator to be tested were installed between the poles of the magnet. Two types of scintillator based on polystyrene were tested: Kuraray SCSN38 and a scintillator prepared in Protvino, IHEP. Figure *II.3.4.8-1* presents the results of these measurements.

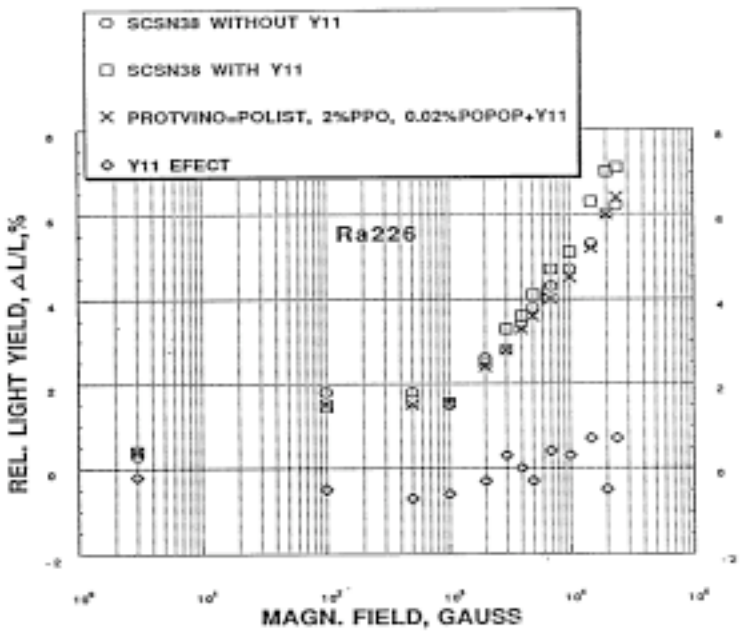


Figure II.3.4.8-1 Light yield dependence of PS scintillator from magnetic fields.

The data show the following:

1. The polystyrene based scintillator irradiated by radioactive source show a relative light yield increase up to 1-1.8% for a magnitude of magnetic field up to 0.1 kG. One can then see further growth between 1 kG and 20 kG. For the maximum STAR magnet field of 5 kG the increase in the light yield will be on the level 4%. DESY measurements with calorimeters in electron beams show same percent increasing light yield in the region of magnetic field up to 5kG in comparison with a single plate irradiated by a source.
2. The data do not depend on the magnetic field orientation. It is also not strongly dependent on the source of irradiation used (less than 1% difference for gammas or electrons).
3. There is no influence of magnetic field (for magnitude up to 140 kg) when scintillator or WLS is irradiated by ultraviolet light. Thus the light yield increase is not due to the fluors.

[1] S.Bennet et al., STAR Note SN303.

[2] O.Grachov and A.Ronzhin – Preprint IHEP 88-74, Protvino, 1988.
T.Asakawa et al., NIM, A 348(1994) 139.
S.Aota et al.,NIM, A 352(1995) 557.

[3] O.Grachov, STAR Note SN274.

[4]P.de Barbaro et al., SDC-93-407

[5]G.Apollinari et al., FERMILAB-Conf.-94/030-E(CDF).

[6]Y.Seiya et al., FERMILAB-Conf.-95/001-E(CDF)

[7]J.Freeman, FERMILAB-Conf.-96/458-E(E892)

[8] E.Bartosz et al., SDC-93-422.

[9] K.Hara et al., SDC-93-442.

[10]- V.Hagopian et al., CMS TN/96-032

[11]-P.de Barbaro et al., UR-1354.
[12]-D.G.Underwood , ANL-HEP-CP-92-94.
[13]-J.F.Camberon, Nucl.Electr.(I.A.E.A.) 1(1962) 93;
[14]-V.G.Vasil'chenko et al., Nucl.Inst. and Meth., A369(1996)55;
[15]-A.Karyukhin et al., ATLAS Note, 1 Aug. 1996.
[16]-D.Blomker et al., NIM, A311, 1992, 505.
[17]-J.Manuish et al., NIM, A312, 1992, 451.
[18]-D.Green, A.Ronzhin and V.Hagopian , FERMILAB-TM-1937, 1995.

---

[i] G. W. Foster, J. Freeman, and R. Hangstrom; Nucl. Phys. B A23(1991) 93, P. de Barbaro *et. al.*; Nucl. Instr. Meths. A315(1992) 317

[ii] P. de Barbaro *et. al.*; University of Rochester, Note UR-1371

[iii] M. Olsson; CDF/DOC/PLUG UPGR/CDFR/2582

[iv] P. de Barbaro *et. al.*; University of Rochester, Note UR-1354

# III The Design of the Shower Maximum Detectors

## III.1 Mechanical Design of the SMD

### III.1.1 Introduction

Since the beginning of the STAR EMC project a variety of technologies were considered for use in the STAR Shower Maximum Detector (SMD). A detectors based on scintillation hodoscope with fiber readout "SciFi" gaseous wire/strip chambers "wire/strip", and plastic streamer tube "PST" were considered as a candidate for SMD at STAR. During 1992-1997 extensive tests and Monte Carlo calculations were carried out to evaluate the three candidate SMD media. Four different "SciFi", four "wire/strip" and "strip/strip" and one "PST" prototypes were designed, constructed and tested on electron and hadron beams at Protvino U-70 and Brookhaven AGS accelerators. The SMDs performances were studied at the energy range from 0.5 to 26.6 GeV, for a different detector positions inside the EMC and different detector granularities. The results of this investigations shows that both "SciFi" and proportional gaseous detector in "strip/strip" readout configuration were well-suited for the STAR where electromagnetic shower must be precisely localized in space and their characteristic transverse size parameters must be measured. An independent energy measurement near the shower maximum is also needed to improve the overall hadron discrimination power of the non-segmented EMC and SMD. In order to accomplish its measurement functionality goals, the EMC/SMD must measure photons and electrons, often in large hadronic backgrounds. An important component of our discrimination between electromagnetic and hadronic showers and our ability to discriminate photon pairs in a single tower will come from the characteristic transverse shower shape and dimensions at a point near the energy density maximum of an electromagnetic shower in the longitudinal direction. The observation direct photons, whether in p+p or Au+Au, will rely in an essential way on the ability to identify an isolate photons in this manner. Furthermore, the construction of an invariant mass for photon pairs or dielectrons, particularly at high Pt, requires precise localization of the showers. The combination of large EMC cell size and fine-grained detector(SMD) at a few radiation length deep is the most economical way to do the required electromagnetic shower localization and characterization. It has been shown that this approach allows direct photon physics with acceptable error bars (e.g. CDF ).The final design consideration for the SMD detector involve compromises between the physics requirements, mechanical constraints, and cost. The SMD is designed as a wire/strip array consisting of a double layer of proportional gas counters which are read out using orthogonal sets of cathode strips ( pads ). The charge collected on the cathode pads provides information on the position of the anode avalanche and finally gives the information about the shower shape and energy deposition at depth 5X0 inside the EMC. Detailed simulation have been conducted to study the optimum depth to place the SMD detector within the EMC. A compromise is required by the very broad energy range of photons and electrons encountered in the entire STA physics program. A depth 5X0 has been found to provide the acceptable gamma/pi0 separation at the highest energies while providing good discrimination for the soft photons encountered in the heavy ion program and in asymmetric pi0 decay.

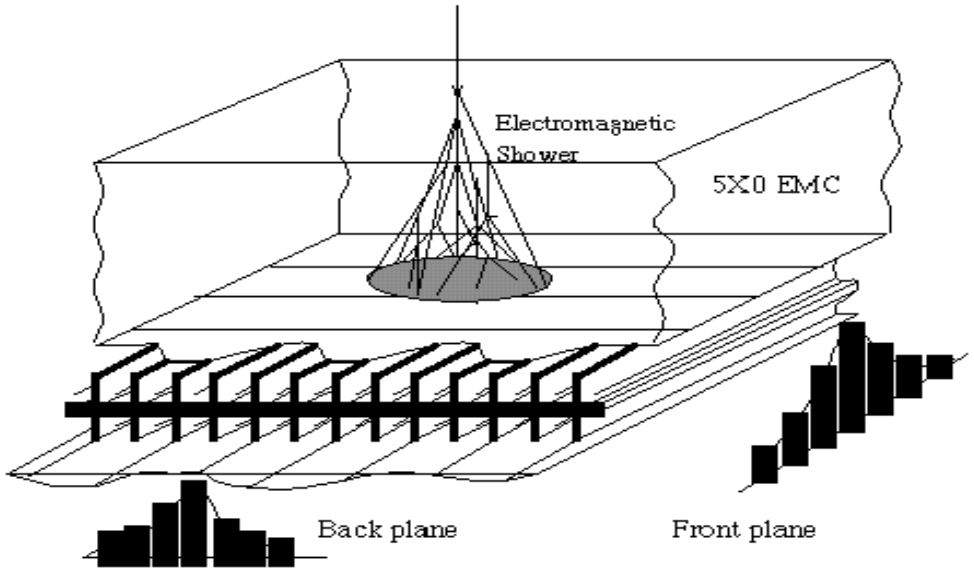


Figure III.1

### III.1.2 Component Design, Fabrication and Quality Control

Careful Monte-Carlo studies at IHEP have led to the following table of parameters for the physical design of the SMD to achieve a reasonable fraction of the physics goals. The physics requirements were to achieve reasonably low occupancy in Au+Au collisions, segmentation comparable with the expected transverse size of the showers and good two-shower resolving power.

Mechanically, the SMD should have as little impact as possible on the performance of the EMC. This places difficult constraints on both the rigidity and flatness of the SMD modules, leading to a design which transports the strip signals to preamplifier electronics boards placed at the end of the modules, rather than embedding the electronics within the EMC. This decision also improves the modularity of the SMD design, enabling better access to the completed units.

**SMD Design Parameters**

| | |
|---|---|
| Chamber Position inside EMC | 5X0 |
| Rapidity Coverage (Single Module) | $\Delta\eta$ = 1.0 |
| Azimuthal Coverage(Single Module) | $\Delta\phi$ = 0.105 (6°) |
| Occupancy (p+p) | ≈1% |
| Occupancy (Au+Au) | > 5 to ≈25% (depends on the threshold cut) |
| Chamber Depth (Cathode to Cathode) | 20.6 mm |
| Anode Wire Diameter | 50 μm |
| Gas Mixture | 90%-Ar /10%-$CO_2$ |
| Gas Amplification | ≈3000 |
| Signal Length | 110 ns |
| Strip Width (Pitch) in $\eta$ for $\|\eta\|<0.5$ | 1.46 (1.54) cm |

| | |
|---|---|
| Strip Width (Pitch) in $\eta$ for $\|\eta\|>0.5$ | 1.88 (1.96) cm |
| Strip Width (Pitch) in $\phi$ | 1.33 (1.49) cm |
| Number of Strips per Module | 300 |
| Total Number of Modules | 120 |
| Total Number of Readout Channels | 36000 |

Table III.1.

### III.1.3 Detector Assembly and Quality Control

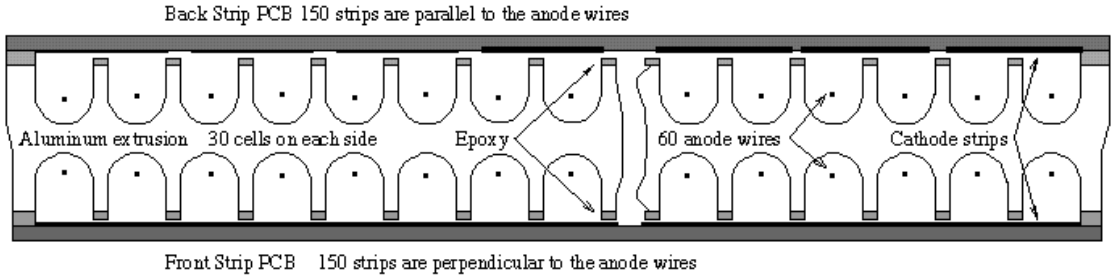


Figure III.2

Schematic diagrams of the SMD detector are given in Figures III.2 and III.3. The detector consists of a two-sided aluminum extrusion. Anode wires are strung in each channel and the cells of the extrusion are sealed by copper-clad PC boards on top and bottom. The strips come on a 2.5 mm thick copper-backed PC board. The back of this board is a continuous ground. These PC boards are glued onto the aluminum profile through three layers of epoxy with a total thickness of about 100 $\mu$m. These layers provide the electrical insulation of the strips from the aluminum profile and form a sealed gas chamber volume. A 90% Ar- 10% $CO_2$ gas mixture is flowed continuously through the chamber. All channels have gas flow in parallel. The pads on the top will read out the $\phi$ position while the bottom will read the $\eta$ position. The ends of the chamber are machined to receive PC boards epoxied into place to provide wire positioning and support, high voltage distribution, and gas inlet/outlet ports.

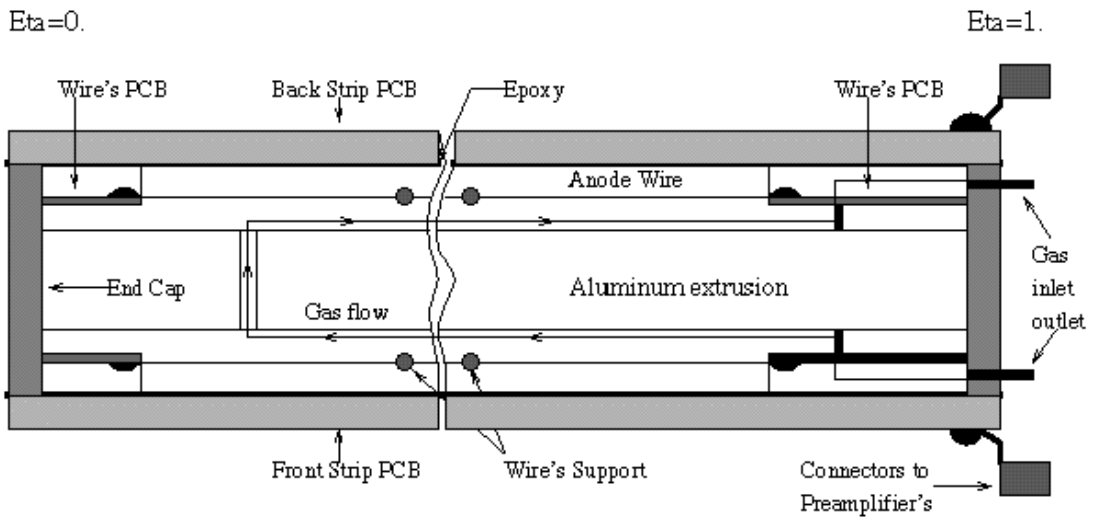


Figure III.3.

We now detail the calculations to achieve our design goal to minimize the channel-to-channel signal variation due to mechanical tolerances. We assumed that space-charge effects are negligible and that the tubes will be operated in the proportional mode. The goal of these calculations is to determine the tolerances required to produce a detector with variation of channel-to-channel performance as low as possible.

The amplification of the primary ionization signal in the proportional counter depends on the high voltage, gas density and geometrical cross section of the electrostatic surfaces. For cathodes of polygonal shape, the potential distribution can be approximated sufficiently well for our purposes as that of a coaxial structure as shown by F. Schneider (F. Schneider, EP Internal Report 78-2, CERN, Apr. 1978). The assumptions is true proportional mode, i.e., that space-charge effects are negligible. In this case, the gas amplification may be expressed as

$$\beta = \int \alpha ds, \qquad \text{(III.1)}$$

where s is the path of the ionization electron and $\alpha$ is the first Townsend coefficient. The integral runs between its locus of production, d, and its termination at the sense wire $r_1$. The nominal dimensions of the cell configuration are as follows. The diameter of the anode wire is 50 $\mu$m, the wire tension is 50 g, and the extrusion cell size is 6x6 $mm^2$. The gas mixture is 90%-Ar/10%-$CO_2$. For this gas mixture at NSTP, the charge collected on the anode wire is well represented as [A.B. Wickland, Private Communication]:

$$Q_c = 1026\, e^{(V-1500\})/78} \qquad [fC/5.9\ keV] \qquad \text{(III.2)}$$

Variation due to voltage and gas density is:

$$\beta=\beta_0 + K_1\, \Delta V/V + K_2\, \Delta\rho/\rho \ , \qquad \text{(III.3)}$$

where the parameter $K_1$ can be measured by a simple voltage variation (Eqn. 2), and $K_2$ is obtained by varying the pressure. For the calculations presented below, we used:

$$K_2 = \beta_0 - K_1 \ .$$

The amplification as a function of anode wire radius:

$$\beta = \beta_0 + [\ K_2 + K_1/\ln(R/r_1)]\ \Delta r_1/r_1 \quad . \qquad \text{(III.4)}$$

Amplification due to variation of the cell radius:

$$\beta = \beta_0 - K_1/\ln(R/r_1)\ \Delta R/R \ . \qquad \text{(III.5)}$$

Amplification for sense wire displacement from the center of symmetry:

$$\beta = \beta_0 + \ K_1/\ln(R/r_1)]\ (\Delta/R)^2 + (K_1 + 9\beta_0\ )\Delta r_1/R^2 \quad , \qquad \text{(III.6)}$$

where $\Delta$ is the wire offset due to initial positioning, gravitation or electrostatic origins. The wire offset due to gravitation is:

$$\delta_g = q\ L^2/8H\ , \qquad \text{(III.7)}$$

where q is the mass per unit length of the wire, L is the length and H is the horizontal wire tension. The wire deflection due to electrostatic forces is [S.H. Oh, W.J. Robertson, Nucl. Instr. and Meth. A309 (1991) 368]:

$$\delta_e = \pi\varepsilon_0 V^2 L^2 \delta_0/[8HR^2\ \ln(R/R_1)^2 - \pi\varepsilon_0 V^2 L^2\ ]\ , \qquad \text{(III.8)}$$

where $\delta_0$ is the wire offset due to gravitation and initial wire positioning.

Using equations III.1-8 we can determine the required tolerances for the anode wire, aluminum extrusion, wire positioning and wire tension to obtain a gas gain variation less than ±10%.

Two crucial characteristics of the wires should be taken into account: variation in the wire diameter and straightness grade. The wire variation will lead to gas amplification variation according to the following table:

| **Diameter Tolerance** | **Variation of Gas Gain** |
|---|---|
| ±1% | ±5.3% |
| ±2% | ±11% |
| ±3% | ±30% |

Table III.2.

Experience with material for the prototype and consultation with the manufacturer [International Extrusions Inc.] has led to an adaptation of the original design for the aluminum extrusion. Achievable tolerances of ±0.006" lead to a variation in the gas gain of about ±10%.

Allowing all the error budget to the tolerances in the cell size and wire diameter, we use equations III.1-8 to calculate acceptable tolerances in the other parameters:

- Total wire displacement from the axis of symmetry due to all effects: < 265 μm
- Extrusion straightness tolerance: < 2 mm over 3 m length
- Extrusion flatness tolerance: < 1.15 mm over 1 m length
- Extrusion cell size tolerance: < ±100 μm
- Extrusion material: Aluminum alloy 6061-T6

Requirements on the chamber assembly fixtures are as follows:

- Table flatness tolerance: <1.15 mm over 1 m length
- Straightness tolerance for second datum: <200 μm at 1 m length
- Material: Aluminum alloy 6063-T5

Requirements on the wire positioning fixtures at the chamber tips and supporting lines:

- Wire positioning tolerance: < ±150 μm

Fixtures and tooling which achieve these tolerances have been built and tested for the mechanical and electrical prototypes at Wayne State University. They will be transported to UCLA for use in the first round of chamber construction in 1998. Later duplicates will be based on our experiences with these fixtures in light of performance of the completed modules.

## III.2 SMD Electronics and Fabrication

### III.2.1 Strip PCB Design

The design of the strip PC board satisfies the following requirements: the strip pitch of 1.42 cm (0.559") is matched to the expected transverse size of the showers. The characteristic impedance of the transmission line from strip to FEE is matched to the input impedance of the preamplifier and the lines are spaced to achieve reasonable strip-to-strip cross-capacitance, low fabrication cost and a minimum number of manufacturing steps required in the final assembly. PC Board manufacture is a 'mature' technology, which minimizes human intervention in the construction process and minimizes the overall cost.

The general design of the strip PC board (Fig. III.4) will be a plane of strips on one side and signal lines to the FEEs on the other. The characteristic impedance, Z, of these lines will depend upon the final design, but is in the neighborhood of 100 Ohms.

The propagation constant, $\gamma$, is given by

$$\gamma = [j\omega C(R + j\omega C)]^{1/2}. \qquad \text{(III.9)}$$

After propagating length l, the current $I_0$ will be

$$I(\omega) = I_o(\omega) \exp\{-\gamma(\omega)l\} \qquad \text{(III.10)}$$

where the real part of $\gamma$ gives the attenuation in the transmission line. For high frequencies, the real part may be approximated as

$$Re[\gamma] = R/2Z \qquad \text{(III.11)}$$

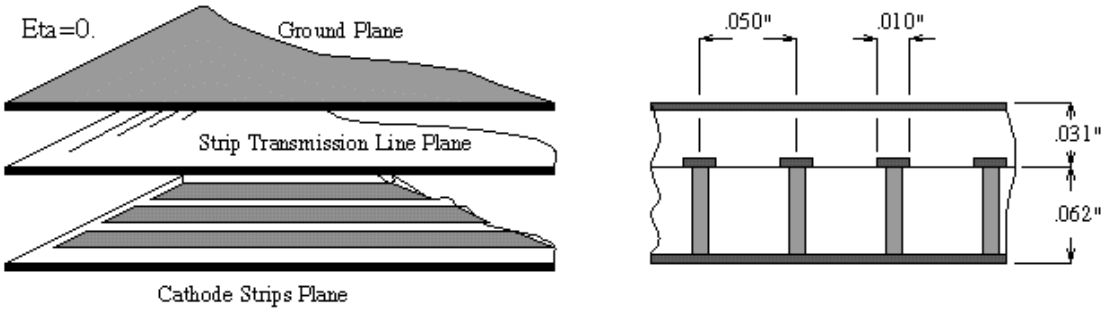


Figure III.4.

Typical line dimensions a = 100 μm, b = 500 μm and ρ = 1.7 $10^{-8}$ Ω-m give an attenuation constant α= 0.0034/m. Thus, we expect a signal attenuation of about 1% for the signals which propagate from the region near η=0 to the FEE cards located near η=1. The maximum delay time for these same signals is about 20 ns. The overall capacitances of the strip plus delay line is given in the following table:

| | η = 0 | η= 0.5 | η=1.0 |
|---|---|---|---|
| η-Strips | 285 pF | 260/347 pF | 333 pF |
| ϕ-Strips | 244 pF | | 246 pF |

Table III.3.

As noted in the first section, there is a jump in the width of the strips at η = 0.5.

### III.2.2 Preamplifiers and Readout

#### III.2.2.1 Design Parameters

The design of the readout electronics was made to satisfy the physics requirements, mechanical consideration, and integration of the SMD into the EMC and STAR. The reliability, accessibility, and possibility to make future upgrades also were considered. The physics requirements ( see section VII.2.b for details ), lead to overall dynamic range 1:640. The smallest signal from MIP need to be detected is around 4fC ( at HV = 1380 V ). The capacitance of the readout strip in average 260 pF and vary depending on the strip position vs. eta ( strip length is projective ) and also on the length of the strip transmission line to the front-end motherboard. The total collection time for ions in SMD gas mixture is around 30 ns, so that ion tale cancellation is desired ( see details in section VII.2.b ). Power consumption is need to be at lowest possible level ( 30-40 W power dissipation or each SMD module is acceptable ) to simplify the integration. High integrity of the readout electronics is preferable to avoid the long transportation of the analog signal in noisy environment. The test run experience with the small prototypes shows that appropriate gain for the preamplifier/shaper need to be close to 20 mV/fC. The noise at level ENC 6000 electrons for strip capacitance around 300 pF is acceptable. This level of noise will allow to operate SMD at high voltage close to 1380 V to detect MIP with reasonable efficiency and to avoid the problems with gas saturation ( space charge effect near the anode wire ) for up to 30 GeV electromagnetic showers. The crosstalk as measured for the full scale chamber electrical pre-prototype is around 3% ( the worst case for the strips located at eta=0 end of the module ) due to cross capacitance of the strip transmission lines. The crosstalk for the preamplifier/shaper at level 1% is acceptable. The precision of the internal calibration of the

channels of preamplifier/shaper is need to be no worse than +/- 7%, so the overall calibration of the channels of the SMD will be known with accuracy +/- 10% prior data taking.

### III.2.3 Preamplifier Mechanical Integration

From a mechanical integration viewpoint, there are several reasons to put the SMD FEE at one end of the EMC module as opposed to a solution which embeds the electronics within the module:

- Operational: The experience with these types of chambers proves that reliability of the FEE is much lower than the reliability of the chamber itself.
- Preamps at this moment are in the prototype stage. To install a few modules on 'Day One' we need to separate the mechanics and electronics of the SMD.
- Simplification of the SMD integration into the EMC. (We avoid the problem of interference between the SMD cables and EMC fibers on the sides of the EMC module.)
- Simplification of the EMC integration into STAR. (Again, problems related to fiber and cable routing through the same channels, as well as the new design of the EMC optical connectors.)

Access to the preamps during RHIC operation. Repairs, upgrades, etc., can be made without disassembling the EMC or even removing the modules from the barrel.

#### III.2.3.1 Envelope

Placement of the FEEs on the end of the modules has a slight ramification on the physics because the gap between the barrel and the endcap must be increased to 38 mm to allow enough room for the SMD preamps. Recent simulations by Akio Ogawa (Penn. State) shows that there are no significant losses in acceptance for this configuration, at least for p-p physics at RHIC.

#### III.2.3.2 Interface

For each SMD module, there are 300 channels of strips to be read out. The preamplifiers will be on the Mother Board at the eta=1 end of the module. The dimensions available for the MB are a trapezoid with a top side of 210 mm, a base of 230 mm and a height of 308 mm. (677 $cm^2$).

All interfaces for the SMD system are located on the top of the EMC module on the $\eta$=1 side in order to simplify the procedure for the installation of the EMC into STAR.

An IDC ribbon cable (Thomas-Betts, Type 20067) of length 3-5 cm will be soldered to the Strip PCB at the $\eta = 1$ end of the chamber. (Thomas-Betts, Type 609) Connectors will be used to connect the Mother Boards to the chambers. The pre-amp cooling tubes will be cooled by compressed air through 1/4" OD Poly-Flo tubing (44-P-1/4, Imperial Eastman).

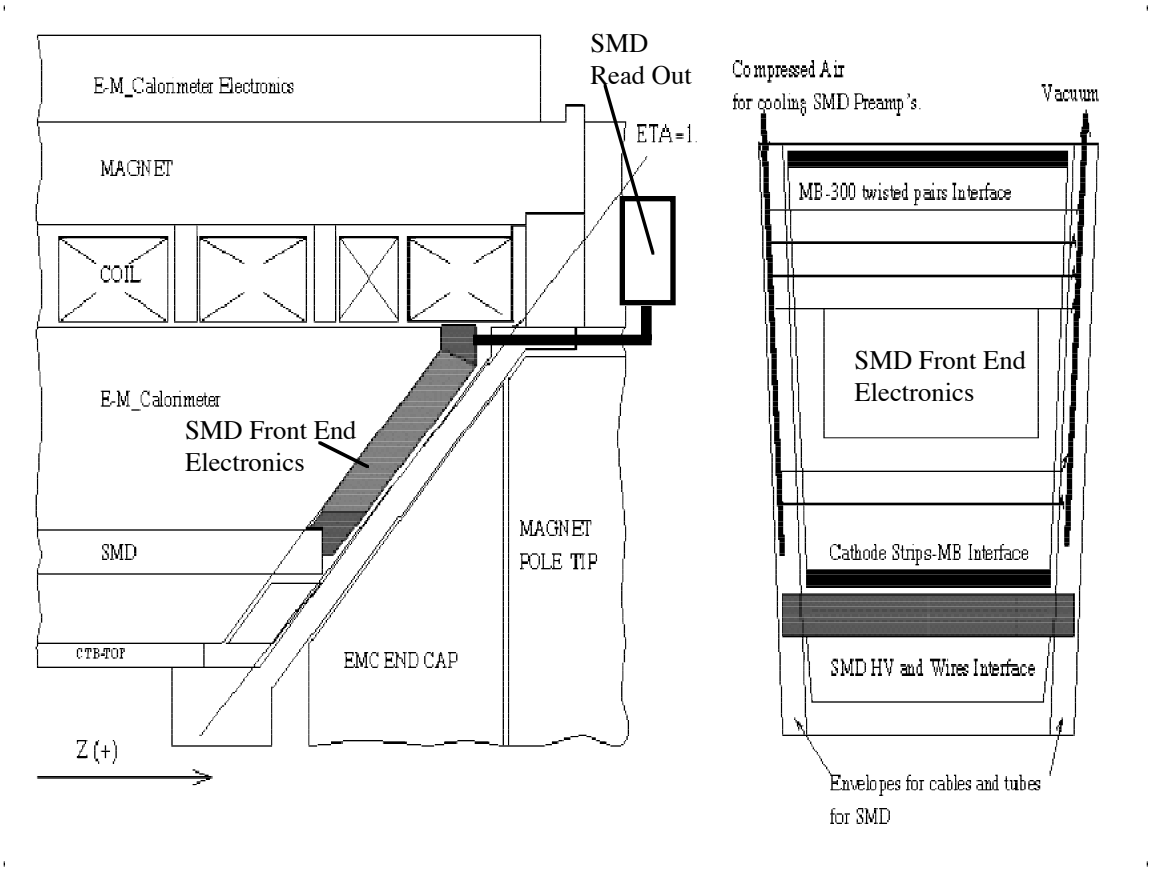


**Figure III.8.**

### III.2.3.3 Cooling System

The total power dissipation in the volume of the electronics at the eta=1 end of the each EMC module is expected to be < 30 W. Using a mechanical 'pre-prototype' we have developed an empirical formula for the temperature of the boards as a function of air flow rate : T=66 - Q/10,
where T(C) and Q (cf/h). The temperature of the input air was 25 C. To allow a safety factor of three, we will specify a cooling flow of 12 cubic feet per minute, again assuming the ambient air temperature is 25 C. The air temperature rise in this case was expected to be 4 C. Pre-cooled air would lead to problems with condensation.

## III.3 Prototype Performance Studies

### III.3.1 Introduction

The performance of the SMD candidate designs were studied over the period from 1992-1997 at the IHEP U-70 accelerator (Protvino, Russia) and at the BNL-AGS. Below, we present the performance of the baseline gaseous prototype designs in the wire/strip and strip/strip configurations only. Complete information about these studies can be found in

- B. Chuiko et al, IHEP Preprint 92-104, Protvino, 1992 First SciFI SMD Prototype

- S. Alimenko et al, Nucl. Instr. and Meth. A365 (1995) 92. The Last SciFI SMD Prototypes
- V. Belousov et al., Nucl. Instr. and Meth. A369 (1996) 45. PST SMD Prototype.
- S. Alimenko et al., Prib. Tekh. Eksp. 1997, N3 39. The Last Gaseous SMD in Wire/Strip Configuration.
- S. Bennett et al., Star Note (in preparation). The Small Gaseous SMD Prototype in the Strip/Strip Configuration, Final Design, Test '97.

The latest strip/strip small SMD prototype in the final design configuration was constructed and tested in 1997. This photograph (Figure III.9) shows the SMD prototypes under construction.

Figure III.9

Figure III.10 shows the assembled small prototype being bench-tested prior to installation into the small EMC prototype.

The detector construction was similar to the procedure described in section III.1.3, with cell size close to the final design and strip dimensions given in Table III.1 The gas mixture used in the prototype test was 90% Ar- 10% $CO_2$. The extrusion used for the prototype was rectangular in cross section with 32 cells of size 222 mm x 685 mm x 24 mm. The readout consisted of 32 x 32 channels of strips. The pulses from each strip were amplified by a two-stage device based on a 'Garantija' current amplifier and digitized by 11-bit LeCroy 4300 ADCs with a sensitivity of 0.25 pC/count and a 400 ns gate.

### III.3.2 Chamber Gain

The optimal value of the wire/strip

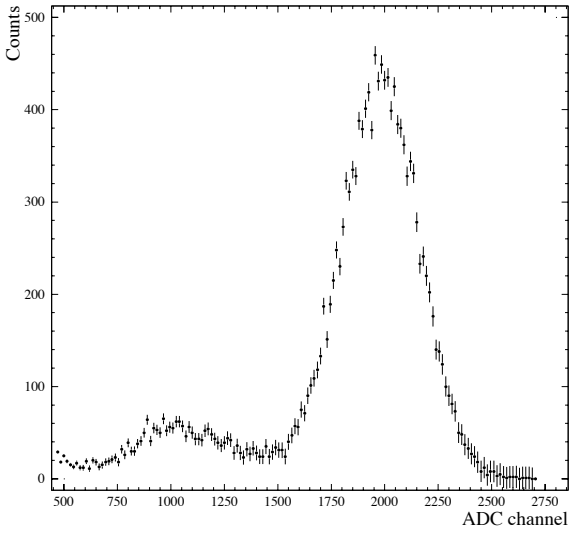


Figure III.11

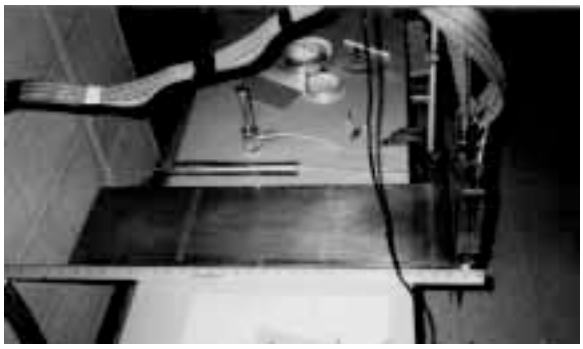

Figure III.10

SMD gas gain is constrained by space charge effects on the one hand and by signal-to-noise considerations on the other. Another important consideration is the reliability of the chamber over long periods. For this reason, it is important to determine the characteristics of the SMD at the lowest possible gas gain. Our goal is to operate

the chamber in the proportional mode. Up to 30 GeV, it is desirable to eliminate problems of signal saturation due to space charge effects. It is important to minimize the systematic uncertainties in the measurement of direct photons with the SMD.

Before placement in the test beam, the chamber was irradiated with $^{55}$FE X-rays to determine the appropriate gas gain. A typical pulse height spectrum is given in Figure III.11.

The ratio of the pulse heights for photons of energy 3 and 5.9 keV for the Fe source indicates that the chamber is operating in the proportional mode. A gain drop was observed when the density of the positive ions along the wire exceeded a critical value equal to 7 x $10^6$ per mm. The optimal value for the applied high voltage in the test beam was constrained
by signal-to-noise considerations. The high voltage was set to 1500 V for test beam in the energy range 0.1-0.7 GeV; corresponding to a gas gain of about $10^4$. Between 13.3 and 26.6 GeV, the voltage was set to 1450 V, corresponding to a gas gain of 3-5 x $10^3$. Under these conditions, Monte-Carlo calculations indicate that the maximum density of positive ions along the wire (in the region of the SMD near the shower axis) was 3 x $10^6$ /mm; which does not exceed the critical value.

### III.3.3 Chamber Response and Energy Resolution

The response of the front and back planes of the SMD for electromagnetic showers is given in the following Figure III.12.

In the energy range from 0.5 to 5 GeV, at a depth of 5X0 inside the EMC, the SMD has an approximately linear response versus energy. The ionization at the back plane of the SMD is about 10% lower than the front plane. The energy resolution in the front plane is given approximately by

$$\sigma / E = 12\% + 86\% / \sqrt{E}\ [\text{GeV}]. \qquad \text{(III.13)}$$

The energy resolution in the back plane is 3-4% worse than the front plane. The difference in behavior between the front and back was observed for the first time in previous studies of the SciFI variant of the SMD ( S. Alimenko et al, Nucl. Inst. and Meth. A365 (1995) 92). The detector response depends on the material inserted in front of the SMD. The presence of low-Z material in front of the detector leads to a partial cutoff and transverse broadening of the soft component of the electromagnetic shower due to multiple scatter in this material. This leads in turn to a signal drop in the detector, as well as a degradation of the spatial and energy resolutions. From this point of view the optimal sequence of the tiles in the EMC would point to a Pb tile just in front of the SMD.

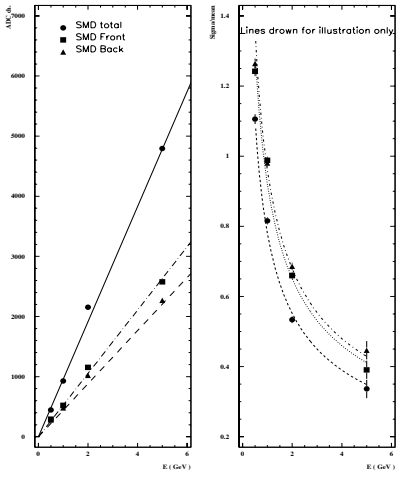


Figure III.12.

### III.3.4 Transverse Shower Profiles

As pointed out above, the shower position resolution, multishower resolving power, and electron-hadron separation provided by the SMD relies on the analysis of the transverse shower profile. A precise measurement of the shower shape is important for the tuning of Monte-Carlo programs and as input for future data analysis. Fig III.13a shows the normalized energy deposition in the SMD for showers for electrons from 1 to 26.6 GeV. The SMD is located 5 $X_o$ inside the EMC. Fig. III.13b gives the shower profile for 26.6 GeV electrons at SMD positions at 3X0 and 7X0 inside the EMC.

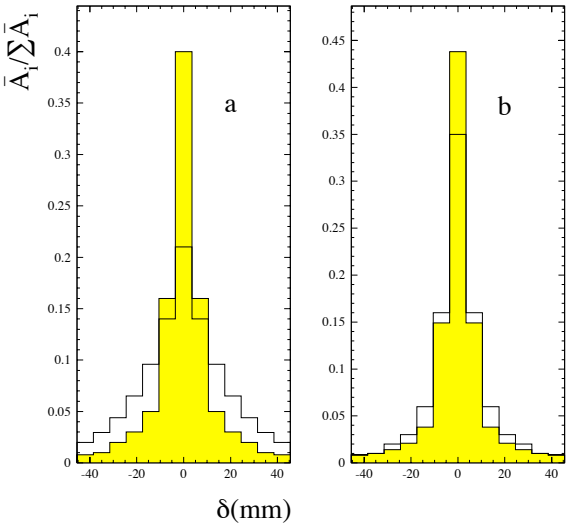


Figure III.13.

It is common to approximate the shower shape as the sum of two exponentials:

$$dE/dx = a_1 e^{-x/b1} + a_2 e^{-x/b2} . \quad \text{(III.14)}$$

This expression is convenient to compare our results with the CDF beam results. As with the CDF results, the shower shape is constant about 7 GeV. Both sets of results show that in this energy range the shower shape is well described with the values $b_1$ = 0.5 cm and $b_2$ = 2.3 cm. for the wire plane and $b_1$ = 0.6 cm and $b_2$ = 2.8 cm for the strip plane. We should point out, however, that this approximation only seems to hold near the shower axis. In future analysis we use a lateral shower density which is the sum of three exponentials whose contributions are noted as A,B, and C. Fig. III.14 shows the mean energy deposited in the SMC vs. the distance from the shower axis. The data points are the results from the test run for 26.6 GeV electrons with the detector positioned at 7 $X_0$ inside the EMC. The solid curve through the data is a fit to the experimental data ($\chi^2$/ndf = 1.18) using the sum of three exponentials. The relative contributions are given by the dashed lines.

The experimental results show that the parameters in the exponentials vary only weakly with position inside the EMC (from 3X0 to 7X0). Their values are 0.35 cm, 0.9 cm and 12.0 cm respectively. In the table below we present the results of the shower shape analysis for the three positions of the SMD inside the EMC.

| **SMD Position** | **Percent Contribution** | | |
|---|---|---|---|
| | A | B | C |
| 3X0 | 48.2 | 33.2 | 18.6 |
| 5X0 | 37.0 | 47.3 | 15.7 |
| 7X0 | 24.3 | 59.8 | 15.9 |

Table III.6

These results show that 90% of the energy is deposited within 3.5 cm of the shower axis. When the position of the SMD inside the EMC is changed, there is a redistribution of the contributions A and B to the energy profile. At the same time, 90% of all the energy deposition for the SciFi SMD was deposited within a distance of about 1.5 cm from the shower axis. We believe this difference comes from the transverse development of the soft components of the electromagnetic shower and depends strongly on the particular detector materials.

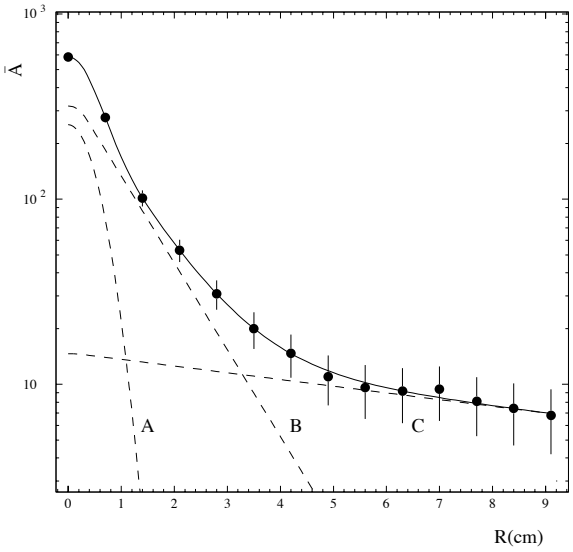


Figure III.14.

### III.3.5 Position Resolution

The position resolution was studied as a function of energy and SMD position. All measurements were made for an impact point at the center of a strip or wire channel. Two methods were used to determine the shower axis ($Y_s$) in the plane of the SMD:

$$Y_s = \Sigma_i w_i y_i / \Sigma_i w_i \,, \qquad \text{(III.15)}$$

where $y_i$ is the geometrical center of the i-th element and $W_i$ is the energy deposition $E_i$ in the i-th element for the simple center-of-gravity method. For the ''logarithmic' algorithm proposed by T.C. Awes et al (T.C. Awes et al., Nucl. Instr. and Meth. A311 (1992) 130), $w_i$ is a weight for the i-th element determined as follows:

$$w_i = \max[\, 0, W + \ln( E_i / \Sigma_i E_i) \,] \qquad \text{(III.16)}$$

where W is a constant determined empirically. The use of the logarithm this expression is motivated by the exponential falloff of the shower profile. This corrects the deficient behavior of the linear weight approach where a centrally hit element will contain most of the energy and will systematically pull the position calculation. The choice of W determines the relative importance of the energy deposition in the tails and provides a natural threshold. For example, for W=2, all the strips with an energy deposit of less than 13.5% of the total energy will not be considered.

Fig III.15 shows the systematic pull in the position calculation in the case of a linear weight. This is the experimental result from the 1997 test with 5 GeV electromagnetic showers. The uniform distribution of the impact parameter across the strip surface in the case of linear weighting in the expression for the center of gravity leads to a systematic shift to the geometrical center of the strip ( in the region ± 2.5 mm from the center of the strip). The logarithmic method appears to be free of this problem. This picture represents data from the front and back planes and is averaged over the entire SMD.

The spatial resolution data for the SMD were determined from shower profiles for four energies in the 1997 beam test. These results are given in the following table. The first column in the table gives the distance from the beam axis in mm. In the next columns are the relative energy deposited in percent. The integral over the shower profile at a given energy is 100%.

| Dist [mm] | E = 0.5 GeV [%] | E = 1. 0 GeV [%] | E = 2.0 GeV [%] | E = 5.0 GeV [%] |
|---|---|---|---|---|
| 0-5 | 29.5 ± 0.9 | 35.7 ± 0.8 | 39.2 ± 0.5 | 42.3 ± 0.5 |
| 5-10 | 22.3 ± 0.8 | 24.8 ± 0.6 | 25.4 ± 0.5 | 25.6 ± 0.4 |
| 10-15 | 18.5 ± 0.8 | 17.2 ± 0.5 | 17.2 ± 0.4 | 15.8 ± 0.4 |
| 15-20 | 10.0 ± 0.5 | 8.2 ± 0.3 | 6.9 ± 0.3 | 6.9 ± 0.3 |
| 20-25 | 5.9 ± 0.4 | 4.2 ± 0.2 | 3.4 ± 0.2 | 3.5 ± 0.2 |
| 25-30 | 4.7 ± 0.4 | 3.3 ± 0.2 | 2.7 ± 0.2 | 2.3 ± 0.1 |
| 30-35 | 3.1 ± 0.3 | 2.3 ± 0.2 | 1.9 ± 0.2 | 1.5 ± 0.1 |
| 35-40 | 2.3 ± 0.3 | 1.9 ± 0.2 | 1.2 ± 0.1 | 0.9 ± 0.1 |

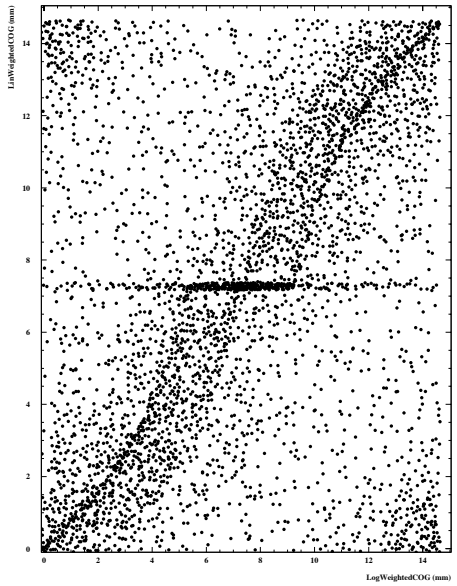


Figure III.15.

| | | | | |
|---|---|---|---|---|
| 40-45 | 1.9 ± 0.3 | 1.3 ± 0.1 | 1.0 ± 0.1 | 0.8 ± 0.1 |
| 45-50 | 1.9 ± 0.3 | 1.0 ± 0.1 | 0.8 ± 0.1 | 0.5 ± 0.06 |
| | | | | |

Table III.7

Dependence of the shower width on energy is presented in fig. III.16. The shower width gets narrower is the energy increases.

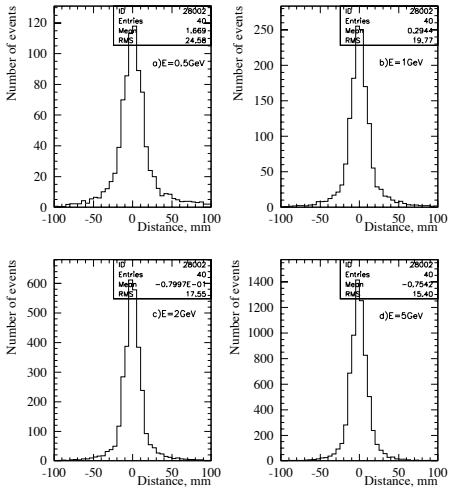


Figure III.16.

Figure III.17 shows the position resolution in the front and back planes of the SMD for the 1997 Test. The resolution in the front and back planes go like

$\sigma_{front}$ [mm] = 2.4 mm + 5.6 mm / √E [GeV] , and
$\sigma_{back}$ [mm] = 3.2 mm + 5.8 mm / √E [GeV] .

The parameter W=2 was taken to calculate the center of gravity of the electromagnetic shower.

We give a comparison between GEANT simulations of the shower profiles and data for four test beam energies in fig. III.18.

The GEANT shower profile is narrower than the experimental one in the energy range from 0.5 to 5 GeV. The central value of the deposited energy in the GEANT calculation is also higher than experiment by about 20-40%, depending on energy. In the tails of the distribution, the experimental data is higher by a factor of 1.5 to 2.5. The GEANT profile agrees more closely with experiment as the energy increases (see fig. III.19)

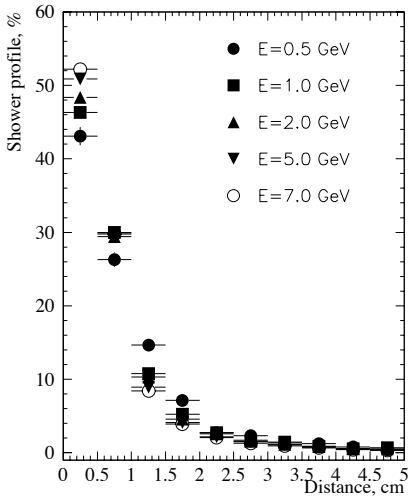


Figure III.18

### III.3.5 Electron-Hadron Rejection

To compare the electron/hadron rejection power for the longitudinally segmented EMC (5X0 + 20X0), a non-segmented EMC (25X0) and a non-segmented EMC with an SMD (25X0 + SMD), these detectors were tested with beams of $\pi^-$ at 39 GeV and $e^-$ at 26.6 GeV. The rejection coefficient K was defined as the probability to identify a hadron as an electron for 90% electron detection efficiency. The 25X0 EMC provided a rejection level of $K = 1.8\ 10^{-2}$. The longitudinal segmentation improved the rejection by a factor of about 6 for $K = 3 \times 10^{-3}$. The information about the energy deposition in the 25X0 EMC and the SMD gave $K = 5.1\ 10^{-3}$. Additional information about the shower width in the SMD slightly improved the rejection, due to correlations between the SMD energy deposition and the shower width. Therefore, the above results show that the SMD improves the hadron rejection power by a factor of 3.5 as compared to the rejection of a non-segmented EMC. It is poorer by 1.7 times compared to a longitudinally segmented EMC.

One of the advantages of the final double-sided design of the SMD is the independent measurement of the primary ionization in two gas samples inside the EMC. Large fluctuations on the ionization in thin gas layers can cause the ionization from a single minimum ionizing particle to be comparable to that of an electromagnetic shower of a few GeV. This leads to a degradation of the SMD electron/hadron rejection power. In the case of two independent gas samples, the probability of such an event is obviously smaller.

A few methods of electron/hadron separation were investigated. The main problem for the SMD is the absence of an energy-independent variable to be used for e/h rejection. Below approximately 10 GeV, the ratio of SMD/EMC signals for electrons is a constant. But as the energy increases, the position of the shower maximum shifts logarithmically and the above ratio decreases. Above about 10 GeV the so-called weighted radius for the

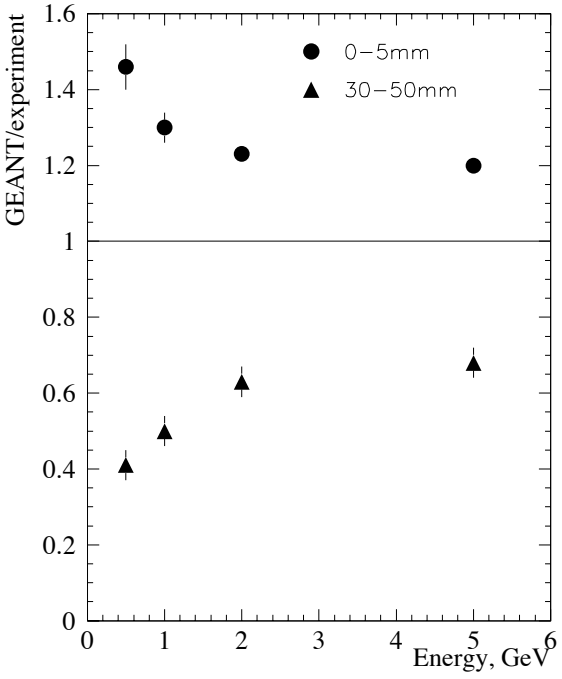


Figure III.19

electromagnetic shower is independent of energy. This follows from the invariance of the transverse shape of the shower as noted above.

Here we show one of the approaches to achieve e/h separation. First, separate cuts on energy deposition are made for the front and back planes: the surviving electrons have 90% detection efficiency. Fig. III.20(a) gives the entire data sample for electrons and hadrons (Run 53, Test 1997, 5 GeV) as well as the cuts applied to identify electrons.

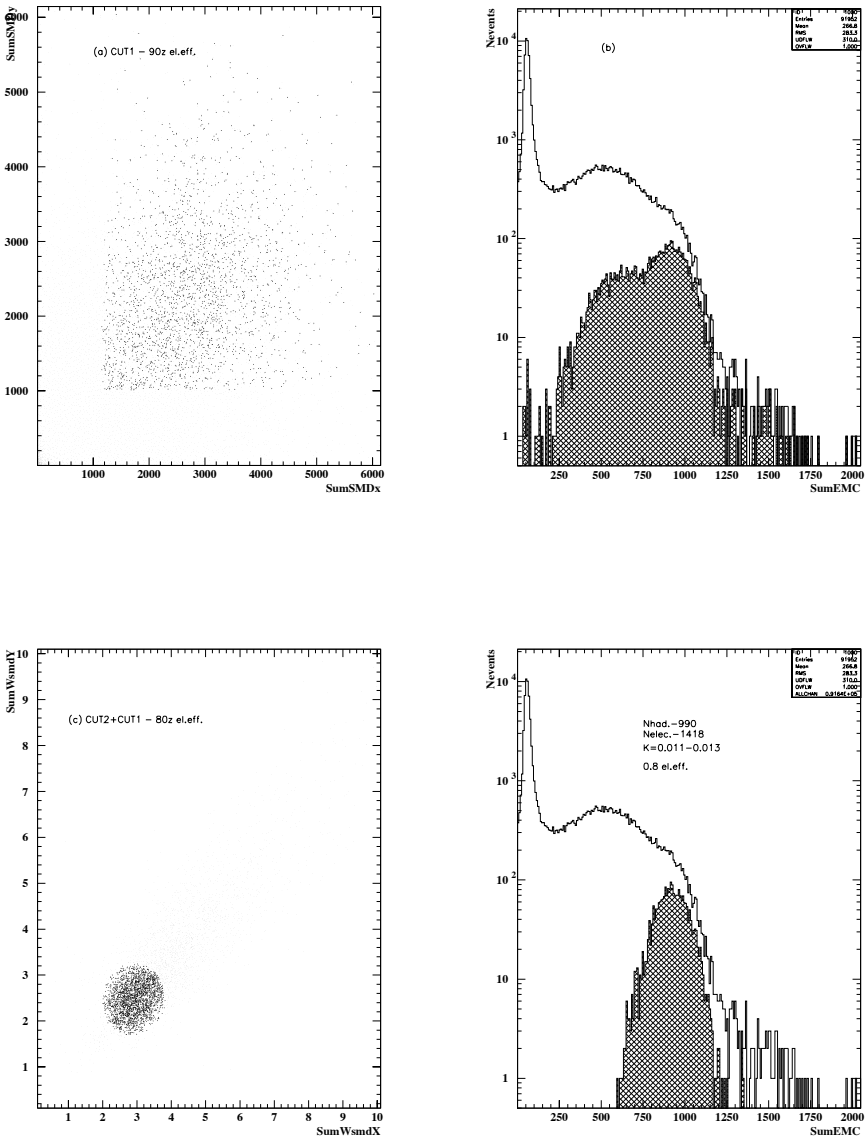


Figure 111.20

This figure also illustrates the independence of the ionization in front and back planes of the SMD in case of hadrons. Fig III.20(b) shows the amplitude spectra in the

EMC for the entire data sample and surviving events after applying cuts in the SMD. The rejection power of SMD itself comparable to rejection power of the non-segmented EMC, and is close to 30:1 for this particular energy, with an electron efficiency of 80%.

As it can be clearly seen from this figure, the SMD reject events different from those rejected by applying single cut on the EMC (for events with small amplitudes in the calorimeter). This allows us to increase the rejection power of the combined detector (EMC/SMD) by applying cuts which take into account information and from the EMC also. Fig III.20(c) shows the distribution of the ratio of the sum of the strips logarithmic weights over energy deposition in the EMC for the front vs. back planes of the SMD for the surviving the first cuts. The electrons events are mostly located in the 'head' of the 'comet', while the hadrons events are in the halo. In this figure, the marked area in the 'head of comet' contains 80% of the all electrons from the original data sample. Fig III.20(d) shows the amplitude spectra in the EMC for the surviving events. The hatched distribution is the amplitude of the surviving hadrons. The overall rejection power for the detector is 0.012±0.001 for 80% electron efficiency. In the energy range from 0.5 to 5 GeV the information from SMD improved the rejection power of the non-segmented EMC about a factor of 3.

### III.3.6 $\pi^0/\gamma$ Separation

A study has been carried out to investigate the use of the SMD to separate showers coming from single photons from those arising from neutral pin decay. All results were obtained for $\eta = 0$ for the STAR geometry. Two parameters of the shower energy deposition in the SMD are defined below: the energy-weighted-radius, R and the 'inertial moment', $ER^2$ of the shower. The coefficient of rejection is defined for 80% single gamma detection. For each shower, these parameters are calculated separately for each of the two SMD planes.

The shower center of gravity was calculated as:

$$X_c = \Sigma w_i x_i / \Sigma w_i \quad , \qquad \text{(III.17)}$$

where $w_i$ and $x_i$ are respectively the logarithmic weight and the coordinate of each element. The energy weighted parameters $R_{x,y}$ were calculated as:

$$< R_x > = [\ \Sigma w_i (x_i - x_c)^2 \ / \Sigma w_i \ ]^{1/2} \quad . \qquad \text{(III.18)}$$

The mean weighted radius, R was defined as

$$R = ( R_x^2 + R_y^2 )^{1/2} \qquad \text{(III.19)}$$

The second parameter, $ER^2$ , which provides information about the longitudinal shower development, was first calculated for each layer and summed in quadrature as above.
On the scatter-plot of $ER^2$ vs. R we have marked off the area containing 80% of the single $\gamma$ showers and consider showers within this area to be 'single $\gamma$' while all showers outside this area are classified as neutral pin showers. Using this definition, we determined the $\pi^0$ probability separation for 80% single $\gamma$ detection as a function of incident shower energy. Fig. III.21 gives the results of this study.

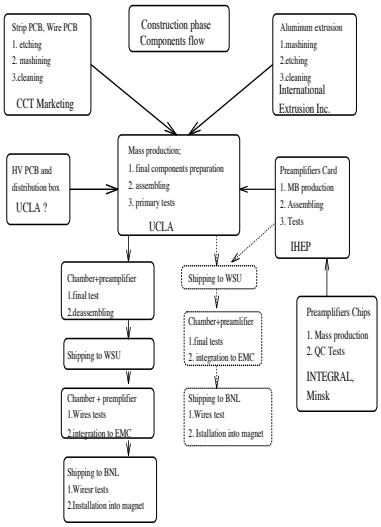


Figure 1 III.21.

The energy region from 3 to 7 GeV is important in the QGP search by measuring single photons. From this point of view, it is preferable to locate the SMD as the 5X0 position inside the EMC.

The study of these parameters defined above shows that a shower initiated by photons and neutral pions can be distinguished mainly by use of the quantity R. The use of the inertial moment parameter resulted in negligible improvement, mainly due to the poor energy resolution of the SMD.

## III.4 Detector Assembly, Tests and Quality Controls

The detectors will be assembled in a production facility to be set up at UCLA. This facility will be located in the Science and Technology Research Building (STRB) which will be available for beneficial occupancy in April, 1998. The physical plant available for STAR will be cost-shared with another group building muon chambers, resulting in a considerable cost savings. The SMD group has been allocated approximately 1500 sq. ft of open floor space for preparation and staging work. Assembly of the modules will be performed in a 1500 sq. ft clean room. Approximately 1000 sq. ft of additional laboratory space in Knudsen Hall can be committed for such purposes as chamber tests or temporary staging work. Finally, the UCLA machine shop is available for support work on a scale consistent with the planned module production schedule.

The total number of modules to be produced is 120 plus some spares which will be decided at a later date.

Economic considerations require us to purchase and store a large fraction of the raw materials for the SMD modules. It is anticipated that the space available in the STRB will be adequate for storage of these materials. During staging of many modules, we may utilize the additional storage or work space in Knudsen Hall.

In the staging for the first 15 modules, we will divide the production procedures approximately as follows: cleaning, light machining and temporary storage will be confined to the main assembly area. After preparation, the pieces will be examined for quality assurance on special test beds and vacuum tables in the clean room.

The modules are assembled by first applying a uniform layer of about 100 μm of epoxy to the extrusion edges and allowing it to dry. This serves to electrically insulate the extrusion from the copper of the readout pads. This step is performed first to avoid contamination of the anode wires by stray droplets of epoxy. Next, the wire PC boards, anode wire nylon support lines and elements of the chamber tips are epoxied in place. The anode wires are strung, then soldered in place. The wire stringing procedure will be checked by means of an automated system which determines the location and tension of each wire by means of a laser diode and photosensor (a bar code reader). The wire is gently set into os-

cillation by means of an air current and the resultant frequency of vibration noted using the Fourier transform of the sensor signal measured on a digital oscilloscope. This method worked very well for the STAR TPC sector construction.

The wires are then glued in position to the nylon support lines to prevent sagging under gravity under any orientation. The gas volume is then sealed by gluing the pad PC board in place. This assembly is then flipped over and the procedure repeated for the other side of the extrusion.

Assembly procedures will incorporate certain quality assurance checks such as measurement of wire tension, gas flow rate/ hermiticity and high voltage breakdown. Finally, the completed modules will be tested in Knudsen Hall for signal uniformity using anode wire pulsing, radioactive sources and/or cosmic rays.

The assembly procedures are as follows:

General Area:

1) Cleansing of extrusion/preliminary inspection
2) Cleansing of PC boards/preliminary inspection

Clean Room:

1) Inspection of extrusion for defects, straightness, flatness
2) Covering extrusion edges by epoxy
3) Gluing of Wire PCs, Wire Support Lines, Chamber Tips
4) Stringing/Soldering of Anode Wires
5) Check of Wire Tension
6) Gluing of Wires to Support Lines
7) Gluing of Strip PC Boards
8) Check for Electrical Isolation/Short Circuits.
9) Reverse Extrusion and Repeat (1-9) for Other Side.
10) Final Chamber Tip Assembly

Testing:

1) Gas Flow/Pressure Drops/Hermiticity
2) Electrical Isolation/Short Circuit Check
3) High Voltage Breakdown Check
4) Pulsing Check for Pad Response
5) Radioactive Source Check

Vendors for the components critical for SMD mass production have now been identified. Figure III.22 gives the overall 'components flow' scenario and major stages of the components preparation.

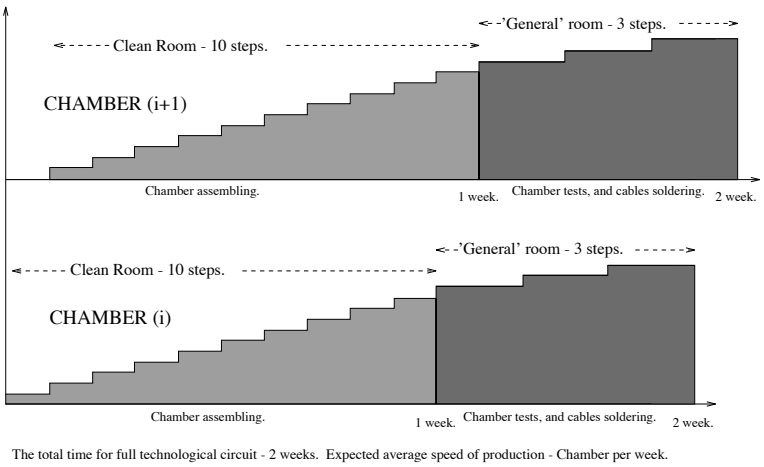


Figure III.22

At the present time, the first set of aluminum extrusions and strip PCBs produced by International Extrusion and CCT have been received. A portion of the assembly fixtures have been made for the construction of the full-scale mechanical prototype and full-scale operational chamber. The full-scale SMD mechanical prototype was constructed to be incorporated into the full-scale EMC mechanical prototype, as well as to test the assembly equipment and assembly protocols. Both the extrusion and strip PCBs passed out quality control tests and satisfy the design requirements. The deviation of the dimensions from the nominal values are in the acceptable range. Fig. III.23 shows the measured flatness of the full-scale SMD mechanical prototype after assembly using a 'vacuum gluing' table.

The conclusion of this study is that the mechanical parameters of the SMD will not lead to any problems related to integration of the SMD into the EMC modules. Our present construction methods will allow us to mass produce SMD modules of the required quality.

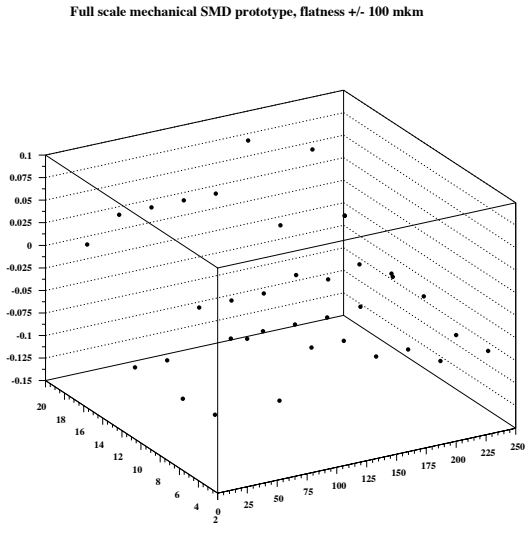


Figure III.23

## IV. EMC Calibration System Design

The calibration system in its broad understanding is the set of tools and procedures to achieve the gain equalization and relative and absolute calibrations of all EMC and SMD channels, and continuous tracking of the gain variations with the subsequent corrections of the calibration constants. If appropriately designed, it can also help very much for continuous monitoring the EMC and SMD functioning, for the fast and unambiguous detection of the malfunctioning channels and their components.

In this section, the designs and characteristics of all EMC and SMD calibration subsystems are presented along with the task and achievable accuracy for each particular tool.

### IV.1 Requirements

The most stringent requirements to the equalization of signals from the EMC towers come from the lowest-level fast L0-trigger. The well equalized towers are those having equal responses ("electric signals") to the electron-photon hits of equal energy, $E$, or equal transverse energy, $E_T = E \cdot \sin\theta$, etc.[1] The usual EMC contribution to the fast trigger is to select events with a high local and/or global energy deposits[2] above the chosen L0-trigger's threshold(s). Along with the other factors, the "sharpness" of thresholds for this kind of "High-$P_T$" triggers depends on how well the signals from the EMC towers have been equalized. On the other hand, due to the finite EMC resolution which also contributes to the widening of the thresholds, it does not make sense clearly to fight too hard for the tower's equalization much better than the intrinsic EMC energy resolution, $\sigma_E / E$. In the range of interest for L0's $E_T$-thresholds in STAR[3] from ~3-5 to 10 GeV, the expected intrinsic resolution is $\sigma_E / E \approx$ 5-10%. This means that the equalization of the EMC towers to the level of ~3-4% would be sufficient in the $E_T$ - interval of ~3-10 GeV, particularly early in the program.

Acceptable statistical uncertainties of the EMC tower's relative calibration, i.e. for the statistical error of the knowledge of the calibration coefficient for every single tower relative to some "base gain" is, to some extent, equivalent to the "tower's equalization" problem but for the data analysis rather than L0-trigger because the statistical errors of the calibration coefficients will effectively contribute to the "final" EMC energy resolution. The difference is that, while the equalization of electric signals is important in a rather limited energy range of L0-trigger thresholds, the requirements to the relative calibration are relevant to the entire energy interval of interest for STAR from

---

[1] The polar angle $\theta = 2\arctan(e^{-\eta})$.

[2] That is either E or $E_T$ or both.

[3] D. Underwood, STAR Note 180, 1994; B. Hubner, G. D. Westfall, A. M. Vander Molen, STAR Notes 275 and 276, 1996.

~0.5-1 to ~50-60 GeV. At the energies below ~10 GeV, the knowledge of the calibration coefficients at the same statistical uncertainty of ~3-4% as for the signal's equalization would be sufficient. The simulations with GSTAR[4] have shown that, at the energies above 20-30 GeV, the intrinsic EMC energy resolution is almost constant and equal to ~3%. With this resolution, for example, the width (RMS) of $Z^0$-peak, $\Delta M_Z/M_Z$, in $e^+e^-$-decay mode, including its natural width, will be 3.5%. For a twice worse EMC resolution of ~6%, the width of $Z^0$-peak would increase by a factor of about 1.5 to $\Delta M_Z/M_Z$ = 5%. The summary of these considerations is that the requirement for the accuracy of relative calibrations of each single tower of no worse than 3-4% seems to be valid for the entire energy range from ~0.5-1 to ~50-60 GeV. Of course, over time, one can and will do better, but the point to note is that relative calibration coefficients with this level uncertainty will not significantly impact the physics program.

The most restrictive requirements for the absolute EMC calibration in STAR arise from the measurements of the steeply falling with $P_T$ differential cross sections. Fits to the SPS data[5] for inclusive direct-$\gamma$ and $\pi^o$-spectra at $P_T > 10$ GeV/c give the dependence of $d\sigma/dP_T \propto P_T^{-(5-5.5)}$. The ISR measured spectra[6] at lower $P_T$'s from ~4 GeV/c and up fall even more sharply, $\propto P_T^{-(6-8)}$. To measure this kind of differential cross sections with the systematic errors of no more than ~10-20%, the EMC absolute scale in the region of interest has to be known at the accuracy of ~2%.

The requirements on tracking the variation of tower gains over time are directly related to the consideration above. Tracking the variation of the mean gain for the entire EMC or quite large patches[7] has to be done at the accuracy of the absolute energy scale, i.e. no worse than ~2%. The statistical errors for tracking the gain variations for each single tower can be allowed to be large, ~3-4% as for the relative calibration and equalization.

## IV.2 Overview of Calibration Methods

### IV.2.1 EMC

The calibration and monitoring systems and methods for the EMC towers are generally a superset of those for (upgrade) pre-shower and shower maximum detector (SMD). The main goal of EMC calibration is to establish the absolute energy scale of each tower to the precision discussed above. However, a full calibration using physics events in STAR may occur on time scales which are long compared to a physics run. It is

---

[4] GSTAR is the STAR configured version of GEANT.

[5] C. Albajar, et al (UA1), Phys. Lett. **B209** (1988) 385; J. A. Appel, et al (UA2), Phys. Lett. **B176** (1986) 239.

[6] E. Anassontzis, et al, Z. Phys, **C13** (1982) 277.

[7] For example, 40 towers of each single EMC module or $\eta$-ring, consisting of 120 towers.

therefore important to monitor the stability of the entire optical system chain including phototubes on shorter time scales. For example, a scan of the towers with radioactive sources may occur only at construction in conjunction with cosmic ray tests or once per year or less after installation. The radioactive source method calibrates the overall system, scintillator, fiber, and phototube, but it occurs very infrequently. The observation of minimum ionizing particles either while running or between runs, like the radioactive source, tests the whole optical system, but like cosmic rays, it irradiates all tiles simultaneously. The light diodes, on the other hand, which will feed into the cookies on the phototubes via fibers can monitor the phototubes alone for each run. This independence is useful, because the light output of the scintillator is expected to increase by about 5% when the magnetic field is on, the light transmission through fibers could change, etc. This can be monitored by comparing the LED and MIP calibrations.

The following techniques have been found to be effective and cost-effective in similar calorimeters in other experiments. We will use them in STAR EMC:

1) Calibration of a sample of modules in a test beam of electrons and hadrons.
2) Cosmic ray testing and calibration at the time of construction.
3) Penetrating charged particles close to minimum ionizing in the testbeam and online during STAR running
4) LED light flashers (green) for the phototubes. These are capable of establishing the (absolute) PMT gains to a fraction of a percent. (See Bencheikh et al., NIM A315 (1992) 349.)
5) Radioactive sources near shower max depth at the time of cosmic ray testing (module construction)and/or periodically thereafter
6) Conversion electrons
7) 2 body decays
8) Electronics / Charge injection

**IV.2.2 SMD**

The calibration of the shower maximum detector poses different issues. We must find the absolute calibration in known conditions, and then monitor the gas gain with temperature and atmospheric pressure and high voltage variations. We will calibrate the electronics separately. The gas gain must be normalized to electron showers of known energy in the calorimeter with known gas mixture, high voltage, pressure, temperature and magnetic field.

For SMD, the objectives are to establish the energy scale relative the EMC towers, to establish a scale at particular values of atmospheric pressure, HV, etc so that gain can be tracked; and to calibrate the channel to channel variation of the 36k channels caused by different strip to wire capacitances and different transmission lines. Clean cosmic ray signals from the SMD require that the HV (and gain) be increased, so this is not completely adequate for the absolute scale, but will provide the channel to channel gain variation measurement. The EMC methods of test beam, MIPS, conversion electrons, and two body decays provide the rest of the calibration.

## IV.3 Some General Features of our General Philosophy

In the long run the absolute calibration comes from physics events such as J/_ decays, conversion electrons, etc. Electrons are used to tie the EMC calibration of each tower to measurements of magnetic field and track curvature. An abundant source of electrons is from conversions of gammas from _$^{o}$'s in the beam pipe and the SVT. This material constitutes about 5% of a radiation length. The resolution of the calorimeter and the tracking are comparable at about 15 GeV if the vertex is used in fitting the track. Above this energy, the means of the E vs. p distributions can be found very well if a number of events are used.

However for EMC calibration, using these electrons requires a rather long time (on the order of a year) to obtain sufficient statistics and do the required analysis to have each tower calibrated in a sufficiently wide energy range. Therefore several other "indirect" methods will be used to reasonably accurately set of tower gains and obtain the initial calibration constant immediately after a module installation and/or during a few first days or even hours of running RHIC. In the rest of this chapter, we'll concentrate on the description and evaluation these of various "indirect" techniques which will be used in STAR EMC for the tower equalization, calibration, and continuous tracking the gains.

As a general principle, it is very useful to cross-calibrate test beam data, cosmic ray response, radioactive source response, response to minimum ionizing hadrons and LED response, fully, on a few calorimeter modules. This method allows reasonable absolute initial calibration of similar modules with cosmic rays and/or radioactive sources and, most importantly, allows the establishment of the relation of this calibration to those methods which can be more readily applied in beam (MIP, LED). The initial calibration of the entire calorimeter can be made traceable to electron results in the test beam by this approach. Of course, the test beam will also pursue the goal of accumulating valuable information about the electromagnetic shower shape in the SMD and shower sharing between the adjacent EMC towers. This information will then be used in the data analysis for reconstructing the particle hits in the EMC and SMD.

## IV.4 Practical Implementation

The practical implementation of EMC calibration technique will include several steps.

An exposure of several EMC modules to the test beam composed of electrons and other charged particles will serve as a basis for all "indirect" calibration approaches. In the test-beam runs, the ratios of the EMC responses to electron and minimum-ionizing particles, mostly penetrating hadrons, (MIP) hits (*e*/MIP-ratios) will be measured for the towers at various $\eta$ as well as the ratios of signals from particle hits to the DC current from the radioactive source (*e*/RS-ratios). These measurements will be made with PMT gains that have been established using the LED system. After an exposed module is installed in the STAR detector, setting the gains for its tower will be done using the LED system and setting the DC currents from radioactive source to the desirable level. In the following discussion we show that beginning from this initial "calibration", a few days of RHIC running with Au+Au is required to establish the calibration coefficients in every tower to an accuracy of a few % from the measurements of MIP-hits. (see Sec. IV.5.2 for details).

For modules untested in the electron test-beam, the *e*/MIP- and *e*/RS-ratios are expected to be very close to those of the tested ones. Therefore, the procedures described above can also be used to set the tower's gains and to measure the calibration coefficients for these modules as well. The main source of the error of the initial calibration coefficients for untested modules is expected from variations of the relative light output from tile-to-tile in otherwise identical towers. On the base of simulations, the design limit of the light yield variation is set to be no more than $\pm 10\%$ (RMS) on a tile by tile basis. With this requirement and after the tower's equalization, using radioactive source or MIP-hits, the deviation of the calibration coefficients in the individual towers from the mean values is not expected to exceed ~2-4% (RMS) in the entire energy range of interest from ~1 to 50-60 GeV (see Fig.IV.4.1[8]).

To make sure these optical design tolerances are maintained, various quality control procedures have been developed for each step of the manufacturing and assembling the EMC and SMD modules. They are described in details in Sec.II of this document.

After the final assembly, every single module will undergo at least three times, quality assurance tests designed to spot broken Light Collecting and Transport Units (LCTU), i.e. broken tile-fiber assemblies, fibers, and/or fiber connectors. This will be done the first time at the manufacturing site just after the module is built; second time, after it has been shipped to BNL, before the installation; and third time, after the module is installed in STAR. The technique being used for these tests is described in Sec. IV.5.4.

It should be underlined that the identification of the missing LCTU's in the towers is an important issue. One or two missing LCTUs can change the tower's light output from an electron-photon hit by up to ~20-30%, depending on the location of the "missing tiles" within the tower (Fig.IV.4.2). The drop of the light output by itself is actually not a big problem. Using the calibration techniques described above, the tower's "mean" calibration coefficient at any particular energy. However, these corrections don't put the end of the story. Due to the "missing tile(s)", the tower's signal functional dependence on the energy of electron-photon hits becomes essentially "individual" and can significantly differ from the "canonical" EMC's "signal-energy" characteristic. Even after correcting the damaged tower's calibration constant(s) at any single energy or in the energy range, the residual deviation of the tower's sensitivity from the "canonical" one beyond this range can be as high as ~10-20% (Fig.IV.2.2). The worst things is that these deviations, even their sign, are essentially unpredictable without an exact knowledge of the position of the missing LCTU in the stack. For a known position of the damaged LCTU in the stack and after the tower "equalization", simulations[9] or, even better,

---

[8] See for details: A. A. Derevschikov and O. D. Tsai, SN216 (1995).

[9] All currently available simulation tools (GEANT, EGS, …) quite satisfactory describe the longitudinal development of electron-photon showers which is virtually the only shower's property relevant to correcting the "missing-tile effect".

experimental data on the effect of "missing tiles"[10] can be used to reduce down the uncertainty of the signal-energy dependence to the acceptable ~3-4% level.

At the manufacturing site, each module will simultaneously be exposed to cosmic rays and radioactive source. The ratios of the cosmic ray signals and the DC currents from the radioactive source (CR/RS-ratios) will be measured for each tower. These measurements will provide some additional information which then can be used to introduce individual module corrections to the calibration constants for the radioactive source calibrations. For a day, few thousands of cosmic rays, crossing all 21 tiles of a single tower, can be accumulated. The detailed description of the setup for cosmic ray measurements is given in Sec. IV.5.5 of this documents.

During the RHIC beam runs, the tracking the variation of the EMC channel's gains on the daily and hourly basis will be performed using MIP-hits in the EMC from the colliding beams. The continuous tracking the stability of PMTs and the electric parts of the chains will be accomplished using green LEDs and charge injection technique.

## IV.5 Calibration methods and system's designs and integration

### IV.5.1 Test Beam

For the first Module, the test beam will provide absolute calibration of towers within 3% from 0.5 to 8 GeV without relying on other STAR detectors. This can later be transferred to other EMC modules. Calibration is be done in the test beam, and then carried to other modules with Sources and Cosmic rays and minimum ionizing particle signals in order to establish absolute scale. The scale of the individual module calibrated in the test beam can also be carried by LED.

The test beam can establish the correlation between SMD and EMC signals vs. energy and establish that both tower and SMD maximum signals are within the range of the electronics (both high and low end).

### IV.5.2 Penetrating Charged Particles (MIP)

Many charged hadrons (along with small admixtures of electrons and muons) will be produced in every collision at RHIC. In the central region covered by the STAR Barrel EMC (BEMC), these are mostly pions. When striking the BEMC, a significant fraction (~30-40%) of high energy charged hadrons do not deposit a large amount of energy via nuclear interactions, instead depositing ~20-25 MeV of energy in the calorimeter's 21 scintillator layers due largely to electromagnetic ionization. In this document, we will loosely call these hadrons (and muons too) as "Minimum Ionizing Particles" (MIP) producing "MIP-hits" in the BEMC towers.

---

[10] For the "frozen" EMC tower's design, it would be very desirable (while not absolutely necessary) to measure at the external beam the "signal-energy" dependencies for each tower in the entire energy range of interest in STAR from ~0.5 to ~50-60 GeV. This experimental study with one or two modules needs to be done just once for the entire STAR EMC's life-time. This experiment would also be the best time for measuring the "missing-tile effect" along with its $\eta$-dependence.

For the relativistic particles, the position of "MIP-peak" is nearly independent of momentum and particle species. This, along with the high yield of charged hadrons, makes it attractive to explore the feasibility of using high energy MIPs for the equalization, calibration, and continuous tracking the stability of the BEMC tower's gains.

The calibration scheme using MIP-hits includes two stages. At the first stage, a sample of BEMC modules is exposed to the external beam, for example, at AGS. The test beam at AGS is a mixture of all kind negative particles of a chosen momentum, selected in the range from 0.3-0.5 to 7-8 GeV/c. The composition of the beam are mainly $\pi$ mesons and other hadrons with some fraction of electrons and muons. Therefore the ratios of each tower's responses to electron's and MIP's hits (*e*/MIP-ratios) of various momenta are measured simultaneously[11]. This makes the measurements of these ratios completely independent of the PMT's and QDC's gains, possible attenuation and distortion of signals in cables, delay lines, etc., i.e. in the equipment which might be necessary for the test run but won't be present or will be different in the STAR detector, and vice versa.

At the second stage, after the modules have been installed in their places in the BEMC, and the RHIC accelerator is producing collisions, the samples of MIP-hits of the particle composition and momenta as close as possible to those in the test beam are accumulated for each tower, and the positions of MIP-peaks are measured. This step essentially completes the procedure of transferring beam-test results to STAR. For those towers exposed to the test beam, their response to electron hits[12] can immediately be predicted, using the known *e*/MIP-ratios that have been measured at the test-beam stage. For non-tested modules, these ratios are expected to be close to those of the tested ones.

It's obvious, of course, that the compositions of MIPs in the test beam and in STAR at RHIC can never be exactly the same and quite often won't be exactly known. To accumulate a sufficient statistics for a reasonably short time, the momentum range of the selected MIPs in STAR cannot be made as narrow as it was in the test beam. Moreover, the STAR 's 5 kGs strong magnetic field may noticeably change the *e*/MIP-ratios compared to those measured with the external beam. These are the main sources of the systematic errors, which set the limits to the achievable accuracy for the absolute calibrations of the STAR BEMC, using MIP-hits.

The expected characteristics of *pp*- and heavy-ion events at RHIC are the basis for evaluating the systematic errors. It's clear that the low-$P_T$ charged particles are useless because their deflection in the STAR's magnetic field causes them to enter the BEMC at large angles. Only a small fraction of these particles pass through all 21 scintillator tiles of a single tower. On the other hand, if a chosen $P_T$-threshold were too

---

[11] Or almost simultaneously for electrons and MIPs of different momenta.

[12] … of the momenta actually used in the test-beam run …

high, the useful event rate would be too low due to the steep drop of the particle yield as $P_T$ increases. The simple estimates suggest MIPs of $P_T$'s just above ~ 1 GeV/c as the best compromise between yield and utility. In the magnetic field of 5 kGs, the trajectories of no fewer than ~50-60% of directly produced[13] charged particles with $P_T \geq 1$ GeV/c will pass through all 21 tiles of a single BEMC tower. For a particle of this transverse momentum, the deflection in the magnetic field increases its path within a tower by no more than ~1-1.5%. As an additional benefit, particles of this momentum are available at the AGS test-beam.

In *pp* collisions, the CTB can select events with at least one charged particle within its acceptance[14]. For Au-Au collisions we consider two sets of data: all events without any additional selection criteria, and low multiplicity events with $1 < N_{CTB} < 100$. In every single event, the potential "target-towers" for MIP calibrations are those, struck by *at least one* "high-$P_T$" charged particle of $P_T > 1$ GeV/c, which are called in this section "*h*-towers", or their even "cleaner" subset of "*1h*-towers", which are struck by *one and only one* charged particle[15] of *any* $P_T$. These towers can easily be pointed out in every single event, using the rich tracking capabilities of the STAR detector. The mean numbers of "*h*-" and "*1h*-towers" per event are each of order 1.

A comprehensive study of the BEMC absolute calibration based on MIP-hits has been undertaken, using simulations and available experimental data. The various systematic shifts of MIP-peak positions due to variations of MIP's composition, momentum, and admixture of neutrals have been estimated as well as the effects due to STAR's magnetic field. GEANT simulated distributions of energy deposits from 1, 1.5, and 2 GeV/c pions in the BEMC[16] have been studied and conpared with the experimental distributions obtained from exposing the STAR BEMC prototype to the AGS test-beam. From both the simulations as well as the experimental data it follows that the variation of MIP-peak's position[17] within 1-2 GeV/c momentum range is just about $\pm$ (0.5-1.5)%.

The MIP-peaks in *1h*-towers with one charged particle at $P_T > 1$ GeV/c have also been simulated for the STAR-at-RHIC. According to these simulations, the shifts of MIP-peak's positions in STAR-at-RHIC won't exceed ~1.5-2% compared to 1-2 GeV/c pions used in the test beam. With the STAR magnetic field "on", the most probable energy deposits by MIPs increase by only ~1-1.5% due to the change in the energy spectrum. Additionally, in the presence of the magnetic field there is a geometric effect

---

[13] … and noninteracting strongly in the BEMC!

[14] Only charged particles with $P_T > 0.15$ GeV/c are counted because lower $P_T$'s will effectively be wiped out by the STAR magnetic field and won't reach the CTB and BEMC (see Fig. IV.4.2.1).

[15] … which would actually be the "high-$P_T$" one.

[16] With no magnetic field.

[17] Parameter "P2". For the sake of simplicity, the "Gaussian + polynomial" fits have been used here. Fits with some other resonable functions provided the similar results.

coming from the curvature of the particle tracks. This effect also produces a shift on the order of a few percent. Due to purely geometric nature of this effect, it can also easily be accounted and corrections introduced.

From the consideration above, calibrations using minimum ionizing particles seems to be a good candidate to calibrate the STAR BEMC to systematic uncertainties of order ~2-3%. To reach comparable or lower statistical errors, the sufficient number of useful hits from noninteracting charged high-$P_T$ particles needs to be accumulated in each tower. The width of MIP-peaks[18] not accounting the photoelectron statistics, is about ~10%. For the mean light yield from a single BEMC tiles at the lowest design limit of 2 phe/MIP, the estimated width of the MIP-peak would be ~17-20%.

The following table gives the running time required to achieve the indicated statistical accuracy on the MIP peak position.

| | 20% | 10% | 5% | 2% | 1% |
|---|---|---|---|---|---|
| pp | 23 min | 1.5 hr | 6 hr | 38 hr | 6.3 day |
| AuAu Peripheral | 5 min | 20 min | 1.3 hr | 8.3 hr | 2.5 day |
| AuAu Min Bias | 1 min | 3 min | 12 min | 1.2 hr | 5 hr |

To minimize a time for accumulation this number of hits, the L3-trigger tracking has to be exploited to select events with high-$P_T$ tracks pointing out to the BEMC's towers, and to reconstruct the parameters of these tracks. Otherwise, the raw data from the entire TPC needs to be recorded, and the event rate would be unacceptably low. By design, the input L3 event rate in STAR can be as high as 100 Hz. It's worth noting that the above estimates are for the time that required to get every BEMC tower calibrated. After the towers are "equalized" to a few percents ,however, the tracking of the mean gain variations for a patch, consisting of $N_{tw}$ towers, will take by a factor of $N_{tw}$ less time compared to what was necessary to calibrate every single tower with the same statistical uncertainties.

To summarize, the above study has shown that, using MIP-hits, the equalization and transfer of the absolute scale from the test beam calibrations can be done to an accuracy $\sim^{\pm}$ 1-1.5% in a reasonable amount of time[19] for the entire EMC. MIP-hits are also an effective tool for continuously tracking the variations of the EMC tower's gains to the level of at least $\sim^{\pm}$ 1-1.5% a day, virtually without interference to the running in parallel STAR's main physics program. This method does not rely on simulations for anything other than geometric and some other small corrections, and also estimates of systematic errors: it directly transfers measured test beam responses to operations at RHIC.

---

[18] Ratios "P3/P2" of the "Gaussian + polynomial" fits.

[19] In heavy-ion collisions.

Further studies, not reported here, show that to achieve the accuracy level of the absolute calibrations above, it is not necessary to strictly control and limit the momentum range of useful MIP-hits, although the rich STAR's tracking capabilities allow us to do this. The limitation of this method (or any other indirect[20] method) is due to the construction tolerances of the calorimeter. Individual tower variations of light yield from tile-to-tile introduce nonliniarities in the energy responses due to the development of mean shower depth with energy. These will always limit our ability to apply the test-beam calibration of a few modules over a restricted energy range to the nontested ones to about ± 2%[21]. MIP calibration allows us to reach this theoretical limit in less than one day of RHIC, running heavy-ion collisions.

### IV.5.3 LED

A system of green LED's can provide a precise (fraction of a percent) calibration of the photomultiplier gain . (See Bencheikh et al., NIM A315 (1992) 349.)

An LED box with 15 LEDs , each driving 7 fibers, will be mounted in each PMT box. This will provide signals to the 80 PMT tubes (and 5 pre-shower tubes if upgraded), with cross correlations to be used in case an LED fails. LED signals (with temperature corrections to the LEDs done offline) can be measured hourly.

To take an LED event, EMC must request a calibration trigger from STAR, and then flash the appropriate LED in synch with the event that the trigger issues to EMC. This will depend upon the STAR trigger issuing a calibration trigger a fixed number of rhic clocks after the request is made or else sending some kind of pre-trigger signal. The LED signal will be at about 3 GeV in each phototube (within a factor of 2).

### IV.5.4 light reflection technique for testing fibers

An important requirement of the calibration techniques which rely on light from the scintillators is that the optical pathway from each scintillator layer to the PMT be functioning. In the presence of broken fibers, different calibration techniques can produce vastly different results. Consequently, we here discuss the diagnostic techniques used to study the condition of the entire optical pathway for each tower. These same techniques, are used during calorimeter construction as quality assurance measures.

The principle of testing the fibers is simple, namely to shine a light into the fiber and measure the amplitude and timing of the reflection from the aluminization at the far end (which is in the tile). This is similar to techniques used for testing telephone lines.

To do this in practice, we need to handle very large numbers of fibers in a short time with simple and rugged equipment. There are two mass connectors on each fiber path, one on the side of the module, and one in the side of the phototube box. The testing

---

[20] "Direct" methods are those, using for calibrations electron and photon hits themselves.

[21] To make it clear, this limit has no any relations to the tracking the stability.

device will have 10 independent channels to test all 10 fibers in a connector simultaneously. To shine light down the same path over which the reflection is measured, a directional coupler is needed. Unfortunately, the directional couplers made of two fibers used for fiber optic gyroscopes, etc, do not work with large, .8 to 1 mm fibers. We therefor need to use half silvered mirrors. Some experiment will be needed to determine the optimum lens system to obtain the best measurements with LED or laser.

The timing will help to isolate the part of the reflection from the end of the fiber. There are other reflections of about 7% of the light at each connection interface. The timing needed is to distinguish a 35 ns round trip from a 45 ns round trip.

The measurements will be analyzed on a PC and the results will go into a data base for future reference.

**IV.5.5 Cosmic ray measurements**

The cosmic ray test stand at RHIC ( and the assembly sites) provides a calibration of each module before installation and in particular a way to set the High Voltages which is separate from the individual phototube calibrations done on the bench. This is essential for operation of the trigger. It also provides a check of performance after shipping. The testing will be done in a small building near the STAR assembly building. This building has floor space and roll up doors for unloading modules.

The test at BNL will take only a few days per module, including connecting temporary fiber assemblies and electronics and light-tightening. After allowing for fiducial cuts, angular cuts, and momentum hardening with absorbers, we expect to have 50 events per tower per day in a module of 40 towers. With 30% resolution on signals from charged tracks which are slightly more than minimum ionizing, this will give a 4% calibration one day.

The cosmic ray test stand set-up will be assembled primarily of existing parts. Large area drift chambers with their associated electronics are available from Argonne. Trigger scintillation counters are available which would cover the module on bottom and top. Data acquisition will be through CAMAC with an inexpensive controller interfaced directly to a PC. Triggered electronics, in contrast to the clocked electronics to be used in RHIC running, will be more efficient for the cosmic ray testing.

Cross calibration with radioactive source will be done while the module is in the cosmic ray test stand. The cosmic rays sample all the scintillator layers equally, while the source deposits energy strongly in the adjacent layers near layer 7, and about a factor of 2 less in each succeeding layer away. Any discrepancy between the two calibrations would indicate a non-uniformity in depth response within a tower. The source runs must be made with separate, dedicated electronics, since an integration time of 10 ms is needed to measure the DC current induced by the source.

There are three sets of data for each module which must be kept in a data base and cross-referenced. These are the phototube gain data (LED), the cosmic ray calibration

data, and the source data. These will eventually be used with both the test beam data on one module, and the calibration in place in STAR from many physics processes.

Cosmic ray tests at the assembly sites will additionally study the response of individual layers in the towers. Special optical connectors will be used to break out the output light from individual layers and send it to separate photo tubes. This test will be documented and serves as the principal quality assurance measure to verify the required layer-to-layer uniformity is being met in each tower in the production modules.

### IV.5.6 Source

The distribution of energy in the layers of scintillator in a lead/scintillator sampling calorimeter can be crudely approximated by the energy distributed by a radioactive source near the shower maximum for EM showers. This method makes the source particularly useful for calibration in that the weighting given to each layer resembles the weighting it has in measuring physical events.

The individual strengths of a radioactive source can be measured adequately, to a percent or two, with simple means. This measurement allows absolute calibration of all modules when only a few have been calibrated in a test beam assuming the fiber systems are in uniformly good condition.

The source system is primarily intended for use off-line in conjunction with test beam studies and/or cosmic ray calibrations. A simple mechanical system pushes the source through thin stainless steel tubes imbeded at 7 radiation lengths in the module. The source motion is continuous and logged by a PC which also integrates the DC current from each of the PMT's. If needed, the source system can be mounted on the module while it is installed in STAR.

Error in the source calibration may come from:

- the dark current in the phototubes. We expect roughly 400 na from the source and roughly 2 na from the dark current, with some tubes having more dark current. (We have measured a factor of 4 increase in dark current in raising the phototube temperature from 23 deg C to 33 deg C. )
- the range of gammas from $^{60}$Co has tails larger than a tower size. The peak seen will depend slightly on the width of the tower and because the towers are exactly projective, they have different linear dimensions. We can both sum and compare adjacent towers to control this effect.
- position of the source in the source tube with respect to the scintillator and lead changes the solid angle and intermediate absorber slightly. We use a small source and a small tube to minimize this effect (_ 1 mm diameter).

Estimate of Source Strength for STAR EMC Calibration

$^{60}$Co has two gamma rays per decay, one about 1.17 MeV and one about 1.33 MeV. The absorption length in Pb and scintillator are both about 10 grams/cm$^2$ at about 1 MeV. This means we can calculate the energy deposition just from the mass. Also, it gives about 1/2 of the gammas absorbed per Pb-Scint pair. So the attenuation goes like 1/2, 1/4, 1/8, 1/16 in calorimeter layers. Assuming a PMT gain of $2x10^5$ we estimate that a 1 mCi source will produce approximately 400 nA DC current which is readily measurable at the 1% or better range. PMT dark currents are expected to be approximately 2 nA but could easily vary from near zero to 10 nA from tube to tube. We will measure the individual tube dark currents before and after source runs to permit subtraction.

### IV.5.7 Conversion Electrons

Electrons are used to tie the EMC calibration of each tower to measurements of magnetic field and track curvature. An abundant source of electrons is conversions of gammas from _$^{o}$'s in the beam pipe and the SVT. This material constitutes about 5% of a radiation length. The resolution of the calorimeter and the tracking are comparable at about 15 GeV if the vertex is used in fitting the track. The means of the E versus p distributions can be found very well at higher energies if a number of events are used in the analysis. When using electrons from either physics at the vertex or conversions of gammas, we depend on the TPC plus Magnet plus vertex calibrations to do our energy calibration.

We can also use conversion electrons to set the relative scale between calorimeter and shower max. and between calorimeter and Pre-shower.

### IV.5.8 Two Body Decays

Very good calibrations of both the EMC and tracking detectors can be done with $e^+$ $e^-$ decays of particles of definite mass such as J/$\psi$ and $Z^o$. The EMC can also be calibrated with 2 photon decays such as $\pi^o$ or $\eta$. The energy range for these 2 photon calibrations is restricted to be low enough that the spatial separation measurement in the SMD can be made with the precision of the desired energy measurement.

### IV.5.9 Electronics and Charge Injection

Electronics cards for PMT, SMD, pre-Shower, and trigger shall be calibrated electronically, independent of the detector, so that they are interchangeable. If the pedestals and gains and linearities are not sufficiently uniform on all cards, then a record will be kept that travels with each card. We want to make it easy to exchange cards because we do not want to lose calibration for large numbers of EMC channels when part of one card with many channels fails.

Different cards will be used in both the test beam and cosmic ray calibration set-ups than in the calorimeter in place, so the scales must be measured and documented.

Some aspects of electronic calibration are:

1) Charge injection on PMT cards.

2) Voltage signal on SMD cards, and charge injection of preamplifiers.

**IV.6 EMC calibration data sets**

We define the EMC calibration data sets for use in the STAR data stream and storage. Simple ASCII files of numbers for the following are sufficient. We should include text headers and comments inside these files. Note also that there may be multiple historical versions of the data sets to be saved for cross checking, to see how the system changes in time. There is extensive documentation in STAR concerning the read-in times required for EMC calibration, and the amount of computer analysis required.

| INPUT CALIBRATION DATA SETS | APPLICATION CALIBRATION DATA SETS |
|---|---|
| PMT | PMT data collector ped. sub. |
| | Trig LVL 0 pedestals and gain |
| cosmic ray<br>( 1 gain + 1 ped) * (4800 + 720) | SMD data collector ped. sub. |
| source<br>(1gain+1ped+1dark-c.) *( + )<br>(multiple sets) | PMT ped, gain LVL 3 |
| LED<br>(1 gain + 1 ped) * (4800 + 720)<br>(multiple sets) | SMD ped, gain LVL 3 |
| pion/muon no TPC<br>(1 gain + 1 ped) * (4800 + 720)<br>(multiple sets) | PMT offline |
| pion/muon with TPC<br>(1 gain + 1 ped) * (4800 + 720)<br>(multiple sets) | SMD offline |
| charge injection - card<br>(1 gain + 1 ped) * (4800 + 720) | PRE-SHR LVL 3 |
| test beam<br>(1 gain + 1 ped) * (4800 + 720) | PRE-SHR offline |
| pi-0 recon mass<br>(1 gain + 1 ped) * (4800 + 720) | Pre-SHR collector ped. sub. |
| eta recon mass<br>(1 gain + 1 ped) * (4800 + 720) | |
| J/psi-recon mass<br>(1 gain + 1 ped) * (4800 + 720) | |
| electron mom in TPC<br>(1 gain + 1 ped) * (4800 + 720) | |

| SMD | |
|---|---|
| charge injection-card | |
| (1 gain +1 ped)*(30k + 10k) | |
| test beam | |
| (1 gain +1 ped)*(30k + 10k) | |
| pre-amp bench calib | |
| (1 gain )*(30k + 10k) | |
| capacitances? | |
| pi-0 recon mass | |
| (1 gain + 1 ped) * (30k + 10k) | |
| eta recon mass | |
| (1 gain + 1 ped) * (30k + 10k) | |
| J/psi-recon mass | |
| (1 gain + 1 ped) * (30k + 10k) | |
| electron mom in TPC | |
| (1 gain + 1 ped) * (30k + 10k) | |
| | |
| | |
| PRE-SHOWER | |
| cosmic | |
| ( 1 gain + 1 ped)*(4800+720) | |
| led | |
| ( 1 gain + 1 ped)*(4800+720) | |
| pion/muon no TPC | |
| ( 1 gain + 1 ped)*(4800+720) | |
| pion/muon with TPC | |
| ( 1 gain + 1 ped)*(4800+720) | |
| charge injection-card | |
| ( 1 gain + 1 ped)*(4800+720) | |
| test beam | |
| ( 1 gain + 1 ped)*(4800+720) | |
| pi-0 recon mass (in EMC twr) | |
| (1 gain + 1 ped) * (4800 + 720) | |
| eta recon mass (in EMC twr.) | |
| (1 gain + 1 ped) * (4800 + 720) | |
| J/psi-recon mass (in EMC twr.) | |
| (1 gain + 1 ped) * (4800 + 720) | |
| electron mom in TPC | |
| (1 gain + 1 ped) * (4800 + 720) | |
| | |
| OLD Application Data Sets to be adjusted | |

| |
|---|
| 3 sets (PMT,SMD,PRE)<br>each in 3 formats |

## VI. Conventional Systems

Conventional systems cover a broad range of support systems for the operation of the EMC. These systems are:

- low voltage DC power for the front end electronics and associated transmission lines
- Cooling systems for all electronics (i.e., power supplies, crates, FEE, SMD etc.)
- HV for SMD and HV transmission and distribution lines
- Gas system for SMD

A series of general requirements are imposed on all of the above systems by:

- BNL and RHIC safety requirements
- STAR Detector constraints (e.g., integration issues, grounding rules, STAR slow control and monitoring requirement etc.)

In this section we will define only those requirements specific to EMC subsystems.

### VI.1.1 Low voltage DC power for FEE

Due to space constraints it is not possible to have self powered crates on the iron backlegs where the FEE crates will be mounted. Therefore, DC power will be supplied from power supplies located in the electronics racks.

Table VI.1 gives the total power requirement for the STAR EMC.

| System | power requirement | Total power | Voltages |
|---|---|---|---|
| EMC FEE crates | 60 crates@900 watts/crate | 54 kW | ±5 |
| SMD on board FEE | 120 modules @30 watt/mod. | 3.6 kW | ±5 |
| CW PMT bases | 4800 bases @ 0.25 watt/base | 1.2 kW | ±12 |
| calibration sys. | LED, $^{60}$Co source ≈ 1 kW | 1 kW | ±12 |
| SMD gas system | 10 watt@120 mod. (elec. valves) | 1.2 kW | +24 |
| cooling system | DC fan trays (estimated) | 2.0 kW | +24 |
| misc. | slow control / monitoring system | 1.0 kW | ±12 |
| reserves | about 20% of total at each voltage | 10 kW | ±5, ±12 |

Table VI.1. DC power requirements of various EMC sub-systems.

Power supply outputs shall be regulated over time and temperature, and hardware current limiting will be implemented. Conducted noise due to power supplies will not contribute to the degradation of FEE operation.

The voltages, currents, and temperatures for all DC power supplies shall be monitored, and power supplies shall be remotely controlled via STAR slow controls. All power supplies in the racks shall be

cooled using the standard STAR water chilled heat exchanger/fan systems. Due to large currents, voltage losses in the transmission lines are expected to be of the order of 1 volt, therefore all electronics load will have adequate on board filtering and voltage regulation. Furthermore, they will have built in fault protection to protect the circuitry against inductive "kicks".

### VI.1.2 Cooling for the FEE Electronics

Due to the large amount of power dissipation of the FEE it is important to cool these systems. The FEE modules located on the crates installed on the magnet backlegs will be cooled by forced air. The SMD FEE shall be cooled by forced air as well. In order to maintain the gain stability and reduce dark current of the PMTs the temperature in the PMT boxes shall be monitored and a water chilled closed cooling system will be used to maintain the PMT temperature changes to less than 2 degrees C.

All external pipes carrying gas/air to the SMD modules shall be non conductive (i.e. copper pipes will pick up the magnet power supply noise and may couple it to the SMD FEE electronics).

### VI.1.3 HV Power for SMD

HV power shall be supplied with low noise power supplies to avoid injection of conducted HF noise into FEE. All supplies shall be remotely controlled via STAR slow controls. Adequate capacitive filtering will be implemented as close to the SMD modules as possible to reduce voltage fluctuations due to transient and avoiding gain fluctuations. The voltages, currents, and temperatures for all HV power supplies shall be monitored, and power supplies shall be remotely controlled via STAR slow controls. The HV transmission lines shall not cause ground loops.

### VI.1.4 SMD Gas System

The SMD gas system shall have a two function.

1. it will be used to supply nitrogen gas to 120 SMD modules for flushing the system, and
2. as well as supplying the $Ar/CO_2$ premixed mixture for normal operation.

The gas system will be un-interruptable, and have enough gas capacity to run for several weeks without the need to replace the gas cylinders. The gas system shall be clean. Oxygen and water vapor impurities shall remain below 100 ppm. The total gas flow rate, and flow through individual SMD modules shall be monitored. The SMD gas system shall not supply a current return path for STAR detector (i.e., main supply line to the Wide Angle hall will stop short of the STAR detector to avoid appreciable capacitive coupling, and the connection to STAR shall be via plastic nonflammable/nonconducting pipes).

## VI.2 Discussion of Systems

The Cooling of PMT boxes has been discussed in Chapter V therefore it will not be discussed here.

### VI.2.1 Low Voltage DC Power Supplies and Distribution Lines

The choice of having DC supplies at the racks is dictated by: 1) lack of adequate space on the backlegs, 2) the fact that AC power is not available on the detector (to avoid ground loop problems), and 3) the fact that due to presence of magnetic fields it is expected that the magnetic components of AC-DC converters supply may saturate.

Two different schemes have been considered. From an economic point of view it is more attractive to chose a few high-density power supplies (i.e., 10 kW or even higher) to power several crates. While it is functionally better to decouple the power transmission lines to avoid complex, load dependent problems (which could render the system less reliable and unpredictable), it would be possible to carefully design a

power grid to avoid most of these problems. In what follows we will describe one scheme, which utilizes individual, isolated power supplies to power each FEE crate. The advantage of this topology is that it is less susceptible to noise.

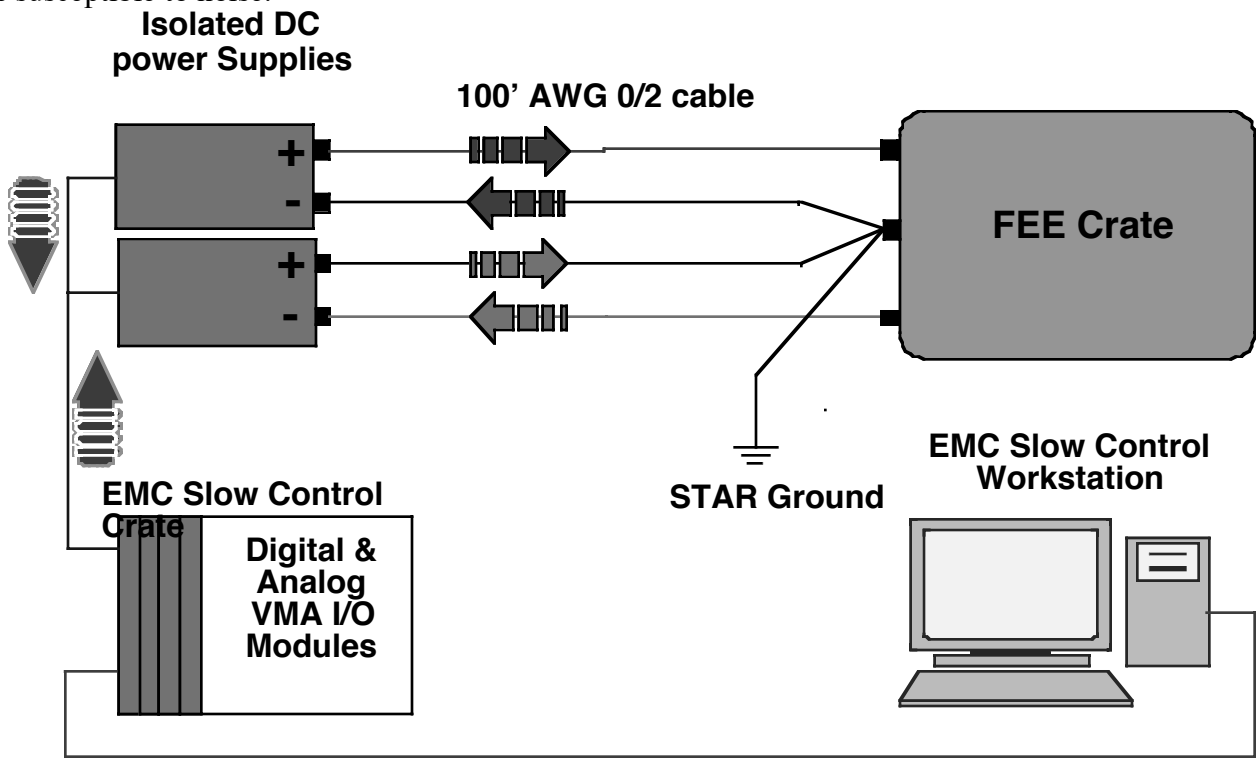


Figure VI.1. A power supply system for FEE crates.

Figure VI.1 shows a conceptual design of a low voltage DC power supply system for the FEE crates. There will be 60 such supply systems arranged in small dedicated crates housed in the EMC racks. Due to the long power transmission lines and large currents involved a large power loss is expected in the transmission lines. For example it is estimated that each FEE crate will dissipate about 900 watts of ±5 DC power. Therefore, the total DC current is 900 watts/5 volts= 180 amps. If we further assume that 125 A of this is in + current, and use AWG 2/0 wire (∅ = 0.3648" resistance/1000' = 0.08021 @ 20°C)[1] and final operating temperature of 40°C then the resistance for a 100' cable at 40°C is given by:

$$R(T) = R_{20}(1 + \alpha_{20}(T - 20))$$

For hard drawn copper $\alpha_{20}$=0.00393/°C, and $R_{20}$ (100') = 0.008021 Ω, $R$(40°C) = 0.00865 Ω. This gives a voltage drop of ΔV=1.1 Volts/conductor. Allowing for 2 volt drop for linear[2] regulators at the crates, and 2.2 volt drop in the transmission lines one requires power supply voltage of 9.2 volts.

The power dissipation per conductor will be 135 watts distributed over 100'. The total heat dissipated by DC power transmission conductors for FEE crates 16.2 kW. This will be handled by the

[1] "Reference Data For Engineers: Radio, Electronics, Computer, and Communications", 8th ed., editor M. E. Van Valkenburg, SAMS, prentice Hall Computer Publishing.

[2] switching regulators are avoided due to possible saturation of their magnetic components in the stray magnetic field.

main air conditioning of the wide angle hall. Assuming 80% efficiency for the power supplies, one obtains heat dissipation of 286 watts/positive DC supply or a total of 17.2 kW.

For the negative DC supply if we chose AWG 2 wire (∅ = 0.2576" resistance/1000' = 0.1625 @ 20°C)[3], one obtains for a 100' cable at 40°C a resistance of 0.0176 Ω. This gives a voltage drop of 1.14 volts. Again allowing for 2 volt drop in the regulators and 2.3 volts in the transmission lines one needs a power supply output of 9.3 volts. The total power dissipation due to -DC power transmission lines is 8.9 kW. The total negative DC power supply dissipation (using the assumptions given for + DC power), is 9 kW.

In addition to the FEE in the crates, the SMD modules will require 30 watts/module in ±5 volts. Due to the large number of SMD modules it is more prudent to use single power supply to power multiple modules. A SMD conventional system distribution box will handle filtering/regulation of DC power on the iron backleg, and transmission of regulated power to the module. The details of this are being worked out at this time.

The power for the CW bases will be derived from ±12 volt DC supplies. The total power is estimated to be 1.2 kW for 4800 PMTs or 4.8 kW if a zener is to be employed between the photocathode and the first dynode stages. If we take the 4800 as an upper limit this gives 80 watts per PMT box (i.e., 60 PMT bases/box). This is equivalent to 6.7 A that will be bussed inside the PMT boxes. The details of power buss and its integration are being designed. The heat deposited by the PMT bases as well as the LED drivers and the cooling fans located inside the boxes will be removed by a water-chilled heat exchanger. This was discussed to some extent in section V.4. Further work on the integration issues on this matter is pending.

### VI.2.2 Cooling for FEE Electronics

The FEE electronics housed in the crates on the backlegs will be cooled with fan trays. This is a fairly large heat load that ordinarily will have to be handled by dedicated closed system water chilled heat exchangers. However, due to lack of space this can not be done. Therefore the heat load will have to be handled by the WAH A/C system.

The SMD electronics will be located inside the STAR magnet. In order to cool it pressurized air will be pumped into the SMD electronics air-cooled heat exchangers via plastic hoses. The hot air will be removed via outlet hoses and vented into the WAH.

### VI.2.3 HV Power for SMD

The HV for SMD modules will be supplied with 6 low noise BERTAN power supplies. These power supplies will be mounted in the EMC racks, and will controlled and monitored via EMC slow controls. Filtering and distribution of the HV to various module will be done by 60 (2 per backleg each located on the end of the detector) SMD conventional systems boxes installed on the iron backleg. Some details of the design of these "Utility" boxes will be discussed in the next section.

### VI.2.3 The SMD Gas System

Some details of gas system and the required gasses and their flow rates have been given in the previous chapters. In this section we will only present some details of the gas manifold, and the distribution system.

---

[3] "Reference Data For Engineers: Radio, Electronics, Computer, and Communications", 8th ed., editor M. E. Van Valkenburg, SAMS, prentice Hall Computer Publishing.

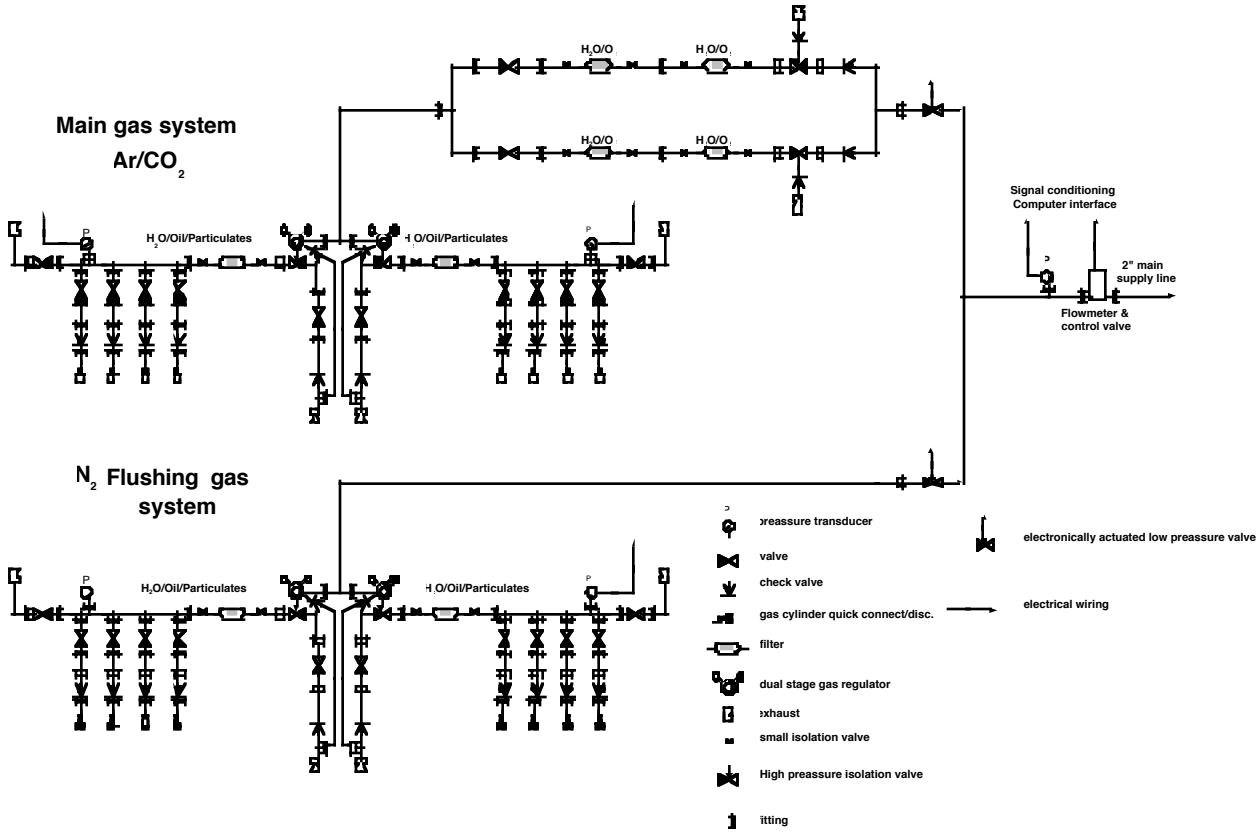


Figure VI.2. The gas supply manifold.

The SMD gas system may be broken down into three parts:

- The gas supply manifold
- The gas distribution system
- The slow control system to control and monitor the gas system.

Figure VI.2 is schematic of a preliminary design for the gas supply manifold. As seen in this figure the manifold consists of two independent gas systems, namely a premixed $Ar/CO_2$ un-interruptable manifold and a $N_2$ flushing gas manifold. Only one of these gas manifolds may be connected to the main supply line at a given time. The rough filtering section is designed to remove oil and dust particles while a second level of filtering will remove the remaining water vapor and oxygen gasses. The pressure and flow rates will be monitored and controlled at all times. Both the gas supply section and the filtering section are designed such that one may replace cylinders and filters without interrupting the main gas flow, or injecting impurities into the main system.

The gas will be supplied to the detector via a 2" copper pipe. This line will be split into two 1" high-pressure plastic hoses that will distribute the gas to each end of the magnet. At that point each 1" diameter pipe will be connected to the inlet port of one of the SMD "utility" boxes. Each "utility" box consists of an inlet and outlet. These boxes will be daisy chained by connecting the outlet port of one box to the inlet of the next via flexible plastic tubing. The pressure drop between the first box and the last will be less a fraction of psi due to low flow rates in the SMD. The advantage of this system is its flexibility and expandability. Internally each box has several functions. As mentioned earlier it will be used to distribute LV, HV, pressurized cooling air for SMD FEE cooling and finally the distribution of the gas to

the SMD and monitoring of flow rate out of the modules. Figure VI.3 shows some of the details of the utility box and its "daisy chained" arrangement at one end of STAR magnet iron backlegs.

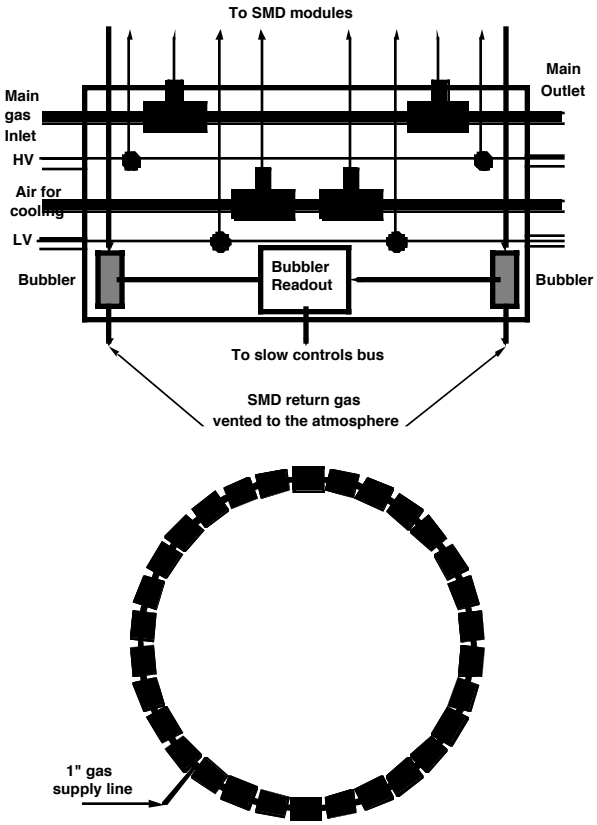


Figure VI.3. Top: conceptual design of the SMD utility box, Bottom: arrangement of 30 utility boxes at one end of the detector.

The third major part of the SMD gas system is the slow control and monitoring of the system. As mentioned earlier the gas pressure, and flow rate will be monitored for the main supply line. In addition as seen in figure VI.3, the outlet gas from each module will be channeled through a bubbler where, by use of a photocell, the bubbling rate will be monitored via the slow control bus.

In order to operate the system in flushing mode (i.e., use nitrogen to flush air and water vapor from the SMD), one will need to use higher flow rates. This may be accomplished by either: 1) keeping the "utility" box outlet (to SMD) orifice the same and increase the gas pressure, or 2) use an electrically controlled solenoid valve with two outlets with two different orifices to switch from higher flow rates to lower ones.

## VII EMC Front End Electronics

### VII.1 Overview

The STAR barrel electromagnetic calorimeter (EMC) is a lead-scintillator sampling calorimeter located inside the STAR magnet as shown schematically in Fig. VII.1. The barrel calorimeter covers $-1 \le \eta \le 1$ and $0 \le \phi \le 2\pi$. The barrel has 4800 towers giving a segmentation of $(\Delta\eta, \Delta\phi) = (0.05, 0.05)$.

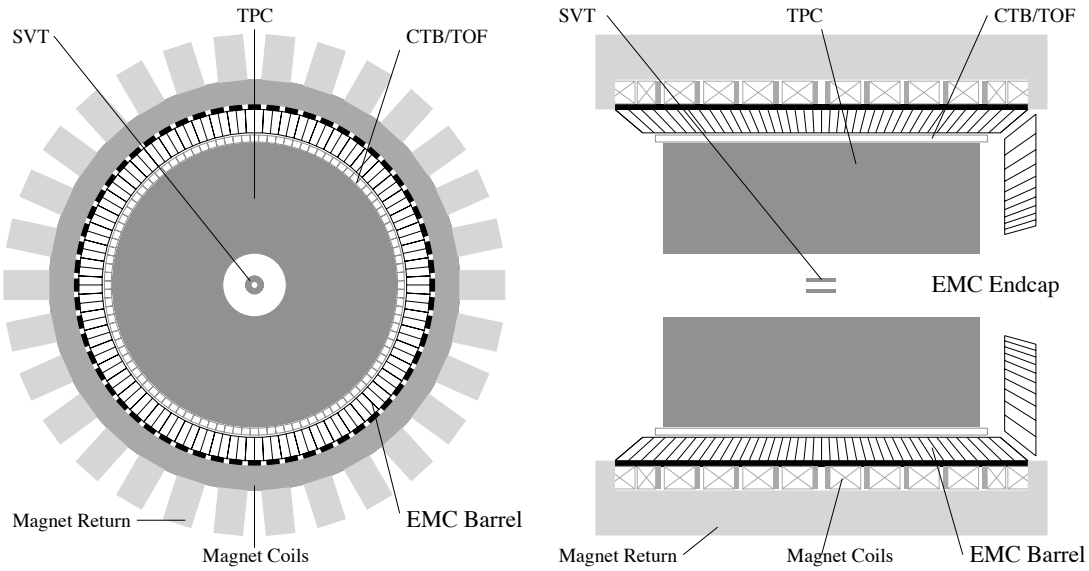


Fig. VII.1. Schematic end view and side view of the STAR EMC showing the EMC Barrel and EMC Endcap.

The EMC is 19 radiation lengths ($X_o$) deep. The calorimeter is composed of 21 layers of 5-mm thick scintillator alternated with 5-mm thick lead converters. The scintillator tiles are read-out with wavelength-shifting fibers coupled with clear fibers connected to photomultiplier tubes (PMT) located outside the magnet. A shower maximum detector (SMD) is located at a depth of 5 $X_o$ that provides high spatial resolution. The SMD is a gas/strip counter composed of 1200 patches of (15,15) strips in $(\eta, \phi)$ giving a spatial resolution of $(\Delta\eta, \Delta\phi) = (0.007, 0.007)$ and 36,000 total strips.

The EMC is arranged in 120 modules each covering $(\Delta\eta, \Delta\phi) = (1.0, 0.1)$. Each module contains 40 towers and 1 SMD chamber as shown schematically in Fig. VII.2. In total, there are 4800 channels of PMT signals for the towers and 36,000 channels of strip signals for the SMD. A schematic drawing of the layout of the strips for the SMD is shown in Fig. VII.3.

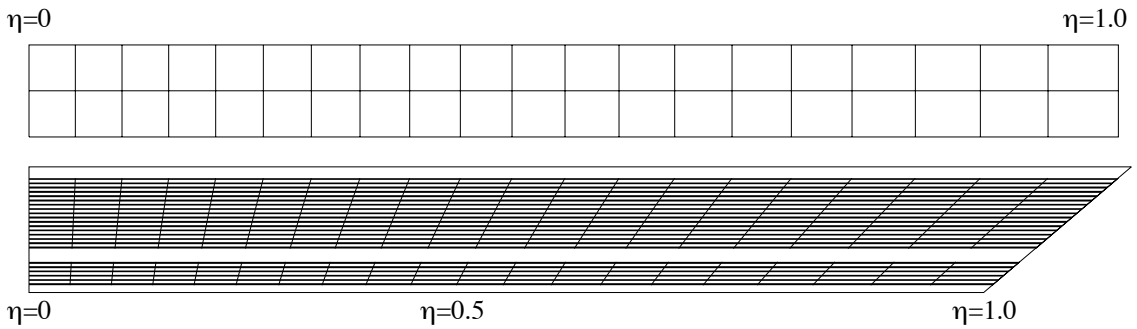


Fig. VII.2. Schematic drawing of one STAR EMC module showing a side view of the module and a top view of the last layer of tiles in the towers.

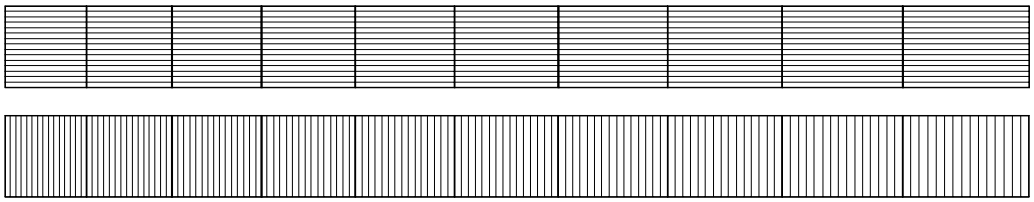

Fig. VII.3. Schematic top view of shower maximum detector showing 10 groups of strips. Each group of strips contains 15 strips in η and 15 strips in ϕ. Each SMD module thus has 300 signals.

For the tower readout, there are 30 electronics crates mounted on the back-leg iron of the STAR magnet. These crates include the digitization of the PMTs and generation of level 0 trigger information. For the SMD, the electronics is mounted on the end ($|\eta| = 1$) of each of the 120 EMC modules which are connected to 8 SMD readout modules mounted on the end of the magnet. The location of the EMC electronics is shown schematically in Fig. VII.4.

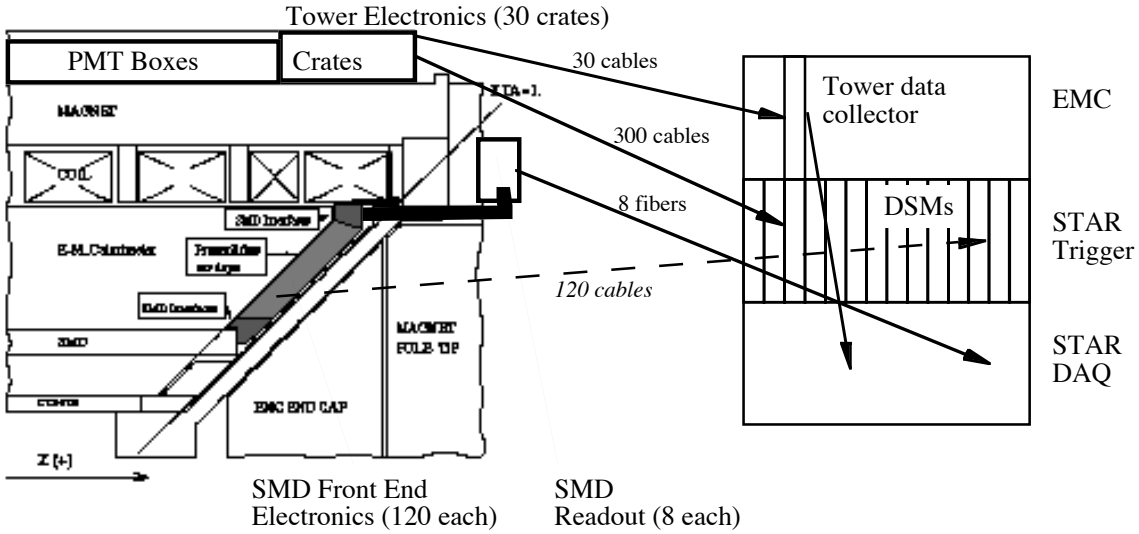


Fig. VII.4. Conceptual layout of EMC electronics showing the tower electronics on the magnet backlegs, the SMD front end electronics on the end of the EMC modules, and the SMD readout located on the end of the STAR magnet.

## VII.2 EMC Electronics

The electronics for the STAR EMC (Fig. VII.5) are designed to take physics data from the tower PMTs and the SMD. The electronics interacts with slow controls to read and set control parameters, sends the data to STAR DAQ, and produces a fast level 0 trigger. The EMC electronics reads all parameters for every crossing in synch with the RHIC clock.

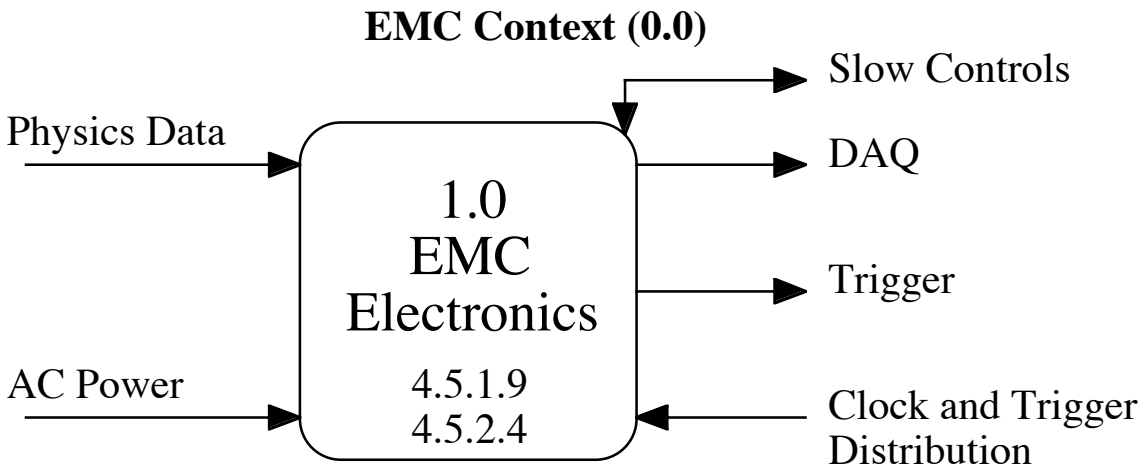


Fig VII.5. Context Diagram for STAR EMC Electronics

Part of the EMC electronics resides on the STAR magnet and part resides on the platform as shown in Fig. VII.6. The tower electronics are located in 30 crates mounted on the back-legs of the STAR magnet. These crates send their data over 30 twisted pair cables to the EMC data collector located on the platform. These crates also send level 0 trigger information to the STAR trigger on 300 twisted pair cables. The tower data collector collects the data from the crates and sends it to STAR DAQ. The SMD electronics is located on the $\eta = 1$ ends of the 120 EMC modules. These 120 sets of SMD electronics are readout with 8 SMD readout modules mounted on the end of STAR magnet. These SMD readout modules send their data to DAQ over 8 fibers.

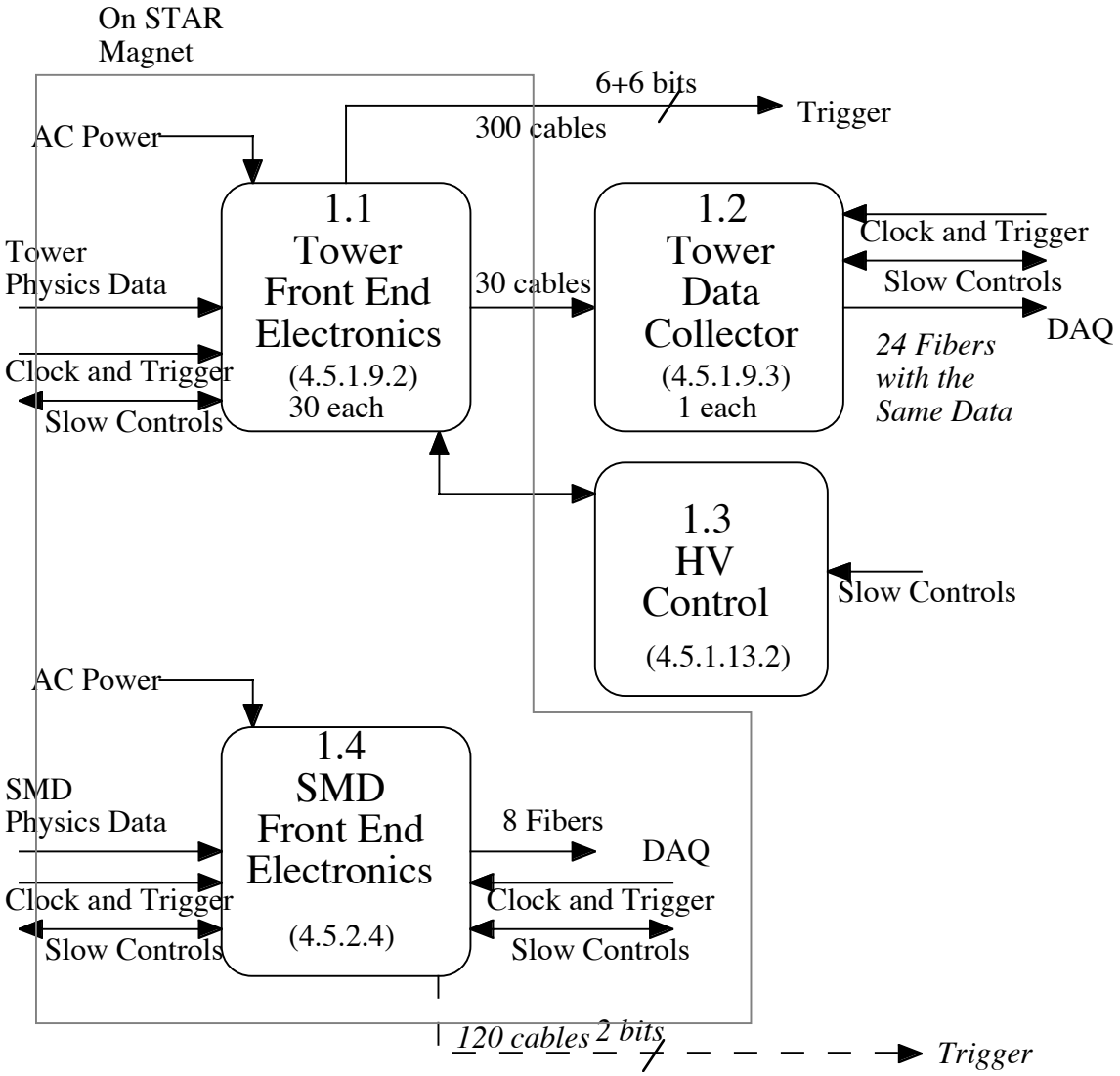


Fig.VII.6. Diagram showing the EMC electronics on the magnet and the EMC data collectors on the platform.

### VII.2.1 Tower Electronics

Each of the tower electronics crates (Fig. VII.7) reads out 160 tower PMTs. In each crate there are 10 tower front-end electronics cards. Each card handles 32 channels of PMT signals. LEDs drivers are located in the tower electronics crates to provide calibration. These LEDs can be turned on to produce various patterns of PMT signals. The tower crate controller contains the interface to the RHIC clock and STAR trigger distribution. The controller takes data from the 10 tower digitizer cards and sends the data to the tower data collector. Thecontroller also contains the interface to slow controls. The tower digitizer also produces level 0 trigger information in the form of 300 trigger towers $(\Delta\eta, \Delta\phi) = (0.2, 0.2)$ and 300 high towers $(\Delta\eta, \Delta\phi) = (0.05, 0.05)$.

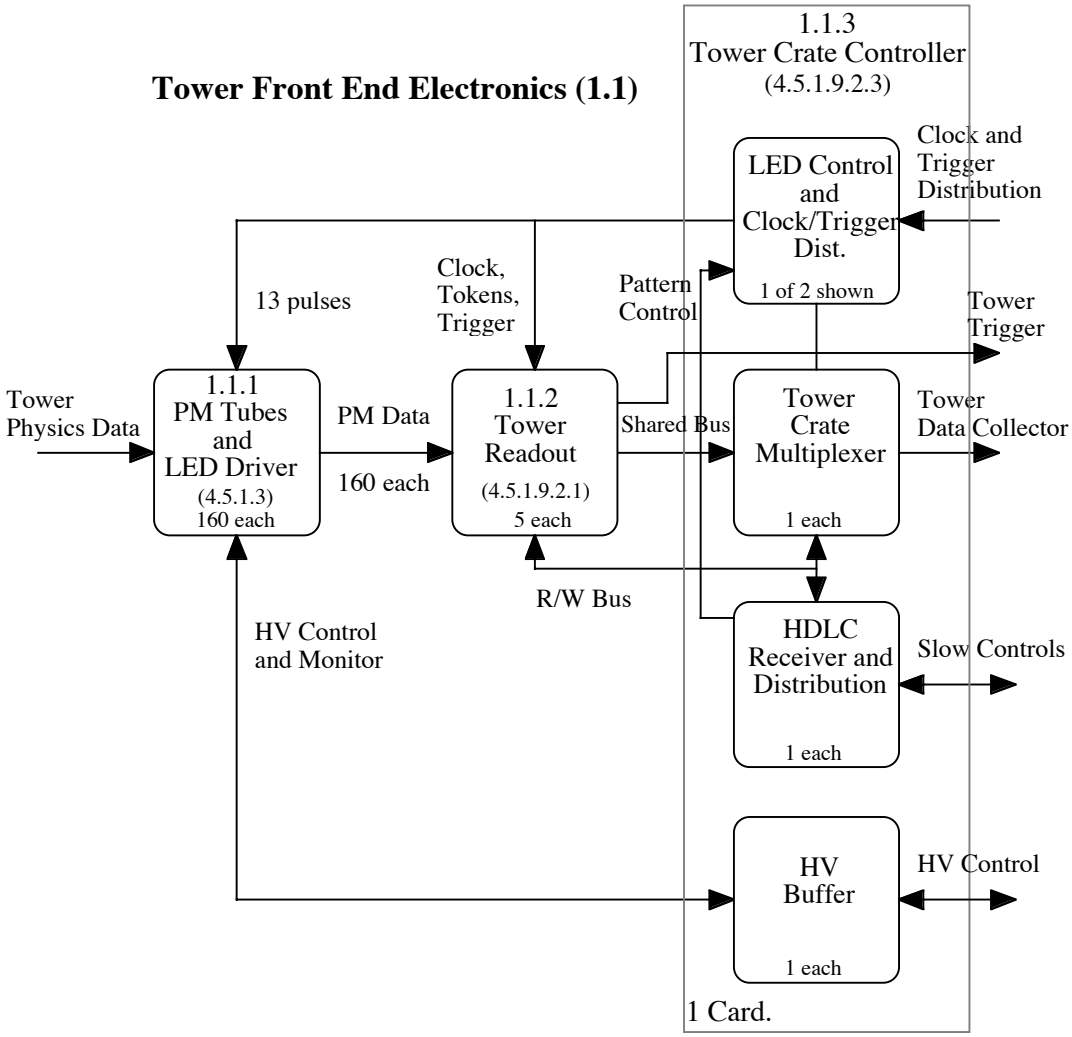


Fig. VII.7 Diagram of the tower electronics crate. This crate contains 10 tower digitizer cards and 1 controller card.

The tower electronics crates reside on the STAR magnet backlegs. There is a crate located near the $|\eta| = 1$ end of every other backleg. These crates are located next to the PMT boxes. Each electronics crate services 4 EMC modules. Each PMT box services 2 EMC modules. The fibers from the tiles of the EMC are routed through the STAR magnet structure to the PMT boxes.

The LED controller can produce $2^{13}$ different patterns of LEDs to test the tower electronics. The 13 different LED drivers each drive 1 LED connected optically to 7 PMTs. The HV for the PMTs is produced using Cockroft/Walton bases using a low voltage DC current. The set point and read-back of the voltages is accomplished using slow controls through an HDLC interface. The voltages are read with an ADC located in the HV control system.

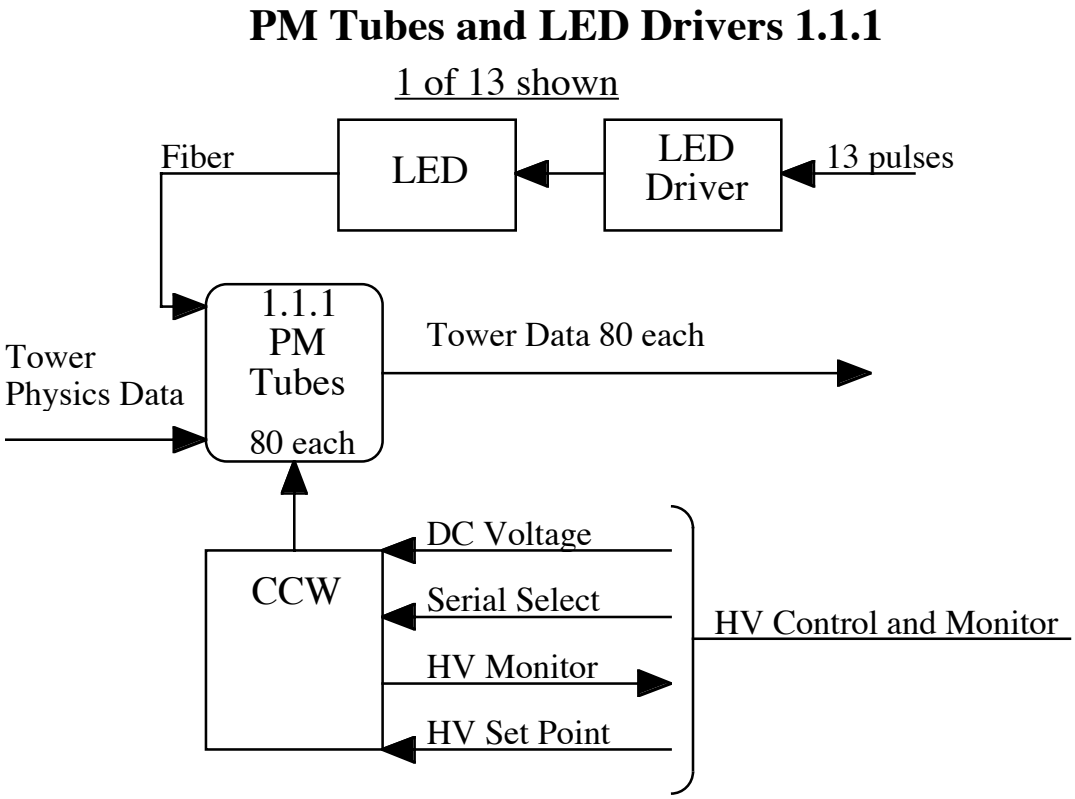


Fig. VII.8. Schematic diagram for the PMT HV supply and LED controller.

The tower digitizer card digitizes the PMT signal using a gated integrator and a 10 bit ADC. There is an integrator and ADC for each channel. The integrator system can be checked using a charge injection system. This system uses a 10 bit DAC to produce a linearity check of the integrator and ADC.

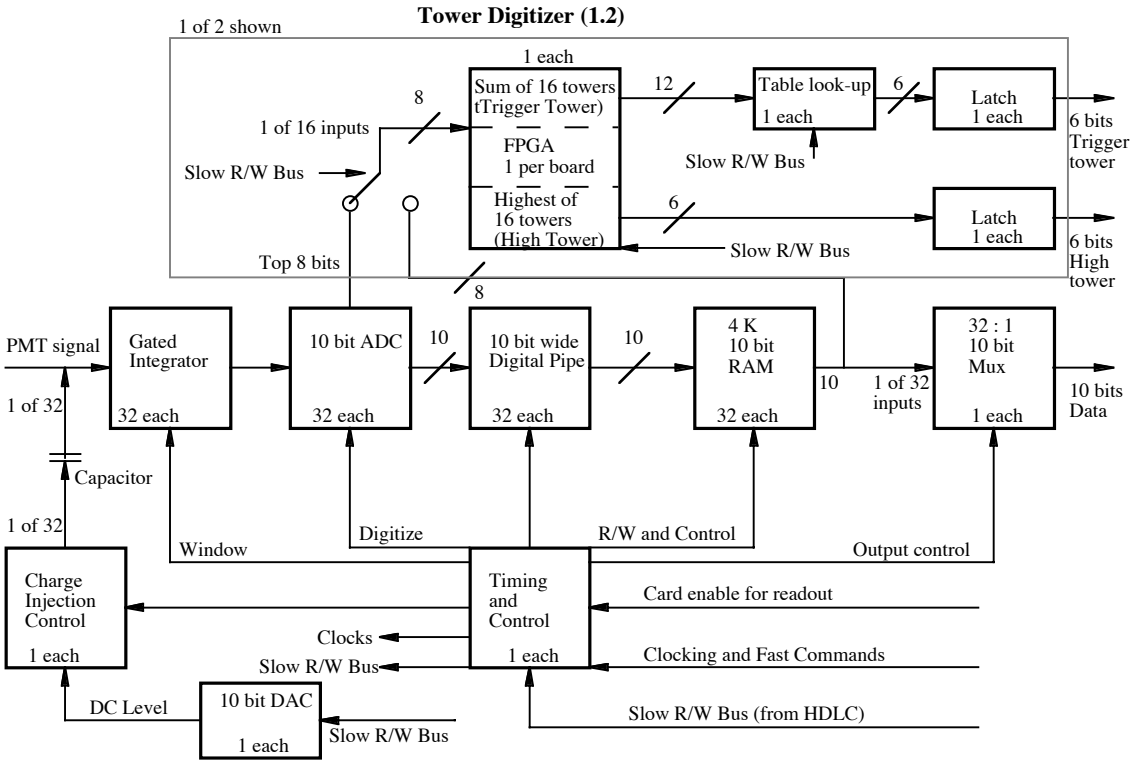


Fig. VII.10. Tower digitizer card located in the tower electronics crate.

The 10 bit output from the ADC is sent to a 10 bit wide digital pipeline to allow time for the Level 0 decision. Upon receipt of the Level 0 trigger, the ADC values are copied to a 10 bit memory with 4096 locations corresponding to the number of available trigger tokens. These data values are then sent to the tower data collector through the tower crate multiplexer. Each digitizer card handles 32 PMTs and is read-out through a single crate multiplexer to the tower data collector.

**Tower Crate Controller (1.1.3)**

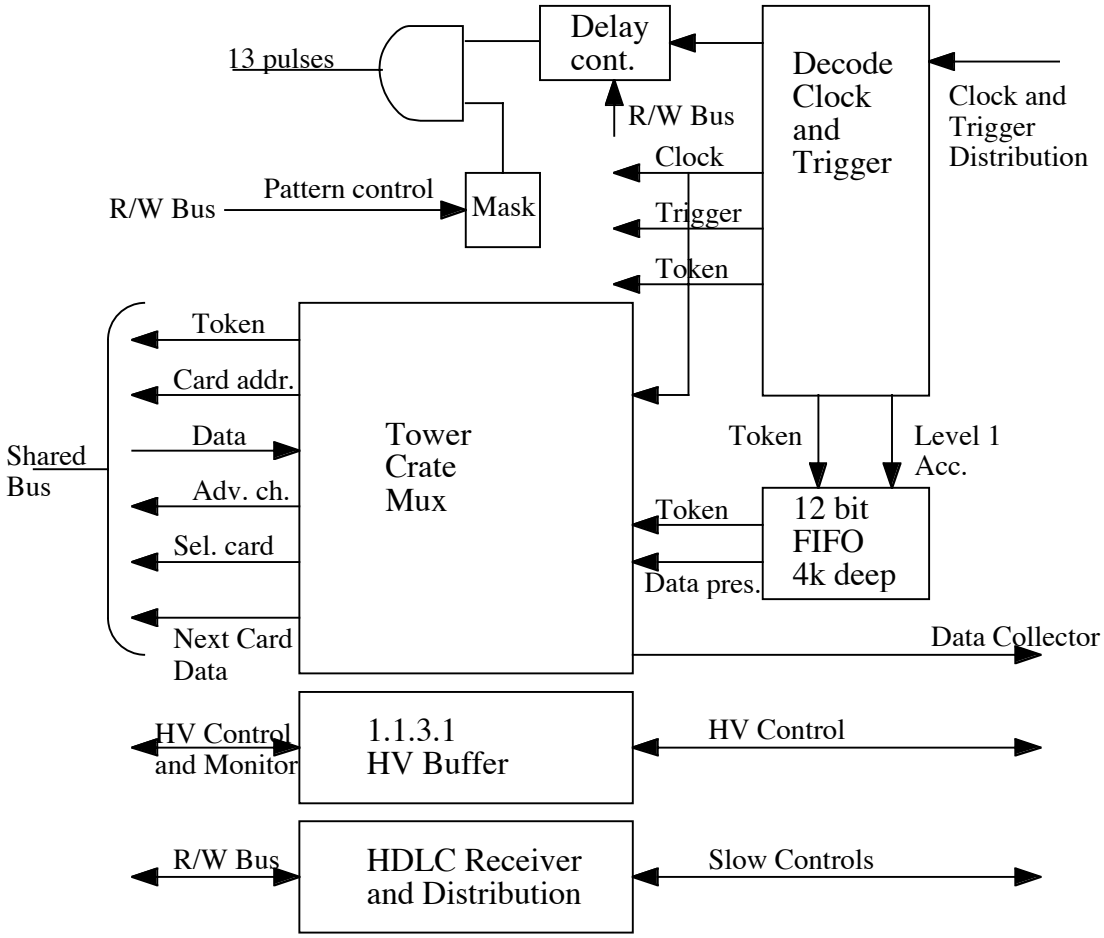


Fig. VII.11. Schematic diagram of the tower electronics multiplexer card.

The tower crate controller card has an HDLC interface to slow controls. The LED pulser system is programmed through this interface. The controller card takes the 10 bit data from a shared bus and sends the information 1 nibble at a time over twisted pair cables to the tower electronics data collector. The controller uses the trigger token from the FIFO to address the data from the tower cards.

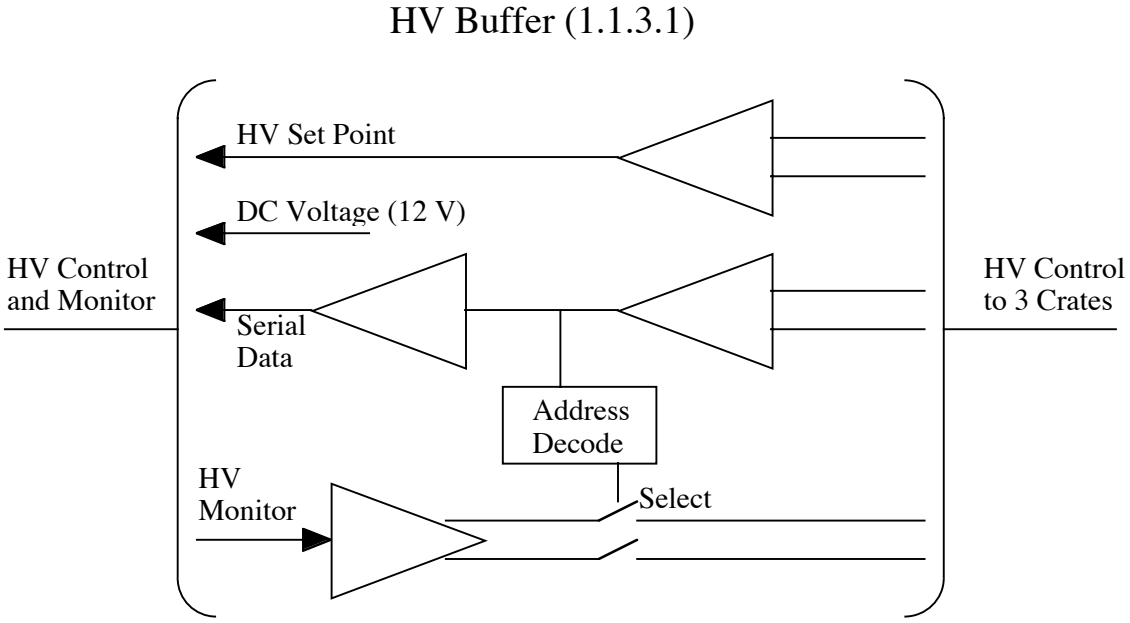


Fig. VII.12. Schematic diagram for high voltage control and monitoring.

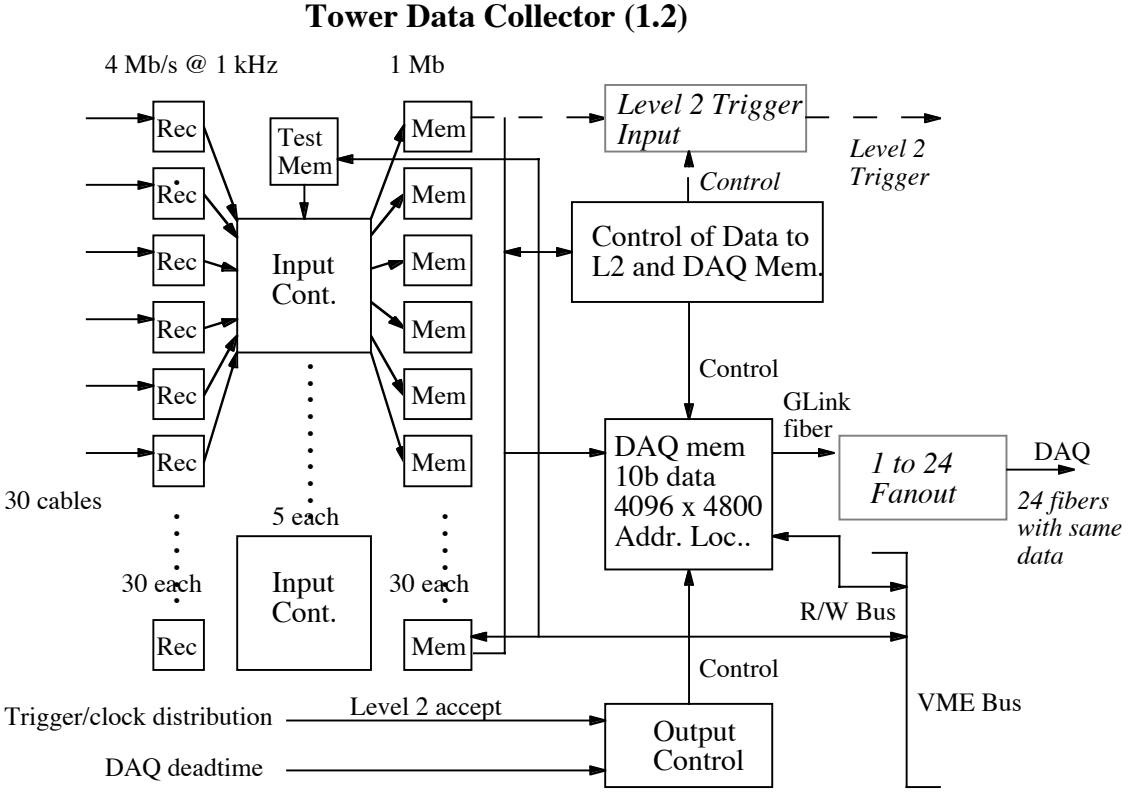


Fig. VII.13. Schematic diagram of the tower electronic data collector.

The tower electronics data collector takes the digital data from the 30 tower electronics crates and derandomizes the information into 1 Mb memories. The data collector then stores the data in a memory designed to handle 4096 x 4800 locations of 10

bit data corresponding to the 4096 trigger tokens and the 4800 tower channels. On the receipt of a Level 2 accept, the data collector sends this information to STAR DAQ. In addition, the data collector can provide the same information to the Level 2 trigger.

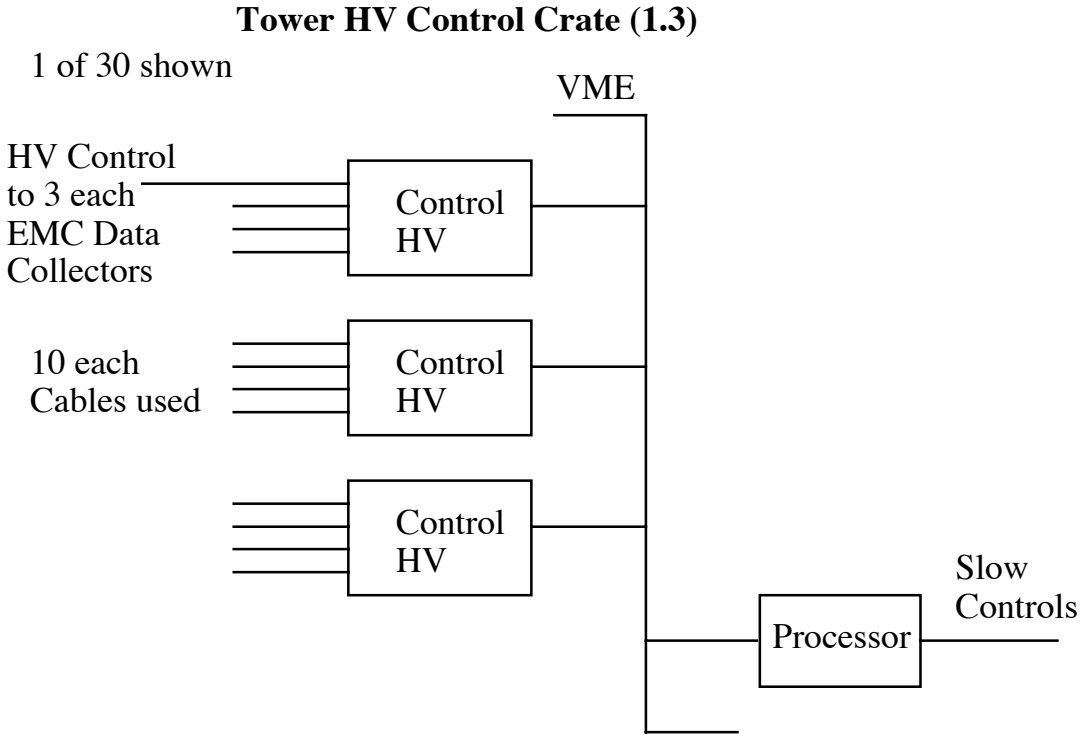


Fig. VII.14. Schematic diagram of tower high voltage crate.

### VII.2.2 SMD Electronics

The overall layout of the SMD electronics is shown schematically in Fig. VII.15.

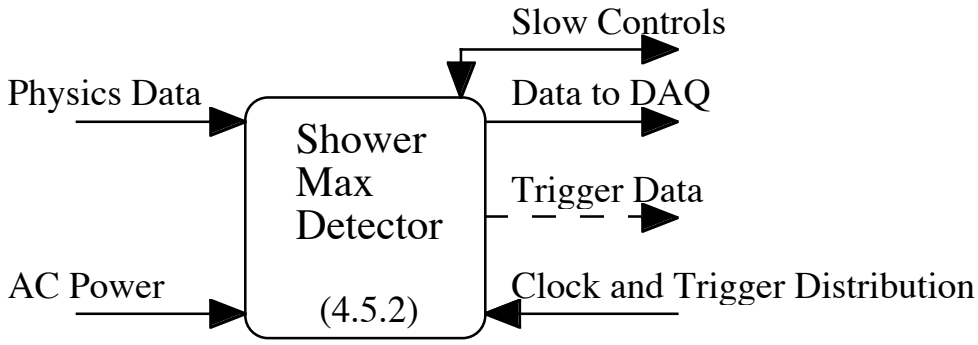


Fig. VII.15. Context diagram for SMD electronics.

The SMD Electronics receive signals from the wire chamber, digitize the signals and pass the data to DAQ over fiber optic links as shown schematically in Fig. VII.16. STAR clock and trigger signals are received and used to create all timing and control signals needed by the SMD electronics. SMD conventional systems provide high voltage

for the wire chamber. An interface to STAR Slow Controls allows the control and monitoring of the high voltage. An interface to the STAR safety system provides interlocks for the high voltage. EMC Calibration Systems provide a serial link for configuring a charge injection calibration of the SMD electronics as well as a calibration pulse, timed to match data acquisition.

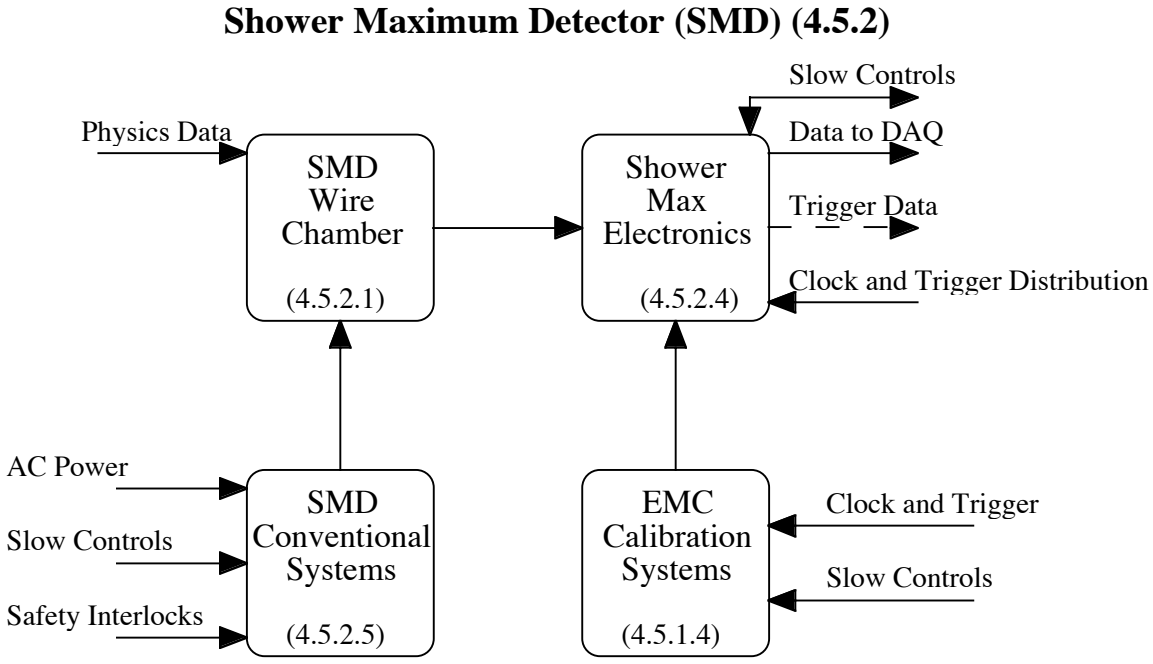


Fig. VII.16. Layout of SMD electronics.

One hundred twenty Front End Electronics cards (FEE) receive the wire chamber signals which are preamplified, shaped and stored in switched capacitor arrays. When a level 0 trigger is received, the stored data are multiplexed out of the SCAs and sent to the Read Out Modules (RDO) via twisted pair cables. Eight RDOs digitize the data and create data packets which are sent to the Data Acquisition System (DAQ) via standard STAR fiber optic links. SMD clock and timing electronics provide the appropriate timing and control signals in response to trigger commands from the Trigger system. The layout of the SMD electronics is shown in more detail in Fig. VII.17.

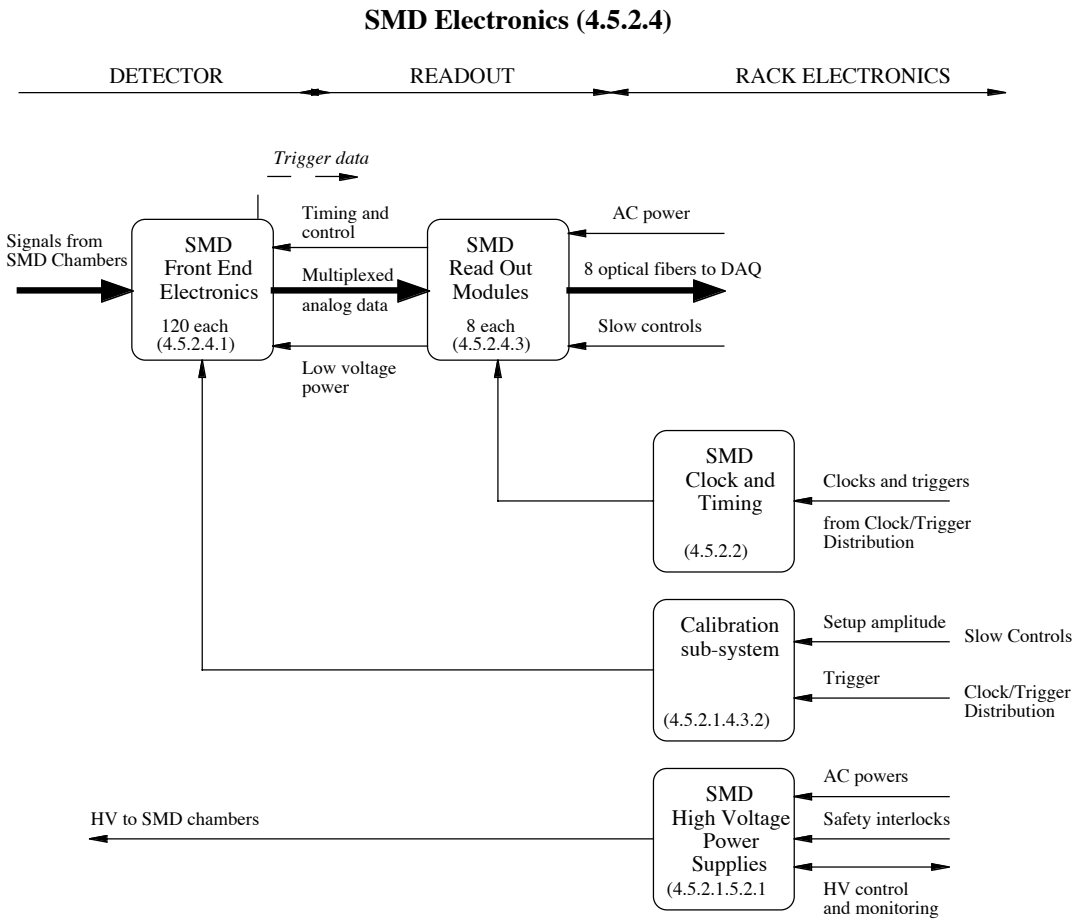


Fig. VII.17. More detailed layout of SMD electronics showing data path in bold.

As shown in Fig. VII.18, each FEE card has 300 wire inputs. Each input goes to one channel of the STAR Amplifier Shaper (SAS) chip where it is amplified and shaped. The SAS chip is an early development of a 16 channel chip that was developed for the STAR TPC as the "SAS16C" and is also used in the STAR MWPC Trigger detector. A production run of this part is currently under way for the MWPC. 15 of the 16 inputs are used on each of 20 SASs to match the wire count. The SAS characteristics are:

| | |
|---|---|
| gain | 24mV/fC |
| linearity | <4% |
| Internal calibration: | +/- 1% |
| Max output swing | 2 Volts |
| Integrator dynamic range | >2.5pC |
| Shaping time(peaking) | 60 to 150 ns |
| Tail correction | 0.5 to 2 us |
| Crosstalk | <+/-0.36% |
| Equivalent Noise Charge in erms | |

((Tp=80ns,Cboard=7.7pF = 560e + 13.7e/pF of detector capacitance.
(We expect 300 pF for the SMD).
Total power consumption <750 mW
output load 50pF
die size 2.6 x 3.6 mm

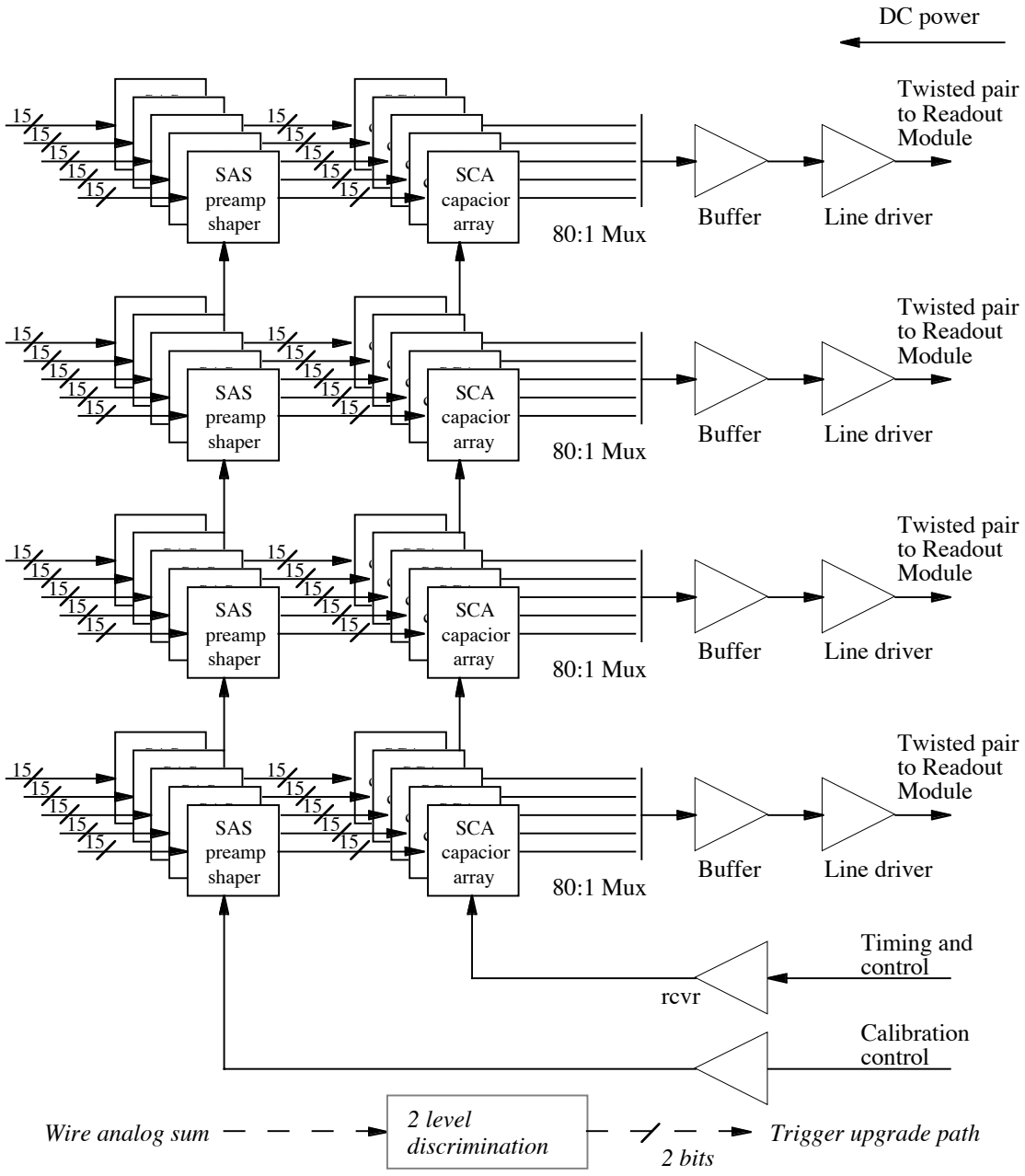


Fig. VII.18. SMD front end electronics showing the preamp/shapesr and switched capacitor arrays.

The output of the SAS is capacitively coupled to the inputs of the 16 channel Switched Capacitor Array (SCA). Capacitive coupling is used here to remove the pedestal variation of the SAS from the signal. The output DC bias of the SAS is settable

by external components for the SAS, but pedestal variation makes capacitive coupling necessary. For SMD operation, the output of the SAS will be from 1 to 3 Vdc This SCA was developed for the STAR Silicon Vertex Tracker (SVT) as "SVT SCA3". A production run for the SVT of this part is currently under way for the SVT. SCAs will be grouped in units of 5. 15 of 16 input channels on each device will be used. A total of 20 SCAs will be used on each FEE card. Details of the SC are shown in Fig. VII.19.

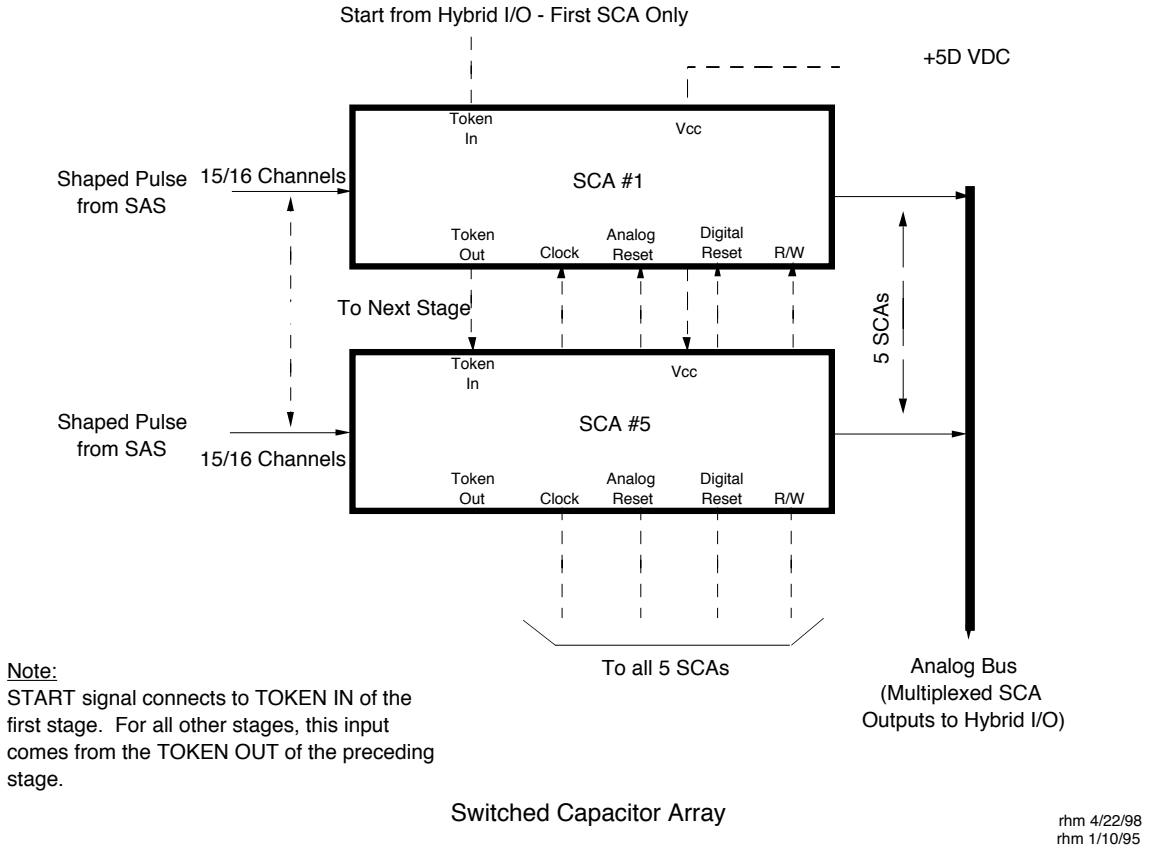


Fig. VII.19. Details of SCA used to read out SMD.

Input to the SCA will be biased externally for a 1 to 3 Vdc input range. The SCA output tracks the input at 1 to 3 Vdc. The SCA consists of 16 channels of circular buffers of 128 storage capacitors, buffer amplifiers and associated timing and control circuitry. The storage capacitors are sometimes called storage elements or pixels or cells or timebuckets. During operation, analog data are sampled and stored on each of the 128 storage elements in turn at a rate up to 3*RHIC strobe or 27 MHz. On the receipt of a trigger, the external clocking circuitry stops the acquire clock, switches from acquire to readout mode and a token is sent to the first SCA in each group of 5 to begin reading out the data. Data are read out channel by channel for the fist time bucket until all 16 have been read out. A token is then output from the first SCA that initiates the readout process in the next SCA. After all 5 SCAs have been read out, a new token is issued and the next time bucket is read out. The process repeats until the desired number of timebuckets has

been read out.

The SCA was designed for the SVT requirement of 128 storage elements or time buckets. The SMD needs only one sample stored. A peculiarity of the SVT makes the first time bucket read out unusable so two samples will be read out for the SMD. For the SVT, data acquisition stops immediately upon receipt of the trigger. For the SMD, dummy acquisition will continue until the readout is properly cued up. Two timebuckets will be read out, the first discarded and the second sent on to DAQ. Because the acquisition can take place at any of the 128 time buckets, calibration of pedestal offsets for all storage cells must and can be provided.

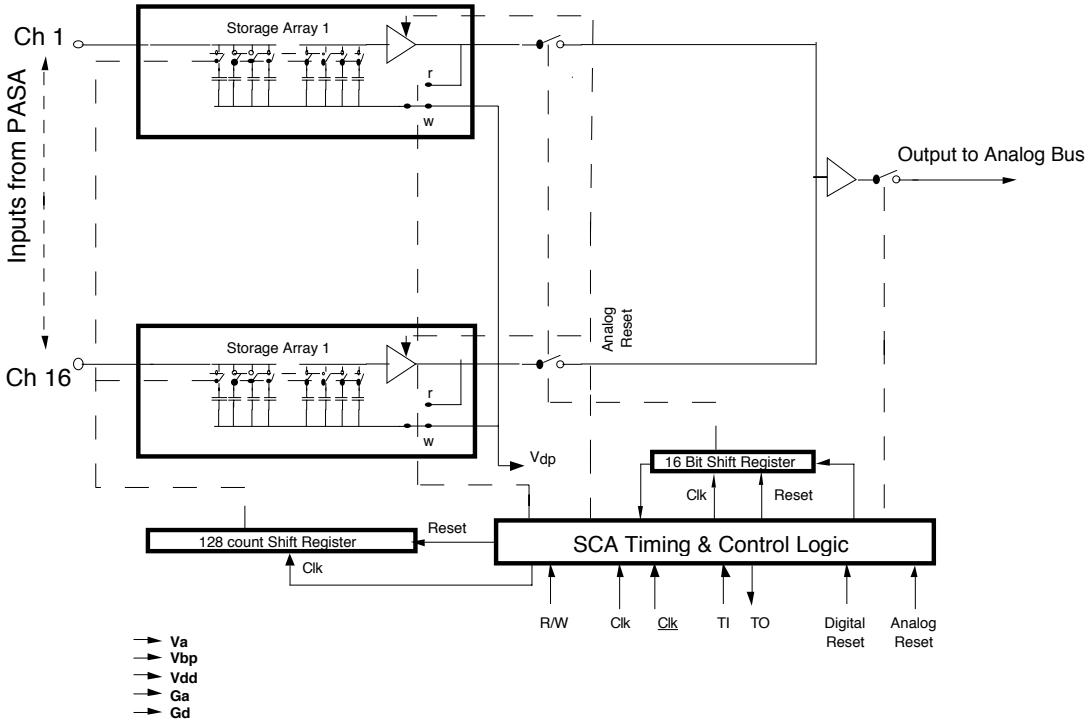


SCA Organization
(Switches shown in write state)

rhm
4/22/98

Fig. VII.20. Organization of the SCA used to read out SMD

The SCA characteristics are:

| | |
|---|---|
| Gain | 1.0 +/- 5% |
| Linearity | <1% |
| Max output swing | 3 Volts |
| Crosstalk | <+/-1% |
| Noise | 2.5 mVrms |
| readout rate | 1 MHz |
| clock signal | pecl |
| output mux | up to 15 SCAs |

| | |
|---|---|
| Total power consumption | <150 mW |
| input capacitance | <10pF |
| die size | 2.5 x 3.6 mm |

The output of a group of 5 SCAs is multiplexed into a buffer and then into line drivers that send the multiplexed signals to the RDOs. The multiplexing is 80:1 but only 15 of each group of 16 channels is connected to a wire. The FEE cards also receive and distribute the calibration serial links and pulse for calibration via charge injection into the SASs.

*Minimal electronics for a two level discriminator and input and output paths are provided for a future upgrade to a 2bit output from each FEE card to trigger.*

Eight RDO modules will readout the SMD data. Four will be mounted at each end of the detector and will support 15 of the 120 FEE cards. Communication from FEE to RDO will be by twisted pair cables. The RDO module hardware uses cards previously developed for the STAR SVT. They consist of Analog and Memory Boards (AMB) used to receive and digitize input data, the Fiber Optic Board (FOB) which formats the data and sends it out to DAQ via the standard STAR fiber link (gigalink), and two variants of the Power and Timing Board (PTB and PTBa) which generate local timing and control signals, generate and distribute timing and control for the FEE cards, and provide voltage regulation for the power sent to the FEE cards. The RDO modules are shown in Fig. VII.21.

Each module is a self-contained replaceable module. In the event of a failure inside the module, the entire module will be replaced with a previously tested unit. The defective unit will be repaired on the bench. Debugging at the installed module is possible but will be avoided.

Each RDO will support 15 FEE cards including analog inputs, dc power for the FEE, and all timing and control signals except for calibration. Each RDO will have 3 PTB cards, 1 FOB and 5 AMB cards and an SMD specific I/O panel for cabling. The modules will use a standard 10 slot VME based crate with local power supply but does not use VME protocol on its backplane. Local cabling between cards supplements the backplane for certain signals. The RDO module receives input from 15 FEE cards as 60 multiplexed analog inputs. Input cables are routed through and I/O panel to the AMB boards for digitization.

AMB Inputs are differential and resistor packs on the card allow customization of the level and offset of the signals passed to the ADCs shifting the 1-3Vdc SCA signal levels to 0-2Vdc for the ADCs. The analog signals are digitized at 10bit resolution and temporarily stored in memory. The on card memory also allows storing an event for later read out by Slow Controls for diagnostic purposes as well as loading and retrieving test data.

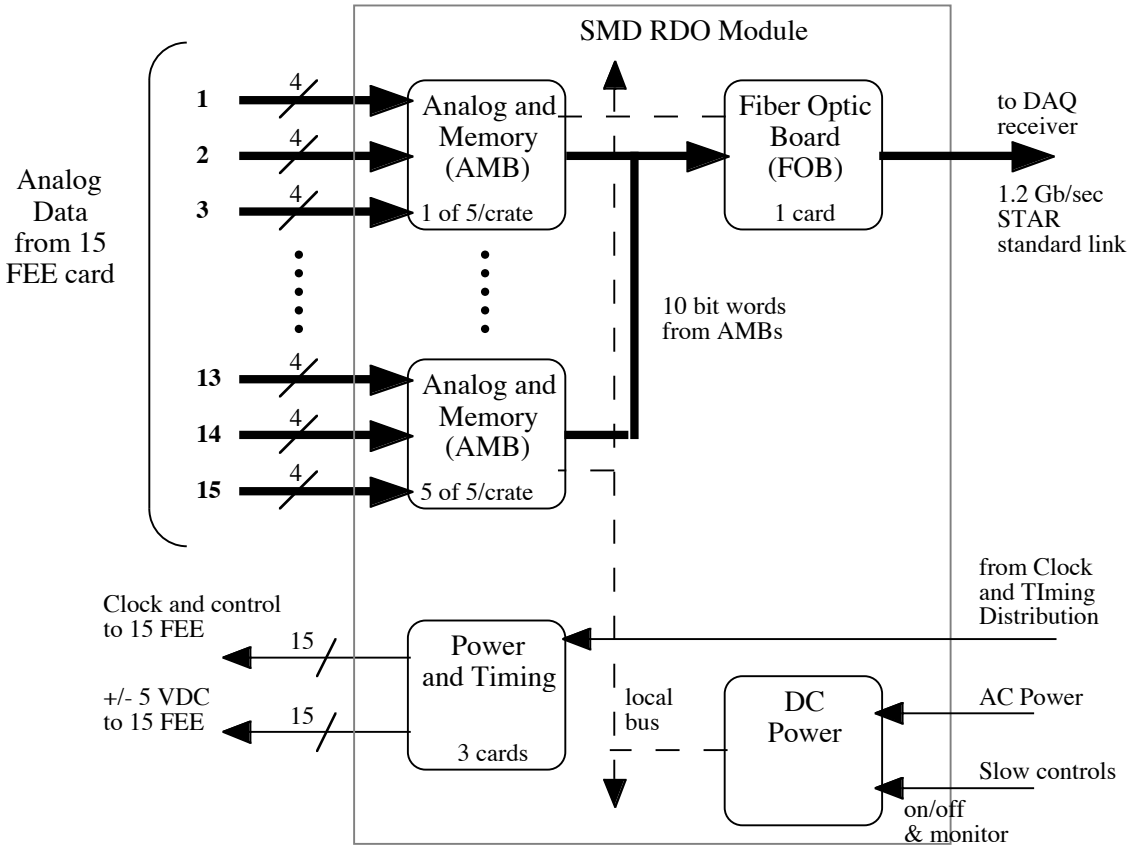


Fig. VII.21. SMD front end electronics showing the preamp/shapesr and switched capacitor arrays.

The data in memory is read out interleaved with the acquisition and transferred to the FOB board as two 10 bit words which are combined for the 20 bit transfer via gigalink to DAQ. The DAQ receiver buffers the data, does a pedestal correction and threshold zero suppression only.

## VII.3 Trigger

### VII.3.1 Trigger Overview

The EMC trigger is produced by the 150 tower readout cards located in 30 crates on the back-legs of the STAR magnet. The trigger information will be produced on each RHIC crossing and sent to data storage and manipulation (DSM) boards to be processed. These boards have been designed by the STAR trigger group and consists of programmable logic with 128 bits of input and 32 bits of output. An overview of the EMC/trigger interface is shown in Fig. VII.22.

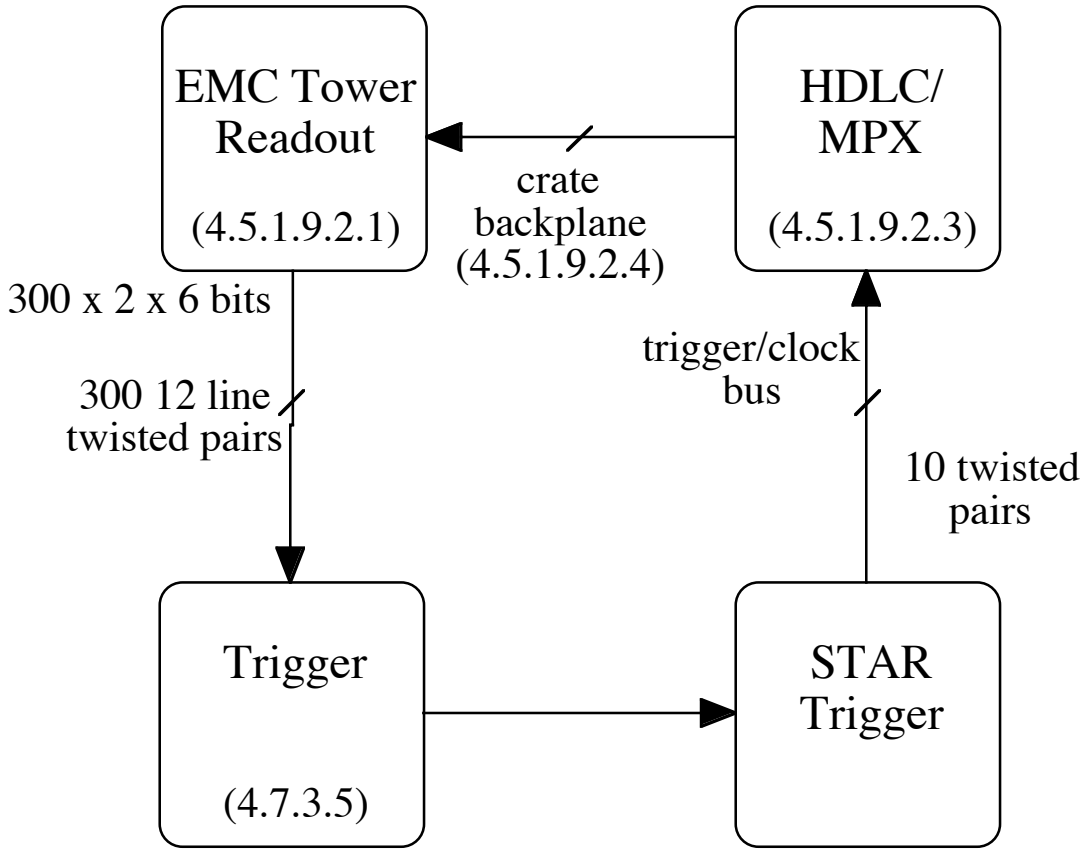


Fig. VII.22. Schematic layout of the EMC/trigger interface.

The EMC electronics will produce the following level-0 trigger information:

- 300 6-bit trigger towers
  - $(\Delta\eta, \Delta\phi) = (0.2, 0.2)$
- 300 6-bit high towers
  - $(\Delta\eta, \Delta\phi) = (0.05, 0.05)$

The trigger towers correspond to the sum of the energy deposited in 16 physical towers. The high towers contain the energy of the highest tower of the 16 towers making up a trigger tower. The EMC FEE produces 300 sets of 12 bit values that are sent over twisted pair cables to the DSM interface (DSMI) boards that convert the differential logic signals to the TTL logic signals required by DSM boards.

The inputs into the DSM (and corresponding DSMI) boards are grouped by $\eta$ and $\phi$ to produce geometric sums. Each DSM is connected to 20 cables. 10 of these cables correspond to trigger towers and 10 to high towers. Each group of trigger towers and high towers in each DSM covers a geometric area of $(\Delta\eta, \Delta\phi) = (1.0, 0.4)$. This arrangement is illustrated in Fig. VII.23.

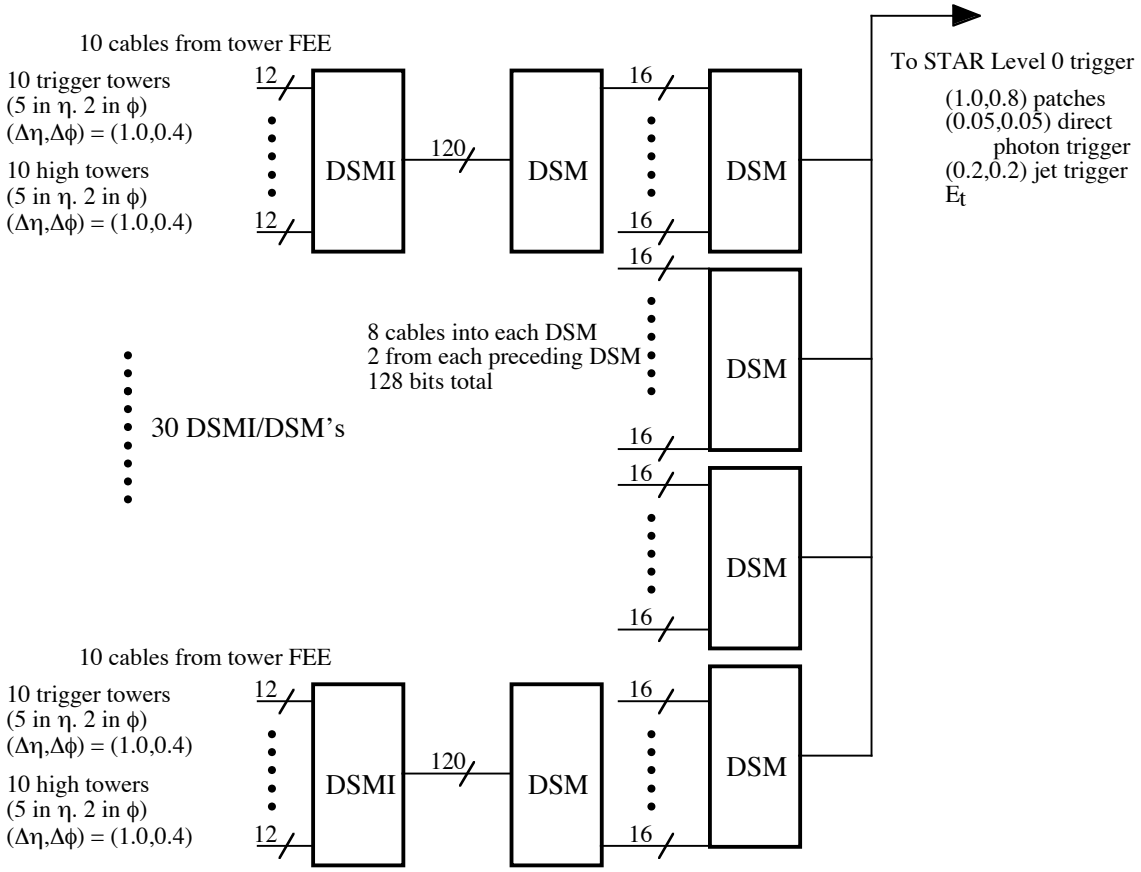


Fig. VII.23. Schematic layout of the EMC level 0 trigger.

The time to produce a level 0 trigger is 8 crossings in the tower FEE. Assuming that each layer of DSM boards can calculate in one RHIC crossing, the EMC level 0 trigger will be ready in 10 crossings to compare with the CTB. In 11 crossings, the EMC trigger will have produced all of its triggers.

- $E_t$, total transverse energy, in the EMC to be compared with the total charged particle multiplicity from the CTB
- (1.0,0.8) patches of transverse energy to be compared with the charged particle multiplicity from the same patches of the central trigger barrel (CTB)
- Direct photon trigger based on high towers
- Jet trigger based in trigger towers and (1.0,0.8) patches
- Two particle triggers

The EMC level 0 trigger requires 30 + 4 DSM boards to produce the basic trigger information. Correlation of this information with CTB will be accomplished by briding the inputs to the second layer of DSMs to the DSM tree of the STAR trigger based on the CTB. Two more DSMs in a third layer complete the EMC trigger by producing bits corresponding to triggers that involve only the EMC.

For example, a jet trigger can be produced based on thresholds on the highest trigger tower. Because the jet trigger rate at low $p_t$ is larger than the rate desired at level 0, several thresholds must be defined. Placing a low threshold on the jet trigger allows

the measurement of low $p_t$ jets that are necessary to understand the phenomena STAR is studying. These triggers must be scaled down to an acceptable rate. Putting a higher threshold on the jet trigger will select higher $p_p$ jets at a lower rate but will also need a scale down factor. Finally, one places a threshold on high $p_t$ jets that one wishes to accept always. This trigger is not scaled down.

Assuming that the EMC were allocated 3 bits in the STAR trigger word, the DSMs could be programmed to produce 8 different triggers. In some cases, the EMC could be allocated more bits and the corresponding number of triggers could be produced. These triggers can be scaled independently. Of course triggers involving the EMC and other detectors are produced by the STAR trigger (up to 2048 assuming that the 11 trigger bits are encoded by the DSM tree). Thus one could program several jets triggers, several direct photon triggers, and several multi-particle triggers.

### VII.3 Interface to DAQ

The EMC electronics will send its data to DAQ over 9 gigalink fibers. One fiber is used to transmit the tower data and eight fibers are used to send the SMD data. The tower data collector will hold all recorded data tagged by the trigger token. On a level 2 accept, the tower data collector will push its data to DAQ. An interface card will reside in one of the TPC DAQ crates. This card will be designed by the STAR DAQ group. An upgrade path exists to send a copy of the tower data to all 24 TPC sector crates to allow level 3 trigger correlations between the EMC and the TPC tracks.

The SMD read out cards also hold the accepted data until a level 2 accept is received. The SMD read out boards then send the SMD data to a DAQ receiver that is to be designed by the STAR DAQ group.

### VII.4 Dynamics Range Requirements for the SMD

The search for the direct photons candidate and detection of electrons from W and $Z^0$ decay lead us to measurement of electromagnetic showers with energy varying from 0.5 GeV to 60 GeV. The low end comes from looking for low energy gammas from the asymmetric $\pi^o$ decays that can fake direct gammas. The measurement of 0.5 GeV electromagnetic showers means the detection of minimum-ionizing particles in the SMD with reasonable efficiency will be needed. The fluctuation of the ionization from MIPs in thin layers of gas finally defines the low threshold that is equivalent to 0.125 keV in terms of total ionization for a $Ar/CO_2$ gas mixture. Monte Carlo calculation show that the total ionization will be ~160 keV in a single channel of the SMD (central strip) from a 60 GeV electromagnetic shower. This number lead us to an overall dynamic range of 1:1240.

Monte Carlo calculations shows that the reasonable signal to noise ratio for the direct photon is expected for the $P_t$ region form ~12 GeV up to 25-30 GeV. Above 30 GeV the main function of the SMD will be the improvement of the overall hadron

suppression power for the non-segmented EMC. The high $P_t$ charged hadrons that can be misidentify as electrons is expected to be the most serious source of background. The information from SMD placed at depth 5 $X_0$ will allow to reduce the level of background (remaining after the selection of the events using TPC and EMC information) in 1.5-2 times, as was calculated in the Monte Carlo.

The invariance of the transverse shower profile in the energy region from ~7 GeV up to 150 GeV allows us to make the identification of electron/photon candidate using the tail distribution in the transverse shower profile even in case when the 'central' strip is saturated. This means that the effective dynamic range needed for the SMD is close to 1:640. The proposed STAR Amplifier-Shaper (SAS) for the SMD readout includes a pole/zero network which cancels the long ion tile. A pole/zero T bridge network in shaper's feedback loop was designed with controlled externally MOS resistor to adjust the tail cancellation depending on the gas mixture in the TPC. The two mixtures P10 and He-Eth was considered in the SAS shaper design.

The gas mixture in the SMD is Ar-$CO_2$. The signals arising from the avalanche region is approximated by a 1/t relationship and the total collection time for the Ar mixture expected to be close to ~30 μs. For SMD gas mixture the shape of the signal arising from the avalanche region will be different compare to shape of signal for the TPC gas mixtures. The rise time expected to be close to ~50 ns, and the ion tail falloff will be in between the ion tails for the P10 and He-Eth mixtures. (This statement is based on extrapolation of the data for the Ar/CH4 (80%/20%) gas mixture , see T.Akesson et al. NIM A361(1995) ) The current design of SAS make it possible to optimize the shaping of the SMD signals to achieve the optimal relation between peaking time and noise. The test measurements with the first full scale operational chamber will be needed, and we expect they will be accomplished during the summer 98, prior the next test run in October 98.

# VIII. Installation and Integration into STAR

This section describes the Interfaces between EMC and the rest of STAR, including the mechanical integration and the installation.

## VIII.1 Installation

### VIII.1.1 Overview of Module installation

As described previously, the EMC modules are supported inside the STAR magnet on pairs of rails. This method was chosen because the EMC is a staged detector and parts of it must be installed over a period of years with the TPC already in place. The rails are supported by a system of support segments sometimes referred to as hangers. These supports fit between the coils of the conventional magnet so that the rail and module loads are transferred to the magnet backleg steel. There are 9 rings of supports, 8 of one type and one type for the center, which supports the rails for two modules. There are two modules end to end to span the length of the barrel, and 60 in phi for a total of 120 modules. Each ring is made of 30 segments, the so-called singles, which support one module and the triples, which support 3. This breakup into 1 and 3 was necessary to make the EMC boundaries match the TPC boundaries after the TPC design was rotated.

The basic approach to module installation is to slide a module off a set of rails in an installation fixture and onto the rails in the magnet. The bundles of fiber optics must be pulled out between the magnet coils in a continuous manner as the module slides into the STAR magnet.

The installation fixture will be supported partially be bolting to the STAR magnet, and partially by the building crane during installation of a module. The fixture is designed with a series of lifting holes related to the module center of mass so that it can be aligned easily when lifting and attaching to the magnet. A second attachment to the crane, a come-along, permits fine adjustment and also compensates for the change
in center of gravity as a module is slid off the fixture and into the magnet.

This basic approach of a fixture with holes over the C.G. for each angle, and a second support for fine adjustment was used to assemble the STAR magnet backlegs. It allowed adjustment of a fraction of a degree in angle while hanging before any attachments to the magnet were made.

This method of installation was chosen because it is simple, economical, and quick to build. Also, there is a problem with using floor-supported installation fixtures because of the rails on the floor for the pole piece supports.

Fiber guides are in place on the rail supports between the coils of the STAR magnet. These protect the fibers by providing a 4 inch radius of curvature for the fiber bundles, and they also guide the fibers into the channel between backleg iron bars.

At the beginning of installation, all the pre-assembled bundles of fibers must be attached to the module. These are laid into a channel along the top of the module, to the side of the spacer plate and carriage. They all extend past the eta=0 end of the module, so that at that point, all the fibers must be in the channel. Ropes are pre-inserted between coils before installation, and these are tied to the appropriate fiber bundles. The ropes are then pulled as the module is inserted. When the module is fully inserted, the fibers are plugged into the connectors on the sides of the PMT boxes.

### VIII.1.2 Analysis of the segments and rails

A Finite Element Analysis (FEA) was performed on the support segments and the rails. The support segments were analyzed in the 12 o'clock and 3 o'clock positions. A .25g seismic load was considered for both of these load conditions. The maximum stress in the segments was 6,200psi. The segments were fabricated from 6061T6 aluminum that has a yield stress of 36,000psi so there is nearly a 6 to 1 factor of safety. The deflection of the segments was negligible.

Similarly, a FEA model was used to examine the rails. The rails were loaded in the 12 and 3 o'clock positions. The load from the module was applied at the estimated center of gravity of the module and between the support segments to simulate module insertion which is the worst case condition. The maximum stress in the rail was 6900psi, which closely matches the 7,500 psi stress from hand calculations.

Rail twist in the 3 o'clock position is a concern since this could result in phi contact between modules during insertion. The calculated twist with the FEA model was .62 degrees and .58 degrees from hand calculations. A twist of .62 degrees would result in modules contacting, assuming that there is only a .5mm gap between modules.

### VIII.1.3 $\phi$ Gap analysis

The cover to cover phi gap between modules is determined by the following factors:

1. Module construction tolerances
2. Module deflection
3. Rail alignment tolerances
4. Rail deflection

The worst position in the detector is in the 3 o'clock location where phi deflections of the module and rail will be the worst. Rail deflections address only the twist and sag in the rail when the module is completely installed. The maximum rail deflections will actually occur during installation. This deflection / twist has been measured with a dummy EMC module on a real set of rails and rail supports. It is smaller than expected. It was believed that the twist of the rails would be so large that designing to this criteria would result in an unacceptably large phi gap. In order to overcome this the plan was that the modules would be installed from the top of the detector down so that no modules would ever be below the one being installed, thereby avoiding interference. An option we have which is not currently deemed necessary is to add additional carriages to the modules near 3 and 9 o'clock to greatly reduce the rail twist during installation

Currently a cover to cover gap of 5.6 mm is anticipated which is a 2.8 mm half gap. This gap is determined by:

1. Module construction tolerances of 1.54mm
2. A module deflection of .5mm based upon measurements of a prototype constructed at Argonne.
3. .5mm is assigned to the alignment of the rails. This is occurring currently so it is to early to determine if the .5mm alignment tolerance is being achieved. An analysis of initial data, however, indicates that this tolerance will be met.

4. .25mm has been assigned to the deflection of the rails with the modules completely installed. This is based upon calculations described above.

### VIII.1.4 Rail Alignment

On the basis of the measurement of 10 installed and aligned rails, none of the rails have any measurable twist. All of the rails have variation along their length in radius of up to .020" which is due to the deflection of the backleg iron. We did not shim this out because radial variation at this level results in less than .1mm phi variation. In phi we have been aligning the two ends of the rail and then locking them into place. We then take measurements along the length of the rail, which show variation of up to .015". We feel that this is due to the rail not being straight. We make the adjustments that we can but it is very difficult to get all five points to line up. We have accepted .012" variation in phi along the length of the rail. Since there is no measurable twist, this is acceptable.

### VIII.1.5 Installation Test

An installation test has been prepared at ANL to test the procedure of installing a module, and to confirm calculated rail twists and clearances. These studies try out various facets of installation such as transferring the module to the rails in a fake magnet from a fake installation fixture, pulling the fiber bundles up between fake coils, and examining deflections. The installation will be performed at angles of 6 o'clock, 9 o'clock, and 12 o'clock.

This test uses real support segments, real rails, real fiber guides, and a mechanical prototype with dummy scintillator and reject fibers.

## VIII.2 Integration

### VIII.2.1 Overview

The mechanical integration involves many facets. The Integration Group at LBL has, in cooperation with each sub-system, defined spatial integration envelopes for each sub-system such as EMC. These are subject to review and change control. There are issues of providing services such as electrical power, detector gas for MSD, cooling gas for SMD, cooling water for Phototubes. These issues are described in chapters on conventional systems or the individual EMC sub-systems. There has been extensive iteration in defining EMC space on the platforms in the racks for Low voltage power, and VME crates for Data collection and Trigger and controls. What we describe below has largely to do with fitting parts of EMC into the available envelope, and establishing connections.

### VIII.2.2 Integration of PMT boxes

The PMT boxes mount on the STAR backleg iron bars, and are separate from the EMC electronics crates.

The PMT boxes provide:

- Light tight environment for phototubes and fiber decoding.
- Mounting support structure for shielded PMT assemblies
- Temperature control
- Interface between fiber bundles and fiber decoding.
- Electrical shielding

Each box has 1680 fibers from the calorimeter towers and 160 fibers from the pre-shower upgrade coming in. There are 80 cables of RG174 leaving each box for the tower phototubes. There are a few flat cables to provide Low Voltage and control signals. In addition, there are two water tubes of 3/8 in copper for cooling.

Due to the constraints of the STAR magnet, there are 3 different areas with different size constraints on the PMT boxes. We have chosen to have only 2 different kinds of boxes for reasons of mass production economy.

The constraint on top of the magnet is that only 9 inches is available to clear the door when the detector rolls in. This means that electronics crates on 9 backlegs will have to be dismounted to roll the detector in and out. However, the calibration would be lost if the fiber optics was disconnected, and there would be danger of damage as well. Thus, the top boxes will be 9 inches high. The electronics crates can be mounted in such a way to allow a length of 90 inches for the top PMT boxes. The boxes are 22.5 inches wide, the same as the backleg iron, to allow access to fibers and connectors during installation, and to protect the fibers coming out the sides of the box at a steep angle.

The constraint at the bottom of the magnet is most severe in length. The cradle for the magnet restricts the space to 66 inches and the integration of the magnet hydraulics and power further restrains the box length to 57 inches.

There are other constraints at the sides of the magnet below the water hoses and power cables. Here the length is not limited, but the width of the box is limited and the radial height is limited. The boxes for the top of the magnet can be made to work here by offsetting them from the center of the backleg bar.

The EMC electronics crates on the magnet backleg iron are the size of 9U VME crates, but of 8 slot width. Thus, they can lie flat on the magnet backleg, consistent with the door clearance for rolling in STAR. The signal are connected through mass connectors,
So that crates can be removed for servicing.

### VIII.2.3 Cables and Tubing

### EMC Cable list

| ITEM | QUAN. | SIZE | PWR | SIG | TYPE | SYS |
|---|---|---|---|---|---|---|
| EMC Detector/boxes to Crates | | | | | | |
| EMC barrel PMT | | | | | | |
| CCW power and controls | 4800 | 0.1 x 0.75 in | x | x | flat | CCW |
| PMT signals | 4800 | 0.1 dia. | | x | coax | CCW |
| LED power/control | 840 | 0.1 x 0.75 | x | x | flat | LED |
| box Temp Probe | 120 | 0.1 x 0.75 | x | x | flat | Conv |
| PMT box water pipe | 120 | 0.38 dia | | | pipe | PMT |

| ITEM | QUAN. | SIZE | PWR | SIG | TYPE | SYS |
|---|---|---|---|---|---|---|
| EMC Barrel SMD | | | | | | |
| FEE to RDO : | | | | | | |
| SMD signal ,clk, temp. | 120 | 0.1 x 1.4 | x | | flat/twist/shield | |
| SMD power | 120 | 0.375 dia | x | | multi | |
| SMD gas tube | 240 | 0.25 dia | | | tube | SMD-Conv |
| SMD cooling gas tube | 240 | 0.25 dia | | | tube | SMD-Conv |
| SMD to Platform: | | | | | | |
| SMD HV | 120 | 0.25 dia | x | | RG59 | |
| SMD FEE to Platform: | | | | | | |
| SMD Calibration | 120 | 0.3 | | x | 2 two pair | |
| SMD RDO to Platform: | | | | | | |
| SMD slow control/HDLC | 8 | 0.3 | x | | multi | HDLC |
| SMD trig / clk | 8 | 0.3 | x | | multi | Trg/Clk |
| AC Power | 8 | | | | | |
| SMD RDO to DAQ | | | | | | |
| Gigalink Fiber | 8 | 0.2 | | fiber | | |
| EMC Barrel Crate to Crate | | | | | | |
| Trg-Clk fanout | 1 | 0.1 x 0.8 | x | | flat | PMT-elec |
| Slow control/HDLC | 2 | 0.3 dia | x | | multi | HDLC |
| SMD gas pipe | 4 | 1.25 dia | | | pipe | gas |
| SMD cooling gas pipe | 4 | 0.5 dia | | | pipe | gas |
| SMD gas flow meas | 120 | | | | | |
| PMT box water pipe | 4 | 1.25 dia | | | pipe | PMT |
| LED etc serial line | 4 | 0.25 dia | x | | multi | LED |

| ITEM | QUAN. | SIZE | PWR | SIG | TYPE | SYS |
|---|---|---|---|---|---|---|
| EMC Barrel Crates to Platform | | | | | | |
| Crate power 120 V | 30 | 0.3 dia | | x | multi | AC |
| PMT data | 30 | 0.2 dia | | x | fiber | MPX |
| PMT trigger | 300 | 0.1 x 0.8 | | x | flat | trg |
| Trg-Clk fanout | 1 | 0.1 x 0.8 | | x | flat | |
| Slow cnt/HDLC | 2 | 0.3 dia | | x | multi | HDLC |
| SMD gas pipe | 4 | 1.25 dia | | | pipe | gas |
| SMD cooling gas pipe | 4 | 0.5 dia | | | pipe | gas |
| LED etc serial line | 4 | 0.25 dia | | x | multi | LED |
| Slow cnt/HDLC | 2 | 0.3 dia | | x | multi | HDLC |
| EMC Barrel Platform to Counting House | | | | | | |
| Optical PMT data | 1 | 0.2 dia | | x | fiber | DAQ |
| Optical spare | 2 | 0.2 dia | | x | fiber | DAQ |

## VIII.3 Interfaces

INTERFACE to DAQ

Data format into DAQ:
64 byte header, first 16 bytes in standard STAR format. Included is token, trigger command word, DAQ command word, and switch to indicate sparsification
Each group of 160 PMT words is preceded by 4 words of header.
Included is token, crate number, and local counter.
The SMD readout has internal headers as in the SVT system which also match the standard format for DAQ.

Event size with No sparsification and no addresses is 10 kB for Barrel Towers, and 50 kB for SMD. With sparsification and the addition of addresses in pp events this may be reduced to less than 1 kB for Barrel Towers and 2 kB for SMD. Sparsification will be done in DAQ.
Event rates into DAQ for events utilizing TPC cannot be more than
100 Hz and will be kept to 60 Hz to accommodate livetime req.

Event Rates of EMC + SMD only will be less than 1000 Hz.
These are small events used for setting up triggers, etc.

EMC data collector must stop pushing upon DAQ busy.

EMC collector must push data upon Level 2 accept.

The data path into DAQ is 1 gigalink from EMC towers for baseline running
(upgrade to 1 for each of 24 TPC crates for High Lum pp)

The data path into DAQ is 8 gigalinks for SMD (stays fixed at 8 for high Lum pp)

**INTERFACE TO TRIGGER**

EMC input to Level 0:

sends to Level 0: 3600 bits to first layer of DSM boards (special grouping of bits )

| Level 0 Latency: | Tics |
|---|---|
| Cable | 2.1 |
| Integrator | 0.5 |
| FADC | 4 |
| FPGA s | 1 |
| Cable | 0.4 |
| | |
| total | 8 |

At least 3 more layers of DSM boards are needed for triggers utilizing EMC.

EMC can utilize Lvl 0 trigger up to 2 u sec after crossing (programmable)

EMC will respond to event Abort ( by clearing token from collector memory) so that the event is not transmitted to a higher level.

SMD sends nothing to LvL 0 in baseline running

EMC does not require LvL 1 or LvL 2 triggers for baseline running, only a level 1 accept at level 1 time.

For High Luminosity running, upgrades to trigger will be required to accommodate thresholds similar to those in baseline running but with a factor of 20 more luminosity and better live time.

Example:

For the High Lum pp upgrade, SMD will send 240 bits to be utilized either in Level 0 or Level 1 or very early Level 2 for correlation with EMC in geometric way.

Scalers:

EMC requires scalers of Luminosity monitor, and TCU (Trigger Control Unit) actions with tagging of all implemented deadtimes and pre-scales. Different pre-scales will be required at different EMC thresholds. These may be implemented upon EMC LVL 0 or upon TCU output.

The Spin Program requires that multiple EMC Luminosity outputs be scaled with both Polarization tagging and dead time tagging, and that TCU actions also be scaled with these tags.

## INTERFACE TO ONLINE

EMC communicates to slow control functions through Online.

EMC calibration data bases must be maintained with a database system within online and made available to DAQ, (and LVL 2 when it exists)

EMC HV data sets must be maintained for Heavy Ion and for pp.

EMC requires updating histograms and scaler displays from online, such as SMD pulse height/noise distributions.

## SLOW CONTROLS FUNCTIONS

Requirement:

There are slow controls inputs to EMC for the following functions:

- HV settings to Cockroft-Walton PMT bases
- Tower Calibration
- LED pulse control (trigger setup, timing, pattern)
- Charge injection to PMT electronics
- Monte-Carlo event downloading
- Trigger threshold programming on EMC cards
- Initialization of some circuits
- Read temperatures of PMT and electronics
- Monitor crate voltages
- Trigger Mapping programming
- Testing of Tower card data path
- Testing of Tower card trigger and LVL 0 interface
- Testing of EMC data collector
- Begin run functions
- Buffer clearing
- Monte-Carlo event downloading to Data Collector
- Bad channel list download to EMC Trigger
- Run Header information download to Data Collector
- Bad channel list downloading for Level-1 or 2 (if this option is exercised)
- SMD slow controls:

  HV control and Monitor
  HV current monitor
  Gas system control and Monitor
  Control cooling gas for SMD
  electronics temperature monitor
  electronics power monitor
  Crate power on/off
  Calibration Pulser Masking and Level Control
  Test data load and read

**INTERFACE TO OFFLINE**

EMC must supply
information on event format,
calibration databases (which have version numbers)
algorithms for energy in EMC towers,
algorithms for SMD shower fitting,

**INTERFACE TO GAS**

EMC requires ArCo2 for SMD operation.
EMC requires compressed air for cooling SMD electronics on the module.

**INTERFACE TO WATER**

EMC requires Water to cool the phototube boxes, in addition to the standard cooling of crates on the platform. The requirement is less than 30 GPM. at 60 to 65 Dec F.

**INTERFACE TO POWER**

EMC requires power for
EMC crates on the magnet, less than 15 kW, supplied by 120 V AC
SMD electronics on the magnet, less than 4 kW, supplied by 120 V AC
Slow controls functions, 5 and 12 V, less than 2 kW
Cooling fans on crates and in Phototube boxes, less than 3 kW
VME crates on the Platform, 4 Standard STAR crates

**INTERFACE TO BUILDING TEMPERATURE CONTROL**

EMC will dissipate the heat form EMC crates and SMD electronics into the building. This will be less than 25 kW.

---

## IX. Electromagnetic Calorimeter (EMC) Safety Issues

### IX.1 Overview

### IX.2 Description of the EMC Sub-system

The STAR electromagnetic calorimeter (EMC) will be capable of analyzing photons, electrons and hadrons. The EMC is a lead-scintillator sampling calorimeter. It is located inside the warm solenoid coils and the iron flux return. The inner radius is 2.20 meters and the length is 6.87 meters. It consists of 120 wedge shaped modules, each of which is 6 degrees in $\Phi$ and 3.43 meters in length. Each module is sub-divided into 40 projective towers. Each tower has 20 layers of lead and 21 layers of scintillator giving a total of 100,800 scintillator tiles of varying shapes. The total weight of the scintillator tiles is about 12 tons. Each scintillator tile is connected to a wavelength shifting optical fiber that will go to Melz FEU115M PMT's. All the fibers from the 21 tiles in each tower will go to a single PMT, of which there will be a total of 4800. The first scintillator tile in each tower will be read out by an additional fiber that will be connected to multi-anode PMT's at a later date, as an upgrade, provided funding becomes available.

The EMC will also include a shower maximum detector (SMD) with a high granularity to increase the two photon resolution of the EMC. The shower max detector in principal is similar in design to those used in the Collider Detector Facility (CDF) at FNAL. It consists of a double-sided wire proportional chamber and strip planes. The chamber will be filled with an Ar - CO2 (5-10 %) mixture at STP. The shower maximum detector will be biased up to 1.6 kV. The Preamplifier/Shaper Electronics cards will be placed at the $\eta$ =1 end of each EMC module. Each of these two cards will contain 150 channels of the strip readout electronics. The total power dissipation in the volume of the preamplifiers will be approximately 30 W. The low voltage power supply for preamplifiers will be +/- 6 V.

Radioactive sources will be used to calibrate the detector. The approach will use what is known as a "gattling gun" arrangement. $Co^{60}$ sources will be stored in lead garages ("pigs") when not in use. When in use the source will be pushed via a narrow diameter hypodermic tube into one of many (e.g. 30) larger diameter hypodermic tubes. Two of these larger diameter tubes will transverse each of the EMC modules at the depth of the Shower Maximum detector. Which of the tubes is followed is determined by the position of a rotating fixture that aligns one of the 30 tubes with the source coming out of the "pig". The purpose of the radioactive sources is to provide relative checks of the gains of the towers and an absolute calibration if correlated to test beam calibrations. The sources will be manipulated on the ends of the thin metal tubes using a motorized driver system.

## IX.3 Safety Analysis

### IX.3.1 Hazards

#### IX.3.1.1 Mechanical Hazards

After assembly the EMC is mechanically a static structure posing no mechanical hazards. Hazards do potentially exist, however, in the 150 ton mechanical system during abnormal conditions such as seismic activity. The EMC mechanical sub-system has been designed to withstand accelerations of 0.25g in all directions, in addition to gravitational loading, to protect against such eventualities.

Mechanical hazards do exist during the assembly and maintenance of the EMC, and these are discussed in section IX.5.

#### IX.3.1.2 Electrical Hazards

The full barrel EMC will utilizes 4800 single channel FEU115 PMTs. These are biased by Cockroft Walton active bases. The total estimated power dissipation of each base is estimated to be 100-150 mW. The input to each tube base will be 12-24 volt DC. The PMTs are each encased in a concentric mu-metal and soft iron magnetic shield. These shields will be grounded to the magnet backlegs via the support structure. Additionally a ground will be supplied via the DC input power line.

The Cockroft Walton bases are low power devices, and their dissipated power is mostly due to the current drawn by the leakage of the diodes and capacitors used in the multiplication chain and the actual current drawn by the PMT dynode structure. As such the overall heat generated in the base is very small. Furthermore the materials used in the construction of the bases are chosen according to specifications of BNL Environmental, Safety, and Health Standard section 1.5.2. The CW PMT base will have, in addition to built in active current limiting, passive current limiting (e.g., fuse or thermistors).

The PMTs and bases will be enclosed in light-tight boxes mounted outside of the magnet return iron yoke. The PMT boxes will be electrically grounded through their mechanical supports to the magnet iron. A second back-up ground will also be provided. Since the PMT bias voltage is confined to the PMT tube base, and the base and PMT are enclosed in a grounded box (e.g. a fire retarding composite light material with grounded conductive shielding), the electrical hazard is safely shielded from personnel exposure. These boxes will be cooled internally with a water chilled heat exchanger and electrical fans. The temperature inside the box shall be monitored through the slow controls at a few places along the length of the box.

The EMC slow controls is a VME/EPICS based system. Its primary function is to control and monitor the functions of various sub systems, and in cases of fault, notify the operators. As such this system is required to interface not only to the EMC sub systems requiring monitoring and control, it will be interfaced to the STAR experiment controls

for detector initialization and run controls. It will adhere to the standards set forth by the slow controls group's requirements document as well as to the SEAPPM 1.5.1. The EMC control is expected to occupy two 9U standard STAR VME crates. Several different commercially available VME I/O modules will be used to monitor and control different EMC sub systems. Of these the HDLC link with the Radstone interface module will be used (same system as the TPC FEE and the CTB) to program the EMC FEE. The remaining modules will be used to monitor analog as well as digital signals from various subsystems.

Because of the possible potential difference between the detector ground and the crate ground, currents may flow in the low impedance signal lines connecting the detector based electronics to the control modules; therefore it is essential to use isolated signal paths. All digital and analog cables shall be twisted pair differential or shielded coaxial to minimize ground loop and EMI problems.

One potential problem in any control application is the possibility of positive feedback in the control loop, which could result in unpredictable behavior of the system being controlled. Systems with multiple overlapping feedback loops are particularly susceptible to these kind of problems. Every effort will be made to avoid such control loop problems and in cases where such loops are necessary additional monitoring systems will be implemented. All control I/O modules shall meet the National Electrical Code specs. The current and voltages of the power supplies on the VME crates will be monitored.

The EMC conventional systems consist of the Low Voltage DC power, the associated power transmission lines, and the cooling systems for the power supplies and the PMT boxes. Significant amounts (60 crates @ 900 watts/crate + 120 SMD FEE @ 50 watts/chamber = 60 kW) of DC +/- 5V will be used by the FEE electronics. In addition approximately 50-100 amps of 24 V DC will be used by the PMT, LED, radioactive source calibration system, the PMT light tight box cooling systems, and the SMD gas system. The distribution of this power will follow guidelines laid out in NFPA-70 (NEC), and will be fused by separate paths to limit current to capacity. All personnel involved in the installation and operation of the EMC will receive training in the use of electrical systems as required by the Brookhaven ES&H and RHIC Departments. The power supplies used to supply the aforementioned currents are 5KW and 10KW DC switching supplies with current limiting and monitoring capabilities (ISO9001 qualified). All power supplies installed on the racks will be isolated from local ground (float with respect to the detector ground). The current and voltage levels of all DC power supplies will be monitored via EMC controls.

The distribution of power is a major concern. Due to the large DC currents involved we expect a large power dissipation in the power transmission lines. The large currents in the power distribution cables may result in DC magnetic fields that potentially could cause physical displacement of cables. Therefore all power cables shall be confined

to electrically grounded trays adhering to SEAPPM 1.5.2. recommendations.

The DC power supplied by the power supplies will be distributed via bus based metallic distribution boxes. The bus system shall adhere to the guidelines laid out in NFPA-70 (NEC). In addition, due to large self-inductance of the power transmission cables, it is expected that large transient current spikes may follow during power shutdown. These currents could cause local heating within the distribution boxes. Therefore special care will be taken to allow for rapid heat removal via a water chilled closed loop crate based cooling system (i.e. standard STAR chillers). In addition reverse biased fast high current schottky diodes will be used to shunt these large current spikes to avoid damage to the power supplies. The large energy stored in the power supply/transmission system also poses a serious health hazard to the personnel working with and around this system. This hazard will be abated by a lock-out tag-out (LOTO) procedure, mechanical barriers, electrical interlocks, and proper training of all personnel involved.

In order not to load the hall A/C system, adequate closed loop water chilled cooling will be provided (in the racks) to remove the dissipated heat in the power supplies. The PMT light tight boxes will be cooled internally by a water chilled cooler system. One potential problem is the possibility of water leakage in the tube fittings at the tube-chiller joints. This problem could be solved by the usage of special quick connect-disconnect Dry-Break high-pressure hose couplings. In addition, since the internal box temperature is monitored at several places along the length, a consistent change in the box temperature may indicate a problem with the chiller system (the fan system includes redundancies and therefore is much less likely to be the cause of a temperature rise).

All of the Shower Max systems will be enclosed inside the grounded metal box forming the environmental and light tight enclosure of the EMC module. The high voltage part of the power distribution system will have additional covering, so the electrical hazard is safely shielded from personnel exposure. Both the high voltage and low voltage power supplies will be fused by separate paths to limit current to capacity. The wire/strip shower max. Chambers will be biased up to 2 kV and would draw less than one mA with a trip set point of one mA during the first few minutes of each beam storage in RHIC. Six HV power supplies, along with fanout boxes, will be used to distribute the anode wire HV to all SMD chambers. Requirements for HV systems at RHIC are listed in section 1.5.0.1 of the RHIC project SEAPPM and BNL ES&HM (sec. 1.5) and will be applied without exception to the SMD high voltage power systems used in the STAR EMC. All personnel involved in the installation and operation of the SMD will receive training in the use of electrical systems as required by the Brookhaven ES&H and the RHIC Department.

The two SMD preamplifier/shaper cards at the $\eta$=1 end of each EMC will contain 150 channels of the strip readout electronics per card. The total power dissipation in the volume of the Preamplifiers will be approximately 30 W. The low voltage power supply

for Preamplifiers will be +/- 6 V.

The SMD conventional systems consist of the LV power, which is common to the EMC barrel (i.e., described in section 4.5.1.15), the SMD anode wire HV system, and the SMD gas system.

### IX.3.1.3 Material Hazards

The main materials that comprise the EMC are lead, plastic scintillator, aluminum, and steel. Of these, only lead presents a significant hazard. The lead used takes the form of sheets, alloyed with 1% Antimony for stiffness. All lead sheets are encapsulated within an aluminum and stainless steel environmental and light tight enclosure at the assembly sites prior to being shipped to BNL.

### IX.3.1.4 Radiation Hazards

Radioactive sources will be used to calibrate the detector. The approach will use what is known as a "Gattling gun" arrangement. The radioactive sources will be stored in lead garages ("pigs") when not in use. When in use the source will be pushed via a narrow diameter hypodermic tube into one of many (e.g. 30) larger diameter hypodermic tubes. Two of these larger diameter tubes will transverse the length of each of the EMC modules at the depth of the Shower Maximum detector. Which of the tubes is followed is determined by the position of a rotating fixture that aligns one of the 30 tubes with the source coming out of the "pig". Fig X-1 below is a photograph of one of these Gattling gun modules. The sources will be manipulated on the ends of the thin metal tubes using a motorized driver system.

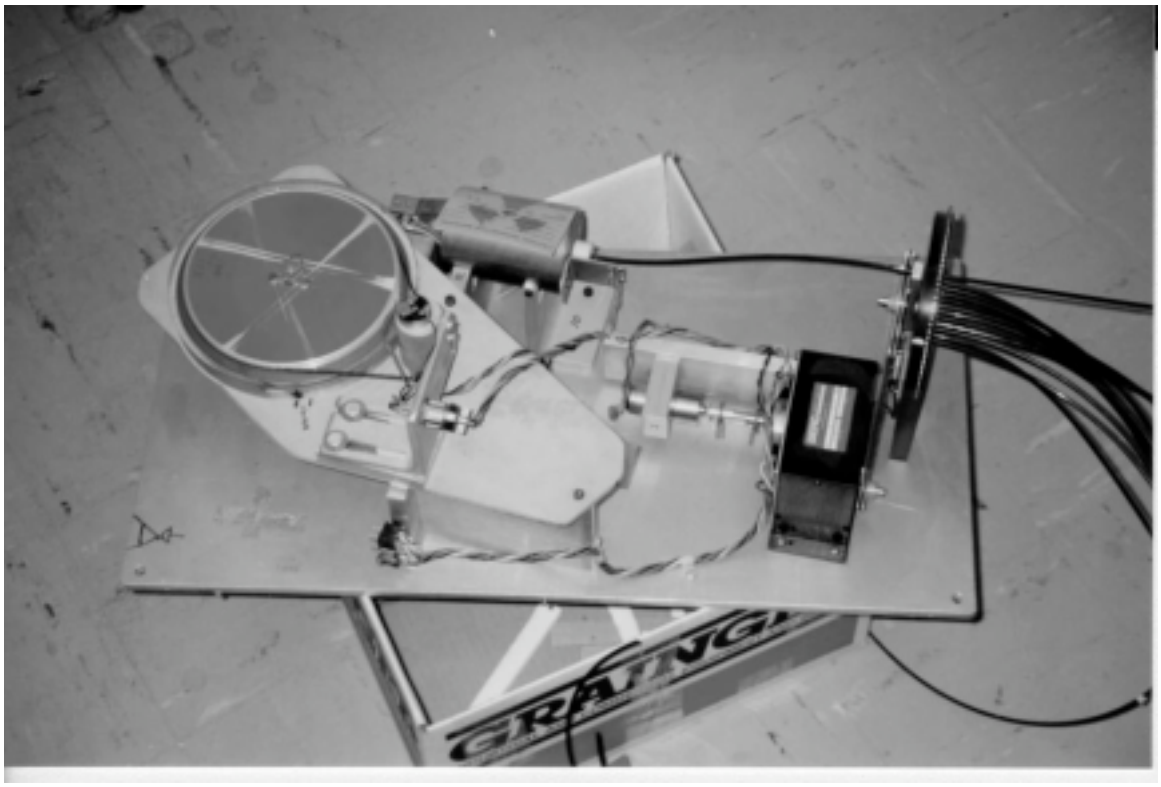

Figure IX-1. Photograph of an operating Gattling Gun from Argonne National Laboratory.

The "Gattling gun" fixtures attach to the outside of the STAR magnet. There will be a small number (1 to 8) of these fixtures. Each of the "Gattling Gun" calibration fixtures contains a single source. The sources will be approximately 3 mCuries of $^{60}$Co. If desirable the entire Gattling gun fixtures can be removed from the magnet and stored. The sources will be encapsulated and as such will not present a hazard of dispersing their radioactive material.

A hazard of this system is that for the brief period of time when the radioactive source is traversing the tube between the lead garage and the EMC module there is little radiation shielding. Once the source reaches the EMC module the levels of radiation are reduced by the considerable shielding factors inherent in the EMC. When the radioactive source calibration system is in use the appropriate area around the detector will be posted and temporary barriers will be put in place to restrict personnel access.

Operating personnel will receive proper radiation worker training as proscribed in the BNL ES&H Manual and the BNL Radiological Control Manual concerning the use and handling of the radioactive material. The radiation environment will be surveyed and ALARA practices strictly adhered to and enforced. All workers will be made aware of the necessity to maintain stringent common inventory control of all radioactive materials.

**IX.3.1.5 Pressure Vessel Hazards**

The SMD gas system consists of a high purity Ar/CO2 premixed gas manifold

system and a nitrogen purge gas system. Both of these systems consist of automatic changeover, high purity, and continuos manifold systems with a maximum inlet pressure of 3000 psi. Multistage regulators will reduce this pressure down to 2-10 psi for delivery to the SMD modules. At any given time one of these gasses can be used in the SMD. While the two gasses used in the SMD are non-flammable and non-hazardous they are delivered in high-pressure vessels and therefore are a source of health hazard. As such all the components of the gas inlet manifold system will comply with the requirements of the BNL ES&HM (sec. 1.4.0 and 1.4.1).

All high-pressure lines will be equipped with pressure relief valves. The pressure in the gas manifolds both on the high pressure and low pressure sides of the regulators will be readout via pressure transducers, and monitored via slow controls. In addition the flow and pressure are also monitored in the main 2 inch gas line and flow may be adjusted via the slow controls.

The distribution of gas to the SMD modules is provided via two manifolds located at the two ends of the detector. Each manifold consists of 30 small distribution systems, which are electronically controlled via the EMC slow controls. These distribution boxes are daisy chained via 1 inch flexible Teflon hoses with stainless steel shielding. The distribution boxes (these are actually open boxes) are metallic and contain electronic PC boards to drive the solenoid gas valves, which control the flow of the gas into the SMD modules. These valves are used to adjust the flow rates for the higher flow rates required during the initial flushing of the system with the nitrogen gas, and to reduce the flow down to the nominal value during the normal operation of the system. The total electrical power dissipation in each valve is less than 1 watt. The power requirement is 30 mA @ 24 V. Therefore, the dissipated heat load can be easily taken care of by convection cooling. Due to the low power dissipation of each distribution box we do not expect any hazards associated with heat or electrical issues. All the electronics design shall adhere to SEAPPM 1.5.1.

The pressure in the inlet of these boxes is 2-10 psi and in the outlet is slightly higher than atmospheric pressure. Flexible, fire retardant tubing will be used to carry the gas from the distribution manifold to the SMD module, and return the exhaust gas to a bubbler. The bubbler will be monitored with an electronic system (e.g., a video system or a photoelectric cell). This will allow one to detect low flow rates in leaky chambers. The gas will be vented to the atmosphere. Since the total flow rate is less than 5 lpm the ventilation system of the hall should be able to easily handle purging of this gas.

### IX.3.1.6 Magnetic Hazards

The close proximity of the EMC phototube boxes to the solenoid magnet power connections and magnet cooling water hoses raises some additional safety issues. In addition the large magnetic fields could present a substantial personnel hazard if the magnet were energized during EMC maintenance work. These hazards will be abated by

a lock-out tag-out (LOTO) procedure, mechanical barriers, electrical interlocks and proper training of all personnel involved.

#### IX.3.1.7 Fire Hazards

The most obvious fire safety issue is the large amount (~12 tons) of combustible fuel present in the polymer scintillator. This fire hazard is minimized by the isolation of the tiles in stainless steel and aluminum light-tight boxes, and by their separation by lead plates. The degree of isolation limits the access of oxygen to support combustion and requires an enormous amount of heat to raise the temperature of the scintillator material to the ignition point. For example, polyvinyltoluene, a typical plastic used for scintillators, is stable up to 300 C. The amount of heat required to raise 150 tons of what is primarily lead to this temperature is enormous. No credible energy source exists in the EMC to generate such amounts of heat. It is also unlikely that a failure in the adjacent solenoid would generate sufficient amounts of heat to pose a combustion hazard for the EMC. As discussed in the section of the STAR safety document on the solenoid magnet, systems will exist to detect failures (i.e. cooling or direct electrical shorts) and shut the magnet down in a controlled fashion to eliminate the risk that the solenoid could generate sufficient heat to damage the EMC.

The shower max chambers will be operated with a non-flammable $Ar/CO_2$ gas mixture and hence will not contribute any significant fire hazard. The shower max chambers themselves do not contain any flammable components. It is possible that the leakage of gases from the TPC could collect in the area where the EMC is located and present a flammable gas hazard. The hazard can be reduced to an acceptable level by sensors to detect the build up of such gases and allow the operators to shut down the flow of flammable gas to the TPC, to purge the flammable gas from the TPC and shutdown electrical power to STAR.

Some of the EMC electrical systems present a level of fire risk. These include the connections to the low voltage power supplies before the fuses for wires to the electronics crates. This hazard will be mitigated by strict adherence to the provisions of NFPA-70 (NEC) and the presence of sensors designed to detect combustion and trigger the shutdown of electrical power and fire suppression systems, or warn the operators that a problem exists.

### IX.3.2 Safety Systems

#### IX.3.2.1 Detection

**Electrical Safety Systems**

The PMTs and bases will be enclosed in light-tight boxes mounted on the outside of the magnet return iron yoke. The PMT boxes will be electrically grounded through

their mechanical supports to the magnet iron. A second back-up ground will also be provided. Since the PMT bias voltage is confined to the PMT tube base, and the base and PMT are enclosed in a grounded box (e.g. a fire retarding composite light material with grounded conductive shielding), the electrical hazard is safely shielded from personnel exposure. These boxes will be cooled internally with a water chilled heat exchanger and electrical fans. The temperature inside the box shall be monitored through the slow controls system at a few places along the length of the box.

Please refer to section X.2 for a description of the EMC slow controls VME/EPICS based system.

**IX.4 Assembly & Maintenance**

Because the EMC has an overall weight of 150 tons for the barrel and 30 tons for each end cap, there are intrinsic safety questions concerning system integration and the movement of heavy articles during assembly or disassembly. The EMC support hardware, which couples the EMC to the STAR solenoid magnet and iron return yoke, is broken up into 270 pieces each weighing up to 50 lb. and will be installed by hand. After the installation of the primary attachment supports, 120 rails, weighing a few hundred lbs. each, will be installed using a lifting fixture on the inside surface of the STAR magnet. Each calorimeter module will weigh about a ton. To install them, a lifting fixture that can be attached to the installed rails will be used. The one ton calorimeter modules will be installed on rails, and lifted into place. The modules will then slide from the fixture rails onto the permanent rails.

The EMC electronics will be mounted outside of the magnet iron and some of the boxes containing PMTs will be as much as 27 ft above the floor. These modules will have to be accessed during detector commissioning. Height may also be a problem on the end cap electronics since there are no readily available electronics platform floors near-by. Man lifts or cherry pickers may have to be used. About 1/3 of the detector electronics will be mounted on the pole pieces.

# X. COST, SCHEDULE, MANPOWER, AND FUNDING

## X.1. Detector Scope

The detector configuration necessary in order to accomplish all the physics goals encompassed in this report includes the following:

- The full EMC barrel consisting of 120 calorimeter modules (with internal shower maximum, and pre-shower detectors)
- One endcap calorimeter (with internal shower maximum, and pre-shower detectors)

In nucleus-nucleus collisions, the barrel calorimeter provides the means to measure the neutral transverse electromagnetic energy. In addition to affording a more detailed understanding of the transfer of energy from the projectile frame to mid-rapidity, the improved resolution in determining the total transverse energy deposition will allow the creation of highly selective triggers in order to search for rare events predicted to result if a color deconfined plasma of quarks and gluons is produced. Since both the coverage of the barrel calorimeter and measurement of the neutral energy are necessary for the detection of jets, the barrel EMC is also necessary to utilize the interaction of hard-scattered partons with the surrounding medium as a penetrating probe of the early stages of the collision. Additionally, the measurement of jets within the coverage of the barrel is necessary for the study of gluon shadowing in pp and pA interactions, which is essential if the particle production in nucleus-nucleus collisions at RHIC is to be understood.

The acceptance of the endcap calorimeter is necessary to study gluon shadowing in pp and pA interactions and to detect gluon and quark jets in polarized pp interactions in order to determine the contribution to the proton spin from the angular momentum carried by gluons. Since both of these studies are most easily carried out by studying the $qg \rightarrow \gamma q$ Compton subprocess, efficient detection of direct photons above $p_t \sim 10$ GeV/c is essential. The shower maximum detector provides the fine spatial resolution necessary to distinguish direct photons from photons emanating from $\pi^0$ and $\eta^0$ decay.

The modular nature of the calorimeter design makes it possible to stage the construction of this detector in a number of ways. Depending upon which staging plan is adopted, the physics capabilities of the EMC also vary. The present report addresses one specific option. In this option, all 120 calorimeter modules will be constructed over a period of four years, starting with fabrication in early 1999. Each module will contain a gas wire-strip shower maximum detector together with its on chamber readout electronics, and the optical components required for the pre-shower detector. The phototubes and readout electronics for the pre-shower detector will be deferred until a later date. However, it is essential that the optical fibers be installed during module construction due to the impracticalities involved in retrofitting them. These fibers only constitute a few percent of those required for the barrel calorimeter and the additional costs involved are small. The completed modules would be installed during summer shutdowns at RHIC, together with their complete readout and triggering electronics allowing the full $\Delta\phi \times \Delta\eta$ segmentation of $0.05 \times 0.05$ to be fully realized for each module after installation. The barrel calorimeter is expected to be complete in 2003, at which time it will have 4800 readout channels. The support system for the calorimeter has been specifically designed for this staged detector construction, and allows for the installation of modules without

removing other detector components from STAR. This system has been built, and is in place in the STAR magnet for the full barrel EMC. Construction of the endcap calorimeter would be deferred at this time. Provisional estimates of the cost of this option is $12.6M in FY98 dollars including $2.2M in contingency. Several areas have been identified in which contributions from participating institutions could result in significant savings. These include machining of mechanical components, labor for module assembly, and fabrication of the shower maximum detector. The estimated total cost of components and labor which will contributed is $11.2M in FY98 dollars, and these savings have been included in generating the $12.6M cost estimate for the calorimeter.

The physics provided by this implementation of the calorimeter is significant. Specifically, with the full EMC barrel, the resolution on the reconstructed global transverse energy for AuAu interactions, for example, will improve to ~2%. The resolution available at the trigger level for the global neutral transverse energy would be ~2.5%. With this resolution, STAR will be able to search at the trigger level for events exhibiting unusual isospin abundances or unusual correlations between energy density and entropy density. Additionally, the improved resolution provided by the EMC will afford a more detailed understanding of the transfer of energy from projectile rapidity to mid-rapidity. As the EMC barrel is large compared to a jet radius ($\sqrt{(\Delta\eta)^2 + (\Delta\phi)^2} \leq 0.7$) it will also be possible to measure inclusive jets and high $p_t$ $\pi^0$s from parton scatters within $|\eta| \leq 0.3$, or larger with out of cone corrections. This will allow STAR to study the energy loss of hard-scattered partons using inclusive jets as well as $\gamma$-jet and jet-jet coincidences.

With the subsequent addition of one of the endcap calorimeters, instrumented with a shower maximum detector, the measurement of gluon shadowing in pA collisions would be possible. This would allow STAR to determine the initial conditions in AA interactions and make full use of perturbative QCD in predicting the pre-equilibrium phase of the collision. Funding for an endcap calorimeter is currently being sought from other sources.

As discussed in section X.3, the back loading of the calorimeter funding profile means that only ~20% of the funding is available in time for Day 1 operations at RHIC. Completing the required electronic and electrical engineering, and the necessity to fund and install all of the barrel calorimeter support system by March 1998, so as to avoid the subsequent removal of the TPC, further reduces available funds for the Day 1 detector. In order to maximize the detector coverage, several aspects of the EMC electronics are also designed to be staged. The interface to DAQ will eventually involve sending all of the EMC data to 24 TPC crates for use in the Level 3 trigger. This will be simplified to one interface card for early running. The EMC Level 0 trigger can provide basic quantities such as $E_t$, high tower energy for photons, a crude jet trigger, and luminosity scaler data at Day 1 with limited electronics. It will be upgraded for more sophisticated electron, photon, and jet triggers as funding allows.

As discussed in section X.3, we expect to have about 10% of the detector modules in place for Day 1 physics. The design, prototyping, and some early production of electronics will be done before Day 1 to ensure our ability to utilize the EMC in the RHIC physics program. The Day 1 detector implementation will have physics

capabilities for several measurements in AuAu and pp within a limited solid angle. The detector's trigger capability, while limited with respect to a full calorimeter, will be a significant addition to STAR as it forms the only trigger based upon energy and not just multiplicity.

## X.2 Detector Summary Cost Estimates

The projected costs of the Barrel EMC and SMD have been re-evaluated since the original estimates, by the Argonne National Laboratory and the Lawrence Berkeley Laboratory, presented in the CDR. This re-evaluation has been done by the participating institutions that will be responsible for delivering each of the appropriate subsystems to the experiment. These cost estimates have taken into account the considerable changes in the mechanical design of the detector required to provide increased mechanical segmentation, along with the considerably more advanced schemes for the electronics, trigger, and data acquisition. The costs presented here include considerable contributions from the participating institutions, both in terms of labor and facilities, as well as significant savings over National Laboratory Labor rates. Such savings amount to $11.2M for detector configuration discussed here.

The summary cost estimates in FY98 dollars for the detector considered here are presented in Table X.2-1. They include EDIA, labor, materials, and contingency, but do not include the EMC prototype funding received in FY96. The average contingency of the EMC barrel and SMD is ~21%. The cost projection below includes funding for the complete module installation tooling, but installation labor for just the Day 1 modules. It is presently thought that by the time the FY00 calorimeter modules are ready for installation, STAR will be eligible for support from RHIC operations. In this instance, most of the installation of the barrel EMC modules would be performed by riggers and technicians supported by RHIC with supervision provided by STAR personnel.

| | | % | K$ | | | | |
|---|---|---|---|---|---|---|---|
| **WBS #** | **WBS OR ACTIVITY DESCRIPTION** | **CONT** | **MATL** | **LABOR** | **WBSBASE** | **CONT** | **TOTAL** |
| **4.5** | **ELECTROMAGNETIC CALORIMETER** | **21** | **6249.1** | **4135.1** | **10384.2** | **2220.0** | **12604.2** |
| **4.5.1** | **BARREL TILE CALORIMETER** | **21** | **5650.4** | **3234.7** | **8885.1** | **1878.3** | **10763.4** |
| 4.5.1.1 | Converter Plates and Module Structure | 18 | 672.7 | 122.8 | 795.5 | 140.6 | **936.1** |
| 4.5.1.2 | Tile-Fiber System | 20 | 1857.1 | 632.1 | 2489.2 | 500.7 | **2989.9** |
| 4.5.1.3 | PMT System | 23 | 1153.9 | 101.9 | 1255.8 | 286.5 | **1542.3** |
| 4.5.1.4 | Calibration Systems | 25 | 79.6 | 44.4 | 124.0 | 30.6 | **154.6** |
| 4.5.1.5 | Module Final Assembly, Tests, and Shipment | 24 | 416.2 | 540.7 | 956.9 | 228.3 | **1185.2** |
| 4.5.1.6 | EMC Prototypes | 0 | 30.0 | 1.4 | 31.4 | 0.0 | **31.4** |
| 4.5.1.7 | Transportation and Handling Systems | | | | | | |
| 4.5.1.8 | EMC Installation and Test | 22 | 226.1 | 361.3 | 587.4 | 131.6 | **719.0** |
| 4.5.1.9 | EMC FEE | 29 | 519.5 | 407.6 | 927.1 | 273.5 | **1200.6** |
| 4.5.1.10 | EMC Contribution to DAQ System | 24 | 34.5 | 191.9 | 226.4 | 54.0 | **280.4** |
| 4.5.1.11 | EMC Contribution to Online System | 25 | 7.0 | 87.6 | 94.6 | 24.0 | **118.6** |
| 4.5.1.12 | EMC Contribution to Trigger | 16 | 177.5 | 0.4 | 177.9 | 28.5 | **206.4** |
| 4.5.1.13 | EMC Controls | 18 | 61.2 | 19.4 | 80.7 | 14.8 | **95.5** |
| 4.5.1.14 | EMC Level 1 Trigger | | | | | | |
| 4.5.1.15 | EMC Conventional Systems | 13 | 140.0 | 17.5 | 157.4 | 20.5 | **177.9** |
| 4.5.1.16 | Project Integration and Management | 22 | 0.0 | 649.8 | 649.8 | 144.7 | **794.5** |
| 4.5.1.17 | Module Supports | 0 | 275.1 | 55.9 | 331.0 | 0.0 | **331.0** |
| | | | | | | | |
| **4.5.2** | **BARREL SHOWER MAX** | **23** | **598.7** | **900.4** | **1499.1** | **341.7** | **1840.8** |
| 4.5.2.1 | Chambers | 20 | 241.5 | 545.0 | 786.5 | 157.7 | **944.2** |
| 4.5.2.2 | Shower Max Prototypes (full scale) | 22 | 21.3 | 29.6 | 51.0 | 11.1 | **62.0** |
| 4.5.2.3 | Transportation and Handling Systems | | | | | | |
| 4.5.2.4 | Shower Max Electronics | 29 | 268.3 | 317.8 | 586.1 | 167.6 | **753.7** |
| 4.5.2.5 | Shower Max Conventional Systems | 7 | 67.5 | 8.0 | 75.6 | 5.4 | **80.9** |

Table X.2-1. The estimated cost of the EMC detector including the EMC modules, their support structure and associated electronics, installation and testing, project management, and systems integration including EDIA in FY'98 dollars. The total cost of the calorimeter and SMD is given in WBS # 4.5. The cost of the EMC and the SMD are given separately under WBS #'s 4.5.1 and 4.5.2 respectively. The costs associated with Transportation and Handling Systems (WBS items 4.5.1.7 and 4.5.2.3) have been relocated under the WBS number of the system to which they pertain, and hence these line items have zero cost. Level 1 trigger is deferred.

## X.3 Funding Profile and Schedule Estimates

All of the engineering required to interface the barrel calorimeter to the STAR detector has already been carried out, and the module supports and rail systems are fully installed into the STAR magnet. In addition, the engineering directed at the design of the calorimeter modules, and the choice of technology has been accomplished, meaning that the EMC modules are now ready to enter a construction phase. Initial funding received would be devoted to completing the electronic engineering of the EMC and SMC readout, and the setup of the module construction facilities, initially at Wayne State, with a second construction facility being added later at Argonne National Laboratory when

funds permit. Upon completion of this setup phase, full-scale module production would commence in early calendar 1999.
The funding profile assumed in the following schedule estimate for the construction of the detector is shown in Table X.3-1 below. This profile, and the previous cost estimates, do not include the EMC prototype funding received in FY96.

| | FY96 | FY97 | FY98 | FY99 | FY00 | FY01 | FY02 | FY03 |
|---|---|---|---|---|---|---|---|---|
| Funding per FY $k | $0k | $600k | $1,000k | $2,000k | $2,300k | $2,300k | $2,300k | $2,104k |
| Cumulative Funding $k | $0k | $600k | $1,600k | $3,600k | $5,900k | $8,200k | $10,500k | $12,604k |

Table X.3-1: Assumed funding profile (FY98 dollars) for the construction of the STAR Electromagnetic Calorimeter including 4800 towers, the barrel SMD, and the pre-shower optical components.

The majority of the funds received in FY97 were required for completion of the EMC support system. Most of the funds received in FY98 and FY99 would be required for the setup of the EMC module production facilities and the remaining electronic and electrical engineering to complete the design of the calorimeter readout electronics and trigger. Module construction would begin in early 1999. Under the assumption that none of the contingency is required to be spent, and that all funds received can be applied to the base cost of the detector, the module production profile would be as shown in Table X.3-2. Table X.3-3 shows the module production profile under the assumptions that the full contingency is needed on each WBS activity as that activity is completed. Table X.3-2 can be regarded as the most optimistic approach, whilst table X.3-3 can be regarded as a pessimistic approach. It is likely that these two table bracket the expected module production rates and thus the expected number of modules available for Day 1 operations will be between 8 and 18 modules.

| | FY96 | FY97 | FY98 | FY99 | FY00 | FY01 | FY02 | FY03 | Total |
|---|---|---|---|---|---|---|---|---|---|
| # Modules per FY | 0 | 0 | 0 | 18 | 33 | 36 | 34 | 0 | 120 |
| Cumulative # of Modules | 0 | 0 | 0 | 18 | 50 | 86 | 120 | 120 | |

Table X.3-2. Estimated rate of module production for the STAR Electromagnetic Calorimeter given the funding profile shown in Table X.3-1, and the assumption that zero contingency is required. This can be regarded as the most optimistic approach. The rate of module production is funding, not facility, limited and consequently the spending of contingency will lead to slippage from these production numbers.

| | FY96 | FY97 | FY98 | FY99 | FY00 | FY01 | FY02 | FY03 | Total |
|---|---|---|---|---|---|---|---|---|---|
| # Modules per FY | 0 | 0 | 0 | 8 | 26 | 29 | 29 | 27 | 120 |
| Cumulative # of Modules | 0 | 0 | 0 | 8 | 34 | 64 | 93 | 120 | |

Table X.3-3. Estimated rate of module production for the STAR Electromagnetic Calorimeter given the funding profile shown in Table X.3-1, and the assumption that the full contingency is needed on each WBS activity as that activity is completed. This can be regarded as a pessimistic approach.

These production profiles are funding limited. Schedule estimates of the production of similar calorimeter modules for ZEUS suggest that such modules could be completed at the rate of ~30 per year, per facility, making the maximum module production rate ~60 per year for the two construction sites.
The resource-loaded schedule is shown in Figures X.3-1 and X.3-2. The schedule again makes the assumption that none of the contingency is required. Figure X.3-1 shows the schedule leading up to Day 1 physics with a calorimeter patch of between 8 and 18 modules. It highlights the principle activities scheduled between now and Day 1. These are:

- The construction of a complete full sized mechanical prototype module and the subsequent tests of the installation protocols with a full sized mockup of a sector of the STAR magnet.

- Installation and removal of the full sized mechanical prototype into the STAR magnet to test the module installation tooling and procedures prior to the TPC being installed.

- The construction of a second, fully functional, prototype and the activities leading to its testing at BNL in October '98 to establish the relationship between the module's response to real particles and the various calibration methods that will be employed.

- The completion of the electronic and electrical engineering required to finalize the design of the readout electronics and trigger.

- The completion of the module construction facilities.

- Construction and installation of the first modules and their associated electronics.

Figure X.3-2 shows the module construction schedule after Day 1 and until the completion of the barrel calorimeter. What is clear from the schedule is that module construction continues over a relatively long period, with major procurements being staged to avoid periods of discontinuity. With the modular design of the EMC, modules

constructed in one year will be installed when the STAR detector is rolled out into the Assembly Building during the RHIC shutdown of the following year. Under the assumed profile and schedule estimate, the last modules are installed during the RHIC summer shutdown in 2002. Spending on contingency will cause some slippage, resulting in the last modules being installed during the summer shutdown in 2003 instead.

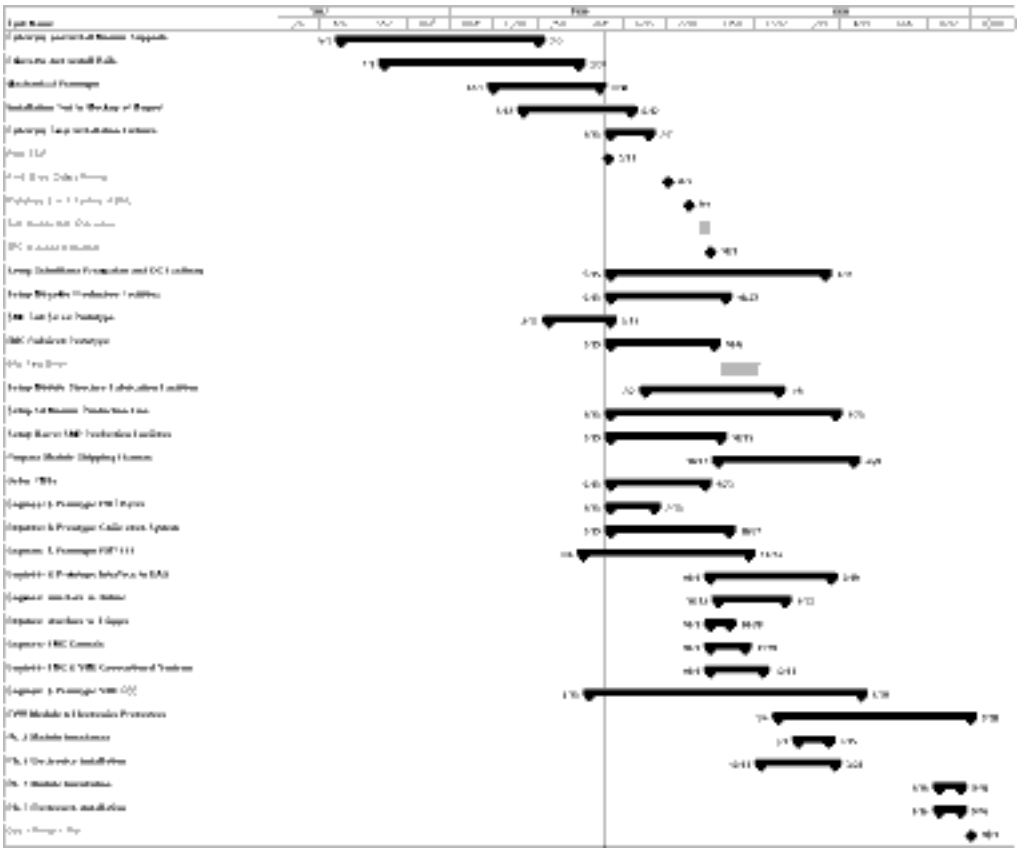

*Figure X.3-1. Schedule projected for the construction of the STAR Barrel Electromagnetic calorimeter up to Day 1, given the funding profile shown in Table X.3-1 under the assumption of needing zero contingency. The time scale is given in financial years.*

*Figure X.3-2. Schedule projected for the construction of the STAR Barrel Electromagnetic calorimeter after Day 1 until completion of the calorimeter, given the funding profile shown in Table X.3-1 under the assumption of needing zero contingency. The time scale is given in financial years*

.

## X.4 Project Effort

The estimated level of effort required in order to complete the full barrel calorimeter, SMD, and optical systems for the pre-shower detector, according to the schedule presented in Figs. X.3-1 and X.3-2 is indicated by fiscal year in Figure X.4-1. The effort is shown for the following categories: Engineering (EN), Engineering Associate (EA), Drafting (DR), Administration (AD), Technician (TE), and Machinist (LA). The workload generally follows the funding profile, peaking at 28 man-years per fiscal year in FY01. The workload is higher in FY98 than FY99 primarily due to engineering associated with the setup of the module production facilities and the design of the electronics and trigger. The total effort required to complete the project is around 90 man-years. The effort level includes the sizable contributions from the collaborating institutions discussed in section X.1.

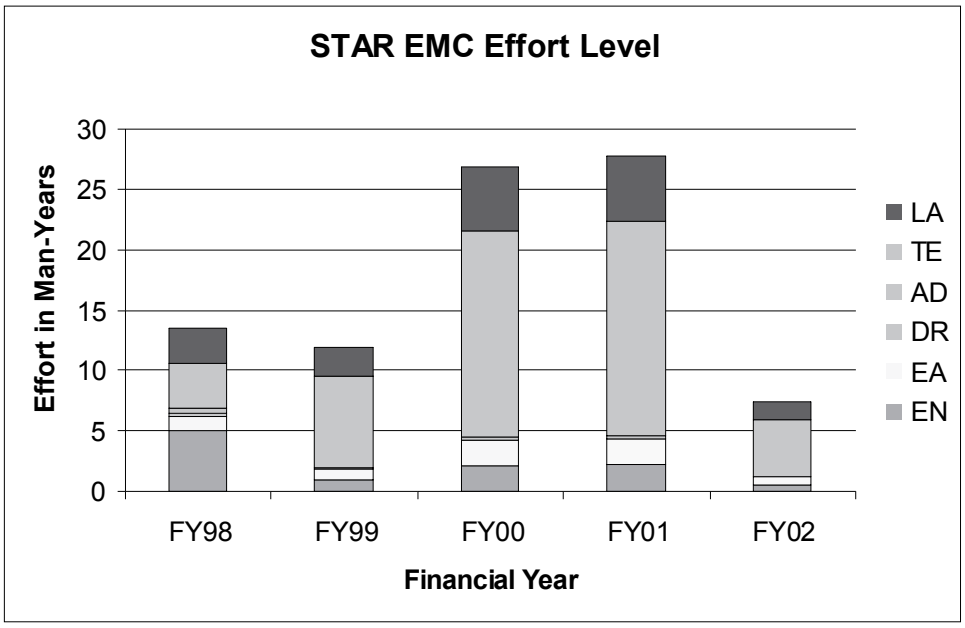


Figure X.4-1. The estimated level of effort in man years necessary for the completion of the STAR Electromagnetic Calorimeter according to the funding profile in Table X.3-1 and the schedule in Figures X.3-1 and X.3-2. The level of effort estimate assumes zero usage of contingency.